Tectonometamorphic evolution of Medium-P granulites of the Namaqua Metamorphic Province at the Richtersveld – Gordonia Subprovince marginal zone, southern Namibia

Teboho Sebetlela

a thesis submitted for the degree of

Master of Science

in the Department of Geological Sciences, University of Cape Town

South Africa.

2017

Abstract

The western Namaqua Metamorphic Complex (NMC) is a Mesoproterozoic medium- to low-pressure, high temperature metamorphic belt that is characterised by a complex, polyphase Mesoproterozoic metamorphic history. Using an integrated approach, the P-T-t evolution of a portion of the marginal zone between two major tectonic domains in the western NMC: the Richtersveld and Gordonia Subprovices is investigated, with the aim of resolving a P-T-t path for the peak to retrograde evolution of a major regional thrust, that will in turn help to elucidate its geodynamic significance.

The Kum Kum Klippe represents a structural outlier of the Gordonia Subprovince, located at the frontal zone of the Grunau Terrane, where the Grunau Terrane (hangingwall), Pella Terrane (footwall) and the bounding Lower Fish River Thrust Zone (LFRTZ) are all well exposed. The Pella Terrane in this region shows significant lithological heterogeneity and is constituted by felsic orthogneisses, metamafic rocks and leucogranite intrusives, while the Grunau Terrane is dominated by pelitic granulites. The LFRTZ along the southwestern margin of the Kum Kum Klippe is a ∼30–40 m wide tabular zone primarily localised in the Pella Terrane.

Phase equilibria modelling of pelitic granulites from the hangingwall constrains peak metamorphic P-T conditions of ∼5.2–5.9 kbar and ∼790–815°C which are correlated to a monazite growth event at c. 1262–1184 Ma. Sheared pelitic granulites constrain the P-T conditions for early stage shearing in the LFRTZ to ∼2.8–5.0 kbar and ∼640–785°C which likely occurred shortly after peak metamorphism. Pella amphibolite samples from the footwall and LFRTZ constrain the conditions of tectonic juxtaposition to ∼2.7 kbar and ∼542°C which must have occurred subsequent to cooling from suprasolidus conditions and is thus constrained at <1184 Ma.

The constrained peak to retrograde P-T-t path is characterised by a short segment

of substantial decompression subsequent to peak metamorphic conditions at c. 1262–1184 Ma. This is followed by a period dominated by cooling with only a small component of concomitant decompression, which together with the early decompressive segment likely correspond to the period of retrograde shearing, which ultimately led to tectonic juxtaposition in the mid-amphibolite facies at c. <1184 Ma.

The P-T path presented suggests that the LFRTZ does not represent a terrane bounadry that juxtasposes crustal entities which converged and collided as the result of Wilson cycle subduction to collision tectonics. Contrastingly the metamorphism at highly elevated geotherms and largely cooling dominated retrograde trajectory determined in this study are more compatible with a continental backarc setting, which has recently been proposed as an alternative model. Thus the P-T constraints presented in this study contradict the collisional model and terrane concept that has long been widely accepted for the western NMC.

Acknowledgements

This research project would not have been possible without funding from the National Research Foundation (NRF) and additional support from the Council for Geosciences (CGS). I would like to express gratitude to my academic supervisor for this research, Dr Johann Diener whose guidance and patience has been invaluable. Thanks are also due to Dr Paul Macey whose experience and support assisted greatly in the completion of the fieldwork leg this project. I am also thankful for my friends and family for thier support and patience throughout my research.

Teboho Sebetlela

Contents

List of Tables

List of Figures

Chapter 1

Introduction

The Namaqua-Natal Province (cf. Namaqua Metamorphic Complex; NMC) is a Mesoproterozoic arcuate metamorphic belt along the southern and western margins of the Archean Kaapvaal Craton in southern Africa (Figure 1.1; Miller, 2008; Becker *et al.*, 2006; Thomas *et al.*, 1994). The belt is understood to form the southern African portion of the global Mesoproterozoic orogen related to the assembly of the Rodinian supercontinent and has been postulated to be contiguous with similar high-grade gneisses of comparable age belonging to the Kibaran and Grenvillian orogens of Central Africa and North America respectively (e.g. Thomas *et al.*, 1994; Hartnady *et al.*, 1985).

The NMC records evidence of two major tectonothermal events, the first of which is of Eburnian age at c. 1.7–2.0 Ga and has been termed the Orange River Orogeny (ORO; Reid, 1979). The second and more regionally dominant of these occurred at c. 1.0–1.2 Ga and has been referred to as the Namaqua Orogeny (Tack *et al.*, 1994; Thomas *et al.*, 1994; Clifford *et al.*, 2004). Although Mesoproterozoic tectonogenesis in the central African type area of the Kibaran Orogeny ended by 1200 Ma, the term 'Kibaran' has nonetheless also been used to refer to this tectonogenesis in the NMC – which is of broadly comparable age, but slightly younger at c. 1210–1020 Ma (Clifford *et al.*, 2004), falling outside of the period which defines the Kibaran Orogeny *sensu stricto*. Thus, as suggested by Tack *et al.* (1994) and Thomas *et al.* (1994), the term 'Namaqua Orogeny' is preferred, and encompasses all tectonogenic events in the NMC related to the global Mesoproterozoic orogeny. Based largely on the apparent presence of two distinct zircon growth events within the Namaqua Orogeny (e.g. Eglington, 2006; Clifford *et al.*, 2004), this event has been postulated in the traditional literature to comprise two distinct tectonothermal episodes which are referred to as the 'Okiepian' and the 'Klondikean', at c. 1190±30 Ma and c. 1040±30 Ma respectively (Clifford *et al.*, 2004; Eglington, 2006).

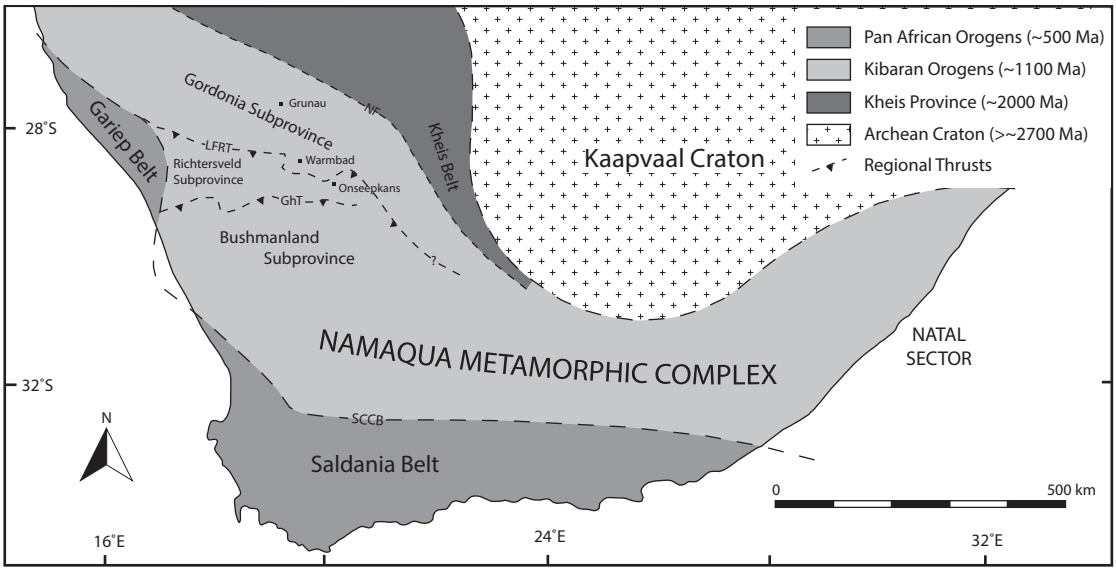

Figure 1.1: Location and regional tectonic setting of the Namaqua Metamorphic Complex in southern Africa and its relationship with Pan African belts as well as pre-existing Eburnian (Kheis Province) and Archean crust. The three major tectonic domains of the western NMC (from South to North: Bushmanland, Richtersveld and Gordonia Subprovinces) are illustrated along with the major regional thrusts (modified after: Hartnady *et al.* (1985); Thomas *et al.* (1994); Pettersson *et al.* (2009)). The Saldania Belt largely subcrops beneath the Cape Fold Belt, which occupies an over-lapping regional domain. GhT - Groothoek Thrust; LFRT - Lower Fish River Thrust; NF - Namaqua Front; SCCB - Southern Cape Conductive Belt.

1.1 The western Namaqua Metamorphic Complex

In western extent of the NMC, the effects of the Namaqua Orogeny included voluminous granitoid magmatism and high-grade, medium- to low-pressure, high temperature (MP/LP-HT) metamorphism in the upper-amphibolite to granulite facies (Waters, 1988; Becker *et al.*, 2006; Diener, 2014). The resultant domain which comprises various Mesoproterozoic granitoids and supracrustal gneisses as well as Paleoproterozoic volcano-sedimetary rocks (Barton & Burger, 1983; Blignault *et al.*, 1983; Colliston & Schoch, 2000) is widely referred to as the western Namaqua Metamorphic Complex (Kröner *et al.*, 1983; Miller, 2008; Bial *et al.*, 2015a). In the Namaqualand region, the western NMC can be subdivided into three major shear zone and crustal linaement bounded tectonic domains. The largest and southern-most of these is the Bushmanland Subprovince which occurs immediately south of the Richtersveld Subprovince (e.g. Colliston & Schoch, 2006; Blignault *et al.*, 1983). In turn, the Richtersveld Subprovince occurs in direct tectonic juxtaposition with the NW-SE trending Gordonia Subprovince which occurs immediately to the north (Figure 1.1; e.g. Blignault *et al.*, 1983; Colliston & Schoch, 1998). The current study is concerned with the tectonometamorphic evolution of the Richtersveld and Gordonia Subprovinces as well as the tectonic boundary

which separates them.

The Richtersveld Subprovince is generally subdivided into two tectonic domains of contrasting metamorphic grade and deformation intensity. The eastern Pella terrane consists of amphibolite facies rocks that experienced relatively high strains, whereas the Vioolsdrif terrane to the west experienced greenschist facies metamorphism and relatively low shear strain (Blignault, 1977; Barton & Burger, 1983; Colliston & Schoch, 2000). The NW-SE trending Southern Namaqua Front – defined as the point at which the regional foliation in Richtersveld Subprovince becomes well-developed such that the rocks have a general gneissic appearance, marks the boundary between the two tectonic domains of the Richtersveld Subprovince (Figure 1.2; Blignault, 1977; Colliston & Schoch, 1998).

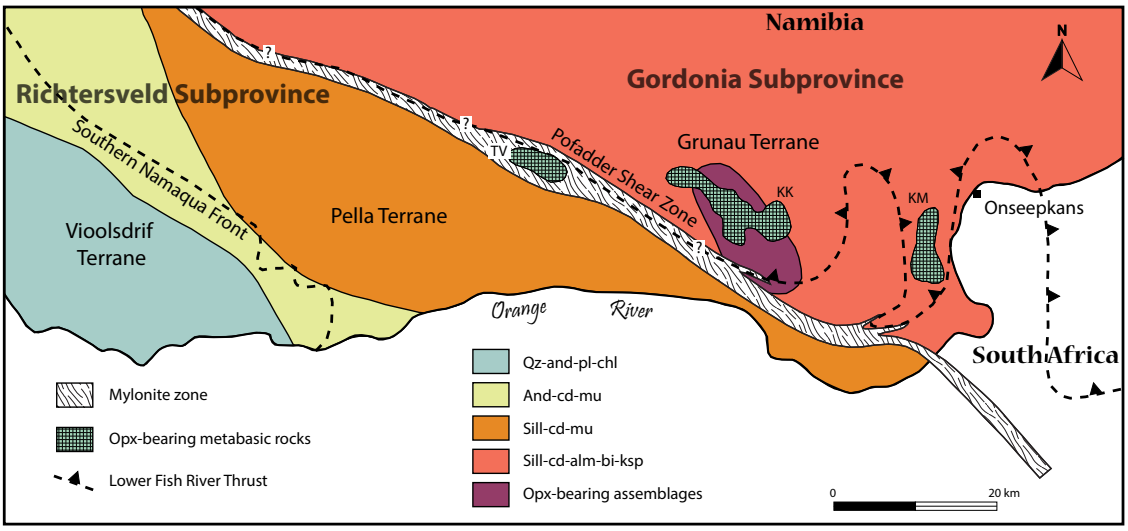

Figure 1.2: Tectonostratigraphy and metamorphic zonation of the western NMC in southern Namibia, modified after Toogood (1976) and Miller (2008) with the position of tectonstratigraphic boundaries after Blignault (1977), Colliston & Schoch (2000) and Miller (2008). The Southern Namaqua Front is a NW-SE trending structure that defines the boundary between Vioolsdrif and Pella Terranes. To the east, the Lower Fish River Thrust separates the Gordonia and Richtersveld Subprovinces.

To the north, the Pella Terrane is in tectonic juxtapostion with the Grunau Terrane: the western-most, NW-SE trending tectonic domain of the Gordonia Subprovince which lies north of the Pella Terrane (Figure 1.2 Blignault *et al.*, 1983; Miller, 2008). The Grunau Terrane has a protracted, polyphase meta-plutonic history (Hartnady *et al.*, 1985) and consists primarily of high grade (upper-amphibolite–granulite facies) aluminous paragneisses as well as sheet-like megacrystic or augen gneisses which are voluminous and regionally extensive (Blignault *et al.*, 1983; Colliston & Schoch, 2006).

The juxtapostion of the various tectonic domains in the western NMC has been postulated

to have occurred as a result of thrusting along regional NW-SE to E-W trending thrust shear zones in Mesoproterozoic times (e.g. Blignault *et al.*, 1983; Van Aswegen *et al.*, 1987; Colliston & Schoch, 1998). The E-W striking Groothoek Thrust separates the Bushmanland Subprovince from the lower grade Richtersveld Subprovince (Van der Merwe & Botha, 1989; Robb *et al.*, 1999). The boundary which separates the upper-amphibolite–granulite facies Grunau Terrane from the amphibolite facies Pella Terrane is marked by the NW-SE striking Lower Fish River Thrust (LFRT Blignault *et al.*, 1983; Colliston & Schoch, 2006) which is a focal point of this study.

The western Namaqua Metamorphic Complex (NMC) has been the subject of a multitude of tectonometamorphic studies over the decades with most of the earliest studies surfacing in the seventies (e.g. Blignault *et al.*, 1974; Jackson, 1976; Toogood, 1976) and to date being largely focused on unravelling the tectonometamorphic histories and evolutions of the terranes which constitute it (e.g. Blignault *et al.*, 1983; Waters, 1989; Diener, 2014; Robb *et al.*, 1999). In attempting to understand the processes which led to the current configuration of tectonic domains, numerous workers have also attempted geodynamic reconstructions (e.g. Cornell *et al.*, 1992; Becker *et al.*, 2006; Colliston & Schoch, 2013; Bial *et al.*, 2015a).

Although there has been much disagreement regarding the specific geodynamic setting responsible for the regional Mesoproterozoic MP/LP-HT signature, most early models advocate some aspect of continental collision (Blignault *et al.*, 1983; Jacobs *et al.*, 1993; Thomas *et al.*, 1994; Eglington, 2006). However, there is a growing consensus that such MP/LP-HT granulite facies metamorphism is incompatible with a collisional tectonic setting and thus alternative models, variously implicating: i) magmatic under- or intra-plating accompanied by compressional tectonics (Robb *et al.*, 1999; Diener *et al.*, 2013) and; ii) a continental back-arc setting (Waters, 1986; Bial *et al.*, 2015a, 2016). Nonetheless, due to clear evidence of protracted compressional tectonics some workers continue to advocate a model which implicates collision of crustal fragments (e.g. Colliston & Schoch, 2013; Colliston *et al.*, 2015). Such proliferation of divergent models has also been the subject of MP/LP-HT terranes globally (e.g. Collins, 2002; Clark *et al.*, 2014) and thus geodynamic reconstructions of the western NMC have had an important part to play in our growing understanding of MP/LP-HT metamorphism.

1.2 Structural development and deformation history

In the traditional literature, the Namaqua Orogeny is generally subdivided into two discrete ductile deformation phases, corresponding to the Okiepian and Klondikean tectonothermal events, at c. 1190 ± 30 Ma and c. 1040 ± 30 Ma respectively (Blignault *et al.*, 1983; Raith & Harley, 1998; Clifford *et al.*, 2004). The early phase (D_2) is the most pervasive of these and resulted in the developement of a penetrative subhorizontal gneissosity during a NE-

SW directed compressional regime under upper-amphibolite to granulite facies metamorphic conditions in the Bushmanland and Gordonia Subprovinces, while in the Pella Terrane of the Richtersveld Subprovince, D_2 deformation occurred under amphibolite facies conditions (Blignault *et al.*, 1983; Raith & Harley, 1998; Miller, 2008). This event pervasively deforms all tectonic domains of the NMC, with exception of the Vioolsdrif Terrane, where Eburnian (D_1) fabrics attributable to the ORO prevail (Blignault *et al.*, 1983). Regionally, a subsequent N-S directed compressional ductile deformation phase (D_3) is postulated to have occurred in the late stages of Namaqua tectonism and led to the developement of kilometre-scale open and upright folds which deform the D_2 fabrics in places throughout the western NMC (Toogood, 1976; Robb *et al.*, 1999). Following soon after D_3, a D_4 deformation phase is represented by right lateral, NW-SE trending transcurrent shear zones of which the most prominent is the Pofadder Shear Zone (Thomas *et al.*, 1994; Miller, 2008).

Blignault *et al.* (1983) recognised the occurrence of a discrete, regionally developed thrusting event which post-dates the D_2 penetrative fabric but pre-dates D_3 deformation. This is supported by findings of Raith & Harley (1998) who show that the D_2 deformation phase comprises two distinct events separated by a period of retrogression, where D_{2a} is represented by a regionally developed, shallow NE dipping penetrative gneissosity while D_{2b} is represented by zonally developed subhorizontal ductile shear zones (Raith & Harley, 1998).

Although the occurrence of a discrete thrusting event has been recognised (Raith & Harley, 1998; Colliston & Schoch, 2006; Colliston *et al.*, 2015), there has not yet been an intergrated study which attempts to elucidate the timing and P-T conditions of tectonic displacements along regional D_{2b} shear zones such as the Lower Fish River and Groothoek Thrusts. Moreover, the conditions and timing underwhich tectonic juxtaposition occurred along the major D_{2b} thrusts has not yet been determined.

1.2.1 Regional Kinematics

As suggested by Blignault *et al.* (1983) and Van der Merwe & Botha (1989) the current arrangement of tectonic domains in the western NMC is best accounted for by a model which involves large-scale subhorizontal movement of thick, ductile crustal sheets towards the southwest (Figure 1.3). Findings presented by Blignault *et al.* (1983) and Van der Merwe & Botha (1989) suggest that the sheets were uplifted along two major ramp structures (i.e. the Groothoek and Lower Fish River Thrusts). These ramp structures are postulated to juxtapose crustal sheets excised from contrasting levels in the crust and are thus believed to constitute major terrane boundaries in the traditional literature (Figure 1.3; Miller, 2008; Van der Merwe & Botha, 1989; Blignault *et al.*, 1983).

Based on kinematic analysis of linear fabric elements, Van der Merwe & Botha (1989) infer a NE-SW transport azimuth and an overall top-to-SW shear sense for Namaqua tectono-

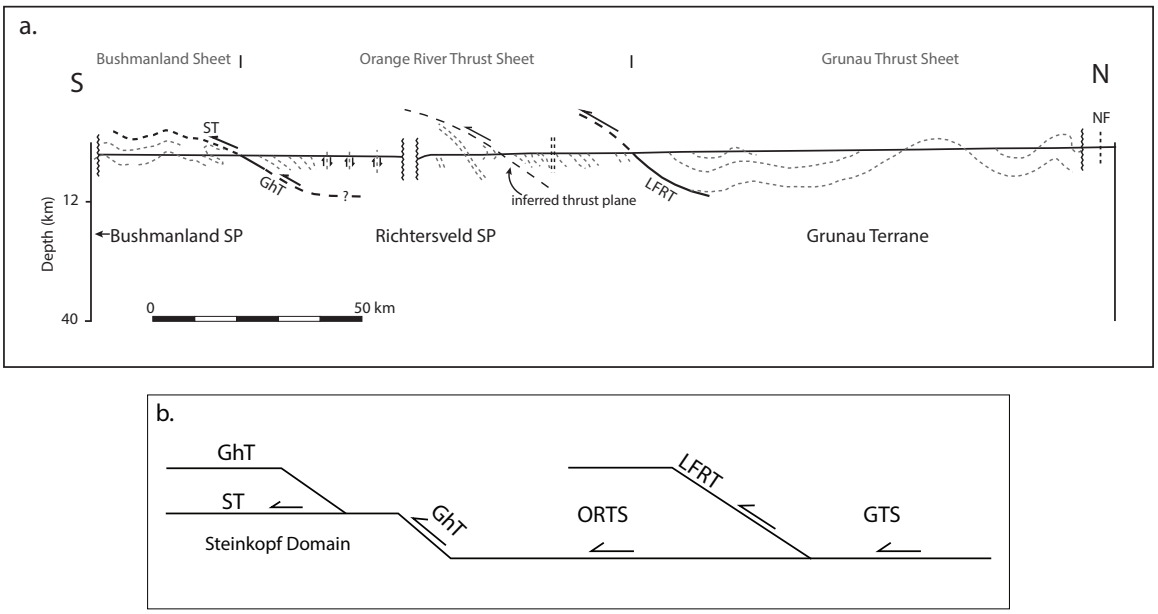

Figure 1.3: a) Simplified structural section (S to N) across the tectonic domains of the NMC illustrating the relationship between major tectonic domains and regional thrust zones (modified after Blignault *et al.*, 1983). ST - Steinkopf Thrust; SP - Subprovince; All other abbreviations as in Figure 1.1. b) Schematic profile (S to N) across western NMC (along section similar to Figure 1.3 (a)) illustarting the major thrust sheets and simplified "ramp-flat" geometry of the western NMC (modified after Blignault *et al.*, 1983). The Steinkopf Domain belongs to the Bushmanland Subprovince. ORTS - Orange River Thrust Sheet; GTS - Grunau Thrust Sheet.

genesis – an observation corroborated by the overall northward dip of the fabrics developed in the thrust shear zones (Colliston & Schoch, 2000). Strain analysis by Van der Merwe & Botha (1989) on the Groothoek Thrust indicates a minimum displacement of 50 km, although Van Aswegen *et al.* (1987) suggests that displacement along regional D_2 thrust zones may be in excess of 100 km.

The presiding view in the traditional literature is that each of the tectonic domains in the western NMC represents a distinct terrane with a unique tectonometamorphic history, such that the major regional shear zones are postulated to represent terrane boundaries (Miller, 2008; Colliston *et al.*, 2015). This view is in favour of a model where amalgamation of tectonic domains in the western NMC occurred in a collisional tectonic setting related to Wilson-cycle tectonics (Miller, 2008, 2012; Colliston *et al.*, 2015). However, more recent studies suggest that each of the tectonic domains which constitute the western NMC more likely share a common tectonometamorphic evolution and the regional thrusts likely represent major internal structures within coherent crustal entity (Bial *et al.*, 2016, 2015a). In this case the western NMC is postulated to have evolved in a continental backarc mobile belt, where it remained at HT-LP conditions for periods exceeding 100 million years. Furthermore, this

model correlates the various tectonometamorphic episodes recorded in the western NMC to episodic contractional and extensional tectonics (as would be expected in a continental back-arc mobile belt), which is suggested to explain the regional variation in the timing and extent of thermal events (Bial *et al.*, 2015a, 2016). Thus, there is a need to understand the tectonometamorphic evolution of regional shear zones in the western NMC with the aim of determining whether their evolution can be correlated to a collisional tectonic setting or a continental backarc mobile belt – this will add significant value to the ongoing debate.

1.3 Metamorphism

Although interpretations of the specific geodynamic setting which resulted in the dominant metamorphic imprint at the NMC have been equivocal, it has been well-established that most of the NMC is characterised by medium- to low-pressure, high temperature (MP/LP-HT) upper-amphibolite to granulite facies metamorphism that occurred under highly elevated apparent geothermal gradients (e.g. Waters, 1989; Raith & Harley, 1998; Robb *et al.*, 1999; Diener *et al.*, 2013). For most parts of the NMC, reported peak P-T estimates indicate that temperatures reached 750–900°C at relatively low pressures ranging between 4–6 kbar (Figure 1.4; Raith & Harley, 1998; Robb *et al.*, 1999; Diener, 2014), with both clockwise and anti-clockwise P-T paths being variously suggested (e.g. Waters, 1989; Diener *et al.*, 2013).

Waters (1989) and Robb *et al.* (1999) infer an anti-clockwise P-T path due to the replacement of cordierite by garnet and sillimanite±biotite subsequent to the development of the peak assemblage. Contrastingly, Diener *et al.* (2013) interprets the replacement of prograde garnet by cordierite to represent minor decompression subsequent to peak conditions, while the replacement of cordierite by fibrolitic sillimanite is ascribed to retrograde cooling and thus infers a clockwise P-T loop. However, while there is some disagreement regarding the exact P-T loop, a common feature of all accounts is that of near isobaric cooling (IBC), with minor or no decompression (Figure 1.4; e.g. Waters, 1989; Robb *et al.*, 1999; Diener *et al.*, 2013).

Recently, Bial *et al.* (2015a) infer a similar IBC path in the South African extent of the Grunau Terrane, although peak P-T condtions constrained from a zone in their study area respectively correspond to lower and higher pressures and temperatures compared to previous P-T constraints in the western NMC (Figure 1.4).

Raith & Harley (1998) correlate each of the discrete D_2 events (D_{2a} and D_{2b}) with two discrete metamorphic events (M_{2a} and M_{2b}) at c. $<$ 1.2 and c. 1.06 Ga (Figure 1.4). Moreover, Raith & Harley (1998) postulate that maximum granulite facies conditions during M_{2a} occurred concurrently with the principal regional tectonogenesis at c. $<$ 1200 Ma, while M_{2b} is characterised by retrograde assemblages zonally developed along late D_2 shear zones at slightly lower temperatures. These findings are in agreement with Clifford *et al.*

(2004) who suggest that granitoid magamatism resulted in peak P-T conditions and occurred concurrently with regional (D_2) deformation at c. 1180–1200 Ma.

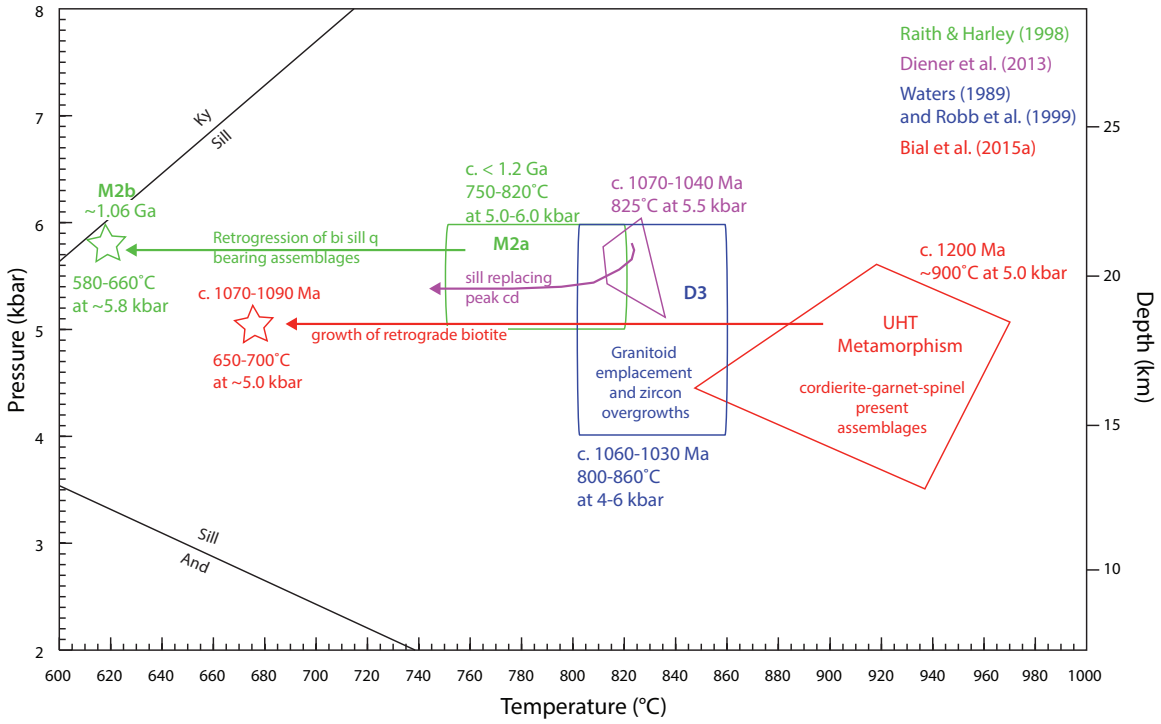

Figure 1.4: Summary of metamorphic P-T constraints in the western NMC from previous studies. Arrows indicate early retrograde trajectories deduced by the respective workers. Note the early, minor decompression invoked by Diener *et al.* (2013). The timing of P-T constraints are indicated as per the relevant studies. UHT = ultra-high temperature.

Contrastingly, Robb *et al.* (1999) interpret zircon overgrowths dated at c. 1060–1030 Ma to correspond to peak metamorphism and postulate that developement of the peak assemblage in the NMC likely post-dated the principal (D_2) period of deformation but was synchronous with the developement of D_3 open folds (Figure 1.4). In broad agreement, Diener *et al.* (2013) constrains peak metamorphic conditions in the Aus region (5.5 kbar at 825°C) to the period c. 1070–1040 Ma (Figure 1.4), attributing this event to magmatic under- or intra-plating.

Termination of Namaqua tectonogenesis is widely understood to be represented by 950 Ma Rb-Sr cooling ages from the Bushmanland Subprovince (Cornell *et al.*, 1992; Eglington, 2006). These dates have been interpreted to signal a period of uplift and/or erosion subsequent to the final tectonometamorphic episode within the Namaqua Orogeny (Thomas *et al.*, 1994).

1.4 Relevance of the study

In the western NMC, almost all tectonometamorphic studies which attempt to elucidate the P-T-t evolution of rocks have been focussed on the interior of tectonic domains, away from

major regional shear zones, with most studies specifically aimed at understanding the P-T-t evolution of individual tectonic domains in isolation (e.g. Waters, 1989; Raith & Harley, 1998; Robb *et al.*, 1999; Clifford *et al.*, 2004; Diener *et al.*, 2013).

In order establish a unified geodynamic model for the western NMC, that is compatible with our understanding of the tectonometamorphic histories of individual tectonic domians, it is necessary to elucidate the P-T-t evolution of rocks at the marginal zones of tectonic domains and thus understand the geologic significance of major regional thrusts. This will add much value to the ongoing discussion on whether the regional thrusts in the western NMC represent suture zones (formed from the collision of crustal fragments; e.g. Miller, 2012) or are simply major internal structures within a coherent crustal entity (Bial *et al.*, 2016, 2015a). The current study represents an intergrated investigation on the timing and P-T conditions of shearing and tectonic juxtaposition of Gruna Terrane and against the Pella Terrane along the Lower Fish River Thrust (LFRT).

Colliston *et al.* (2015) has partially addressed the timing of deformation events along the South African extent of the Lower Fish River Thrust in the western NMC, using U-Pb ion microprobe dates of zircons from Grunau Terrane supracrustals – however, an intergrated tectometamorphic study that encompasses phase equilibria modelling, *in situ* dating of metamorphism along with field and petrographic observations is needed. Such a study, focussed on the rocks at the marginal zone between the Richtersveld and Gordonia Subprovince, should provide the insight needed to elucidate the the geodynamic significance of the LFRT.

Moreover, although it has been well-established that the western NMC has been subject to upper-amphibolite to granulite facies polyphase deformation and metamorphism in the Mesoproterozoic Namaqua Orogeny (1.2–1.0 Ga; Blignault *et al.*, 1983; Colliston & Schoch, 1998; Raith & Harley, 1998; Clifford *et al.*, 2004) there is much disagreement regarding the timing of specific events during this period. As more and more high quality radiometric age constraints have become available in the literature it has become increasingly evident that the traditional model implicating two distinct Mesoproterozoic tectonometamorphic episodes within the Namaqua Orogeny of the western NMC may not be appropriate as it does not entirely account for the assortment and distribution of radiometric ages (Bial *et al.*, 2015a).

Prior to the emergence of *in situ* radiometric dating techniques as a routinely applied method – metamorphic events in much of the previous literature, have been indirectly dated by correlating zircon U-Pb ages derived from the voluminous granitoid intrusives which occur throughout the western NMC to MP/LP-HT metamorphism (e.g. Robb *et al.*, 1999; Clifford *et al.*, 2004). Consequently, while there is an apparent abundance of age constraints on specific tectonothermal events in the western NMC, there is undoubtedly a dearth in published radiometric ages which directly constrain the date of metamorphism experienced by metamorphosed supracrustal rocks. In this regard, the emergence and more frequent application

of *in situ* dating techniques such as LA-ICP-MS on metamorphic zircon and/or monazite grains have recently been (Macey *et al.*, 2013; Bial *et al.*, 2015a,b) and will continue to be of pivotal importance to filling the gap.

1.5 Aims of the study

The current study represents an integrated approach using calculated pseudosections and *in situ* U-Pb analyses on monazite cores combined with various field and petrographic observations to elucidate the P-T-t evolution at a portion of the marginal zone between the Richtersveld and Gordonia Subprovinces. Of primary focus is to gain an understanding of the P-T-t evolution of the Lower Fish River Thrust (and adjacent rocks) during the principal Mesoproterozoic tectonogenesis in the western NMC and thus gain insight on its geological significance. In doing so it is envisaged that the study will form the foundation from which more comprehensive geodynamic models can be constructed for the western NMC by extrapolating key findings from this research.
The principal aims of the study are as follows:

- Constrain the conditions and timing of peak metamorphism at the frontal zone of the Grunau Terrane;
- Constrain the P-T conditions of shearing in the LFRT as well as juxtaposition of the Grunau Terrane against the Pella Terrane along the LFRT;
- Determine a P-T-t path for the Mesoproterozoic metamorphic evolution of the studied portion of the Richtersveld-Gordonia Subprovince marginal zone;
- Elucidate the geodynamic significance of the LFRT

Chapter 2

Geologic background

2.1 Solving P-T problems in granulites

2.1.1 Equilibrium approach to metamorphism

The fundamental premise which underpins modern thermobarometry is that of local equlibrium (Powell *et al.*, 2005). This concept is based on the understanding that during prograde metamorphism of first cycle metamorphic rocks (i.e. those that have not been subject to any previous metamorphism and are constituted by an essentially hydrous assemblage) the mineral assemblage and the composition of minerals is continuously evolving to reflect the P-T conditions at every point in time along the P-T path (Powell *et al.*, 2005; Powell & Holland, 2008).

The local equilibrium view supports the widely held understanding that once the becomes essentially anhydrous due to progressive dehydration and melt loss during prograde metamorphism it will experience very limited change in mineral assemblage during cooling (Brown, 2002; White & Powell, 2010, 2011). Thus, the preserved mineral assemblage in granulite facies metamorphic rocks should ideally be compatible with the stable equilibrium established at the peak of metamorphism (Brown, 2002, 2010). However, while it is agreed upon that this concept is universally applicable, it is also well documented that it is an idealised view since granulite grade metamorphic rocks commonly show minor evidence of chemical re-equlibration and fluid-related back-reaction during retrograde cooling (Brown, 2002; Vernon *et al.*, 2008; White & Powell, 2011).

2.1.2 Thermobarometric methods

Thermobarometry – most simply defined as the estimation of the P-T conditions of metamorphism, is one of the principal elements necessary for us to learn about the tectonometamorphic evolution of metamorphic rocks exposed at the Earth's surface and can be carried through

the use of phase equilibria models as well as by applying conventional methods (Powell & Holland, 2008; Powell *et al.*, 2005).

Almost all recent advancements in thermobarometry have primarily been focussed on forward modelling of phase equilibria, principally in the form of pseudosections – this has largely been driven by advancements in the thermodynamic datasets of end-member mineral properties (Powell *et al.*, 2005; Powell & Holland, 2008). Such advancements have facilitated better and more reliable petrological calculations and phase equilibria models (e.g. White *et al.*, 2003; Powell *et al.*, 2005; Powell & Holland, 2008). However, perhaps one of the greatest factors which has harnessed our ability to consistently produce powerful and informative phase equilibria models has been the developement of the approriate software. In this regard, *THERMOCALC*, initially developed by Powell & Holland (1988, ;with multiple subsequently improved iterations over the decades) arguably stands alone as it has been routinely used by scientists in the metamorphic community (e.g. Diener *et al.*, 2008; Tam *et al.*, 2012; Clark *et al.*, 2014; Ulmius *et al.*, 2015, and many others).

Unlike conventional thermobarometric methods, which rely on mineral compositions for P-T constraints – calculation of pseudosections relies principally on the establishment of the composition of an equilibration volume (Powell *et al.*, 2005; Powell & Holland, 2008). The equibration volume is defined as the volume of rock where all minerals within that volume were in chemical communication with each other at the time/ point in P-T space when the assemblage was "frozen-in" (e.g. White *et al.*, 2003; Powell *et al.*, 2005). In many instances – this is taken to be equlivalent to the bulk rock compostion (typically determined by XRF analysis; e.g. Powell *et al.*, 2005; Powell & Holland, 2008). However, it has been well documented that any significant occurrence of: i) textural heterogeneity (e.g. in the form of segregated melt) or; ii) prominent growth zoning in porphyroblast phases (which would have the result of sequestering certain chemical elements in mineral cores) can result in discrepencies between bulk-rock and equilibration volume composition (e.g. Powell & Holland, 2008; Brown, 2002, respectively). For this reason, due care needs to be taken when selecting the samples which will be subject to phase equilibria modelling, particularly in the case of granulite facies rocks – which commonly show pronounced textural heterogeneity (Brown, 2002; Powell *et al.*, 2005; Powell & Holland, 2008).

In granulite facies metamorphic rocks individual mineral grains are susceptible to chemical change during retrograde cooling due to high temperature volume diffusion – this often results in the composition of minerals not being representative of peak metamorpism (e.g. Tuccillo *et al.*, 1990; Vernon *et al.*, 2008; White & Powell, 2011). This fact precludes any meaningful application of conventional thermobarometry on mineral grains which have undergone such post-thermal peak chemical modification (Powell & Holland, 2008). This problem is largely circumvented by pseudosection modelling since this method is principally reliant on whole

rock composition (corresponding equilibration volume), although mineral chemical data can help to narrow the P-T temperature constraints in some instances (Brown, 2002; Vernon, White & Clarke, 2008)

P-T pseudosections graphically display all possible multivariant mineral equilibria for a given rock composition within a specified P-T range. In this sense pseudosections are predictive as they allow us to comapare the P-T distribution of the model mineral equilibria with the observed (actual) equilibrium assemblage (e.g. White *et al.*, 2003; Powell & Holland, 2008). The thermobarometric constraints are contained in the location and coverage of the phase field corresponding to the observed equilibrium assemblage in pseudosection P-T space. Clearly, accurate application of this method is dependent on the correct inferrence of an equlibrium assemblage (Powell & Holland, 2008; Vernon *et al.*, 2008).

When applied correctly, microtextural analysis of metamorphic rocks can be used in parallel with pseudosection models in order to deduce geologically meaningful P-T trajectories which can help to elucidate the broader tectonometamorphic evolution of a rock (Brown, 2002; White *et al.*, 2003; Vernon *et al.*, 2008).

2.2 U-Pb monazite dating and its application to granulite facies rocks

The U-Pb isotope system has long been one of the favoured methods of dating for Proterozoic rocks containing minerals with low amounts of common (non-radiogenic) Pb (e.g. Williams & Jercinovic, 2002; Vance *et al.*, 2003; Schoene, 2014) this is due to the convenient half-lives of each of the parent isotopes in its dual decay scheme, which are perfectly fitting for rocks in this age range (Bateman, 1910; Schoene, 2014). U-Pb isotope geochronology is based on a pair of chain decay schemes where a) ^{238}U decays to ^{206}Pb and; b) ^{235}U decays to ^{207}Pb; both of these involve a series of intermediate radioactive daughter isotopes. Each of these decay schemes are respectively governed by the following chronometer equations:

$$\frac{^{206}Pb}{^{204}Pb} = \left(\frac{^{206}Pb}{^{204}Pb}\right)_0 + \left(\frac{^{238}U}{^{204}Pb}\right)(e^{\lambda_{238}t} - 1) \tag{2.1}$$

$$\frac{^{207}Pb}{^{204}Pb} = \left(\frac{^{207}Pb}{^{204}Pb}\right)_0 + \left(\frac{^{235}U}{^{204}Pb}\right)(e^{\lambda_{235}t} - 1) \tag{2.2}$$

Where the subscript *0* corresponds to the initial ratio of the Pb isotopes, λ is the decay constant and t corresponds to time. In order to visualise U-Pb isotope data, Wetherill (1956) introduced the Wetherill concordia plot. This diagram plots the $\left(\frac{^{206}\text{Pb}}{^{283}\text{U}}\right)$ and $\left(\frac{^{207}\text{Pb}}{^{235}\text{U}}\right)$ ratios from the same analysis on a set of axes. The solutions to Equations 2.1 and 2.2 above define an isochron (the concordia curve); analyses which lie on the concordia curve are said to be concordant, while those that do not plot on the isochron are said to be discordant (Schoene,

2014). In the latter case, the most frequent interpretation is that the grain being analysed did not behave as a completely closed system since crystallisation (Wasserburg, 1963; Schoene, 2014).

In the past, a major challenge in the application of geochronology to metamorphic rocks has been establishing a link to the petrogenesis of accessory phase chronometer minerals (e.g. zircon and monazite) to that of the main mineral assemblage, which provides constraints on the P-T conditions of metamorphism and can also record the occurrence of any deformation events where fabrics are developed (Vance *et al.*, 2003; Lasalle *et al.*, 2014). However, since *in situ* techniques such as LA-ICP-MS came to prominence, gechronologists have had the ability to link geological ages to petrographical information and deformation textures at an increasing spatial resolution – this has allowed for more robust constraints on the timing of tectometamorphic events (e.g. Zhu & O'Nions, 1999a; Lasalle *et al.*, 2014; Williams & Jercinovic, 2002). In contrast to conventional, bulk mineral techniques such as ID-TIMS which are applied to a single grain, high resolution *in situ* techniques have the ability to date specific zones in a mineral (Paquette & Tiepolo, 2007; Lasalle *et al.*, 2014). Linking the geochronological results of such techniques with textural information, combined with careful interpretation of data provides a powerful tool for dating metamorphic rocks with a complex tectonometamorphic history (Vance *et al.*, 2003; Paquette & Tiepolo, 2007; Lasalle *et al.*, 2014).

Monazite is light rare earth elememt (LREE)-rich phosphate mineral, with the generalised chemical formula (LREE)PO_4, the mineral has been widely used for U-Pb dating of metamorphic rocks, due largely to the fact that like zircon, monazite contains high and low concentrations of U and common Pb respectively (Overstreet, 1967; Parrish, 1990; Williams *et al.*, 2007). In addition, it is increasingly widely documented that monazite remains exceptionally impervious to isotopic disturbance (e.g. Pb loss) at high temperature (Smith & Giletti, 1997; Cherniak *et al.*, 2004), while unlike zircon, it is also well recognised for being highly resistant low temperature fluid related isotopic resetting (Schaltegger *et al.*, 1999). In metamorphic rocks, monazite occurs widely as an accessory phase in high grade (typically upper amphibolte to granulite facies) metapelites and has been used effectively as a geochronometer on granulite facies rocks which have experienced a protracted high temperature history (e.g. Zhu & O'Nions, 1999a; Williams & Jercinovic, 2002; Lasalle *et al.*, 2014).

In granulite facies anatectic rocks, monazite is understood to form along the prograde path, largely via allanite breakdown reactions (e.g. Parrish, 1990; Catlos *et al.*, 2002). On heating to suprasolidus temperatures (beyond the wet solidus), prograde monazite is largely predicted to dissolve in the melt due to corrosion (Figure 2.1). It is widely viewed that new monazite will then crystalize subsequent to peak temperature conditions during retrograde cooling until the dry solidus is intersected (Figure 2.1; e.g. Catlos *et al.*, 2002; Iizuka *et al.*,

2010; Lasalle *et al.*, 2014). As such, numerous workers have suggested that inheritance of relict monazite (detrial or of from a previous metamorphic event) should be exceptionally rare (e.g. Parrish, 1990; Zhu & O'Nions, 1999a). However, it is increasingly being accepted that inheritance is a commonly observed phenomenon in monazite (Iizuka *et al.*, 2010; Lasalle *et al.*, 2014). In a study on granulite facies metasediments, Iizuka *et al.* (2010) documents the occurrence of Archaen detrial monazite ages in granulite facies rocks which had been subject to a protracted polymetamorphic history – thus underlining the potential of monazite to be inherited.

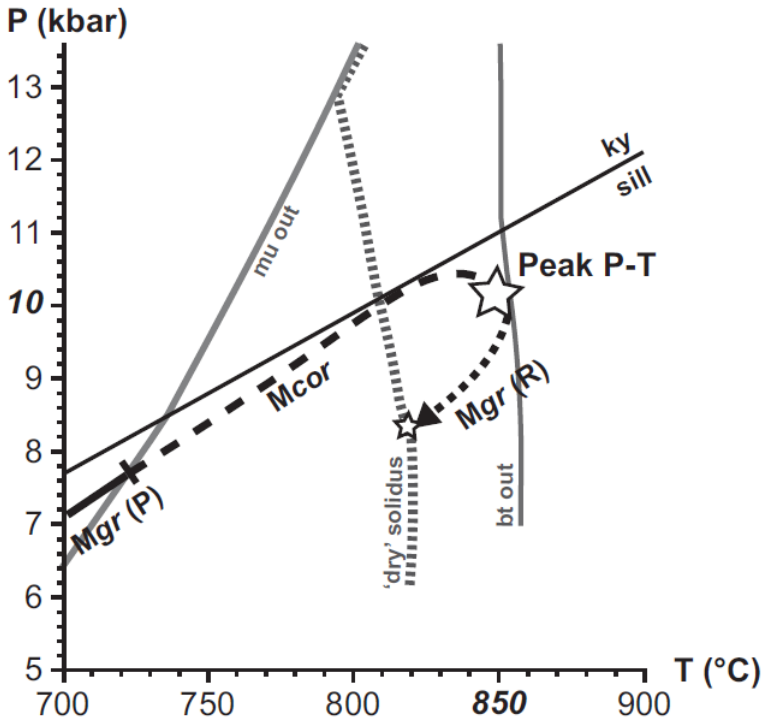

Figure 2.1: Stages of monazite formation and breakdown along a hypothetical granulite facies P-T path (Lasalle *et al.*, 2014). Mgr(P) – monazite growth during subsolidus prograde metamorphism; Mcor – monazite corrosion during suprasolidus prograde metamorphism; Mgr(R) – monazite growth during retrograde cooling (image source: Lasalle *et al.*, 2014).

A commonly observed characteristic of metamorphic monazite is the occurrence of both chemical compositional and age zonation structures. Zhu & O'Nions (1999b) and later Catlos *et al.* (2002) noted that in granulite facies metapelites monazites almost invariably exhibit well-developed zoning profiles with very sharp boundaries between compositional domains; in each case this was interpreted as an indication that diffusive element transfer is slow even at the high temperatures of granulite facies metamorphism, thus supporting the widely accepted view that monazite has a high closure temperature (Catlos *et al.*, 2002; Foster *et al.*, 2002; Iizuka *et al.*, 2010). Early estimates of monazite closure temperature – based largely on qualitative observations suggested that high temperature volume diffusion is inhibited

below temperatures of 725°C. Contrastingly, an experimental study by Cherniak *et al.* (2004) showed that, in line with the observations of Zhu & O'Nions (1999b), the closure temperature of monazite is likely in excess of 900°C.

However, in a study dedicated to isotopic closure, Villa (1998) cautions against a simplistic view of closure temperature, noting that fluid interaction, and the occurrence of lattice strain significantly enhance the rate of element and isotope transport in a mineral. Villa (1998) concludes that in the presence of these fast phenomena, temperature is no longer rate controlling – a view mirrored by numerous subsequent studies (e.g. Zhu & O'Nions, 1999a; Iizuka *et al.*, 2010).

Zhu & O'Nions (1999b) identifies three main patterns of zoning in monazite, namely: i) concentric zoning; ii) intergrowth zoning and iii) patchy zoning, this is in line with observations by Catlos *et al.* (2002) and Foster *et al.* (2002).

In granulite facies anatectic rocks, the occurrence of concentric zoning in monazite is generally accepted to represent a record of the changing P, T and effective bulk rock composition of the melt as the grain crystallises (Foster *et al.*, 2002; Catlos *et al.*, 2002). Due to the observance of the typical monazite zonation with sharp compositional and age domain boundaries, Foster *et al.* (2002) and Catlos *et al.* (2002) attribute the concentric zonation observed in their respective studies to episodic cycles of discontinuous growth and resorption during a protracted period of high temperature, suprasolidus residence. In addition, these workers attribute the observation of a wide age dispersion within the same sample and in many cases the same grain, to episodic growth of monazite during this protracted period, as reflected by the zoning preserved. Numerous studies (e.g. Lasalle *et al.*, 2014; Tucker *et al.*, 2015) subsequent to this have made similar observations on age dispersion in monazites, with broadly the same interpretation.

A major challenge in U-Pb geochronology is the interpretation of discordant analytical data – this is largely due to fact there can be numerous causes of discordance and the distinction between each possibility cannot always be easily made (Parrish, 1990; Paquette & Tiepolo, 2007). The most commonly invoked causes are: i) Pb-loss due to open-system mineral behaviour and; ii) the mixing of more than one age domain in an analysis (Parrish, 1990; Gerdes & Zeh, 2006; Paquette & Tiepolo, 2007). In the latter case, the possibility of acquiring discordant ages can be mitigated by careful selection of the analysis spot using the relevant imaging techniques (Gerdes & Zeh, 2006).

The U-Pb isotope system in monazite for anatectic rocks can be complex. Consequently, careful consideration of numerous factors (e.g. zoning, analytical method, closure temperature and concordance) is required for the correct interpretation of ages (Parrish, 1990; Zhu & O'Nions, 1999a; Vance *et al.*, 2003).

Chapter 3

Field Relations

This chapter outlines the outcrop scale petrographical relationships of the study area, with particular emphasis on the Lower Fish River Thrust Zone[1] (LFRTZ) and its surrounding wall rock. The character of the LFRTZ is also described.

3.1 Overview

Field work was carried out in the Kum Kum region largely in the vicinity of the central-south western margin of the Kum Kum Klippe during the period 7 to 14 July 2014 and mainly involved structural data and sample collection as well as sketching and photography. The samples used in the current study were collected during this period as well as during a field expidition carried out by the Council for Geoscience earlier in the same year. Most of the samples originate from the Kum Kum Klippe, while others were collected at locations in and around the Keimasmund Complex, the Sandfontein Klippe and the Tantelite Valley Complex (Figure 3.1).

In general, the study area is characterised by pervasive upper-amphibolite to granulite grade ductile deformation fabrics and structures with the prominent occurrence of thrust zones at various scales. However, while ductile deformation fabrics are dominant, the style of deformation across Richtersveld-Gordonia Subprovince marginal zone is not homogeneous and varies significantly as a function of lithology.

Various areas in and around the Kum Kum Klippe were studied, with particular attention directed to those areas where the most complete structural section across the Richtersveld-Gordonia mariginal zone is best exposed. Owing to this, the central-southwestern margin of the Kum Kum Klippe presented an ideal focal point for field work in this study since the footwall, thrust zone and hangingwall are all well exposed, with the hangingwall contact

[1]Field observations indicate that the LFRT is a broad feature. It is thus viewed more appropriate incorporate the word 'zone' into its naming. 'LFRTZ' will thus be used for the remainder of the thesis.

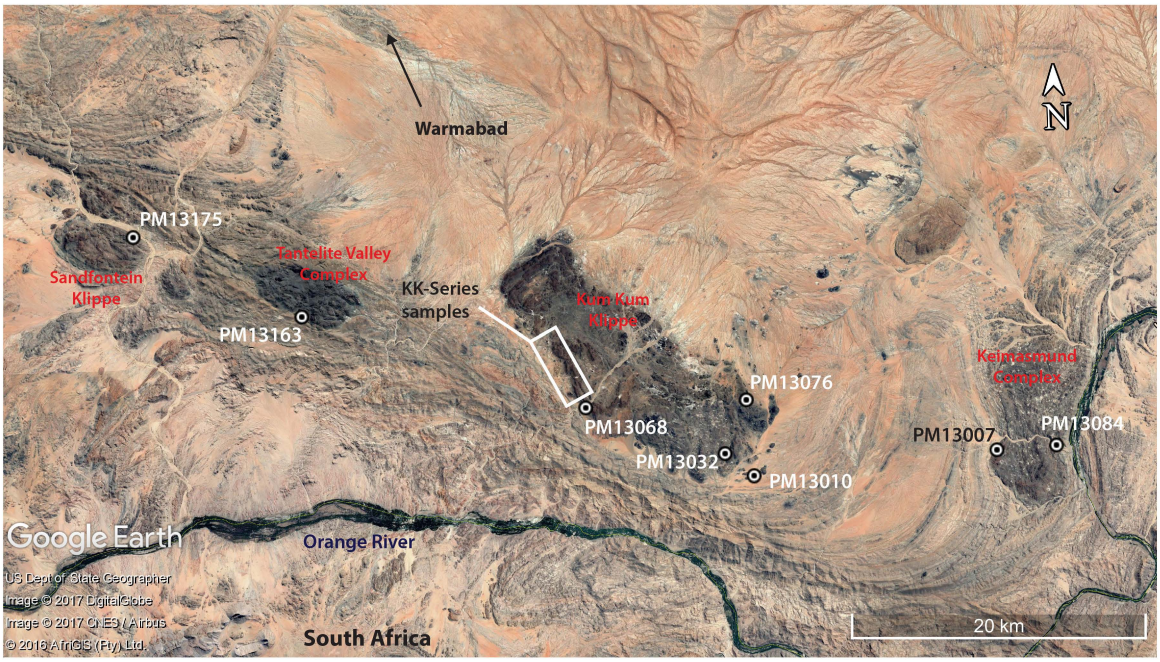

Figure 3.1: Location of samples collected at areas in and around the Kum Kum Klippe, Sandfontein Klippe, Keimasmund Complex and Tantelite Valley Complex. Note: KK-Series samples = KK02, KK04, KK10, KK12, KK14, KK19, KK27, KK28 and KK29. JMTV45 orginates from the eastern margin of Kum Kum Klippe in hangingwall (exact sample location not available).

particularly well-developed in places.

In the study area, the marginal zone between the Richtersveld and Gordonia Subprovinces along the southwestern margin of the Kum Kum Klippe can broadly be subdivided into a distinct footwall, thrust zone and hangingwall, respectively occuring from southwest to northeast. These three primary structural domains are distinguished largely on the basis of deformation intensity and lithology (Figure 3.2). In general, the footwall to the LFRTZ is constituted entirely by rocks of the Pella Terrane and is thus referred to as the Footwall Pella, while the hangingwall is entirely constituted by rocks of the Gordonia Subprovince (c.f. Grunau Terrane) and is thus referred to as the Hangingwall Gordonia (Figure 3.2). The Hangingwall Gordonia may be further subdivided into various allochtons. Whereas the contact between the LFRTZ and Hangingwall Gordonia is a distinct, approximately planar feature across which there is an abrupt change in lithology and decreased intensity of deformation in the Hangingwall Gordonia, the boundary between the Footwall Pella and the LFRTZ is largely gradational – marked by a gradual decrease in strain intensity towards the footwall.

Additionally, the competent Hangingwall Gordonia domain is often easily distinguished from the underlying Pella dominated LFTRZ on the basis of topography as it forms steep jagged peaks, while the LFRTZ typically forms comparatively gentle topography (Figure 3.2).

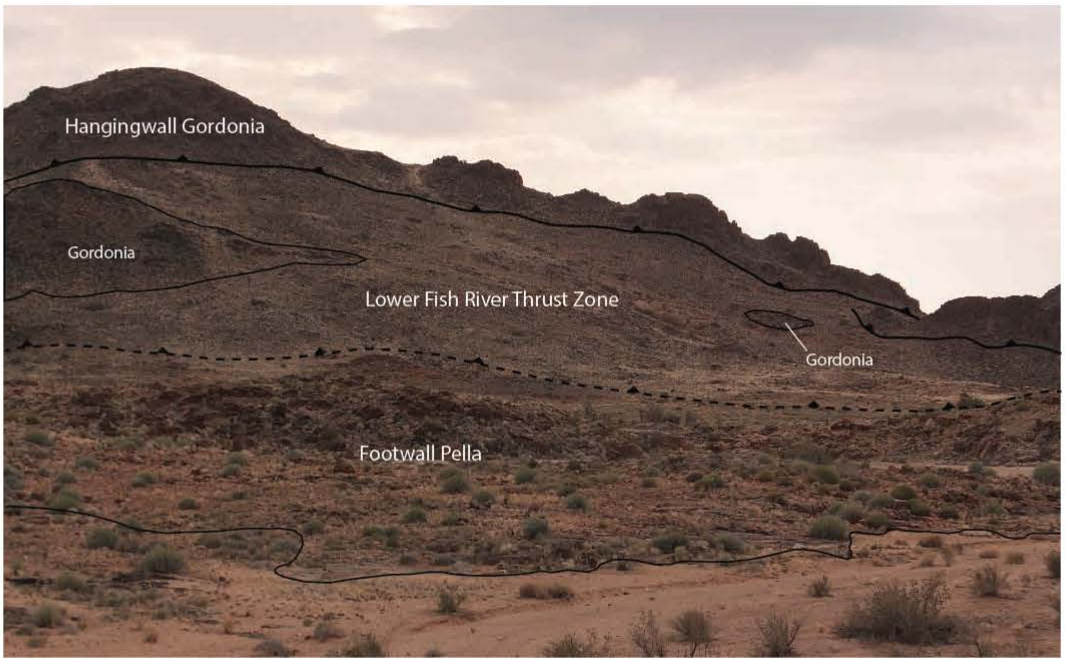

Figure 3.2: The Richtersveld-Gordonia Subprovince marginal zone along the southwestern margin of the Kum Kum Klippe. The contact between the Footwall Pella and structurally overlying Lower Fish River Thrust Zone (broken line) is identified mainly on the basis of increased deformation intensity in the LFRTZ, while the contact between the LFRTZ and Hangingwall Gordonia (thick solid line) is well-constrained, occurring where strain intesity diminishes abruptly in the Hangingwall Gordonia. Facing direction: northeast.

3.2 Lithology

In this section, key rock types observed in the field will be described in terms of their petrographical and textural characteristics with the aid of field photographs. In many instances, lithologies of both the Pella and Grunau Terranes occur in more than one distinct textural variety which have broadly similar mineralogical compositions. In such frequent instances; in order to prevent unnecessary proliferation of names, these rocks are described as the same unit.

3.2.1 Pella Terrane

The lithology of the Pella Terrane at the current study area displays significant heterogeneity. In addition, the effect of shearing along the LFRTZ has resulted in the occurrence of highly strained Pella Terrane rocks within the LFRTZ exhibiting a dominant $L > S$ tectonite fabric, which is in contrast to the footwall, where Pella Terrane rocks exhibit significantly less shear strain and a dominant $S > L$ tectonite fabric. Five major rock types have been recognised in this domain, namely: stromatic gneiss, pink gneiss, mafic lenses, Pella diatexite and felsic intrusives.

Stromatic gneiss

This lithological unit represents one of the major rock types of the study area and occurs in both the Footwall Pella domain and within the LFRTZ where it is respectively present as both relatively low strain (Figure 3.3 (a)) and comparatively higher strain textural variants (Figure 3.3 (b, c)). Typically, this unit is medium-grained and characterised by a well-developed cm-scale stromatic gneissic banding defined by alternating white or whitish-pink leucocratic and dark melanocratic bands. Where weathering is prevalent, outcrops of this unit are characterised by a dark grey to grey brown colour – this is most notable in the sheared variant. Elongated amphibolite lenses occur sporadically as inclusions in this lithology (Figure 3.3 (b, c)). The mineralogy is dominated by quartz, feldspars (plagioclase and K-feldspar in varying proportions) and biotite, with quartz and feldspars predominating in the leucosome, while biotite and hornblende are most prevalent in the melanocratic layers. In the low strain textural variant, individual leucosome bands are typically rimmed by a biotite-rich selvage (Figure 3.3 (d)).

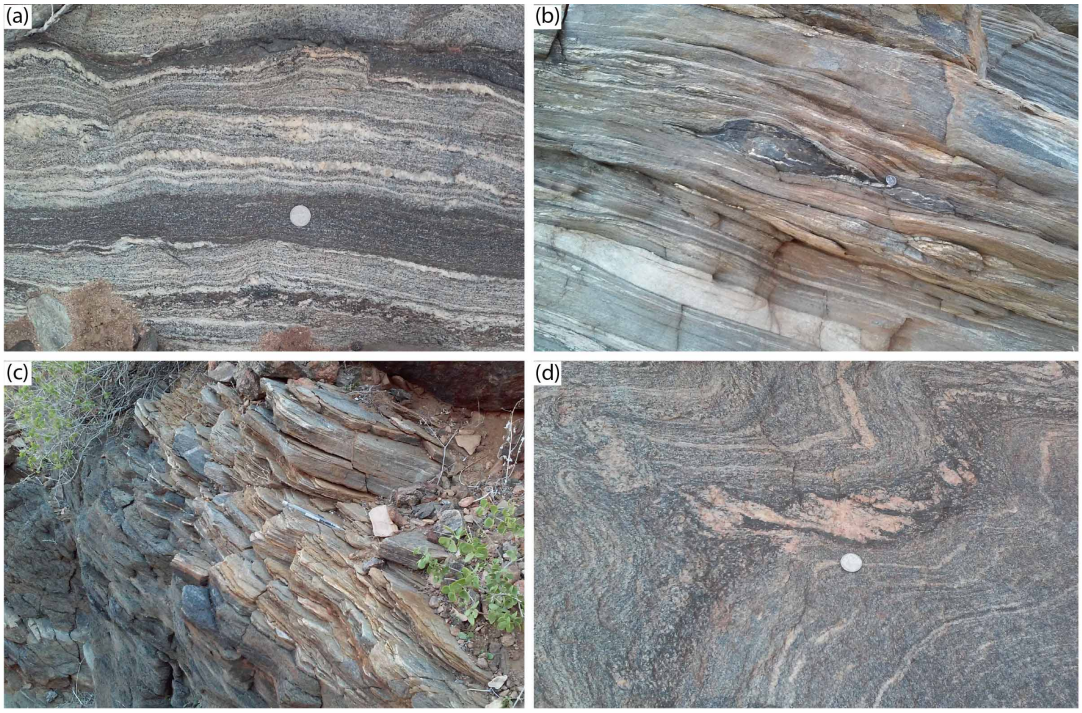

Figure 3.3: (a) Stromatic banding, with alternating leucocratic and melanocratic bands in typical Footwall Pella stromatic gneiss. (b) High strain (sheared) stromatic gneiss occurring in the LFRTZ, hosting an elongated mafic lense. (c) Sheared stromatic gneiss in the LFRTZ overlying an amphibolite unit. (d) Biotite selvage occurring in association with leucosome rims in the Footwall Pella domain.

Mafic lenses

Amphibolite lenses occur sporadically throughout both the LFRTZ and the Footwall Pella domain as isolated, discontinuous lenses or boudins within the more voluminous orthogneisses – individual amphibolite units generally do not exceed 3 m in thickness (e.g. Figure 3.3 (b) and 3.4). Amphibolite in the Footwall Pella generally exhibits a dark, massive appearance while in the LFRTZ, the amphibolite is similarly dark but typically exhibits a moderate- to well-developed foliation (Figure 3.3 (c)). The mineralogy of this rock type is largely constituted by hornblende and plagioclase, with plagioclase being much less predominant. In addition to the amphibolite lenses, two-pyroxene mafic units occur less commonly within the stromatic gneisses of the LFRTZ as isolated, relatively competent and well-rounded inclusions that are black with a dark greenish tone. The mineralogy of this lithology is typically dominated by clinopyroxene and orthopyroxene (thus two-pyroxene) as well as relatively subordinate hornblende and plagioclase. Although the margins of the inclusions are typically foliated, no well-developed internal ductile fabric is discernible in outcrop.

Figure 3.4: Large approximately 2.5 m wide amphibolite lense hosted within pink gneiss of the Footwall Pella domain.

Pink gneiss

This unit occurs in both the LFRTZ and the Footwall Pella, but is significantly more prevalent in the Footwall Pella domain. The relatively low strain variant in the Footwall Pella is medium grained, with a distinctive orange-pink colour and a well-developed planar foliation (Figure 3.5 (a)), while in the LFRTZ this unit has distinctive light pink colour, exhibiting a significantly higher level of strain and a fine grained, often mylonitic texture (Figure 3.5 (b)). In the Footwall Pella, this unit frequently occurs interlayered with subordinate amphibolite

units (∼0.5–3.0 m thick) which are often lensoidal (Figure 3.4). The high strain variant in the LFRTZ is relatively subordinate and occurs as isolated mylonitic pods within the sheared stromatic gneisses. The mineralogy predominantly comprises K-feldspar, quartz and biotite, with biotite being less prevalent in the high strain variant in the LFRTZ.

Figure 3.5: (a) Pink gneiss in the Footwall Pella domain exhibiting a characteristically well-developed platy foliation. (b) Fine grained, mylonitic pink gneiss occurring as isolated pods in the LFRTZ.

Pella diatexite

Pella diatexite occurs sporadically in isolated domains within sheared Pella orthogneisses and exhibits highly heterogeneous strain intensity. This unit comprises distinct leucosome and a mafic suspension which may occur in the form of brecciated fragments or elongated stringers (Figure 3.6 (a) and (b) respectively). The mafic material is dark, and gabbroic in composition and is reminiscent of the two-pyroxene granulite in appearance. This mafic component is dominated by greenish clinopyroxene, orthopyroxene as well as subordinate hornblende and plagioclase, while the leucosome is generally milky white, dominated by quartz and plagioclase feldspar. The relative modal proportion of leucosome and mafic suspension varies widely and

appears to be intimately related to deformation style and intensity. In places the diatexite is mylonitized such that it exhibits a relatively homogeneous appearance where the leucosome and mafic suspension are not easily discernible and the rock has an overall greyish colour (Figure 3.6 (c)).

Felsic intrusives

Various felsic intrusive phases occur sporadically in the LFRTZ, intruding orthogneiss and diatexite units as narrow (<1 m wide) aplitic and leucogranitic dykes (Figure 3.6 (d) and (e)). The felsic intrusives are fine grained and typically occur in light grey or orange-pink compositional variants (Figure 3.6 (d) and (e) respectively). The mineralogy of the light grey intrusions is constituted by quartz, plagioclase and minor biotite; this variant commonly occurs intruding the Pella diatexite (Figure 3.6 (d, f)). The mineralogy of the orange-pink compositional variants of felsic intrusives is constituted by quartz, K-feldspar and minor biotite – this variant often occurs cross-cutting the foliation developed in the orthogneisses of the LFRTZ (Figure 3.6 (e)). For both variants, the felsic intrusives exhibit evidence of a poorly developed internal shear fabric.

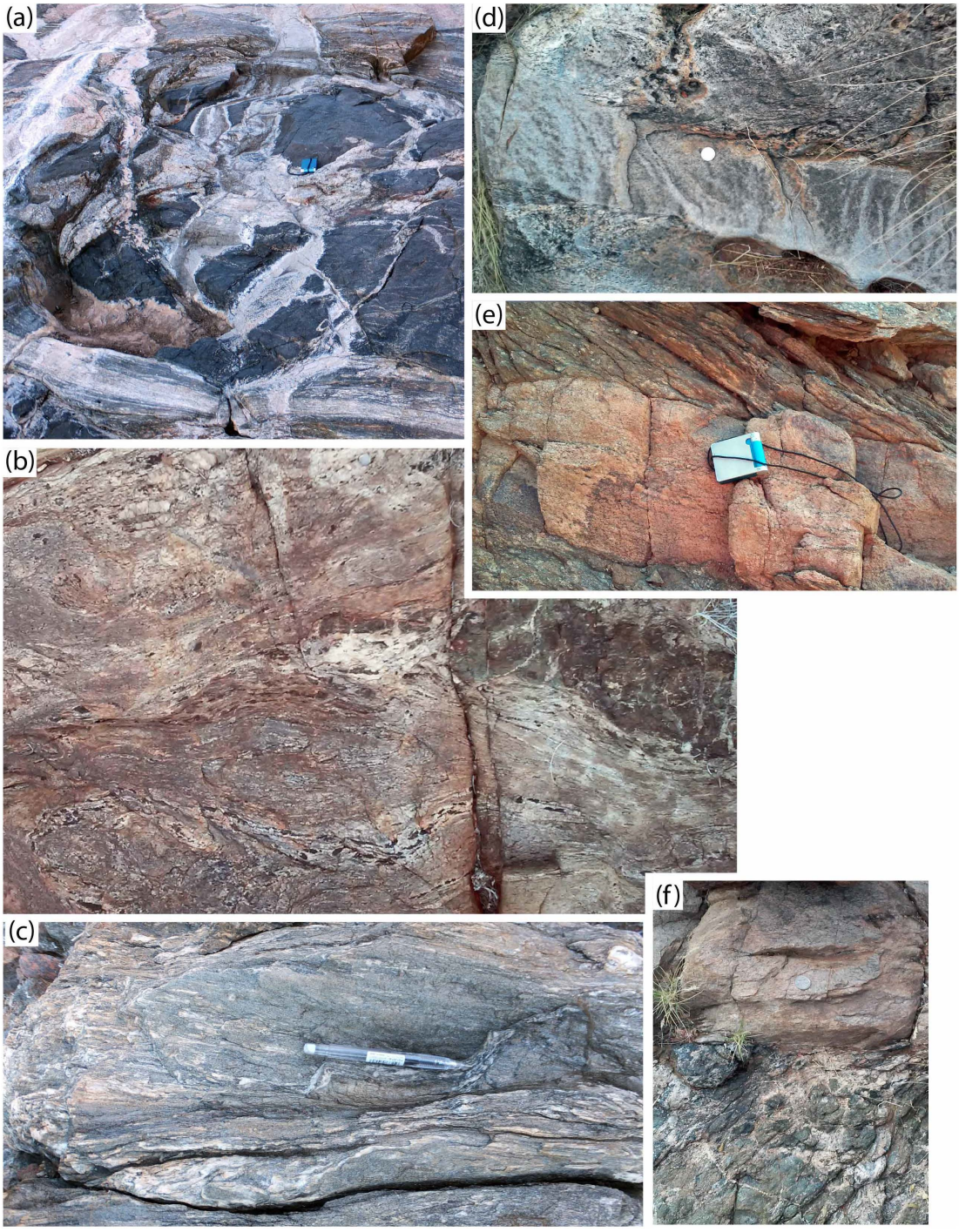

Figure 3.6: (a) Pella diatexite in the LFRTZ, dominated by brecciated mafic fragments which are suspended in a leucosome phase. Strain intesity is heterogeneous (note the shear band developed at the base of the image). (b) Sheared Pella diatexite in the LFRTZ. Note the elognated mafic fragments which also occur as stringers in the leucocratic matrix. (c) Highest strain variant of the Pella diatexite. Brecciated texture has been completely obliterated by shearing. (d) Fine grained aplitic dyke intruding leucosome-rich Pella diatexite in the LFRTZ. (e) Leucogranite dyke cross-cutting the LFRTZ shear fabric. (f) Aplite (top) intruded into Pella diatexite in the LFRTZ.

3.2.2 Grunau Terrane

The rocks of the Grunau Terrane occur primarily in the hangingwall of the LFRTZ, but in some instances also occur incorporated into the LFRTZ near the hangingwall contact. The Grunau Terrane in the current study area is constituted by pelitic granulites, occurring in various textural forms.

Pelitic granulites

Pelitic granulites primarily crop out either as dark-brown, highly competent boulders with a relatively massive appearance or occur exhibiting a finely banded (mm- to cm-scale) metatexitic texture (Figure 3.7 (a)). Additionally, a leucosome-rich variant, which in places exhibits a texture vergent on diatexitic (Figure 3.7 (b)) occurs sporadically as a narrow (<1 m thick), discontinuous layer at the base of the Hangingwall Gordonia. Occurrences of this are limited to the hangingwall immediately overlying the LFRTZ, although it is not extensively developed.

In the relatively minor instances where pelitic granulite has been incorporated into the LFRTZ near the hangingwall margin, it typically exhibits a grey-brown colour and is sheared (Figure 3.7 (c)), with a moderately developed mm-scale cleavage. Apart from the sheared version of the pelitic granulite which is fine grained, all other textural variants of this lithology are medium grained. The mineralogy is dominated by quartz, K-feldspar, bioitite, sillimanite, garnet and cordierite. In the migmatitic variant, K-feldspar and quartz constitute the characteristically pink-orange leucosome (Figure 3.7 (a)), while biotite, sillimanite, garnet and cordierite predominate in the dark melanosome. The sheared variant in the LFTRTZ typically exhibits distinct patches or rosettes of sillimanite set in the fine grained, grey-brown matrix.

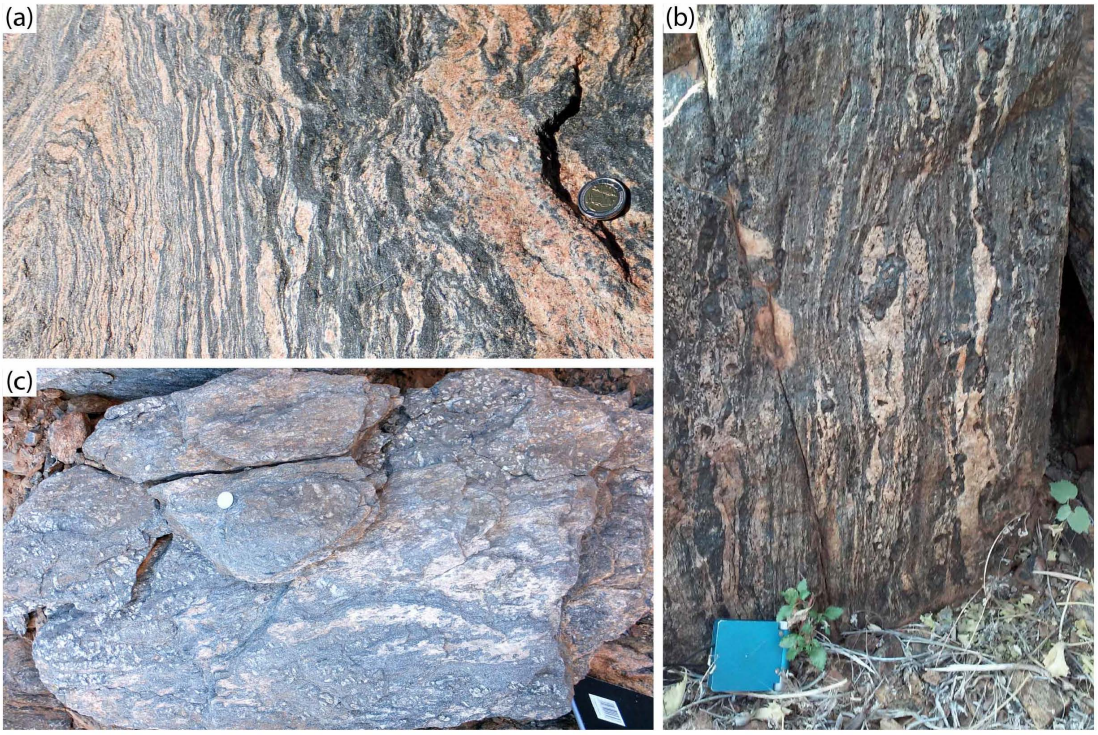

Figure 3.7: Various textural variants of pelitic granulite in the Hangingwall Gordonia domain (a,b) and the LFRTZ (c), exhibiting: (a) A prominent metatexitic texture defined by (mm- to cm-scale) banding with alteranting leucosome-rich and restitic componenets. (b) A texture vergent on diatexitic, where there is evidence of dismemberment of restitic components in leucosome-rich pockets. (c) A prominent shear fabric. This textural variant is typically spotted with sillimanite rosettes which are often aligned in the foliation.

3.3 The Lower Fish River Thrust Zone

The Lower Fish River Thrust Zone (LFRTZ) along the southwestern margin of the Kum Kum Klippe can broadly be described as a wide (∼30–40 m) compositionally and rheologically heterogeneous, tabular zone predominantly localised within (but not limited to) rocks of the Pella Terrane. However, the character of the LFRTZ is not uniform and varies from complex and imbricated along the southeastern margin of the Kum Kum Klippe to discrete and tabular along the central southwestern edge of the Kum Kum Klippe.

The character of the fabric in the LFRTZ is generally gneissose, with locally developed mylonites in isolated domains. The LFRTZ frequently hosts relatively competent units which are predominantly of mafic composition (e.g. amphibolite or two-pyroxene granulite), this results in an anastomosing ductile foliation which deflects around these competent units. Such relationships are well illustrated by a well exposed cliff outcrop of the LFRTZ and its overlying hangingwall (Figure 3.8).

Along the southwestern margin of the Kum Kum Klippe, Grunau Terrane rocks have

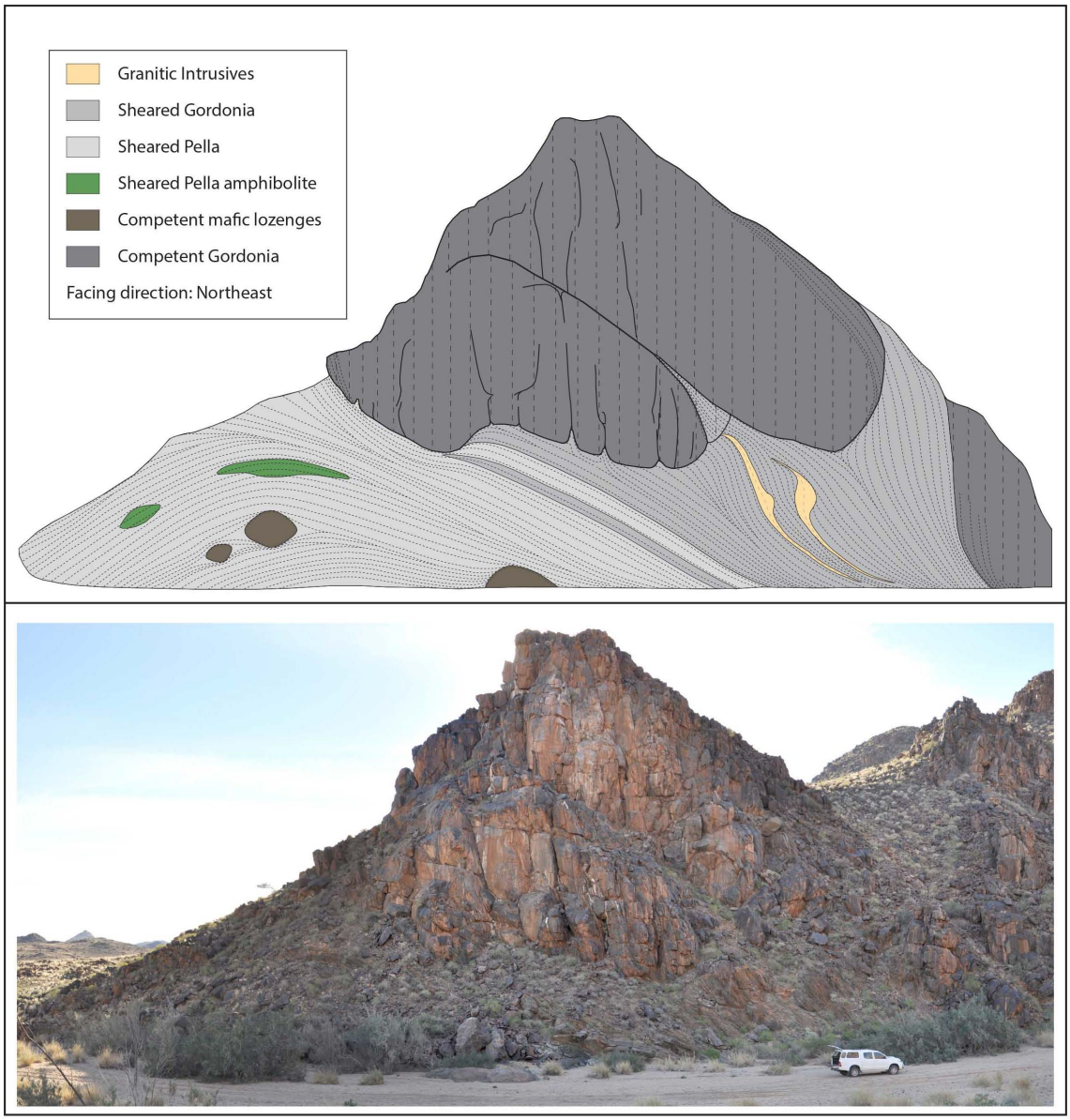

Figure 3.8: Schematic illustration (top) of a well exposed cliff outcrop of the LFRTZ and its immediate hangingwall. Original photograph is also provided (bottom; Toyota Hilux for scale). Note the anastomosing nature of the LFRTZ as well as the relationship between the shear fabric (finely stippled, anastomosing lines) and regional ductile fabric (vertical, stippled lines) in Gordonia rocks.

only locally been affected by LFRTZ fabrics in isolated domains which largely occur in the vicinity of the hangingwall contact, where fragments of overlying pelitic granulite have been incorporated into the shear zone. The pelitic granulite fragments in the LFRTZ typically occur as relatively competent lozenges which frequently display a sigmoidal geometry and are wrapped around by the LFRTZ shear fabric (Figure 3.9). These lozenges are of similar composition to the immediate hangingwall rocks.

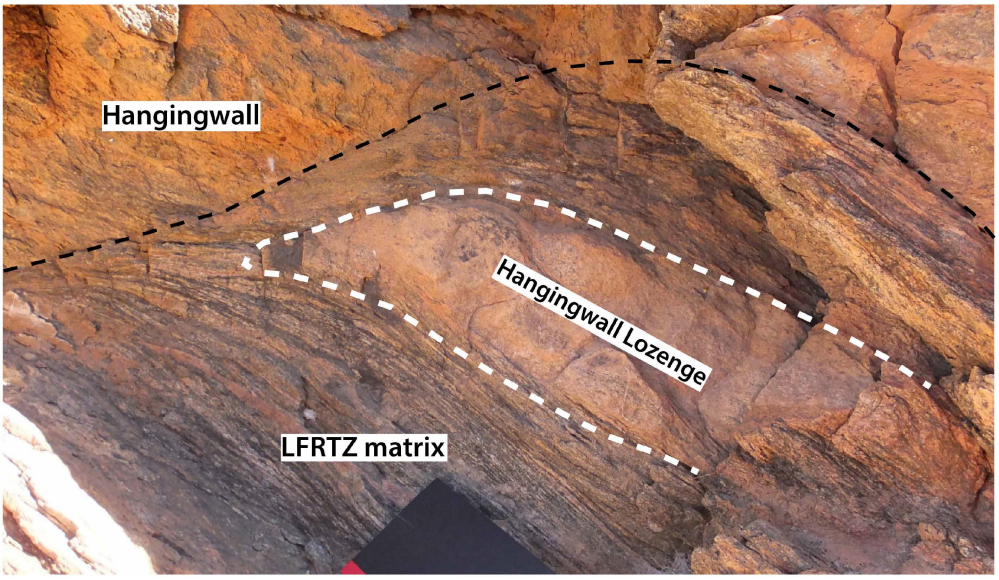

Figure 3.9: A sigmoidal, relatively competent lozenge of pelitic granulite which has been incorporated into the LFRTZ.

Chapter 4

Fabrics and Structures

This chapter provides a description of the nature and geometry of the major deformation fabrics and structures which were observed in the study area. Geometrical observations of the three major structural domains will be presented with the aid of lower-hemisphere, equal area stereonets.

4.1 Overview

Ductile deformation in the study area is mostly typified by solid-state, high grade (upper-amphibolite to granulite facies) deformation fabrics, boudins and thrusts which occur at varying scales (e.g. Figure 4.1 (a)), while folding is not as prominent. However, small-scale parasitic folding occurs widely in the Footwall Pella domain where it locally deforms the foliation (Figure 4.1 (b)). While the LFRTZ is affected by a localised shear fabric, the Footwall Pella and Hangingwall Gordonia are affected by a regional ductile fabric which varies significantly in character between the domains. Whereas the Footwall Pella domain is generally charactersied by prominent $S > L$ fabrics, the Lower Fish River Thrust Zone (LFRTZ) is typified by dominant, well-developed $L > S$ fabrics, while the Hangingwall Gordonia fabrics are broadly $L \approx S$.

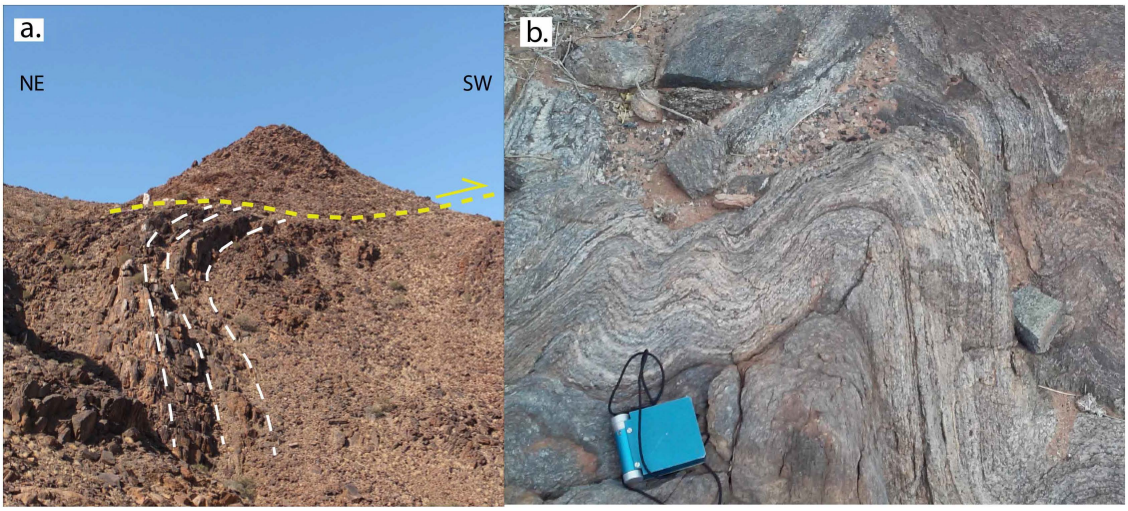

Figure 4.1: Representative examples of structures in the study area. (a) A subhorizontal thrust detachment in the Hangingwall Gordonia within the Kum Kum Klippe. Note the relationship between the regional fabric (white dotted lines) and the thrust (yellow). (b) Typical small-scale parasitic folding, locally deforming the foliation within the Footwall Pella orthogneisses.

4.2 Footwall Pella domain

The fabric intensity in the Footwall Pella domain varies widely, largely as a function of lithology. In general, the foliation is moderate- to well-developed, while the lineation is typically poorly developed.

In the stromatic gneiss, planar fabric elements are characterised by a foliation defined by the preferred orientation of biotite together with a stromatic gneissic banding which is defined by alternating leucosome-rich and melanocratic layers. This results in an overall moderately developed planar fabric (Figure 4.2 (a)). The lineation in this rock type, within the Footwall Pella domain is generally always poorly developed and defined by stretched quartz and biotite alignment.

The fabric in the pink gneiss is characterised by a distinctive S-tectonite appearance where the foliation is defined by the preferred orientation of biotite and flattened, elognated quartz ribbons, resulting in a prominent platy, cleavage (Figure 4.5 (b)). The lineation is moderately developed and defined by stretched quartz and biotite alignment.

The planar fabric in amphibolite lenses is generally defined by a poorly developed foliation, with a similarly poorly developed lineation which is defined by the alignment of prismatic hornblende. The fabric geometry in this lithology generally mimics that of the host Footwall Pella orthogneisses.

The fabric geometry in the Footwall Pella domain is characterised by a foliation which generally dips steeply to the northeast (Figure 4.2 (a)), with the measured dip direction varying between 006° and 134°, while the dip angle occurs between 40° and 84° (Figure 4.3

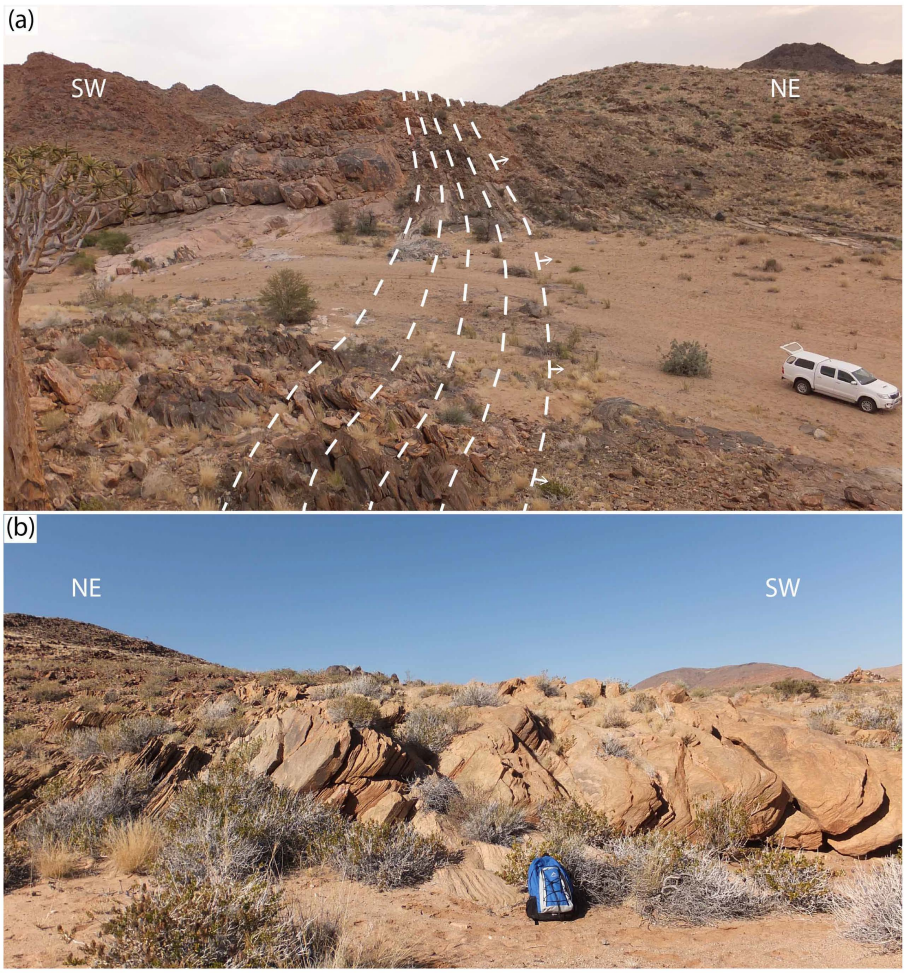

Figure 4.2: Field photographs showing fabrics developed in Footwall Pella orthogneisses. (a) Orientation and large-scale appearance of stromatic gneiss fabrics. Stippled lines trace the strike of the foliation and arrows point down dip. (b) Typical appearance and attitude of fabrics developed in the pink gneiss. Photograph taken approximately along strike.

(a, b)). The lineation in this domain displays a broad range in orientation, mostly trending between north and southeast and plunging at steep to moderate angles in the foliation with the measured lineation trend varying between 357° and 138°, plunging at angles between 20° and 60° (Figure 4.3 (c)).

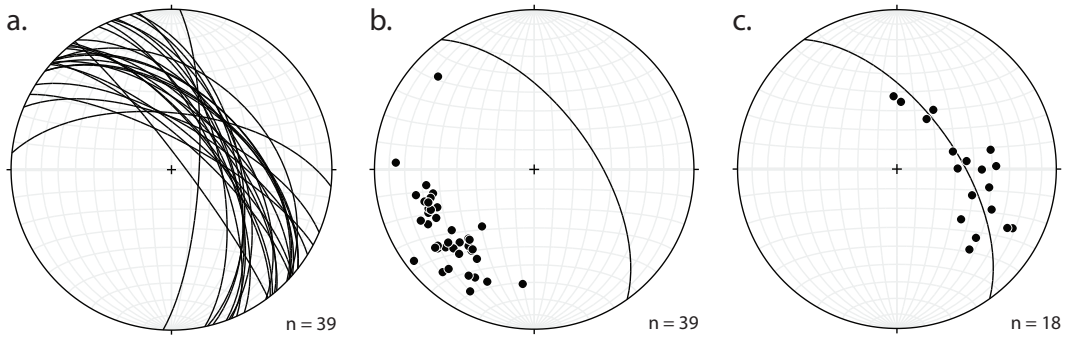

Figure 4.3: Stereonets showing the orientation of fabrics in the Footwall Pella domain. (a) All measured foliation orientations in the Footwall Pella domain. (b) Poles to all measured foliations (in the Footwall Pella domain) plotted along with the average foliation plane for the domain. (c) Lineation orientations plotted along with the average foliation plane for the domain.

4.3 Hangingwall Gordonia domain

Fabrics in the pelitic granulites of the Hangingwall Gordonia domain are characterised by a foliation which is moderately to poorly developed and defined by gneissic banding and preferred orientation of biotite, while the lineation is poorly developed and defined by aligned sillimanite needles.

In the study area, the pelitic granulite (within the Hangingwall Gordonia domain) is highly competent and typically crops out as rounded boulders; consequently, cleavage and foliation planes from which fabric orientations can be measured, are rarely exposed. Owing to this, the geometrical dataset for fabric orientations in this domain is exceedingly small in comparison to the LFRTZ and the Footwall Pella domain.

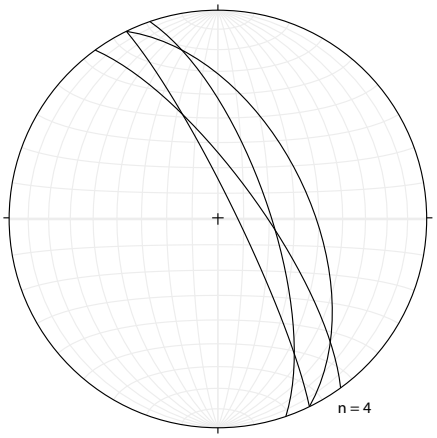

Figure 4.4: Stereonet showing the orientation of the foliation in Hangingwall Gordonia domain.

The orientation of the foliation in the Hangingwall Gordonia domain (in the vicinity of

the hangingwall contact) is steeply dipping to the northeast, with the measured dip direction varying between 054° and 071°, while the dip angle varies between 54° and 74° (Figure 4.4).

4.4 Lower Fish River Thrust Zone

The LFRTZ exhibits pronounced outcrop scale lithological and rheological heterogeneity and is charaterised by typically high strain $L > S$ ductile shear fabric, where both the foliation and lineation are well-developed.

Fabrics developed in the sheared Pella orthogneisses (stromatic gneiss and pink gneiss) of the LFRTZ are characterised by a well-developed foliation which is defined by quartz shape preferred orientation (SPO) and biotite alignment, with the latter being more prominent in the stromatic gneiss, while the former is most prevalent in the pink gneiss. These planar fabric elements typically result in a well-developed cleavage (Figure 4.5 (a, b)). The lineation is generally well-developed and defined by stretched quartz, but varies widely in intesity, with leucosome-rich and mylonitic domains exhibiting the most prominent lineation (Figure 4.5 (b)).

Amphibolite lenses typically display a less prominent solid-state deformation fabric in comparison to surrounding orthogneisses. The foliation in the amphibolites is typically moderately developed, while the lineation is always well-developed and defined by the alignment of prismatic hornblende.

The sheared pelitic granulite is characterised by a well-developed shear fabric. The foliation is moderate- to well-developed and defined by biotite alignment and quartz SPO, while the lineation is generally very well-developed and defined by aligned sillimanite clusters and stretched quartz (Figure 4.6 (a)).

The Pella diatexite may be described in relation to two end-member textural varieties which may be defined in terms of strain intensity. Where deformation intensity is low, the unit typically comprises brecciated mafic fragments suspended in a leucosome phase (Figure 3.6 (a)), while the high strain end-member is typically characterised by stringer-like, prismatic mafic laths hosted within the leucosome. Relatively leucosome-rich domains are typically characterised by an intense $L > S$ deformation fabric, where the lineation is defined by the elongated mafic stringers (Figure 4.6 (b)). The foliation in such domains is typically defined by poorly developed compositional zonation of leucosome and mafic material. As such, the fabric developed in this lithology is dominated by the lineation such that no reliable foliation measurements could be taken. In certain instances, where the relative leucosome proportion is exceedingly high, a whispy magmatic fabric predominates (Figure 3.6 (b)).

Aplitic intrusives are characterised by a poorly developed foliation defined by flattened quartz and aligned feldspars (to a lesser extent), while the lineation is well-developed and largely defined by stretched quartz. This unit frequently occurs truncating the ductile defor-

Figure 4.5: Fabrics developed in orthogneisses within the LFRTZ. (a) Prominent shear fabric developed in stromatic gneiss within the LFRTZ. Facing direction is approximately NW (b) Well-developed lineation (orientation indicated by pencil) and prominent cleavage in mylonitic pink gneiss within the LFRTZ.

mation fabrics developed within the Pella diatexite (Figure 3.6 (d)).

The foliation orientation in the LFRTZ is generally north to northeast dipping at steep to moderate angles, with the measured dip direction ranging between 329° and 080°, while the dip angle varies from 21° to 87° (Figure 4.7 (a, b)). The lineation in the LFRTZ is mostly northeast trending with a highly variable plunge angle. Measured trend orientations range between 295° and 090°, with plunge angles varying between 18° and 82° (Figure 4.7 (c)).

Fabric geometry in the sheared Pella Terrane orthogneisses and pelitic granulites are broadly similar. The foliation generally dips to the north-northeast and exhibits a moderate range in orientation with the dip direction ranging between 329° and 046° while the dip angle occurs between 21° and 78° (Figure 4.7 (a, b)). The lineation trend in these rock types mostly ranges between 355° and 089°, with the plunge occurring at angles between 19° and 55° – although a small number of measurements fall outside of this range (Figure 4.7 (c)).

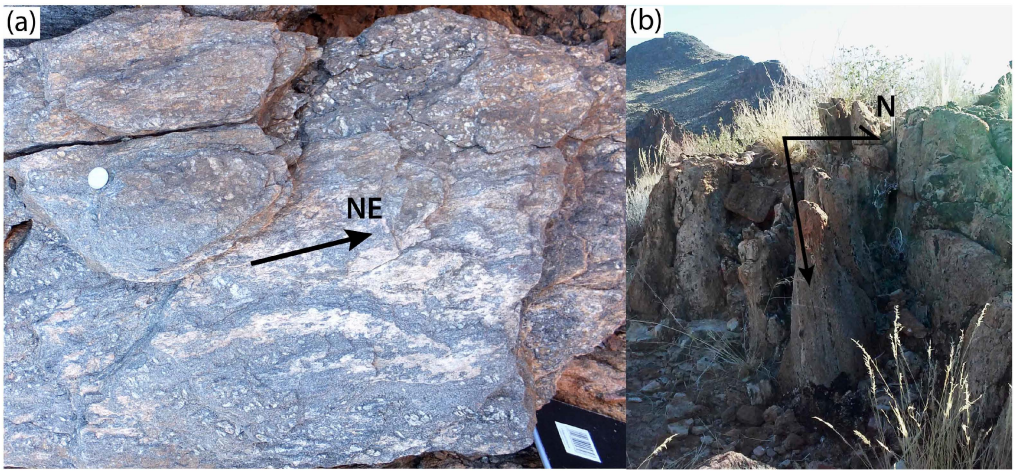

Figure 4.6: Fabrics developed in sheared pelitic granulite and Pella diatexite within the LFRTZ. (a) Typical well-developed sillimanite lineation in sheared pelitic granulites. Average lineation plunges approximately northeast in the foliation. (b) Sheared Pella diatexite with characteristically prominent lineation plunging steeply to the north. Note the lack of a well-developed foliation.

Contrastingly, the Pella diatexite lineation is characteristically always steeply plunging, mostly to the north, with trend varying between 325° and 073°, while the plunge angle occurs between 51° and 84° (Figure 4.7 (c)).

Fabric geometry in the felsic intrusives (aplite) is characterised by a foliation which is generally steeply dipping to the northeast, with the dip direction ranging between 022° and 077°, while the dip angle occurs between 51° and 87° (Figure 4.7 (a, b)). The lineation in this lithology generally plunges steeply down-dip in the foliation, trending between 043° and 090°, with the plunge angle ranging between 42° and 65° (Figure 4.7 (c)).

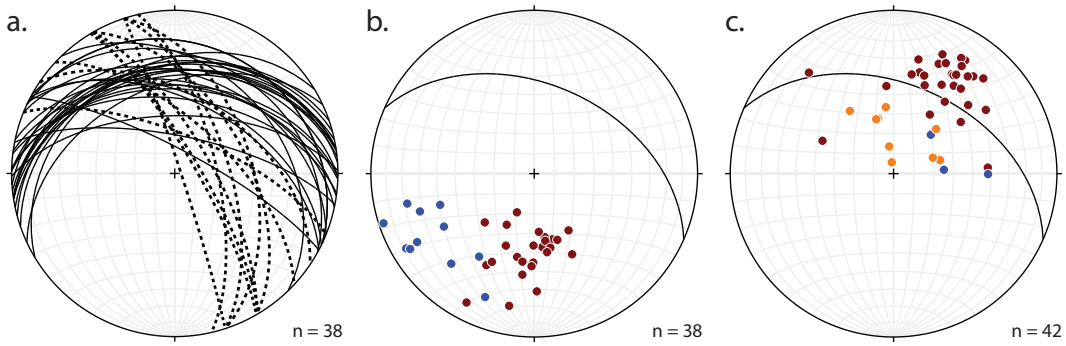

Figure 4.7: Stereonets showing the orientation of fabrics in the Lower Fish River Thrust Zone (LFRTZ). (a) Foliation orientations in the LFRTZ. Solid lines = sheared ortho- and paragneisses; dotted lines = aplitic intrusives. (b) Poles to all foliation measurements in the LFRTZ plotted along with the average foliation plane. (c) Lineation orientations in the LFRTZ plotted along with the average foliation plane. Legend: Maroon = sheared ortho- and paragneisses; Blue = aplitic intrusives; Orange = Pella diatexite.

4.5 Fabric Geometry: Summary and Comparison

This section summarises the overall geometry of fabrics in the study area, highlighting any notable or systematic differences in fabric geometry between structural domains (in particular, the LFRTZ and Footwall Pella domain).

Overall, fabric geometry in the study area is characterised by planar fabrics which largely range in dip direction between north-northwest and east. Preferred foliation orientations are indicated by clusterings of poles to measured foliations (Figure 4.8). Although the spread in foliation orientations is relatively broad – these clusterings suggest a preferred north dipping planar fabric orientation which is relatively isolated from the rest of the data. Additionally, the data shows a broad clustering of northeast to east-northeast dipping foliations; where the most dense (highest percentage area) clustering of poles in this range is indicative of foliations dipping in the latter direction (Figure 4.8).

Measured lineations in the study area predominantly trend between north-northwest and east-southeast. While this is a relatively broad spread of orientations, the occurrence of a single, relatively high percentage area clustering is indicative of a dominant north-northeast trending preferred lineation orientation (Figure 4.8).

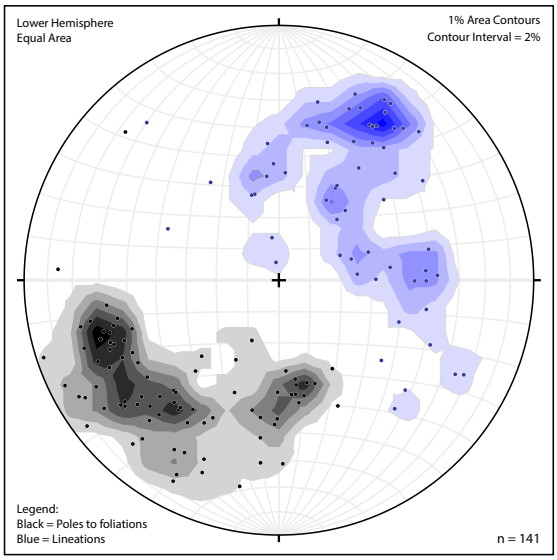

Figure 4.8: Stereonet showing the orientation of all lineations (blue) and poles to measured foliations (black). All orientation data has been contoured using 1% areas at a 2% contour interval.

4.5.1 Differences and similarities

For the sake of comparison, all fabric orientation data for the Footwall Pella domain and the LFRTZ have been separately plotted on individual stereonets (Figure 4.9).

The data presented on Figure 4.9 indicates that, in general, fabric orientations in the Lower Fish River Thrust Zone (LFRTZ) exhibit narrower and more focussed clustering (compared to the Footwall Pella domain), with high percentage areas (i.e. dense clusterings) occupying relatively narrow ranges.

In the LFRTZ, the most dominant clustering of poles corresponds to a preferrentially north dipping foliation orientation which exhibits a relatively narrow range (Figure 4.9 (a)). Contrastingly, in the Footwall Pella domain, the largest percentage of polar data occurs within a relatively broad range corresponding to northeast to east-northeast dipping foliations (Figure 4.9 (b)).

Similarly, although there is a wide spread of lineation orientations in the LFRTZ, a single clustering – which corresponds to a relatively narrow, high percentage area indicates a dominant, northeast trending lineation orientation (Figure 4.9 (a)). In the Footwall Pella domain, although there is some preferrential clustering of approximately east trending lineation orientations – virtually all lineation orientations lie on a broad 'girdle' distribution (Figure 4.9 (b)), and the clustering of lineation orientations is not as focussed as observed in the LFRTZ.

For the Hangingwall Gordonia domain, the small nature of the geometrical dataset precludes any meaningful use of contours to identify any dominant orientations. However, it should be noted that the small dataset of foliation orientations is characterised by significantly

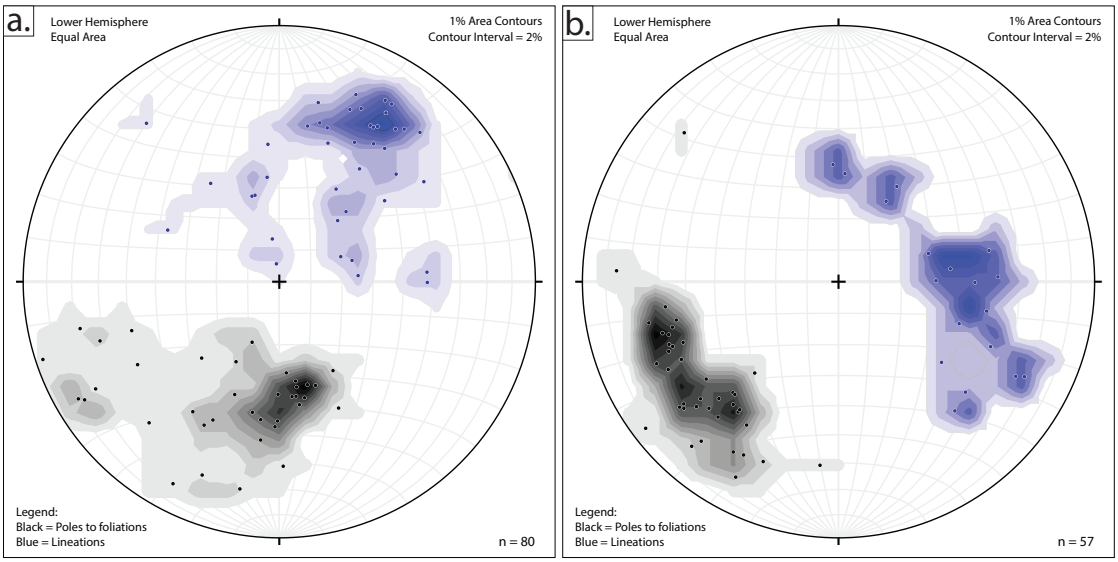

Figure 4.9: Stereonets showing the orientation of all measured lineations and poles to all measured foliations in (a) the Lower Fish River Thrust Zone; and (b) the Footwall Pella domain. Orientaion data is contoured using 1% areas at a 2% contour interval. Legend: poles to foliations = Black; Lineations = Blue.

steeper dip angles in comparison to the LFRTZ and Footwall Pella domain. Additionally, all foliation measurements for this domain dip approximately to the northeast.

Kinematics

For the Footwall Pella domain, the broad range in lineation orientations is consistent with a large coaxial component of deformation where linear fabric elements develop and/or are rotated in a poorly directed manner in the absence of a large component of directional shear – such fabrics are characteristic of dominant pure shear (e.g. Ramsay, 1980). Contrastingly, in the LFRTZ – the narrower more focussed clusterings in lineation orientation are consistent with a dominant non-coaxial component of deformation where the linear fabric elements would have tracked the shear direction with increasing shear strain – this is indicative of dominant simple shear (e.g. Ramsay, 1980).

Although a more comprehensive kinemtic investigation (which is beyond the scope of the current study) would be required to definitively determine the shear sense in the LFRTZ, the dominant northeast dipping clustering of lineation orientations observed for the LFRTZ (Figure 4.9) is consistent with a top-to-SW shear sense. This is corroborated by the findings of Blignault *et al.* (1983) and Van der Merwe & Botha (1989) who also deduce a top-to-SW shear sense for the various regional thrust shear zones in the western NMC.

Chapter 5

Petrography and Microtextures

5.1 Kum Kum Pelitic Granulites

5.1.1 Hangingwall Pelitic Granulites

Samples PM13068, JMTV45, PM13010, PM13032 and PM13076 were used to model P-T pseudosections in order to constrain peak metamorphic conditions. These samples are all pelitic granulites from various locations within the Kum Kum Klippe (Figure 3.1) and broadly have similar mineralogy. The mineralogy of these samples is constituted by quartz (18-52 vol%), feldspars [K-feldspar (14-27 vol%) and plagioclase (0-12 vol%)], sillimanite (8-20 vol%), garnet (3-20 vol%), cordierite (4-18 vol%), biotite (4-15 vol%) as well as oxide minerals (2-4 vol%): ilmenite and magnetite which most often occur interstitially with ilmenite being the most dominant of them. Monazite occurs as an accessory mineral while bottle-green spinel is present in trace amounts in some samples (Table 5.1).

Broadly, the hangingwall pelitic granulites occur in both unfoliated and foliated varieties (Figure 5.1 (a) and (b) respectively) – these are distinguished purely on the basis of fabric intensity and are made up of the same mineral assemblages. Matrix minerals (for both varieties) are constituted by biotite, quartz, feldspars and ilmenite with garnet typically occurring as porphyroblasts and porphyroclasts, while for foliated samples the fabric is typically defined by sillimanite and biotite to lesser extent. For both varieties the parageneses are generally mutually well-equilibrated with little evidence for retrogression (Figure 5.1 (a, b)).

Abbreviations: ab = albite; act = actinolite; and = andalusite; bi = biotite; cd = cordierite; chl = chlorite; cu = cummingtonite; di = diopside; ep = epidote; g = garnet; hb = hornblende; ilm = ilmenite; ksp = K-feldspar; ky = kyanite; mt = magnetite; opx = orthopyroxene; pl = plagioclase; q = quartz; ru = rutile; sill = sillimanite; sp = spinel; sph = sphene; liq = silicate melt; H_2O = aqueous fluid

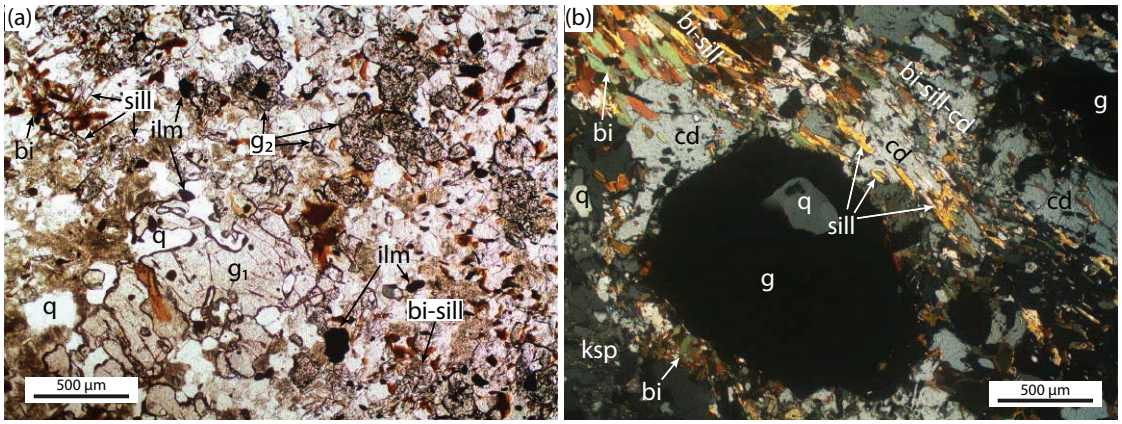

Figure 5.1: Photomicrographs showing the texture and well-equilibrated mineral assemblage of unfoliated and foliated pelitic granulite samples. (a) Typical matrix assemblage in unfoliated samples, largely constituted by fine grained sillimanite, biotite, quartz, feldspars and ilmenite while garnet occurs as porphyroblasts of varying size (in this case garnet occurs in two distinct textural forms). Note the lack of reaction textures and/or pervasive retrogression. JMTV45; plane-polarised light. (b) Typical equilibrium textural relations in foliated samples, where biotite interfingers with sillimanite in the fabric, which is in turn intergrown with cordierite. Note that the cordierite is in direct contact with the garnet porphyroblast, with no evidence of disequilibrium between the two minerals. PM13032; cross-polarised light.

Table 5.1: Approximate modal proportions (vol %) of minerals constituting hangingwall pelitic granulites samples from the Kum Kum Klippe.

	Quartz	K-Feldspar	Sillimanite	Garnet	Plagioclase	Cordierite	Biotite	Ilmenite	Magnetite	Spinel
PM13068	52	18	8	3	2	10	4	1	2	trace
JMTV45	22	20	18	18	8	4	8	2	0	0
PM13010	18	15	20	3	7	18	15	1	3	0
PM13032	30	14	10	16	12	8	8	2	0	0
PM13076	26	27	13	22	0	5	5	2	0	0

PM13068

Quartz is the most common mineral in this sample and is well recrystallised, displaying a prominent annealed texture. Sillimanite occurs in numerous textural varieties, of which the most dominant are: i) a medium grained (0.2–0.6 mm) acicular variety which defines a prominent gneissic foliation occurring in widely spaced folia (Figure 5.2 (a)) and; ii) a fine grained (<0.1 mm) fibrolitic variety, which commonly occurs rimming cordierite and K-feldspar (Figure 5.2 (b)). Cordierite is generally strongly xenomorphic and often occurs rimming the outer edges of sillimanite folia. In some isolated instances the cordierite may be locally overgrown by randomly oriented biotite (Figure 5.2 (b)) and also occurs rimmed by beards of fibrolitic sillimanite in this sample (Figure 5.2 (b)). Garnet is sparse, where present it is relatively fine grained (<0.8 mm) and often partially or completely enclosed by

cordierite.

JMTV45

Quartz occurs as grains and grain aggregates interspersed with a fine grained (<0.1 mm) sericitic groundmass such that quartz grains do not form an interconnected framework. Feldspars exhibit a moderate grain size (0.2–0.4 mm) and constitute part of the equilibrium matrix assemblage. Garnet occurs as coarse grained (∼1–8.5 mm) poikiloblasts (g_1) enclosing inclusions which mostly comprise quartz, along with biotite and ilmenite to a lesser extent (Figure 5.2 (c)). An additional texturally distinct, finer grained (<0.5 mm) variety of garnet (g_2) is distinguishable from the poikiloblastic garnet based on the following criteria: i) significantly finer grains which occur in clusters, and; ii) the ubiquitous occurrence of fibrolitic sillimanite as inclusions within this textural variety (Figure 5.1 (a)). Sillimanite also occurs as medium to fine grained (<0.3 mm) prismatic grains which are randomly oriented. Biotite often occurs as clusters of randomly oriented grains which rarely occur in association with garnet porphyroblast rims (Figure 5.2 (c)). Cordierite in this sample is sparse.

PM13010

Quartz displays triple junction grain boundaries and mostly occurs as recrystallised aggregates which frequently form bands coplanar with the foliation. Sillimanite occurs in three main textural varieties of which the most prominent is a highly acicular, medium grained variety (0.2–0.4 mm), which together with a less common coarse grained (0.5–1.5 mm) porphyroblastic variety are both aligned with the foliation and help to define a wavy, gneissic fabric (Figure 5.2 (d, e)). Sillimanite also occurs as fine grained (∼0.1 mm), randomly oriented fibrolite (e.g. Figure 5.2 (e)). Cordierite is often intergrown with the needle-like, foliation defining sillimanite such that the sillimanite enclosed by the cordierite is continuous with that outside of the cordierite (Figure 5.2 (d)). Biotite often occurs as clusters of randomly oriented grains which frequently occur as selvages lining the edges of fabric defining sillimanite folia as well as cordierite rims, although there is no evidence of resorption (Figure 5.2 (e)). Together with the randomly oriented sillimanite, the biotite forms a large proportion of the groundmass. Garnet in this sample is relatively sparse and occurs as small isolated grains or clusters of grains which are often completely or partially enclosed by cordierite. In places, garnet occurs rimmed by both cordierite and plagioclase which have been noted to occur as a coronitic symplectite in some instances (Figure 5.2 (f)).

PM13032

Quartz displays irregular grain boundaries and defines a moderately developed shape preferred orientation (SPO) which is subparallel to a well-developed anastomosing fabric defined

by aligned, interfingering biotite and sillimanite (Figure 5.1 (b)); this foliation deflects around garnet poikiloblasts (and poikiloclasts) of varying grain size (0.5–7 mm). Garnet inclusions predominantly comprise biotite, quartz and feldspar, whereas cordierite and randomly oriented clusters of biotite tend to proliferate along garnet rims (Figure 5.1 (b)). As with other pelitic granulite samples, garnet is normally poikiloblastic, hosting an inclusion assemblage dominated by quartz and feldspars (e.g. Figure 5.2 (g)).

PM13076

This sample exhibits well-developed compositional layering where layers dominated by equigranular K-feldspar alternate with domains largely devoid of K-feldspar where garnet, cordierite and sillimanite tend to proliferate (Figure 5.2 (h)); this layering helps to define a stromatic gneissosity. Garnet occurs as coarse grained (1–6 mm) poikiloblasts (g_1); with an inclusion assemblage dominated by quartz, while minor fibrolitic sillimanite inclusions are limited to the rims. Garnet also occurs as a significantly finer grained (<0.5 mm) textural variety (g_2) rich in fibrolitic sillimanite inclusions (Figure 5.2 (h)). Ilmenite is fine grained (<0.3 mm), occurring as variably shaped grains. Cordierite in this sample is sparse and generally limited to the domains devoid of K-feldspar (Figure 5.2 (h)).

Figure 5.2 ***(following page)*:** Microtextures observed in hangingwall pelitic granulites of the Kum Kum Klippe. (a) Folia of acicular sillimanite define a well-developed gneissic fabric extending diagonally across the field of view. Note that oxide minerals often occur interstitially. PM13068; crossed-polarised light. (b) Biotite overgrowth locally partially overprints ovoid cordierite rimmed by fibrolitic sillimanite. PM13068; plane-polarised light. (c) Quartz-ilmenite inclusion-rich garnet poikiloblast is partially rimmed by biotite. JMTV45; plane-polarised light. (d) Acicular sillimanite is intergrown with cordierite and K-feldspar; significantly coarser grained sillimanite variety (top right) is less common. PM13010; cross-polarised light. (e) Biotite selvage lines sillimanite folia. Note distinct sillimanite textural varieties occurring in: the foliation, groundmass (center) and as aligned, acicular inclusions in cordierite (top-center). PM13010; cross-polarised light. (f) Sillimanite-ilmenite inclusion-rich garnet is rimmed by cordierite and plagioclase. The cordierite-plagioclase rim is in-turn partially rimmed by biotite. PM13010; plane-polarised light. (g) Garnet partially encloses and contains inclusions of quartz and plagioclase. PM13032; cross-polarised light. (h) Prominent compositional layering defines a stromatic banding. PM13076; plane-polarised light.

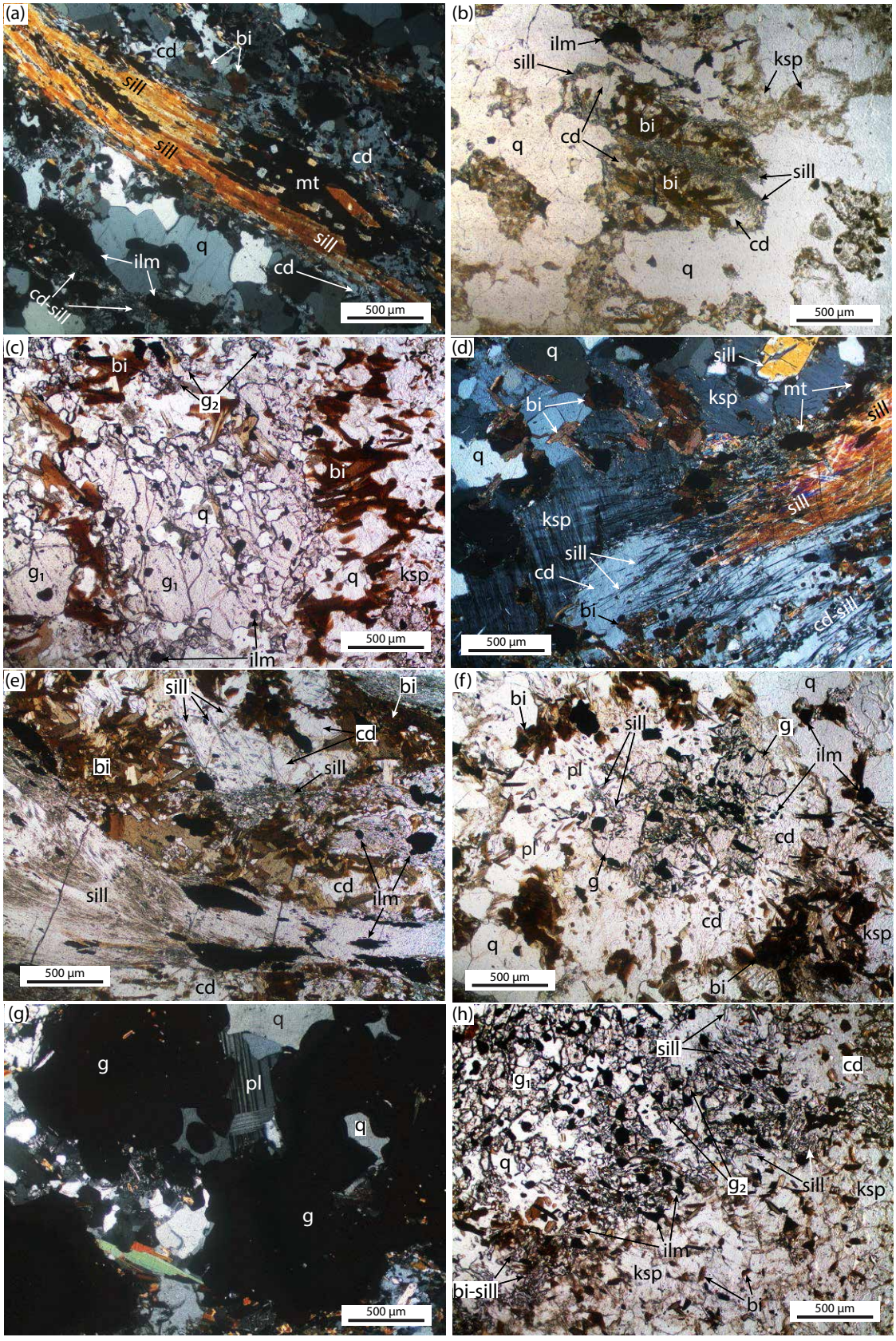
(a)
bi
cd
sill
sill
cd
mt
sill
q
ilm
cd
cd-sill
500 µm
(b)
ilm
sill
ksp
bi
q
cd
sill
bi
cd
q
500 µm
(c)
bi
g2
bi
q
g1
g1
q
ksp
ilm
500 µm
(d)
q
sill
bi
ksp
mt
sill
q
sill
ksp
sill
cd
bi
cd-sill
500 µm
(e)
sill
bi
cd
bi
sill
sill
cd
ilm
500 µm
cd
(f)
bi
q
sill
g
ilm
pl
cd
pl
g
cd
ksp
q
500 µm
bi
(g)
q
g
pl
q
g
500 µm
(h)
sill
cd
g1
q
g2
sill
ksp
ilm
ksp
bi-sill
bi
500 µm

5.1.2 Sheared Pelitic Granulites

Sheared pelitic granulite samples KK02, KK04, KK10, KK27, KK28 and KK29 were collected from various localities within the LFRTZ at the Kum Kum Klippe (Figure 3.1) – these samples were selected to model pseudosections in order to constrain the P-T conditions under which the localised shearing which resulted in tectonic emplacement of the Grunau Terrane above the Richtersveld Subprovince along the LFRTZ occured. The mineralogy of these samples comprises quartz (64-13 vol%), feldspars [K-feldspar (1-20 vol%) and plagioclase (5-20 vol%)], biotite (7-20 vol%) and magnetite (<1-3 vol%) ±cordierite (0-13 vol%) ±garnet (0-10 vol%) ±sillimanite (0-25 vol%). Monazite occurs as an accesory mineral while spinel occurs in trace amounts in some samples (Table 5.2).

Table 5.2: Approximate modal proportions (vol %) of minerals constituting sheared pelitic granulite samples from the LFRTZ at the Kum Kum Klippe.

	Quartz	K-feldspar	Plagioclase	Biotite	Sillimanite	Garnet	Cordierite	Magnetite	Spinel
KK02	52	13	5	10	13	2	2	3	0
KK04	45	11	13	16	8	2	2	3	trace
KK10	64	14	15	7	0	0	0	0	0
KK27	55	12	8	15	trace	10	0	trace	0
KK28	40	20	18	9	4	6	2	1	0
KK29	13	1	14	20	25	10	13	4	trace

KK02

Quartz is the most common mineral in this sample, forming a polycrystalline framework which in places defines a mildly developed shape preferred orientation (SPO) subparallel with a sillimanite-biotite foliation. Both K-feldspar and plagioclase are highly sericitised and occur within the quartz dominated matrix, with K-feldspar being more prevalent and occurring as irregularly shaped grains (Figure 5.3 (a)), while plagioclase is comparatively sparse. Sillimanite as well as biotite to a lesser extent are the principal fabric defining minerals, with the discontinuous sillimanite-biotite folia pervading the quartz dominated framework matrix (Figure 5.3 (a, b)). Fine grained (<0.3 mm), aligned sillimanite mats are partially rimmed and overprinted by biotite which occurs both aligned in the foliation and as randomly oriented grains associated with the rims of the sillimanite mats (Figure 5.3 (a, b)); apart from this, biotite is generally in equilibrium with the matrix assemblage. Magnetite occurs as irregularly shaped grains associated with the rims of sillimanite folia, while it also occurs less prominently as variously shaped fine grains (<0.3 mm; Figure 5.3 (a)). Garnet and cordierite occur in very small amounts, forming part of the matrix assemblage.

KK04

The fabric in this sample is continuous and well-developed, defined by greenish-brown biotite and sillimanite to a lesser extent. Fabric defining biotite partially pseudomorphs sillimanite which occurs relict in the foliation (Figure 5.3 (c)). The matrix assemblage largely comprises quartz and partially sericitised feldspars (K-feldspar and plagioclase) which form a framework which is locally pervaded by the narrow (<1 mm thick) biotite-sillimanite folia (Figure 5.3 (c)). Additionally, garnet and cordierite occur in very small amounts. Magnetite occurs as irregularly shaped grains which in places are associated with trace amounts of bottle-green spinel.

KK10

The fabric in this sample is poorly developed, discontinuous and defined by the alignment of greenish-brown biotite and a quartz SPO which occurs in localised domains (Figure 5.3 (d)). The matrix assemblage is largely constituted by fine grained (<0.25 mm) quartz, plagioclase and K-feldspar. Grain size layering is evident, with coarser (0.25–1 mm) matrix domains occurring in places. The poorly developed fabric wraps around relatively large (>1 mm) porphyroclastic plagioclase (Figure 5.3 (d)).

KK27

Moderate to well-developed, but not completely interconnected biotite alignment defines the fabric (Figure 5.3 (e, f)). The matrix assemblage is largely constituted by fine grained (<0.25 mm), equigranular quartz along with partially sericitised plagioclase and K-feldspar, where plagioclase is the most prevalent of the feldspars, in places occurring as ∼1 mm porphyroclasts. Garnet grain size varies considerably (<0.3–1.5 mm), with coarser grains often occurring as porphyroclasts which deflect and are enveloped by the foliation (Figure 5.3 (e)). The smaller garnet grains often form aligned trails along the foliation (Figure 5.3 (f)). Larger garnet porphyroblasts (and porphyroclasts) contain inclusions dominated by biotite and quartz, while magnetite inclusions are relatively sparse. In some cases, garnet is characterised by highly irregular or serrated grain boundaries. In places, biotite in the foliation appears to be intermingled with subordinate, relict sillimanite in the foliation (Figure 5.3 (f)).

KK28

The fabric in this sample is defined by: a) the preferred orientation of red-brown biotite and sillimanite which forms discontinuous folia and; b) elongated, partially recrystallised quartz ribbons which define a well-developed SPO subparallel to the biotite-sillimanite foliation

(Figure 5.4 (a)). Garnet occurs as porphyroclasts which often appear to be elongated and forming an aligned trail along the foliation which wraps around the garnet (Figure 5.4 (b)). The garnet porphyroclasts are generally rich in quartz, biotite and sillimanite inclusions while grain boundaries are generally not pristine, showing evidence of partial resorption (Figure 5.4 (b)). Quartz and feldspar form an equigranular framework which shows evidence of grain size layering, where well foliated domains correspond to zones of very fine grain size (<0.5 mm; Figure 5.4 (c)). Compositional layering is evident in places, where feldspar-rich domains alternate with garnet-sillimanite-biotite rich layers (e.g. Figure 5.4 (c)). Cordierite occurs sporadically in small amounts.

KK29

A highly prominent and well-developed, wavy fabric is defined by the alignment of interfingering biotite and sillimanite (Figure 5.4 (d)). The prominent sillimanite-biotite foliation is generally continuous and pervades fine grained (<0.25 mm) matrix dominated by quartz and plagioclase feldspar to a much lesser extent. Quartz is particularly fine grained where it is in close association with well foliated domains. The fabric is deflected by relatively coarse grained (1.5–4 mm) garnet porphyroclasts which host a broad inclusion assemblage comprising biotite, sillimanite, quartz and plagioclase (Figure 5.4 (e)). Garnet is generally partially to completely rimmed by cordierite which embays and corrodes garnet grains, resulting in highly irregular grain boundaries as well as fragmentation of individual garnet grains in places (Figure 5.4 (e)). Cordierite porphyroclasts are generally intergrown with and pervaded by the biotite-sillimanite foliation, while in some cases, the foliation is deflected by the xenomorphic cordierite porphyroclasts (Figure 5.4 (d)). Biotite also occurs as a randomly oriented and clustered textural variant. This biotite typically occurs in the vicinity of garnet rims and is generally associated with a similarly unfoliated and clustered sillimanite textural variety (Figure 5.4 (f)). Magnetite generally occurs as irregular interstitial blebs which are frequently aligned with the foliation (e.g. Figure 5.4 (d)) and associated with bottle-green spinel in places.

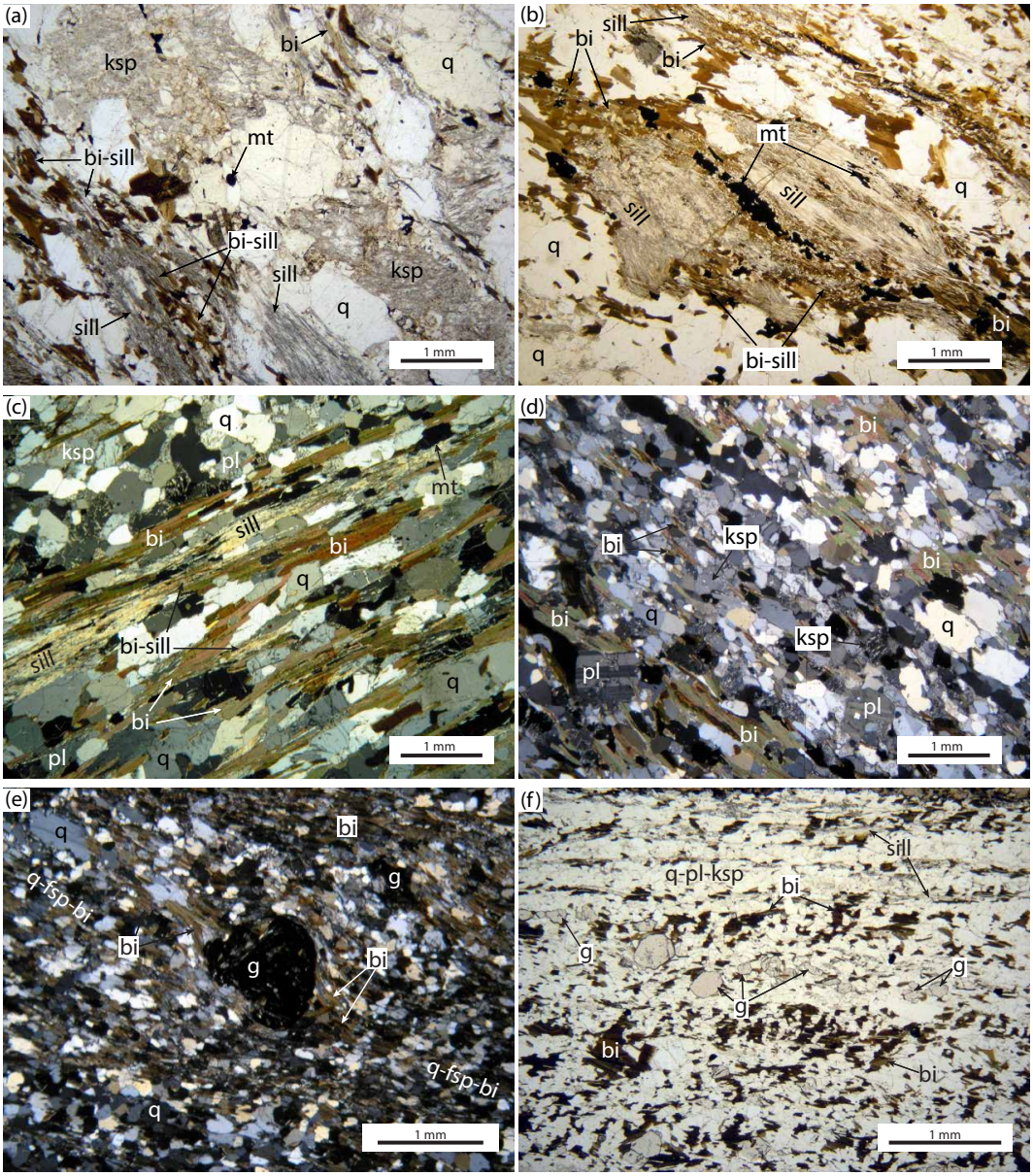

Figure 5.3: Representative microtextures observed in sheared pelitic granulites of the Kum Kum Klippe. (a) Fine grained sillimanite folia are rimmed by biotite which is aligned in the foliation. KK02; plane-polarised light. (b) Fine grained sillimanite mats form discontinuous folia which are partially rimmed by poorly aligned biotite. KK02; plane-polarised light. (c) Biotite and sillimanite define a well-developed, penetrative fabric where the sillimanite in the foliation is largely overprinted by biotite. (d) Highly discontinuous biotite foliation and quartz SPO define a poorly developed fabric. In places, biotite in the foliation wraps around plagioclase porphyroclasts (bottom left). KK10; cross-polarised light. (e) Biotite in a relatively fine grained matrix defines a discontinuous foliation which wraps around biotite-quartz inclusion rich garnet. KK27; cross polarised light. (f) Fine grained garnet forms a trail aligned with a foliation defined by biotite which overprints subordinate sillimanite occurring relict in the foliation. KK27; plane-polarised light.

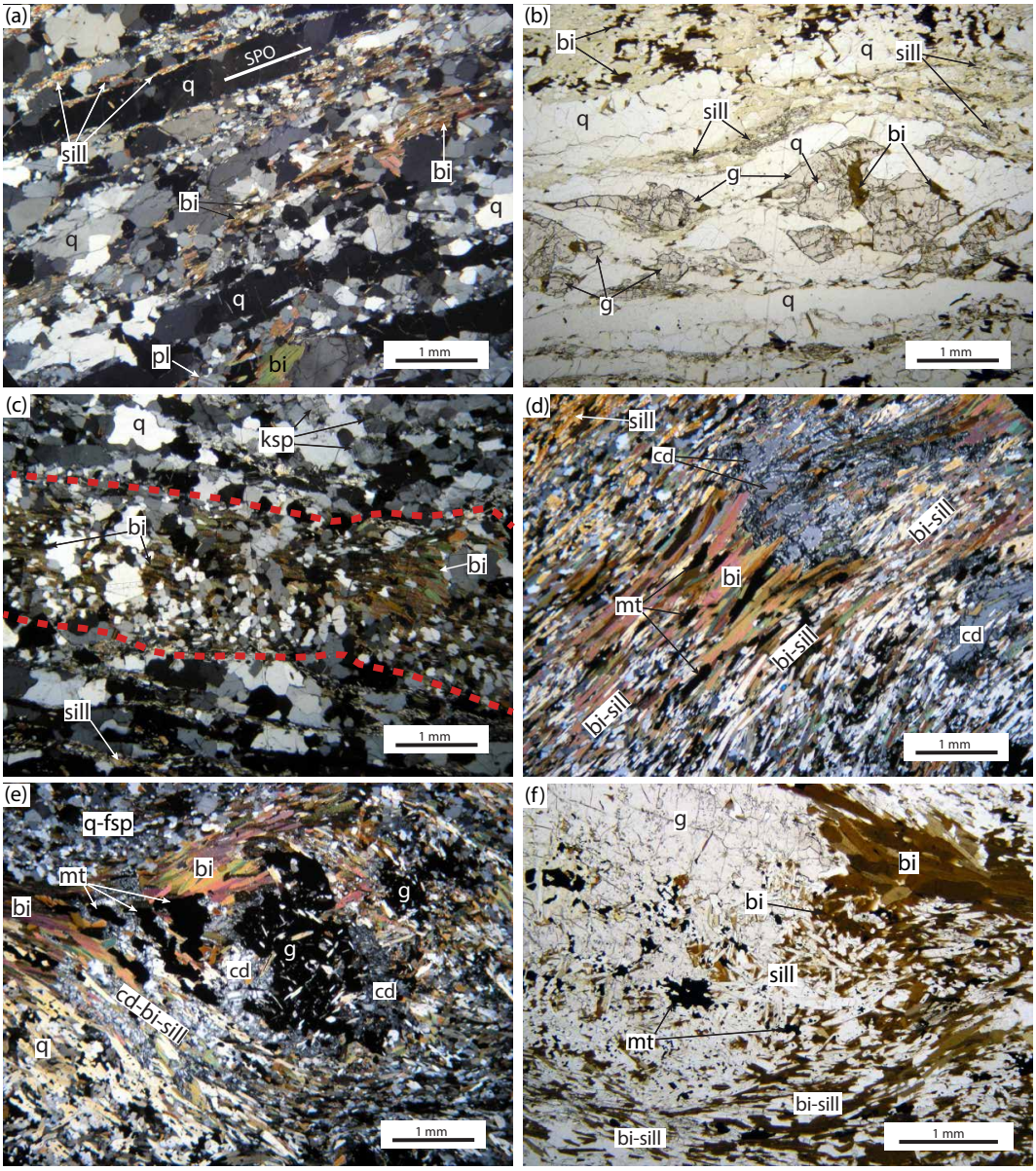

Figure 5.4: Representative microtextures observed in sheared pelitic granulites of the Kum Kum Klippe (continued). (a) Fabric defined by discontinuous biotite alignment and well-developed quartz SPO. KK28; cross-polarised light. (b) Garnet porphyroclasts enclosed by and containing inclusions of quartz, the garnet is also partially rimmed by biotite appear to form an aligned trail along the foliation. KK28; plane-polarised light. (c) Grain size zonation where foliated domain shows notably finer grain size (between the red dotted lines). KK28; cross-polarised light. (d) Well-developed, penetrative fabric defined by interfingering biotite and sillimanite is partially deflected by xenomorphic cordierite which is rimmed by fibrolitic sillimanite. KK29; cross-polarised light. (e) Highly corroded, inclusion-rich garnet is partially enclosed by cordierite. The biotite-sillimanite fabric is deflected by the garnet porphyroclast. KK29; cross-polarised light. (f) Interfingering biotite and sillimanite define a well-developed fabric, while unfoliated biotite and sillimanite textural varieties occur in the matrix. KK29; plane-polarised light.

5.2 Footwall Metamafic Rocks

Samples KK12, KK14 and KK19 are Pella amphibolites which were collected immediately adjacent to the Kum Kum Klippe in the LFRTZ and Footwall Pella domain (Figure 3.1), these samples were collected in order to constrain the P-T conditions experienced by rocks of the Pella Terrane in the LFRTZ and its footwall. KK12 and KK19 were sampled from the immediate footwall of the LFRTZ, while KK14 was sampled from within the LFRTZ. The mineralogy of these samples is dominated by hornblende (58-72 vol%) and plagioclase (20-33 vol%), while quartz (0-8 vol%), opaques (0-3 vol%): ilmenite and magnetite, chlorite (0-8 vol%), and titanite (0-1 vol%) also occur, but are not common to all of the samples (Table 5.3).

Table 5.3: Approximate modal proportions (vol %) of minerals constituting Pella amphibolite samples in the LFRTZ and its immediate footwall at the Kum Kum Klippe.

	Hornblende	Plagioclase	Quartz	Magnetite	Chlorite	Titanite	Ilminite-rutile
KK12	64	31	2	3	0	accessory	0
KK14	72	20	8	0	0	0	trace
KK19	58	33	0	0	9	0	trace

KK12

A moderate- to well-developed foliation is defined by green-brown pleochroic, aligned, prismatic hornblende which exhibits large variation in grain size (<0.5–5 mm; Figure 5.5 (a)). The matrix is mainly constituted by medium grained (<1 mm) equigranular plagioclase, with quartz being subordinate. Magnetite occurs as blebby patches in symplectitic intergrowths with hornblende, where the hornblende in the symplectite exhibits brownish alteration where it is in contact with the magnetite (Figure 5.5 (b)). Fine grained (<0.25 mm) accessory titanite occurs sporadically (Figure 5.5 (a)).

KK14

Fine grained prismatic and equigranular hornblende defines a moderately developed fabric (Figure 5.5 (c, d)). In addition to hornblende, the matrix assemblage is also constituted by medium to fine grained (<1 mm) plagioclase along with fine grained (<0.5 mm) quartz to a lesser extent – with plagioclase typically being partially sericitised. In general, fine-scale (<1 mm) compositional banding is well-developed, where plagioclase-rich layers alternate with aligned hornblende domains (Figure 5.5 (c)). In places, plagioclase occurs as recrystallised, lensoidal porphyroclasts (Figure 5.5 (d)). Ilmenite is rare, occurring sporadically as variously shaped grains of very fine grain size.

KK19

A predominantly granoblastic texture is defined by medium to coarse grained hornblende (<0.5–3 mm) and medium grained plagioclase (<0.5–1 mm; Figure 5.5 (e)). Hornblende exhibits a large variety in grain size, where particularly coarse grains occur as recrystallised porphyroclasts (Figure 5.5 (e, f)). The matrix is predominantly constituted by medium to fine grained hornblende and plagioclase where plagioclase is generally highly sericitised and hornblende is weakly aligned in places (Figure 5.5 (e)). Chlorite is relatively sparse and occurs as fine grained, foliated lenses which are occasionally deflected by the coarse grained porphyroclastic hornblende which is lensoidal in some instances (Figure 5.5 (f)). Rutile is sparse, occurring sporadically in the matrix as very fine grains.

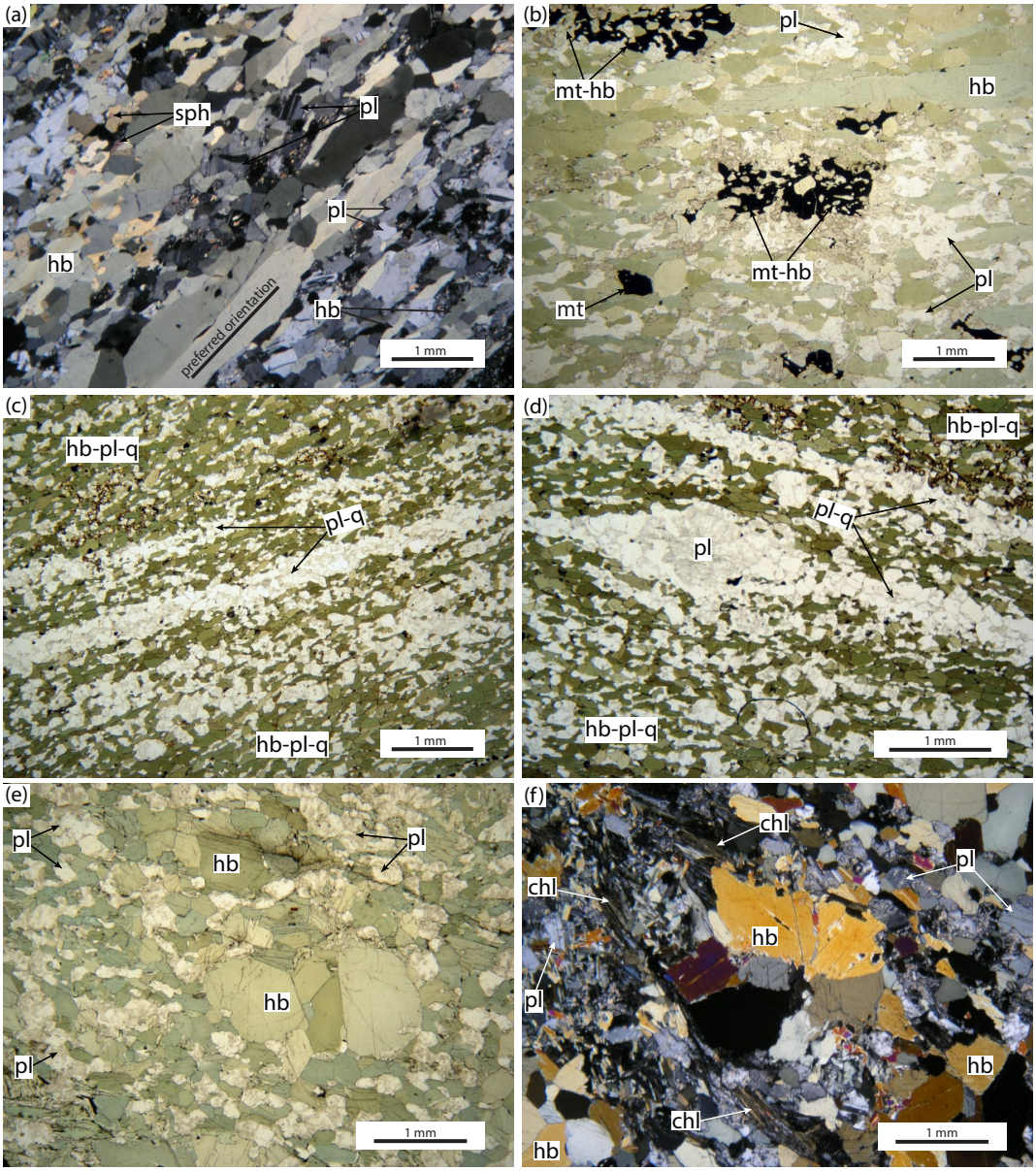

Figure 5.5: Representative microtextures observed in Pella amphibolites from the Kum Kum Klippe. (a) Well-developed fabric is defined by preferred orientation of coarse grained, prismatic hornblende. The matrix is predominantly constituted by medium grained hornblende and plagioclase. KK12; cross-polarised light. (b) Magnetite frequently occurs as irregular blebs in vermicular hornblende-magnetite symplectites where hornblende displays evidence of alteration. KK12; plane-polarised light. (c) Well-developed fabric defined by preferred orientation of fine grained, equigranular and prismatic hornblende. Fine-scale compositional banding is defined by interlayering of hornblende-plagioclase-quartz domains with narrow plagioclase-rich domains. KK14; plane-polarised light. (d) Plagioclase occasionally occurs as elongated, lensoidal and recrystallised grains. KK14; plane-polarised light. (e) Granoblastic texture, where hornblende occurs as coarse grained recrystallised porphyroclasts in an equigranular hornblende-plagioclase matrix. KK19; plane-polarised light. (f) Narrow, fine grained chlorite folia are deflected by coarse grained, recrystallised hornblende porphyroclast. KK19; cross-polarised light.

5.3 Characterisation of microtextures and inferred equilibrium assemblages

In this section important microtextural features of hangingwall pelitic granulites, sheared pelitic granulites and Pella amphibolites are characterised and equlibrium assemblages are deduced for each of these rock types.

5.3.1 Hangingwall pelitic granulites

The two distinct textural varieties of garnet noted in JMTV45 and PM13076 are ascribed to distinct garnet growth phases. The quartz, feldspar and biotite inclusion rich, poikiloblastic garnet (g_1; e.g. Figure 5.2 (c)) is interpreted to represent peritectic garnet. The significantly finer grained garnet which is rich in fibrolitic sillimanite inclusions (g_2; e.g. Figure 5.1 (a)) is interpreted to represent minor, late garnet growth since this textural variant of garnet often occurs along the rims of g_1. This is most easily explained by invoking late growth of g_2 along the rims of already formed g_1 grains.

The occurrence of distinct textural varieties of sillimanite in most samples is interpreted to represent distinct sillimanite growth phases: i) the acicular fabric defining sillimanite (Figure 5.2 (a, d, e)) likely reflects the development of the regional ductile deformation fabric at or near peak metamorphic conditions while; ii) the randomly oriented prismatic sillimanite occurring in the matrix of unfoliated samples (e.g. Figure 5.1 (a)) likely represents growth at peak conditions as it does not occur as inclusions in any of the major porphyroblast phases and is thus much less likely to have formed during prograde metamorphism (e.g. Vernon, 1996) and; iii) the occurrence of minor fibrolitic sillimanite rimming cordierite (Figure 5.2 (b)) is consistent with an increment of cooling which likely occurred soon after peak metamorphism (e.g. Boger & White, 2003; White *et al.*, 2004; Diener *et al.*, 2013).

For Hangingwall pelitic granulites, where samples have no well-developed foliation, the presence of sillimanite, biotite, garnet, ilmenite, K-feldspar, quartz and cordierite coexisting and in mutual contact with no evidence of disequilibrium (e.g. embayment and pseudomorphing; only rare occurrences of biotite reaction textures occur in some samples) between the minerals, indicates that these minerals form part of the equilibrium assemblage (Figure 5.1 (a)). Furthermore, since high grade minerals are relatively well-preserved in all samples, with no evidence of pervasive rehydration and/or replacement by lower grade minerals – it follows that the equilibrium assemblage should be representative of peak metamorphic conditions.

In general, the equilibrium assemblage observed in foliated samples is similar to that observed in unfoliated samples (Figure 5.1). Moreover, well-foliated samples occasionally exhibit a fabric characterised by interfingering biotite and sillimanite – this fabric may occur intergrown with cordierite (e.g. Figure 5.1 (b)), thus suggesting stable coexistence of these

minerals.

In many instances, it is observed that garnet is highly poikiloblastic hosting abundant feldspar (both plagioclase and K-feldspar) and quartz inclusions (Figure 5.2 (g)). This is a feature typical of peritectic garnets, and indicates that these garnet grains (g_1) grew in the presence of melt (Sawyer & Brown, 2008; White *et al.*, 2004). Thus, it follows that the minerals constituting the peak assemblage would have been in equilibrium with a silicate melt phase at suprasolidus P-T conditions.

In many instances garnet crystals seem to coexist with euhedral crystals of feldspars and cuspate domains of quartz (Figure 5.2 (g)). These microstructures are likely to represent former patches of melt (Sawyer & Brown, 2008; White *et al.*, 2004), and thus provide evidence that garnet grew in the presence of melt. Thus, it follows that the minerals constituting the peak assemblage would have been in equilibrium with a silicate melt phase at suprasolidus P-T conditions.

Although cordierite has been noted to occur rimming both garnet porphyroblasts and sillimanite folia (Figures 5.1 (b) and 5.2 (a)), this does preclude the inclusion of garnet and sillimanite as part of the equilibrium assemblage since these textures could represent changes in the equilibrium mineral modes within a single mineral assemblage field (e.g. White *et al.*, 2002; Vernon *et al.*, 2008). Similarly, whereas the observation of cordierite being rimmed by fibrolitic sillimanite is clearly an indication of sillimanite growth at the expense of cordierite (Figure 5.2 (b)), this need not imply that cordierite exist metastabley (with respect to the peak assemblage) – particularly because foliation defining sillimanite is seen intergrown with cordierite in certain textural settings (Figure 5.1 (a)).

Thus, for hangingwall pelitic granulites, the textural relationships described above are consistent with an (equilibrium) peak assemblage characterised by coexisting **garnet, biotite, cordierite, sillimanite, quartz, K-feldspar, plagioclase and ilmenite** – which would have all been at equilibrium with a silicate melt phase at suprasolidus P-T conditions.

5.3.2 Sheared pelitic granulites

With exception of KK29[2], garnet either occurs in low modal proportions or is not present at all (Table 5.2). This is in contrast to the hangingwall pelitic granulites where on average, garnet occurs in significantly higher modal proportions (Table 5.1).

The relative scarcity of garnet in these rocks, given the significantly higher modal proportion of garnet in the hangingwall pelitic granulites, likely indicates that prexisting garnet (formed during peak and/or prograde metamorphism) was variably resorbed in sheared pelitic

[2]Textures observed in KK29 are in some aspects reminiscent of those observed for hangingwall pelitic granulites. This is interpreted to suggest that this particular sample was not subject to as significant shearing induced textural reworking – thus leaving the peak mineral textural relationships less changed.

granulites during the post thermal peak metamorphic history. Moreover, in KK29 where garnet is relatively abundant, it is rimmed and corroded by cordierite (Figure 5.4 (e)). Such garnet resorption and development of cordeirite coronae can be correlated with decompression due to the shallow dP/dT of garnet consuming reactions (e.g. Hand *et al.*, 1992; Brown, 2002; White & Powell, 2011).

In KK28, garnet enclosed by quartz (and containing inclusions of quartz) and is partially rimmed by biotite in places (Figure 5.4 (b)). The inclusions of quartz and biotite are consistent with the garnet being peritectic as they likely represent the remnants of melt (Cesare *et al.*, 2009; White *et al.*, 2004). Similarly, the quartz enclosing the garnet is interpreted to represent the remnants of melt, and the partial biotite rim may be attributed to melt crystallisation (White & Powell, 2011). This texture is consistent with the fact that although sheared pelitic granulites preserve a solid state shear fabric, these rocks underwent melting prior to subsolidus shearing.

The prevalence of a quartz SPO where in some instances quartz forms highly elongated ribbons subparallel with the foliation (Figure 5.3 (a)) indicates that quartz accomodated significant strain by disclocation creep (Hirth & Tullis, 1992). Moreover, the occurrence of well-foliated domains which are associated with a significantly finer grain size of quartz (Figure 5.4 (c)) is attributed to grain size reduction by dynamic recrystallisation due to preferrential intracrystalline slip along aligned biotite cleavage planes in well-foliated domains (e.g. Imber *et al.*, 1997; Montési, 2013). These microstructures are indicative of deformation by crystal plasticity (Hirth & Tullis, 1992; Stipp *et al.*, 2002).

As is the case with hangingwall pelitic granulite samples, the occurrence of fibrolitic sillimanite rimming cordierite (e.g. Figure 5.4 (d)) is consistent with a cooling dominated retrograde segment.

For sheared pelitic granulite samples from within the LFRTZ, matrix minerals predominantly comprising quartz, K-feldspar, plagioclase and magnetite are noted to occur in mutual contact, with no evidence of reaction textures between the minerals. Moreover, the ubiquitous occurrence of matrix minerals as inclusions in garnet porphyroblasts and porphyroclasts suggests the garnet grew in equilibrium with the these minerals (e.g. Figures 5.3 (e) and 5.4 (b, e)).

The frequent occurrence of fabric defining biotite and sillimanite interfingering in the foliation, indicates that these minerals would have been mutually stable (Figure 5.4 (d, f)). However, in some cases, aligned biotite appears to rim or mimetically overgrow sillimanite folia (e.g. Figure 5.3 (b, c)). This suggest a shift in the equilibrium to conditions in favour of the growth of biotite at the expense of sillimanite. However, the noted widespread interfingering of these minerals provides compelling evidence for their stable coexistance.

For sheared pelitic granulite samples, significant amounts of cordierite occur only in KK29

where cordierite occurs as part of a well-equilibrated assemblage and is intergrown with a biotite-sillimanite foliation in places (Figure 5.4 (d)), this suggests that these minerals were mutually stable during foliation developement.

Although magnetite forms part of the stabley coexisting assemblage, the frequent occurrence of interstitial magnetite may suggest that at least part of its growth was late in the paragenesis relative to the equlibrium assemblage (e.g. Figure 5.3 (b)).

Observed textures in sheared pelitic granulite samples are consistent with an equilibrium assemblage characterised by coexisting **garnet, biotite, cordierite, sillimanite, quartz, K-feldspar, plagioclase and magnetite**. This equilibrium assemblage is viewed to reflect P-T conditions at the time of shearing, subsequent to cooling from peak metamorphic conditons. Since these samples preserve a well-developed solid-state deformation fabric, it should follow that the latest stages of shearing recorded by sheared pelitic granulites occurred at subsolidus P-T conditions – thus indicating that the equilibrium assemblage would not have coexisted with a silicate melt phase.

5.3.3 Pella amphibolites

The fabrics observed in KK14 are compatible with that of a protomylonite and the fine grain-size (Figure 5.5 (c)) reflects high levels of strain and is consistent with grain size reduction by dynamic recrystallisation (Behrmann & Mainprice, 1987; Hirth & Tullis, 1992). Similarly, the fine-scale compositinal layering where plagioclase-rich layers alternate with hornblende-rich layers (Figure 5.5 (c)) is interpreted to have resulted from deformation and recrystallisation during shearing – this effect of ductile deformations is well-documented (e.g. Vernon, 1974). Preservation of the fine grained mylonitic texture is consistent with shear deformation occurring at temperatures below the upper-amphibolite to granulite facies conditions experienced by the pelitic granulites (e.g. Jessell, 1987).

In KK12, the moderately developed hornblende foliation (Figure 5.5 (a)) represents deformation at conditions of hornblende stability. In KK19, the granoblastic texture and relatively coarse grain size with no well-developed foliation (Figure 5.5 (e)) indicates that it was not subject to significant deformation. The foliated lenses of chlorite (Figure 5.5 (f)) which appear to be deflected by hornblende porphyroclasts in places provide evidence for limited shearing at conditions of chlorite stability. Thus, the fabrics developed in KK12 and KK19 indicate that the footwall accomodated minor shear deformation during late stage LFRTZ shearing before tectonic juxtaposition. The intesity of late stage shearing in the LFRTZ was significant enough and at low enough temperatures to result in the development of protomylonite in some Pella amphibolites.

Since the Pella amphibolites show no evidence of ever bearing melt – any fabrics developed are viewed to be representative of late-stage deformation (in the LFRTZ and Footwall Pella

domain) associated with shearing in the LFRTZ after there had been substantial cooling of the Hangingwall Gordonia block (to subsolidus P-T conditions). Moreover, considering that the Pella Terrane can be assumed to have resided under shollower, likely cooler crustal conditions prior to being overthrust by the hotter Grunau Terrane which was excised from depth. The equilibrium (peak) assemblage preserved in the Pella amphibolites is argued to represent the conditions of juxtaposition, where burial of the Pella Terrane by the hotter Grunau Terrane crust would have resulted in heating to the peak P-T conditions experienced by the Pella Terrane. This is based on the assumption that the Hangingwall Gordonia would have been hotter than any temperatures experienced by the Footwall Pella prior to juxtaposition and would have reached thermal equillibrium with the Footwall Pella not long after being emplaced.

In Pella amphibolite samples, all matrix minerals are annealed and in mutual contact, indicating that they form part of single well-equilibrated assemblage and there is generally no evidence for reaction textures where one mineral is at disequilibrium with another. Microtextures observed in Pella amphibolite samples are thus consistent with an equilibrium assemblage characterised by coexisting **hornblende, plagioclase ±quartz ±magnetite ±chlorite ±titanite ±ilmenite**.

Chapter 6

Mineral Chemistry

In this Chapter, the results of mineral chemistry analysis carried out on hangingwall pelitic granulites, sheared pelitic granulites and Pella amphibolites are presented and described. All analyses were carried out using a JEOL Superprobe JXA-8100 Electron Probe Microanalyzer housed at the University of Cape Town. A complete record of the results of mineral chemistry analysis is provided in Appendix A. All pelitic granulite samples referred to in this chapter were collected from the LFRTZ and its footwall and hangingwall at the Kum Kum Klippe (specific locations of samples are indicated in Figure 3.1).

6.1 Pelitic Granulites

6.1.1 Garnet

There is generally no notable difference between the composition of garnet in hangingwall pelitic granulite samples compared to sheared pelitic granulite samples, with X_{alm}, X_{py} and X_{Fe} of hangingwall pelitic granulite samples occurring in the ranges 0.59 to 0.80, 0.16 to 0.28 and 0.71 to 0.83 while sheared pelitic granulite samples exhibit values occuring in the ranges 0.66 to 0.77, 0.16 to 0.26 and 0.71 to 0.83 respectively.

For hangingwall pelitic granulite samples JMTV45 and PM13076, peritectic garnet (g_1) as well as late garnets (g_2; small grains) were analysed – these textural varieties are distinguishable on the basis of contrasting X_{alm}, X_{py} and X_{Fe} composition, with the X_{alm} and X_{Fe} of g_2 characterised by higher values when compared to that of g_1, while X_{py} is higher for g_1.

For both hangingwall and sheared granulite samples, garnets are almandine-pyrope with highly subordinate grossular and spessartine components. For all samples analysed, compositional zoning in garnet is poorly developed with almost flat core-to-rim compositional profiles occurring for X_{alm}, X_{py} and X_{Fe} (Figure 6.2).

X_{alm} = Fe/(Fe+Mg+Mn+Ca); X_{py} = Mg/(Mg+Mn+Ca+Fe); X_{Fe} = Fe/(Fe+Mg); X_{An} = Ca/(Ca+Na); X_{Or} = K/(K+Ca+Na); a.p.f.u = atoms per formula unit

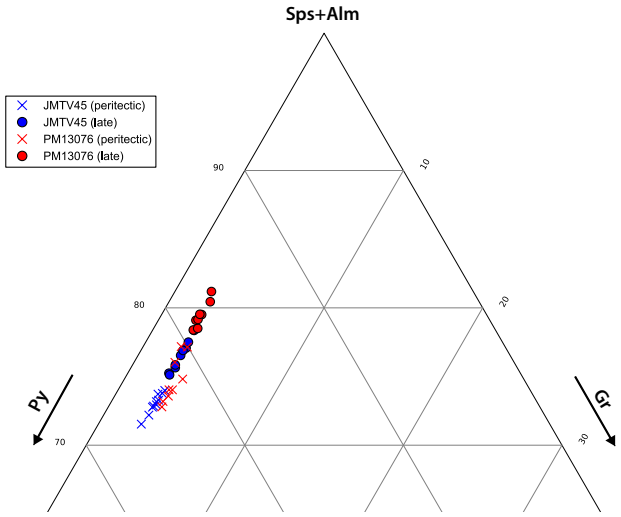

Figure 6.1: Spessartine(Sps)+Almandine(Alm)–Grossular(Gr)–Pyrope(Py) ternary diagram for garnet grains analysed in samples JMTV45 and PM13076 showing the compositional contrast between peritectic garnet (g_1) and late garnet (g_2).

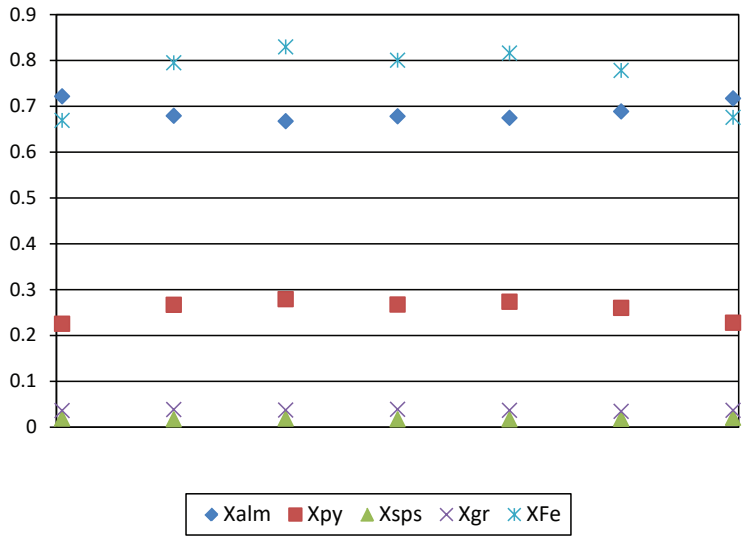

Figure 6.2: Compositional profile across a representative garnet porphyroblast from sample PM13032 showing close to flat X_{alm}, X_{py} and X_{Fe} core-to-rim compositional profiles typical of garnet in both hangingwall and sheared pelitic granulite samples.

Table 6.1: Representative electron microprobe analyses of garnet in pelitic granulites.

	PM13032		PM13076		JMTV45		KK29		KK27		KK28	
	gt5_core	gt9	gt27(8)	gt28(b)	gt17_int	gt21(b)_int	gt57_int_kk29	gt60_int_kk29	gt46_rim_kk27	gt52_int_kk27	gt53_int_kk28	gt54_rim_kk28
SiO_2	37.28	37.89	37.86	37.41	37.44	37.97	38.50	38.16	37.10	37.84	37.77	37.42
TiO_2	0.02	0.00	0.01	0.02	0.04	0.05	0.01	0.00	0.00	0.03	0.00	0.00
Al_2O_3	22.93	22.27	21.96	21.96	21.64	21.83	22.02	21.95	21.82	22.06	22.08	22.02
Cr_2O_3	0.04	0.03	0.03	0.04	0.07	0.00	0.01	0.03	0.04	0.00	0.01	0.00
FeO	30.78	30.25	32.84	34.95	32.92	33.79	31.04	31.91	33.94	31.95	32.73	32.77
MnO	0.92	0.93	0.55	0.64	0.69	0.63	2.32	2.80	1.91	1.49	1.37	1.29
MgO	6.72	7.03	5.65	4.68	5.96	5.69	5.94	5.02	4.27	5.95	5.63	5.41
CaO	1.26	1.30	1.14	0.83	1.04	0.93	0.99	0.90	0.98	0.81	0.99	1.06
Na_2O	0.04	0.04	0.05	0.01	0.02	0.02	0.08	0.01	0.00	0.03	0.00	0.01
K_2O	0.00	0.00	0.00	0.00	0.00	0.00	0.00	0.00	0.01	0.01	0.01	0.00
Total	99.99	99.74	100.08	100.53	99.81	100.91	100.92	100.78	100.07	100.17	100.59	99.98
Oxygen	12	12	12	12	12	12	12	12	12	12	12	12
Si	2.92	2.97	2.98	2.97	2.97	2.98	3.00	3.00	2.96	2.98	2.97	2.96
Ti	0.00	0.00	0.00	0.00	0.00	0.00	0.00	0.00	0.00	0.00	0.00	0.00
Al	2.12	2.06	2.04	2.05	2.02	2.02	2.02	2.03	2.05	2.05	2.05	2.06
Cr	0.00	0.00	0.00	0.00	0.00	0.00	0.00	0.00	0.00	0.00	0.00	0.00
Fe	2.02	1.98	2.17	2.32	2.18	2.22	2.02	2.10	2.27	2.10	2.15	2.17
Mn	0.06	0.06	0.04	0.04	0.05	0.04	0.15	0.19	0.13	0.10	0.09	0.09
Mg	0.78	0.82	0.66	0.55	0.70	0.67	0.69	0.59	0.51	0.70	0.66	0.64
Ca	0.11	0.11	0.10	0.07	0.09	0.08	0.08	0.08	0.08	0.07	0.08	0.09
Na	0.01	0.01	0.01	0.00	0.00	0.00	0.01	0.00	0.00	0.00	0.00	0.00
K	0.00	0.00	0.00	0.00	0.00	0.00	0.00	0.00	0.00	0.00	0.00	0.00
Total	8.02	8.01	8.00	8.01	8.02	8.01	7.99	7.98	8.01	8.00	8.01	8.01
X_{alm}	0.68	0.67	0.73	0.78	0.72	0.74	0.69	0.71	0.76	0.71	0.72	0.73
X_{pyr}	0.26	0.28	0.22	0.19	0.23	0.22	0.23	0.20	0.17	0.24	0.22	0.21
X_{sps}	0.02	0.02	0.01	0.01	0.02	0.01	0.05	0.06	0.04	0.03	0.03	0.03
X_{grs}	0.04	0.04	0.03	0.02	0.03	0.03	0.03	0.03	0.03	0.02	0.03	0.03
X_{Fe}	0.78	0.82	0.66	0.55	0.70	0.67	0.75	0.78	0.82	0.75	0.77	0.77

6.1.2 Biotite

For all samples and textural varieties of biotite in both sheared and unsheared samples, there is no evidence of compositional zoning. Whereas the composition of biotites in hangingwall pelitic granulites varies as a function of rock composition as well as the textural setting of the biotite (Figure 6.3 and 6.5), textural varieties of biotite in sheared pelitic granulite samples are not obviously distinguishable on the basis of their composition – the main variability in biotite composition of these samples is controlled by the different bulk rock compositions (Figure 6.4 and 6.6).

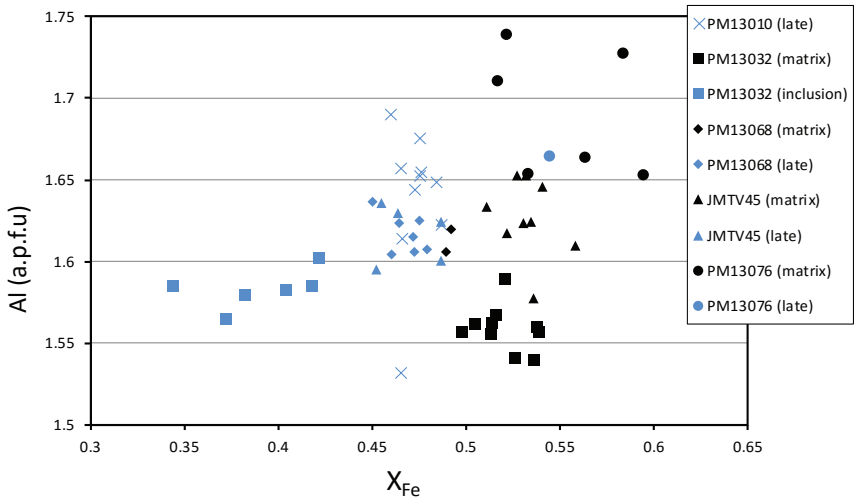

Figure 6.3: Al v. X_{Fe} chemical variaton diagram for biotite analysed in hangingwall pelitic granulites in the Kum Kum Klippe.

Biotite from hangingwall and sheared pelitic granulites exhibit similar Al (a.p.f.u) values and both show moderate variability in composition, with Al (a.p.f.u) values occurring between 1.53 and 1.75 for hangingwall samples while sheared pelitic granulites are characterised by values between 1.54 and 1.82 (Figures 6.3, 6.4, 6.5 and 6.6).

Hangingwall pelitic granulites are charaterised by a moderate range in X_{Fe}, with values occurring between 0.34 and 0.59. For samples where both grains which are interpreted to be at equilibrium with matrix minerals (matrix biotite) as well as those which occur as rims and selvages (late biotite) were analysed – matrix biotite generally displays a notably higher X_{Fe} composition than the late biotite (Figure 6.3). Where bioite occurring as inclusions in garnet (inclusion biotite; in almandine-rich garnet) as well as matrix biotite were analysed in the same sample (i.e. PM13032), the inclusion biotite shows significantly lower X_{Fe} values than the matrix biotite (Figure 6.3).

Compared to hangingwall samples, sheared pelitic granulites show less variability in X_{Fe}, with values ranging between 0.42 and 0.57 (Figure 6.4). Sample KK10 is characterised by the lowest X_{Fe} for sheared samples, where values occur between 0.42 and 0.44, while the X_{Fe}

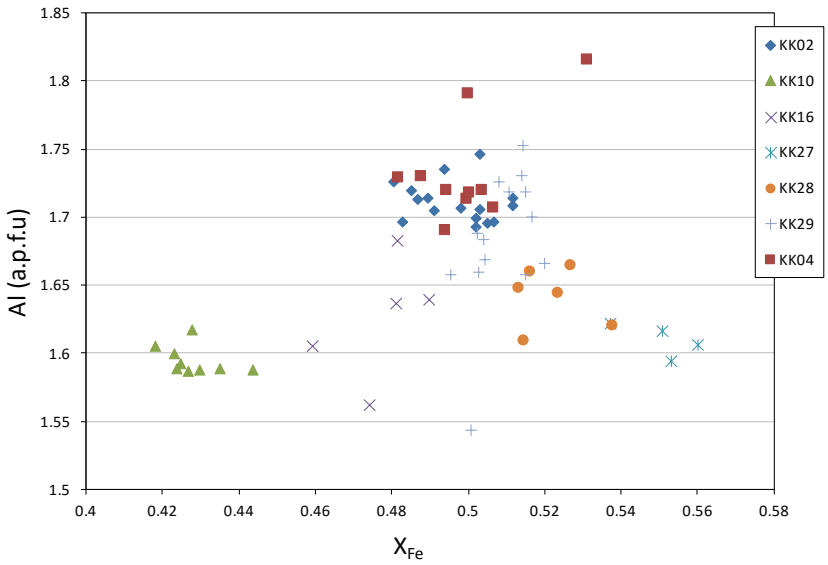

Figure 6.4: Al v. X_{Fe} chemical variaton diagram for biotite analysed in sheared pelitic granulites from the LFRTZ.

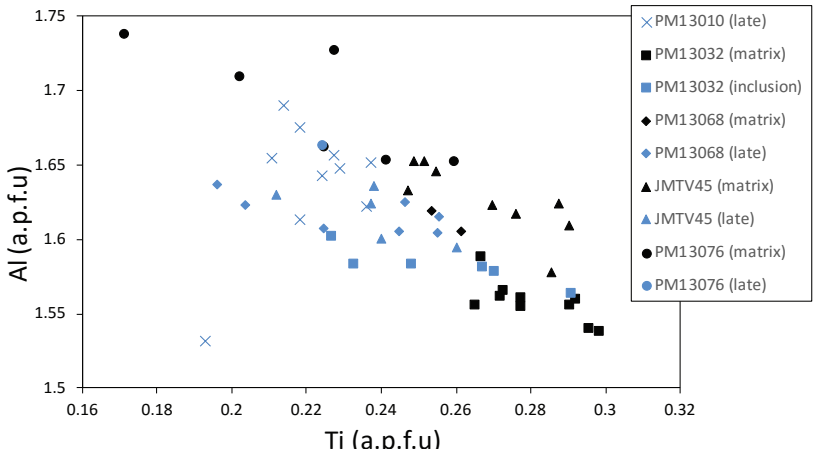

Figure 6.5: Al v. Ti chemical variaton diagram for biotite analysed in hangingwall pelitic granulites in the Kum Kum Klippe.

composition for the remainder of the sheared granulite samples is marginally higher, occurring between 0.46 and 0.57. There is no systematic difference in X_{Fe} composition between textural varieties of biotite for sheared pelitic granulite samples (Table 6.2).

Both the hangingwall pelitic granulites and the sheared pelitic granulites show moderate variability in Ti (a.p.f.u), however, the Ti (a.p.f.u) values in hangingwall pelitic granulite samples (0.17–0.30) are notably higher than in sheared pelitic granulites (0.06–0.21). For hangingwall samples matrix biotite is characterised by slightly higher Ti (a.p.f.u) values compared to late bioite and biotite which occurs as inclusions in garnet (Figures 6.5 and 6.6).

Variation in the Ti (a.p.f.u) of sheared pelitic granulites is largely controlled by the dif-

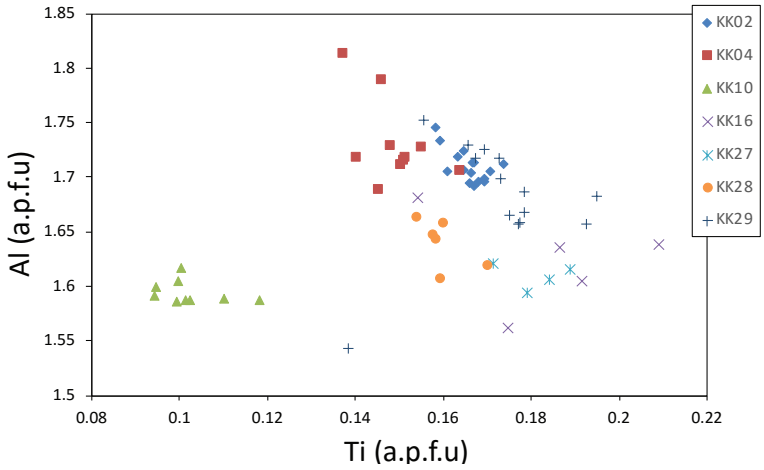

Figure 6.6: Al v. Ti chemical variation diagram for biotite analysed in sheared pelitic granulites from the LFRTZ.

ferent bulk rock compositions of each sample (Figure 6.6). Whereas sample KK10 is characterised by the lowest Ti (a.p.f.u) for sheared samples with values occurring between 0.09 and 0.12 – the rest of the sheared pelitic granulite samples are charaterised by significantly higher values, which occur between 0.14 and 0.22.

Table 6.2: Representative electron microprobe analyses of biotite in pelitic granulites.

	PM13068		JMTV45		PM13076		KK02		KK29		KK16	
	bi24(c)	bi26(b)	bi34(b)_int	bi27(c)	bi41(c)	bi43(b)	bi48(b)_int	bi53_rim	bi80(a)_int	bi88(b)_kk29	bi69(b)_kk16	bi70(b)_kk16
SiO_2	34.35	34.69	34.05	34.83	34.68	34.78	35.58	35.55	35.54	35.12	36.37	35.91
TiO_2	4.40	4.49	4.12	4.47	4.56	3.94	2.93	2.95	3.07	3.45	3.41	3.29
Al_2O_3	17.95	18.03	18.00	18.42	18.54	18.66	19.25	19.32	19.49	19.01	18.25	18.44
Cr_2O_3	0.02	0.00	0.14	0.22	0.14	0.23	0.02	0.03	0.03	0.06	0.05	0.06
FeO	17.82	17.29	18.52	19.80	21.27	19.68	17.9	17.49	18.82	18.76	16.95	17.5
MnO	0.05	0.11	0.02	0.07	0.04	0.02	0.49	0.51	0.12	0.12	0.05	0.09
MgO	10.33	11.39	10.98	9.44	8.14	9.23	9.58	10.24	10.12	10.35	11.2	10.58
CaO	0.04	0.00	0.06	0.00	0.03	0.00	0.00	0.00	0.00	0.00	0.07	0.00
Na_2O	0.16	0.08	0.12	0.10	0.11	0.22	0.18	0.11	0.16	0.13	0.14	0.11
K_2O	9.55	9.59	8.42	8.09	9.74	9.73	9.69	9.45	9.08	9.45	9.55	9.58
Total	94.67	95.67	94.42	95.44	97.26	96.49	95.62	95.66	96.43	96.45	96.05	95.56
Oxygen	11	11	11	11	11	11	11	11	11	11	11	11
Si	2.63	2.62	2.61	2.64	2.62	2.63	2.69	2.67	2.66	2.64	2.71	2.70
Ti	0.25	0.25	0.24	0.25	0.26	0.22	0.17	0.17	0.17	0.19	0.19	0.19
Al	1.62	1.60	1.62	1.65	1.65	1.66	1.71	1.71	1.72	1.68	1.61	1.64
Cr	0.00	0.00	0.01	0.01	0.01	0.01	0.00	0.00	0.00	0.00	0.00	0.00
Fe	1.14	1.09	1.19	1.25	1.34	1.25	1.13	1.10	1.18	1.18	1.06	1.10
Mn	0.00	0.01	0.00	0.00	0.00	0.00	0.03	0.03	0.01	0.01	0.00	0.01
Mg	1.18	1.28	1.25	1.07	0.92	1.04	1.08	1.15	1.13	1.16	1.25	1.19
Ca	0.00	0.00	0.00	0.00	0.00	0.00	0.00	0.00	0.00	0.00	0.01	0.00
Na	0.02	0.01	0.02	0.01	0.02	0.03	0.03	0.02	0.02	0.02	0.02	0.02
K	0.93	0.92	0.82	0.78	0.94	0.94	0.93	0.91	0.87	0.91	0.91	0.92
Total	7.79	7.79	7.76	7.67	7.77	7.79	7.77	7.76	7.75	7.79	7.76	7.76
X_{Fe}	0.49	0.46	0.49	0.54	0.59	0.54	0.51	0.49	0.51	0.50	0.46	0.48

6.1.3 Cordierite

Cordierite analysed from both hangingwall and sheared granulite samples is Mg-rich with X_{Fe} occurring in the ranges 0.21 to 0.37 and 0.21 to 0.33 respectively (Table 6.3). While the X_{Fe} composition of cordierites varies significantly between samples as a function of bulk rock composition, the X_{Fe} of cordierite within each of these samples is largely homogeneous (Figure 6.7). For all hangingwall pelitic granulite samples except PM13010, cordierite forming a corona associated with garnet is in most cases compositionally distinct (in terms of X_{Fe}) from cordierite grains which form part of the matrix assemblage (Figure 6.7); this is also the case for sheared granulite sample KK16, where matrix cordierite is characterised by X_{Fe} values of $\sim$0.26 while garnet-corona cordierite is characterised by lower X_{Fe} values occurring in the range 0.21 to 0.22 (Table 6.3).

For hangingwall pelitic granulite samples PM13010, PM13032 and JMTV45 weak compositional zoning in cordierite is defined by a variably small rim-ward decrease in X_{Fe} of up to 0.02. Contrastingly, cordierite grains analysed in PM13068 and PM13076 generally show a slight rim-ward increase (of up to 0.02) in X_{Fe}. For sheared pelitic granulite samples, cordierite is typically strongly xenomorphic such that cores and rims are not well-defined.

Cordierite was analysed in sheared pelitic granulite samples KK16 and KK29. In general, the cordierite in these samples is significantly more Mg-rich than that of hangingwall

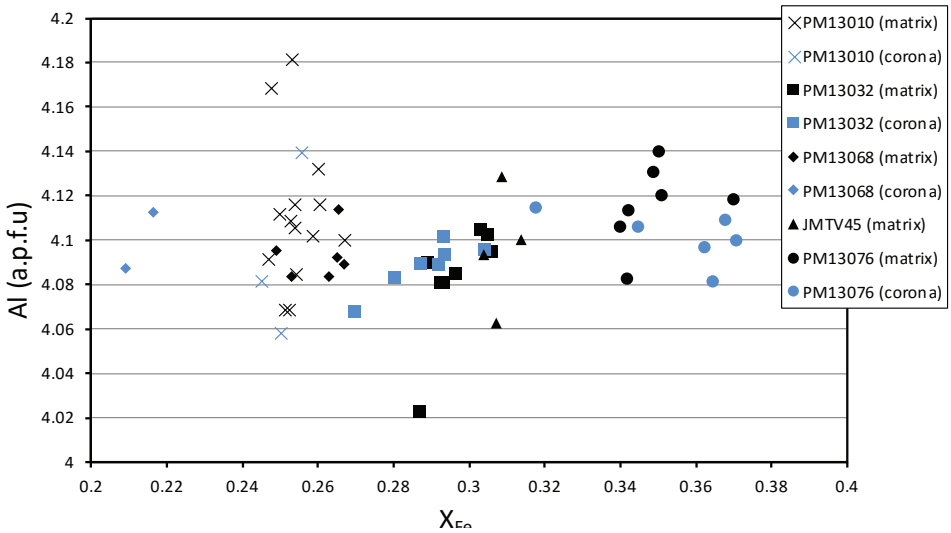

Figure 6.7: Al v. X_{Fe} chemical variaton diagram for cordierite electron microprobe analyses of various hangingwall pelitic granulites.

samples. The X_{Fe} composition of cordierite varies significantly between KK16 and KK29 such that there is no overlap in values. Contrastingly, variation of cordierite X_{Fe} composition within each of these samples is comparatively small, with samples KK16 and KK29 exhibiting relatively low X_{Fe} values occuring in the ranges 0.21 to 0.27 and 0.30 to 0.33 respectively.

Table 6.3: Representative electron microprobe analyses of cordierite in pelitic granulites.

	PM13010		PM13068		JMTV45		KK16		KK29	
	cd3b_int	cd6_int	cd19_rim	cd20(gt_crn)	cd22_int	cd23_core	cd45_int	cd48_rim	cd51_int	cd53_kk29
SiO_2	49.79	49.24	48.99	48.75	48.13	48.21	49.63	49.75	48.44	48.15
TiO_2	0.00	0.03	0.02	0.03	0.01	0.00	0.00	0.00	0.00	0.04
Al_2O_3	35.00	34.75	34.47	34.70	34.01	33.70	33.90	34.05	34.37	34.65
Cr_2O_3	0.00	0.01	0.01	0.05	0.00	0.00	0.04	0.00	0.00	0.03
FeO	5.88	5.77	6.15	5.13	7.30	7.27	6.15	6.01	7.43	7.43
MnO	0.54	0.52	0.25	0.17	0.01	0.06	0.19	0.15	0.28	0.24
MgO	9.46	9.52	9.58	10.42	8.96	9.21	10.03	10.06	8.88	8.52
CaO	0.00	0.00	0.02	0.00	0.02	0.01	0.01	0.00	0.01	0.01
Na_2O	0.12	0.15	0.08	0.09	0.09	0.11	0.10	0.13	0.12	0.09
K_2O	0.01	0.03	0.01	0.02	0.01	0.02	0.01	0.01	0.01	0.00
Total	100.80	100.01	99.59	99.36	98.54	98.60	100.05	100.15	99.55	99.16
Oxygen	18	18	18	18	18	18	18	18	18	18
Si	4.95	4.94	4.93	4.90	4.92	4.93	4.97	4.98	4.91	4.90
Ti	0.00	0.00	0.00	0.00	0.00	0.00	0.00	0.00	0.00	0.00
Al	4.10	4.11	4.09	4.11	4.10	4.06	4.01	4.01	4.11	4.16
Cr	0.00	0.00	0.00	0.00	0.00	0.00	0.00	0.00	0.00	0.00
Fe	0.49	0.48	0.52	0.43	0.62	0.62	0.52	0.50	0.63	0.63
Mn	0.05	0.04	0.02	0.01	0.00	0.01	0.02	0.01	0.02	0.02
Mg	1.40	1.42	1.44	1.56	1.37	1.40	1.50	1.50	1.34	1.29
Ca	0.00	0.00	0.00	0.00	0.00	0.00	0.00	0.00	0.00	0.00
Na	0.02	0.03	0.02	0.02	0.02	0.02	0.02	0.02	0.02	0.02
K	0.00	0.00	0.00	0.00	0.00	0.00	0.00	0.00	0.00	0.00
Total	11.01	11.03	11.03	11.05	11.04	11.05	11.03	11.03	11.05	11.03
X_{Fe}	0.26	0.25	0.26	0.22	0.31	0.31	0.26	0.25	0.32	0.33

6.1.4 Feldspar

Whereas K-feldspar (orthoclase) was analysed in all hangingwall pelitic granulite samples, plagioclase was not found in samples PM13068 and PM13076. For samples PM13010 and PM13032 plagioclase is andesine with X_{An} components occuring in the range 0.34 to 0.36 and 0.38 to 0.45 respectively [where $X_{An} = Ca/(Ca + Na)$]; while for JMTV45 the plagioclase analysed is oligoclase in composition with X_{An} occuring between 0.27 and 0.28 (Figure 6.8). There is no discernable compositional zoning in terms of X_{An} for plagioclase in hangingwall pelitic granulites. For all hangingwall samples, the K (a.p.f.u) content of plagioclase is low and does not exceed 0.015. The X_{Or} composition of K-feldspar in hangingwall samples is broadly similar between the samples and occurs between 0.64 and 0.92 [where $X_{Or} = K/(K + Ca + Na)$]. No compositional zoning (in terms of X_{Or}) is discernable.

Feldspars were analysed in each of the sheared pelitic granulite samples except KK16. Both K-feldspar and plagioclase were analysed in the remainder of these samples except KK29. Plagioclase in all sheared pelitic granulite samples is oligoclase (although compositions vergent on andesine occur in KK27, KK28 and KK29), with X_{An} ranging between 0.21 and 0.31 (Figure 6.9). Weak compositional zoning of plagioclase occurs in KK04 and KK28 where there is a slight, rim-ward X_{An} increase of up to 0.02. There is no discernable compositional zoning in the remainder of the sheared pelitic granulite samples.

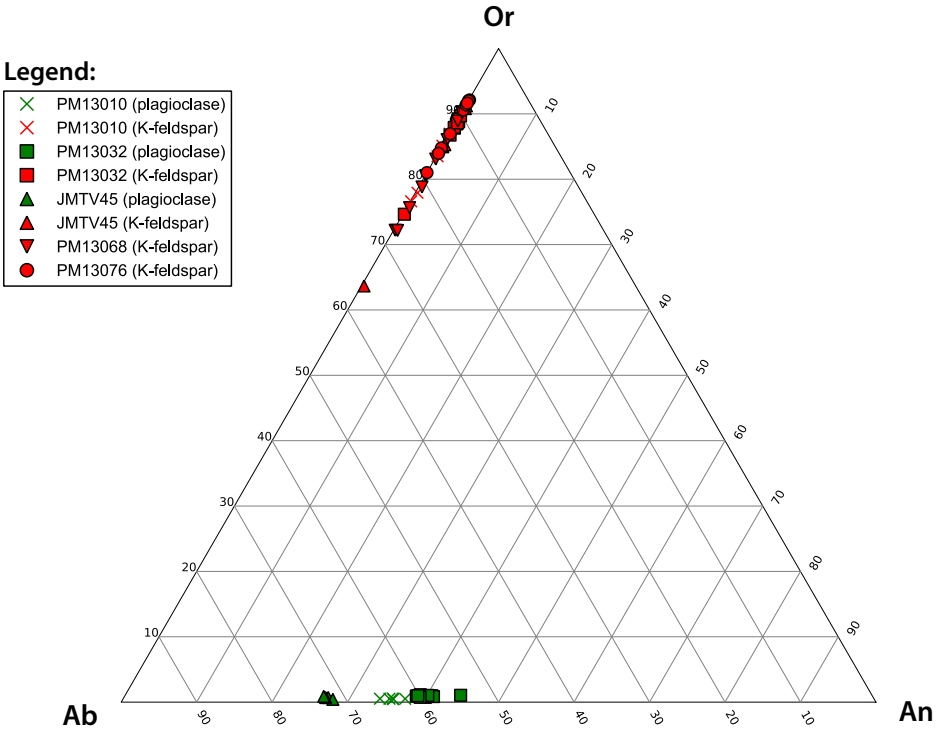

Figure 6.8: Orthoclase(Or)-Anorthite(An)-Albite(Ab) ternary diagram showing the composition of feldspars in hangingwall pelitic granulites.

The K (a.p.f.u) content of plagioclase in hangingwall pelitic granulites is comparable to that in sheared pelitic granulites, with values reaching a maximum of 0.015. There is no discernable compositional zoning in terms of K (a.p.f.u) in plagioclase from either of the hangingwall or sheared pelitic granulite samples.

The X_{Or} composition of K-feldspar analysed in sheared pelitic granulite samples shows little variability, with values typically occurring between 0.82 and 0.90 – however, unusual instances of values as low as 0.65 occur in sample KK02. There is no evidence of compositional zoning in terms of X_{Or} for K-feldspar in sheared pelitic granulite samples.

Whereas the compositional range of K-feldspar in hangingwall and sheared samples is broadly similar, plagioclase in sheared samples is generally more albite-rich (Figure 6.10 and Table 6.4).

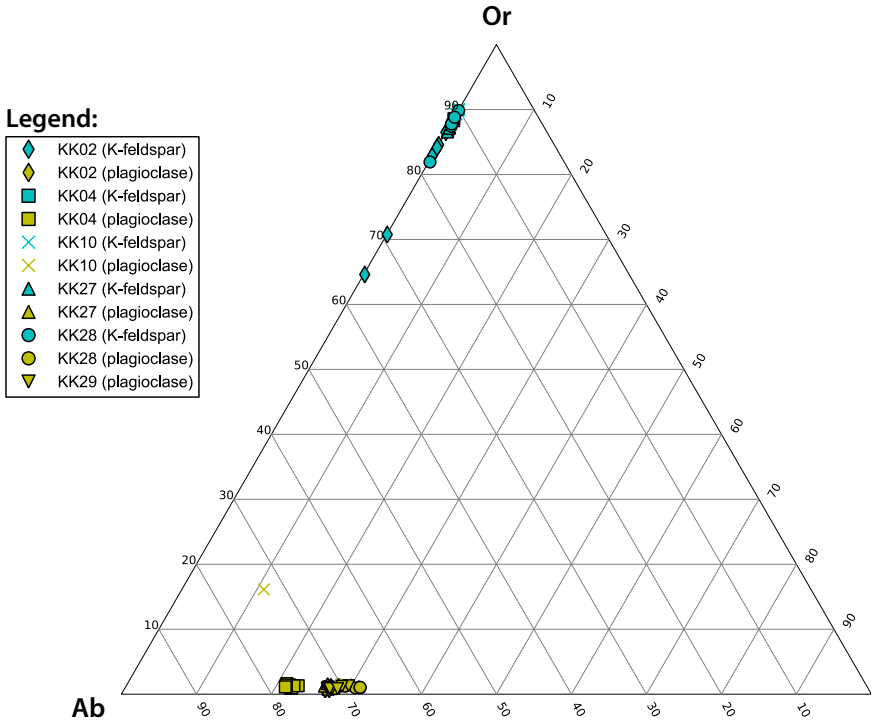

Figure 6.9: Orthoclase(Or)-Anorthite(An)-Albite(Ab) ternary diagram showing the composition of feldspars in sheared pelitic granulites.

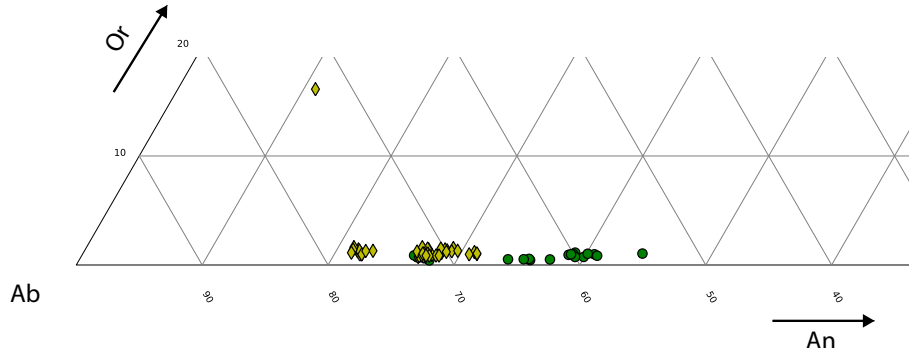

Figure 6.10: Compositional contrast between plagioclase analysed in hangingwall pelitic granulites (green circles) and sheared pelitic granulites (yellow diamonds).

Table 6.4: Representative microprobe analyses of feldspars in pelitic granulites.

	Alkali Feldspars								Plagioclase					
	PM13068		PM13076		KK10		KK27		PM13010		KK04		KK29	
	fsp19_int	fsp20_int_pm13068	fsp44_int	fsp42_int	fsp65_int	fsp66_rim	fsp72_rim	fsp78_int	fsp2b	fsp_corona1d	fsp62_rim	fsp63_rim	fsp88_kk29	fsp89_kk29
SiO_2	65.40	65.21	64.87	64.90	64.34	64.22	64.6	64.06	58.97	58.20	62.69	63.58	61.85	60.5
TiO_2	0.02	0.04	0.01	0.02	0.04	0.07	0.03	0.01	0.00	0.00	0.02	0.03	0.00	0.00
Al_2O_3	18.90	19.12	19.08	19.17	18.91	19	19.01	19.32	26.75	26.87	24.00	23.69	25.63	26.04
Cr_2O_3	0.02	0.00	0.00	0.00	0.00	0.00	0.00	0.00	0.00	0.02	0.00	0.01	0.02	0.00
FeO	0.03	0.03	0.13	0.00	0.00	0.03	0.01	0.02	0.10	0.05	0.00	0.05	0.00	0.00
MnO	0.00	0.00	0.03	0.04	0.05	0.02	0.06	0.05	0.00	0.07	0.07	0.04	0.00	0.02
MgO	0.02	0.02	0.01	0.02	0.00	0.00	0.00	0.00	0.00	0.03	0.01	0.01	0.00	0.03
CaO	0.03	0.08	0.01	0.02	0.00	0.00	0.04	0.03	7.09	7.37	4.47	4.26	5.46	5.99
Na_2O	1.50	2.65	1.66	1.45	1.17	1.09	1.46	1.26	6.97	6.77	8.44	8.58	8.04	7.71
K_2O	14.23	12.71	14.08	14.80	14.75	14.83	14.48	14.57	0.07	0.08	0.22	0.19	0.18	0.22
Total	100.15	99.86	99.88	100.42	99.26	99.25	99.68	99.31	99.96	99.46	99.91	100.44	101.18	100.52
Oxygen	8	8	8	8	8	8	8	8	8	8	8	8	8	8
Si	2.99	2.98	2.98	2.97	2.98	2.97	2.98	2.96	2.62	2.61	2.77	2.79	2.71	2.67
Ti	0.00	0.00	0.00	0.00	0.00	0.00	0.00	0.00	0.00	0.00	0.00	0.00	0.00	0.00
Al	1.02	1.03	1.03	1.04	1.03	1.04	1.03	1.05	1.40	1.42	1.25	1.23	1.32	1.36
Cr	0.00	0.00	0.00	0.00	0.00	0.00	0.00	0.00	0.00	0.00	0.00	0.00	0.00	0.00
Fe	0.00	0.00	0.00	0.00	0.00	0.00	0.00	0.00	0.00	0.00	0.00	0.00	0.00	0.00
Mn	0.00	0.00	0.00	0.00	0.00	0.00	0.00	0.00	0.00	0.00	0.00	0.00	0.00	0.00
Mg	0.00	0.00	0.00	0.00	0.00	0.00	0.00	0.00	0.00	0.00	0.00	0.00	0.00	0.00
Ca	0.00	0.00	0.00	0.00	0.00	0.00	0.00	0.00	0.34	0.35	0.21	0.20	0.26	0.28
Na	0.13	0.23	0.15	0.13	0.10	0.10	0.13	0.11	0.60	0.59	0.72	0.73	0.68	0.66
K	0.83	0.74	0.82	0.86	0.87	0.88	0.85	0.86	0.00	0.00	0.01	0.01	0.01	0.01
Total	4.98	4.99	4.99	5.01	4.99	4.99	5.00	5.00	4.98	4.98	4.97	4.96	4.98	4.99
X_{an}									0.36	0.38	0.22	0.21	0.27	0.30
X_{or}	0.86	0.76	0.85	0.87	0.89	0.90	0.87	0.88						

6.1.5 Sillimanite

Sillimanite was analysed in hangingwall pelitic granulite samples PM13010, PM13032, PM13068 and sheared pelitic granulite samples KK02, KK04, KK16 and KK29. The sillimanite analysed is almost pure Al_2SiO_3 with low Fe_{Total} and there is no compositional variability of sillimanite from sample to sample. All textural varieties of sillimanite are indistinguishable from each other on the basis of their composition (Table 6.5).

Table 6.5: Representative electron microprobe analyses for sillimanite in pelitic granulites.

	PM13068		PM13010		PM13032		KK02		KK16		KK29	
	sill20(a)	sill20(a)	sill8(a)	sill10(c)	sill15	sill16(c)	sill44	sill41	sill57	sill58	sill60	sill61
SiO_2	36.04	36.33	36.06	36.09	35.91	35.90	35.84	36.22	36.22	36.24	36.44	36.89
TiO_2	0.00	0.00	0.00	0.00	0.02	0.03	0.00	0.01	0.01	0.01	0.01	0.00
Al_2O_3	63.20	62.86	62.70	62.82	62.45	62.18	63.35	62.24	63.45	63.32	63.65	63.44
Cr_2O_3	0.05	0.01	0.00	0.00	0.06	0.11	0.02	0.04	0.01	0.01	0.02	0.08
FeO	0.93	1.05	0.68	0.91	0.94	0.89	0.96	1.25	1.02	0.61	0.79	0.89
MnO	0.00	0.04	0.03	0.03	0.02	0.04	0.03	0.05	0.03	0.02	0.03	0.03
MgO	0.02	0.02	0.02	0.02	0.00	0.01	0.00	0.03	0.03	0.02	0.00	0.02
CaO	0.03	0.04	0.07	0.07	0.05	0.01	0.00	0.06	0.01	0.01	0.00	0.00
Na_2O	0.02	0.00	0.01	0.00	0.02	0.02	0.01	0.02	0.00	0.00	0.02	0.04
K_2O	0.01	0.01	0.00	0.00	0.03	0.02	0.00	0.02	0.01	0.00	0.00	0.01
Total	100.30	100.36	99.57	99.94	99.51	99.23	100.22	99.94	100.79	100.23	100.97	101.40
Oxygens	5	5	5	5	5	5	5	5	5	5	5	5
Si	0.98	0.98	0.98	0.98	0.98	0.98	0.97	0.99	0.98	0.98	0.98	0.99
Ti	0.00	0.00	0.00	0.00	0.00	0.00	0.00	0.00	0.00	0.00	0.00	0.00
Al	2.02	2.00	2.01	2.01	2.01	2.01	2.02	2.00	2.02	2.02	2.02	2.00
Cr	0.00	0.00	0.00	0.00	0.00	0.00	0.00	0.00	0.00	0.00	0.00	0.00
Fe	0.02	0.02	0.02	0.02	0.02	0.02	0.02	0.03	0.02	0.01	0.02	0.02
Mn	0.00	0.00	0.00	0.00	0.00	0.00	0.00	0.00	0.00	0.00	0.00	0.00
Mg	0.00	0.00	0.00	0.00	0.00	0.00	0.00	0.00	0.00	0.00	0.00	0.00
Ca	0.00	0.00	0.00	0.00	0.00	0.00	0.00	0.00	0.00	0.00	0.00	0.00
Na	0.00	0.00	0.00	0.00	0.00	0.00	0.00	0.00	0.00	0.00	0.00	0.00
K	0.00	0.00	0.00	0.00	0.00	0.00	0.00	0.00	0.00	0.00	0.00	0.00
Total	3.02	3.01	3.01	3.01	3.02	3.01	3.02	3.02	3.02	3.01	3.01	3.01

6.1.6 Oxide Minerals

Whereas ilmenite was analysed in all hangingwall pelitic granulite samples except PM13032, no ilmenite was analysed in the sheared pelitic granulite samples. Lower wt% totals for some Fe-Ti oxide analyses (e.g: ilm7 in PM13010; Table 6.6) are consistent with larger proportions of Fe^{3+} (which is undetectable by microprobe analysis). In those cases, this is sypmtomatic of minor solid-solution towards hematite (i.e. in the binary series $FeTiO_3$–Fe_2O_3). In general, manganese and magnesium components in the ilmenite are subordinate, with wt% concentrations typically not exceeding 1.48 and 0.78 wt% respectively. However, minor solid-solution towards magnesian ilmenite is suggested by MgO concentrations reaching 5.0 wt% in PM13068.

Where present (i.e. PM13076) the globular (interstitial) ilmenite textural variety is compositionally indistinguishable from the acicular ilmenite. Similarly, in PM13076, where il-

menite occurring as inclusions in garnet as well as matrix ilmenite were analysed – the two varieties are indistinguishable on the basis of their composition.

Magnetite was analysed in all sheared granulite samples except KK10 while for hangingwall samples, magnetite was only analysed in samples PM13010 and PM13032. There is generally no notable systematic variation in the composition of magnetite within individual samples and between samples (Table 6.6). Al_2O_3 concentrations in magnetite for both hangingwall and sheared samples generally does not exceed 0.5 wt% while MgO typically occurs in trace amounts – this indicates that the magnetite is relatively pure and that there was minimal substition of Al and Mg towards the spinel end-memeber in the magnetite-spinel solid-solution series.

Low wt% totals are due to the presence of Fe^{3+} in magnetite (i.e. pure magnetite is $2Fe^{3+}Fe^{2+}O_4$) which is not detected by electron microprobe analysis.

Table 6.6: Representative electron microprobe analyses of oxide minerals in pelitic granulites.

	Ilmenite						Magnetite					
	JMTV45		PM13076		PM13010		PM13068		KK29		KK02	
	ilm22(gt_incl)	ilm26	ilm32(a)	ilm33(b)	ilm6	ilm7	mt21	mt22	mt47	mt48	mt26	mt27
SiO_2	0.00	0.00	0.00	0.00	0.00	0.00	0.00	0.00	0.00	0.00	0.00	0.00
TiO_2	49.09	49.17	49.16	48.15	49.45	41.50	0.00	0.00	0.01	0.00	0.04	0.02
Al_2O_3	0.00	0.00	0.00	0.00	0.00	1.28	0.13	0.18	0.11	0.09	0.05	0.09
Cr_2O_3	0.03	0.09	0.08	0.19	0.06	0.18	0.34	0.29	0.40	0.29	0.25	0.27
FeO	43.93	44.02	46.79	46.49	43.38	41.79	92.31	89.98	88.00	87.56	83.51	82.60
MnO	0.48	0.46	0.18	0.19	0.95	0.38	0.03	0.05	0.07	0.08	0.10	0.05
MgO	0.00	0.08	0.04	0.04	0.03	1.34	0.00	0.03	0.00	0.01	0.00	0.00
CaO	0.00	0.00	0.00	0.00	0.00	0.00	0.00	0.00	0.00	0.00	0.00	0.00
Na_2O	0.00	0.00	0.00	0.00	0.00	0.00	0.00	0.00	0.00	0.00	0.00	0.00
K_2O	0.00	0.00	0.00	0.00	0.00	0.00	0.00	0.00	0.00	0.00	0.00	0.00
Total	93.55	93.83	96.26	95.09	93.87	86.47	92.83	90.56	88.67	88.04	83.95	83.07
Oxygens	3	3	3	3	3	3	4	4	4	4	4	4
Si	0.00	0.00	0.00	0.00	0.00	0.00	0.00	0.00	0.00	0.00	0.00	0.00
Ti	1.00	1.00	0.98	0.97	1.00	0.92	0.00	0.00	0.00	0.00	0.00	0.00
Al	0.00	0.00	0.00	0.00	0.00	0.04	0.00	0.00	0.00	0.00	0.00	0.00
Cr	0.00	0.00	0.00	0.00	0.00	0.00	0.00	0.00	0.00	0.00	0.00	0.00
Fe	0.99	0.99	1.04	1.04	0.98	1.03	2.99	2.99	2.99	2.99	2.99	2.99
Mn	0.01	0.01	0.00	0.00	0.02	0.01	0.00	0.00	0.00	0.00	0.00	0.00
Mg	0.00	0.00	0.00	0.00	0.00	0.06	0.00	0.00	0.00	0.00	0.00	0.00
Ca	0.00	0.00	0.00	0.00	0.00	0.00	0.00	0.00	0.00	0.00	0.00	0.00
Na	0.00	0.00	0.00	0.00	0.00	0.00	0.00	0.00	0.00	0.00	0.00	0.00
K	0.00	0.00	0.00	0.00	0.00	0.00	0.00	0.00	0.00	0.00	0.00	0.00
Total	2.00	2.00	2.02	2.03	2.00	2.06	3.00	3.00	3.00	3.00	3.00	3.00

6.2 Pella Amphibolites

6.2.1 Amphiboles

Amphibole was analysed in each of the amphibolite samples: KK12, KK14 and KK19. Amphibole analysed in each of the samples is hornblende, with X_{Fe} between 0.19 to 0.52, while Al(VI) is between 0.06 and 0.25 (Table 6.7). Na (a.p.f.u) is similar between the three amphibolite samples, ranging from trace amounts to a maximum of ∼53 a.p.f.u in KK12. K (a.p.f.u) varies from sample to sample as a function of bulk rock composition with KK19 (0.0–0.1) characterised by the lowest values, while samples KK12 (0.0–0.17) and KK14 (0.26–0.28) are characterised by comparatively higher values. Similarly, Ti (a.p.f.u) varies largely as a function of bulk rock composition with values occurring in the ranges 0.04–0.14, 0.18–0.22 and 0.01–0.07 for KK12, KK14 and KK19 respectively.

There is generally no overlap in compositional range (in terms of X_{Fe}) for hornblende between each of the samples, with X_{Fe} values occurring in the ranges 0.19–0.30, 0.35–0.39 and 0.49–0.52 for KK19, KK12 and KK14 respectively. Al(VI) is lowest in KK14, ranging between 0.06 and 0.12, while the Al(VI) composition of KK12 and KK19 are broadly similar, ranging between 0.13 and 0.25. While there is no evidence for compositional zoning of hornblende in KK12 and KK14, well-developed compositional zoning in KK19 is defined by a moderate rim-ward increase in X_{Fe} (of up to 0.03), coupled with a sharp rim-ward increase in Al(VI) (of up to 0.20).

6.2.2 Feldspar

Plagioclase was analysed in each of the amphibolite samples KK12, KK14 and KK19. The X_{An} of plagioclase in each of the samples is distinct, with no overlap in composition between samples (Figure 6.11). The most calcic compositions occur in KK12 where plagioclase is anorthite with X_{An} occurring between 0.84 and 0.97. Plagioclase analysed in samples KK14 and KK19 is andesine (vergent on labradorite in the case of KK19), with X_{An} occurring in the ranges 0.32 to 0.44 and 0.46 to 0.52 respectively (Table 6.7). Whereas sample KK12 exhibits no discernable core-to-rim compositional zoning in terms of X_{An}, compositional zoning in samples KK14 and KK19 is defined by a rim-ward increase in X_{An}.

Plagioclase in each of the samples is characterised by low concentrations of potassium with the lowest concentrations realised in KK12 where it occurs in trace amounts. The concentration of potassium in plagioclase from KK14 is relatively constant, with values typically occurring in the range 0.25–0.27 wt%. Similarly, for plagioclase in KK19, the concentration of potassium is also largely constant, but is characterised by significantly lower values ranging between 0.04 and 0.06 wt%.

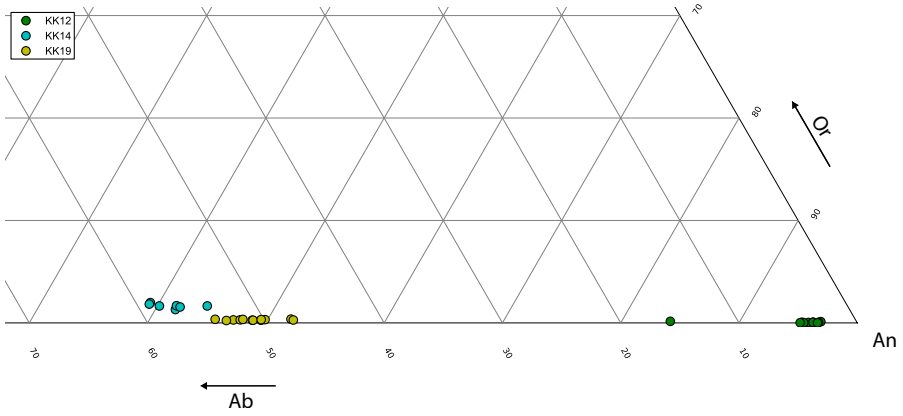

Figure 6.11: Orthoclase(Or)-Anorthite(An)-Albite ternary diagram for plagioclase in Pella amphibolites showing the compositional contrast of plagioclase analysed in each of the samples.

Table 6.7: Representative electron microprobe analyses of amphibole and plagioclase in Pella amphibolites.

	Amphibole						Plagioclase					
	KK12		KK14		KK19		KK12		KK14		KK19	
	amp2	amp3_rim	amp12	amp16_int	amp19_int	amp19_rim	fsp94_int	fsp95_rim	fsp104_int	fsp105_int	fsp107_int	fsp107_rim
SiO_2	41.41	41.75	41.87	41.98	48.64	46.93	43.73	44.01	57.76	58.02	56.26	54.89
TiO_2	1.28	1.21	1.88	1.89	0.59	0.64	0.00	0.00	0.00	0.00	0.00	0.01
Al_2O_3	13.92	14.02	11.62	11.95	7.80	9.96	37.30	37.72	28.04	27.59	28.95	29.47
Cr_2O_3	0.03	0.03	0.04	0.00	0.45	0.16	0.01	0.01	0.00	0.02	0.00	0.00
FeO	14.73	14.42	18.38	18.62	11.86	11.87	0.25	0.09	0.08	0.12	0.10	0.08
MnO	0.25	0.22	0.50	0.47	0.23	0.19	0.01	0.01	0.06	0.05	0.00	0.01
MgO	12.94	12.63	10.41	10.04	17.44	15.41	0.00	0.00	0.01	0.01	0.00	0.01
CaO	11.53	11.72	10.92	10.90	10.32	11.03	17.78	18.08	7.77	7.72	9.27	10.05
Na_2O	1.75	1.87	1.39	1.46	0.75	1.18	0.47	0.39	6.43	6.41	5.72	5.10
K_2O	0.87	0.89	1.43	1.43	0.42	0.49	0.00	0.01	0.33	0.30	0.05	0.06
Total	98.71	98.76	98.44	98.74	98.50	97.88	99.54	100.31	100.48	100.24	100.35	99.67
Oxygen	23	23	23	23	23	23	8	8	8	8	8	8
Si	6.11	6.15	6.32	6.32	6.96	6.79	2.02	2.02	2.57	2.58	2.51	2.47
Ti	0.14	0.13	0.21	0.21	0.06	0.07	0.00	0.00	0.00	0.00	0.00	0.00
Al	2.42	2.43	2.07	2.12	1.32	1.70	2.03	2.04	1.47	1.45	1.52	1.56
Cr	0.00	0.00	0.00	0.00	0.05	0.02	0.00	0.00	0.00	0.00	0.00	0.00
Fe	1.82	1.78	2.32	2.34	1.42	1.44	0.01	0.00	0.00	0.00	0.00	0.00
Mn	0.03	0.03	0.06	0.06	0.03	0.02	0.00	0.00	0.00	0.00	0.00	0.00
Mg	2.85	2.77	2.34	2.25	3.72	3.32	0.00	0.00	0.00	0.00	0.00	0.00
Ca	1.82	1.85	1.77	1.76	1.58	1.71	0.88	0.89	0.37	0.37	0.44	0.48
Na	0.50	0.53	0.41	0.43	0.21	0.33	0.04	0.03	0.55	0.55	0.49	0.45
K	0.16	0.17	0.28	0.27	0.08	0.09	0.00	0.00	0.02	0.02	0.00	0.00
Total	15.9	15.8	15.8	15.8	15.4	15.5	5.0	5.0	5.0	5.0	5.0	5.0
X_{Fe}	0.39	0.39	0.50	0.51	0.28	0.30	-	-	-	-	-	-
X_{An}	-	-	-	-	-	-	0.95	0.96	0.39	0.39	0.47	0.52
Al(VI)	0.53	0.58	0.38	0.44	0.28	0.49	-	-	-	-	-	-

Chapter 7

Major oxide chemistry

Bulk rock (major oxide) compositions of the samples used for the calculated pseudosections were derived from XRF analyses using a *Philips X'Unique II* wavelength dispersive spectrometer housed at the University of Cape Town.

The major oxide analyses were carried out on fusion discs prepared from a mixture of 0.7 grams pulp of each sample with 6 grams of a LiT-LiM (Li Tetraborate-Li Metaborate) flux. *Phillips X40* software was used to collect intensity data and corrections were made for background, spectral overlap and matrix effects. The full set of operating parameters and analytical data processing techniques are as described in Willis (1999).

Results of the analyses are reported as weight percent (wt%) concentrations of the major oxides: Na_2O, CaO, K_2O, Fe_2O_3, MgO, Al_2O_3, SiO_2, NiO, Cr_2O_3 and P_2O_5 (Table 7.1). H2O– represents the sample weight lost upon heating the sample powder at 110 °C overnight. LOI is "loss on ignition", and represents the weight change (positive if weight lost) upon heating the sample to 800°C for 4 hours.

The SiO_2 concentration of hangingwall and sheared pelitic granulite samples are broadly similar and range between approximately 50 and 75 wt%. Contrastingly, the SiO_2 concentrations of Pella amphibolite samples is lower and occurs between 39 and 53 wt%.

With the exception of K_2O, CaO and Na_2O the major oxide analyses of pelitic granulite samples tend to fall on an approximately linear trend defining a negetive correlation in each case, when plotted against SiO_2. However, K_2O and Na_2O tend to show more clustering when plotted against SiO_2. When plotted against each other, CaO vs. SiO_2 wt % forms a flat trend as there is very little variation in CaO compared to SiO_2 variability.

Similarly, most Pella amphibolite major oxide analyses define approximately linear trends when plotted against SiO_2. Whereas Al_2O_3, FeO_{Total} and CaO all define negetive correlations with SiO_2 concentration, Na_2O and MnO both define positive correlations. Conversely, MgO and TiO_2 show clustering with no discernable trend when plotted against SiO_2.

Al_2O_3 variability in Pella amphibolites (10–17 wt%) is limited compared to the Al_2O_3

Table 7.1: Results of XRF analysis for samples chosen for pseudosection modelling are presented as wt% concentrations of major oxides.

	Hangingwall pelitic granulites					Sheared pelitic granulites					Pella amphibolites	
	PM13010	PM13032	PM13068	PM13076	JMTV45	KK02	KK04	KK10	KK28	KK29	KK14	KK19
SiO_2	55.26	66.86	73.63	57.18	57.97	66.64	66.84	72.12	74.91	54.64	52.96	48.85
TiO_2	0.94	0.78	0.70	1.57	1.34	0.91	0.83	0.41	0.42	0.97	1.19	0.48
Al_2O_3	22.29	15.61	12.88	21.70	19.41	14.66	12.67	11.89	11.38	21.34	13.31	13.34
FeO_{Total}	11.39	8.24	6.27	12.04	10.51	9.40	8.42	3.77	4.15	11.15	12.23	10.13
MnO	0.14	0.12	0.08	0.11	0.11	0.12	0.11	0.09	0.06	0.17	0.34	0.21
MgO	2.72	2.56	1.63	2.98	3.06	2.27	2.16	2.34	1.16	2.96	5.87	11.89
CaO	0.15	1.28	0.06	0.32	0.84	0.12	0.59	1.76	0.93	1.18	8.63	8.83
Na_2O	0.82	1.10	0.57	0.62	1.39	0.29	1.20	2.67	1.55	1.58	2.40	1.84
K_2O	5.21	2.44	2.99	2.77	3.88	2.66	3.21	2.55	2.89	2.93	1.25	1.07
P_2O_5	0.05	0.03	0.03	0.08	0.07	0.05	0.04	0.07	0.04	0.04	0.17	0.14
SO_3	0.00	0.04	0.00	0.00	0.01	0.00	0.00	0.00	0.00	0.00	0.00	0.00
Cr_2O_3	0.02	0.02	0.01	0.02	0.02	0.02	0.02	0.00	0.01	0.02	0.03	0.10
NiO	0.01	0.01	0.01	0.02	0.01	0.01	0.01	0.01	0.01	0.01	0.01	0.03
H_2O-	0.01	0.04	0.01	0.01	0.00	0.11	0.26	0.08	0.12	0.16	0.07	0.05
LOI	0.48	0.53	0.71	0.31	1.31	1.61	2.04	0.76	0.87	1.38	0.72	1.79
Total	99.50	99.65	99.60	99.71	99.93	98.90	98.41	98.52	98.50	98.54	99.19	98.75

variability in pelitic granulite samples (10–33 wt%). Similarly, variability in FeO_{Total} (10–14 wt%) and K_2O (0–1.3 wt%) in Pella amphibolite samples is small when compared to pelitic granulites, with FeO_{Total} and K_2O concentrations occurring in the ranges 3–19 wt% and 0–5.2 wt% respectively. Conversely, there is greater chemical variation in CaO (8–16 wt%) and MgO (5.8–12 wt%) for Pella amphibolite samples than there is in peltic granulite samples where corresponding values occur in the ranges 0–2 wt% and 0–6 wt%.

The extent of chemical variation in MnO, TiO_2 and Na_2O is broadly comparable for pelitic granulite and Pella amphibolite samples (although slightly greater in each case for pelitic granulites). MnO, TiO_2 and Na_2O occur in the ranges 0.05–0.3 wt%, 0.4–1.5 wt% and 0–2.7 wt% for pelitic granulites samples, with the corresponding values occurring at 0.17–0.35 wt%, 0.4–1.2 wt% and 1–2.5 wt% for Pella amphibolites.

Overall, the scatter of analyses in each of the Harker plots in Figure 7.1 indicate that the hangingwall pelitic granulites are indistinguishable from the sheared pelitic granulites on the basis of composition.

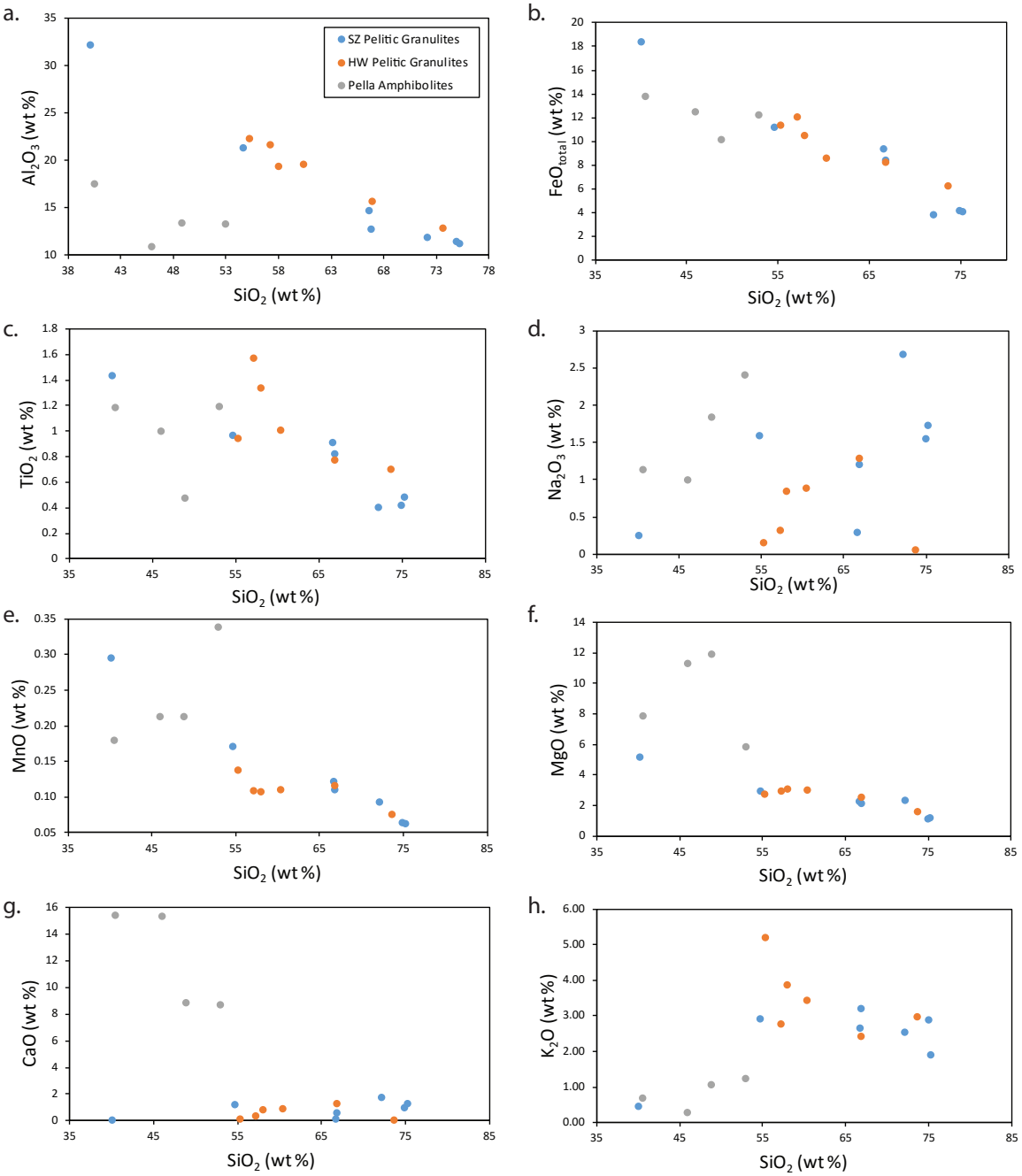

Figure 7.1: Harker diagrams showing major oxide chemical variabilitiy for pelitic granulite and Pella amphibolite samples.

Chapter 8

Calculated Phase Equilibria

8.1 Overview

In this chapter, P-T pseudosections calculated from bulk rock compositions of selected pelitic granulite and Pella amphibolite samples are presented and described. Pelitic granulites samples: PM13010, PM13032, PM13068, PM13076 and JMTV45 (from the Hangingwall Gordonia) and KK02, KK04, KK10 and KK29 (from the LFRTZ) were used for pseudosection calculation. Pseudosections for mafic compositions were calculated from Pella amphibolite samples KK14 and KK19. The specific locations of each of these samples is indicated in Figure 3.1.

These samples were selected for pseudosection calculation in order to constrain the peak-to-retrograde P-T evolution of the rocks at the study site and to determine the most likely P-T conditions of shearing and tectonic juxtaposition on the LFRTZ along the Richtersveld-Gordonia Subprovince marginal zone.

The use of pseudosections for mineral equilibria modelling is favoured over conventional and optimal thermobarometric methods since: a) pseudosection modelling does not rely on mineral compositions to constrain P-T conditions, and thus circumvents problems related to the susceptibility of mineral compositions to re-equilibration during post-peak metamorphism (Fitzsimons & Harley, 1994; Pattison *et al.*, 2003; Powell & Holland, 2008); b) the topology and P-T distribution of phase assemblages on pseudosections (for a particular chemical system) is dependent only on the bulk rock composition and thus incorporates minimal interpretive error (Powell & Holland, 2008) and; c) textural information can often be used to constrain segments of the P-T path, not just a single point (Powell & Holland, 2008).

8.2 Assumptions made during pseudosection calculation

Isochemical P-T pseudosections show all the stable multivariant phase assemblages in a chosen chemical system, for a specified bulk rock composition and can be used to constrain metamorphic conditions and P-T paths (e.g. White *et al.*, 2004; Diener *et al.*, 2008, 2013; Clark *et al.*, 2014). Pseudosections were calculated using THERMOCALC 3.40 (Powell & Holland, 1988, updated June 2014) with an updated version of the internally consistent thermodynamic dataset of Holland & Powell (2011, dataset file tc-ds62.txt, created 06/02/2012). Calculation of pseudosections was performed in the Na_2O–CaO–K_2O–FeO–MgO–Al_2O_3–SiO_2–H_2O–TiO_2–Fe_2O_3 (NCKFMASHTO) model chemical system for metapelites, while Na_2O–CaO–FeO–MgO–Al_2O_3–SiO_2–H_2O–TiO_2–Fe_2O_3 (NCFMASHTO) was used for amphibolites – these are currently the most realistic approximations of actual rock composition where modelling can be undertaken for pelitic and mafic compositions respectively (White *et al.*, 2001, 2003, 2007).

MnO is ommitted as a component from each system since the calibrations for Mn bearing phases were derived using simple ideal-mixing models and would be incompatible with activity-composition (a–x) models used for the current model systems, where non-ideal mixing was taken into account for each component (White *et al.*, 2007). The bulk of the calculations where carried out prior to the publication of the re-parameterised Mn models of (White *et al.*, 2014a).

The phases considered in the modelling and the corresponding a–x models used are garnet, cordierite, biotite, orthopyroxene, muscovite-paragonite, silicate melt (all from White *et al.*, 2014b), plagioclase–K-feldspar, epidote (Holland & Powell, 2003), hornblende, gedrite, cummingtonite, anthophyllite, diopside (pre-publication version of Green *et al.*, 2016), spinel-magnetite and ilmenite-hematite (White *et al.*, 2002). The aluminosilicates, quartz and aqueous fluid (H_2O) are taken as pure end-member phases.

Analyses for the selected samples were converted to NC(K)FMASHTO by disregarding the small amount of MnO, Cr_2O_3 and P_2O_5 and converting a portion of the total Fe (Fe_{total}) to Fe^{3+}. The percentage of Fe_{total} converted to Fe^{3+} for each sample is chosen on the basis of the oxide minerals present, which can provide insight on the oxidation state of the rocks (Diener & Powell, 2010). For PM13032, PM13076 and JMTV45, 9 to 10% of Fe_{total} was converted to Fe^{3+}, in line with the observation that ilmenite is the main oxide mineral in these rocks. For samples PM13010, PM13068, KK04, KK27, KK28 and KK29, 12 to 20% of Fe_{total} was converted to Fe^{3+}, this is in line with the observation that magnetite is the dominant oxide mineral in these rocks, but occurs in small amounts. However, in the case of KK10, no oxide minerals were identified – thus the 10% conversion of Fe_{total} to Fe^{3+} was chosen on the basis of the inferred oxidation state of other samples from the immediate vicinity.

For amphibolite samples, 10 and 15% of Fe_{total} was converted to Fe^{3+} for KK19 and KK14 respectively. This was decided taking into consideration that significant amounts of Fe^{3+} can be accomodated by hornblende (Diener & Powell, 2010) and that rutile and ilmenite are the oxide phases occuring in these rocks – indicating that they likely evolved in a relatively reduced environment (e.g. Diener & Powell, 2010; Diener, 2014).

The bulk rock compositions (presented as mol% values of each component) used to calculate the pseudosections are presented in Table 8.1.

Table 8.1: Bulk rock compositions (in mol %) used to model pseudosections. "O" represents the extra oxygen added, which is required to oxidise Fe^{2+} to form Fe^{3+}.

	Hangingwall pelitic granulites					Sheared pelitic granulites					Pella amphibolites	
	PM13010	PM13032	PM13068	PM13076	JMTV45	KK02	KK04	KK10	KK28	KK29	KK14	KK19
Si	64.16	73.67	80.48	65.39	66.10	75.18	75.59	78.45	82.17	63.87	57.37	51.68
Ti	0.83	0.65	0.58	1.35	1.15	0.78	0.70	0.33	0.35	0.85	0.97	0.38
Al	15.25	10.14	8.30	14.62	13.04	9.75	8.44	7.62	7.36	14.70	8.50	8.32
Fe_{total}	9.95	6.83	5.16	10.36	9.01	7.98	7.16	3.09	3.42	9.81	9.97	8.07
Mn	0.13	0.11	0.07	0.10	0.10	0.12	0.10	0.09	0.06	0.17	0.31	0.19
Mg	4.71	4.21	2.66	5.07	5.20	3.82	3.64	3.79	1.89	5.15	9.47	18.75
Ca	0.19	1.51	0.07	0.39	1.03	0.14	0.72	2.05	1.09	1.48	10.02	10.01
Na	0.92	1.17	0.60	0.69	1.54	0.31	1.31	2.82	1.65	1.79	2.52	1.88
K	3.86	1.71	2.09	2.02	2.83	1.92	2.32	1.77	2.02	2.18	0.86	0.73
O	0.75	0.31	0.52	0.47	0.41	0.60	0.54	0.15	0.26	0.74	0.75	0.40

Although omission of MnO would be expected to result in lowering the temperature of the garnet-in phase boundary in P-T space (White *et al.*, 2004), these effects are likely to be minor for the high metamorphic grades (upper-amphibolite to granulite facies) experieced by Namaqualand gneisses (White *et al.*, 2004, 2007). Moreover, the observation that the MnO content of the modelled samples is relatively low (0.06–0.3 wt%) and spessartine in garnet is subordinate, will further limit the effects of this omission. Similarly, due to their occurrence in small concentrations (both typically less than 0.1 wt%) the omission of Cr_2O_3 and P_2O_5 from the chemical system is likely to have an insignificant effect on the P-T distribution of the calculated phase assemblage fields.

Field and petrographic evidence indicates that the pelitic rocks were subject to supra-solidus metamorophic P-T conditions (Chapter 3). However, the generally high level of preservation of the peak metamorphic assemblage in residual metapelite samples, with only minimal evidence of retrogression implies open-system behaviour of melt, where melt-loss occurred prior to significant cooling (White *et al.*, 2002). This would allow the escape of fluids with the melt and thus preclude reversal of incongreunt melting reactions (e.g. Powell, 1983; White *et al.*, 2001). For this reason, the bulk rock compostion for the modelled residual metapelite pseudosections approximates that of residuum, since melt-loss would have modified the subsolidus (protolith) composition of the rocks (Diener *et al.*, 2008, 2013). Consequently, the residuum pseudosections are only appropriate for investigating the post-melt-loss (i.e. peak-to-retrograde) evolution of these rocks since the pre-melt-loss evolution occurred

in different rock compositions (White *et al.*, 2004; Diener *et al.*, 2008, 2013).

For hangingwall pelitic granulite samples, H_2O content was estimated such that the inferred peak assemblage is stable at conditions immediately above the residuum solidus, to reflect conditions where the assemblage would have been in equilibrium with the last vestiges of melt (White *et al.*, 2004; Powell & Holland, 2008; Diener *et al.*, 2008, 2013). This was done using an iterative approach where the amount of H_2O (in mol%) was varied in the bulk-rock composition (that was inputted into Thermocalc) until the modal proportion of minerals in the modelled equlibrium (peak) assemblage field best reflected what was estimated from thin section analysis.

Sheared pelitic granulites are a texturally reworked variant of the hangingwall peltic granulites (Chapter 3) – these rocks show little evidence of post-peak temperature rehydration during shearing (Section 5.1.2). Thus, the H_2O content of sheared pelitic granultes was estimated in the same manner as the hangingwall pelitic granulites – consistent with the fact that their compositions is residual and anhydrous.

Contrastingly, metabasic samples comprise a relatively hydrous assemblage and show no evidence of ever melting (Chapter 3). Thus, H_2O is taken as a phase in excess for pseudosection calculations of metabasic rocks.

Whereas for all metapelite samples, phase equilibria were calculated for the pressure range 2–8 kbar at temperatures ranging between 640 and 900°C; for amphibolite samples pseudosection calculations were carried out for pressures ranging between 2 and 9 kbar at temperatures between 500 and 800°C.

Pseudosections are calculated on the assumption that chemical equilibrium was reached in all samples such that all reactions proceeded to completion and no phases within the preserved assemblage exist metastabley.

8.3 Results: HW Pelitic Granulites

Pseudosections for five hangingwall pelitic granulites samples (PM13068, JMTV45, PM13010, PM13032 and PM13076) from various locations within the Kum Kum Klippe were calculted and are presented in Figures 8.1 to 8.5.

These rocks were selected specifically to constrain the peak metamorphic P-T conditions and were thus chosen based on specific criteria: i) the rocks were selected from the high grade core of Kum Kum Klippe in order to most accurately represent peak conditions; ii) the rocks were selected away from significant zones of high strain where localised pervasive fluid flow during cooling may have resulted in retrogession and; iii) the rocks do not show evidence of strain beyond the intesity of the background regional ductile fabric such that there is no reworking of peak metamorphic textures by subsequent discrete, localised structures.

The topologies of hangingwall pelitic granulite pseudosections are broadly similar to

each other. Differences in pseudosection topology for these samples is most prominent between compositions in which plagioclase is calculated to be stable (PM13032, PM13076 and JMTV45) and those where it is absent (PM13010 and PM13068). Spinel is only modelled to stabilise in one sample (PM13076) and thus the topology of this pseudosection displays some unique properties compared to other pseudosections.

For each of the hangingwall pelitic granulites (except PM13076), the inferred peak assemblage stability field is three sided and extends diagonally from relatively low P-T conditions (∼775–795°C at ∼4.7–5.3 kbar) at the solidus to higher P-T conditions (∼835–845 °C at ∼6.3–6.7 kbar) where it terminates at the cordierite-biotite absent invariant. In general, peak assemblage fields are bounded by the biotite-out and cordierite-out phase boundaries at low-pressures and high-pressures respectively, while the solidus bounds the low temperature extent. However, for PM13076 this phase field is four-sided such that the lower temperature extent of this phase field is also defined by the plagioclase-out phase boundary.

As a general trend, the solidi of each of the pseudsections (in order of increasing pressure) are intersected by the: garnet, orthopyroxene, magnetite (where present), sillimanite, biotite and cordierite (highest pressures) phase boundaries. In the case of PM13032 and PM13068, the biotite phase boundary crosses the solidus on more than one occassion within the pressure range being considered. For PM13076, spinel is only stable at relatively high temperatures for pressures between ∼2.2 and 5.6 kbar, while plagioclase is absent only at high temperatures and pressures. These phase boundaries (spinel and plagioclase) do not occur in the pseudosections for any of the other hangingwall pelitic granulite samples. At high pressures all pseudosections are characterised (in order of increasing temperature) by K-feldspar-biotite-garnet-sillimanite, K-feldspar-biotite-garnet-sillimanite-liquid and K-feldspar-garnet-sillimanite-liquid present assemblages – the shapes of these phase fields for each of the pseudosections are nearly identical.

In each of the pseudosections, the higher pressure extent of the biotite phase boundary crosses the solidus just below the cordierite phase boundary. Magnetite is stabilised for the P-T window in consideration only for samples PM13032 and PM13076 where it is stable over the entire temperature range in consideration at pressures below ∼4.2 to 4.6 kbar for PM13032 and below ∼4.2 and 2.4 kbar at low and high temperatures respectively for PM13076. For all pseudosections, orthopyroxene becomes stable only at low pressures and high temperatures. Moreover, the introduction of orthopyroxene is accompanied by the removal of garnet at pressures below the orthopyroxene phase boundary.

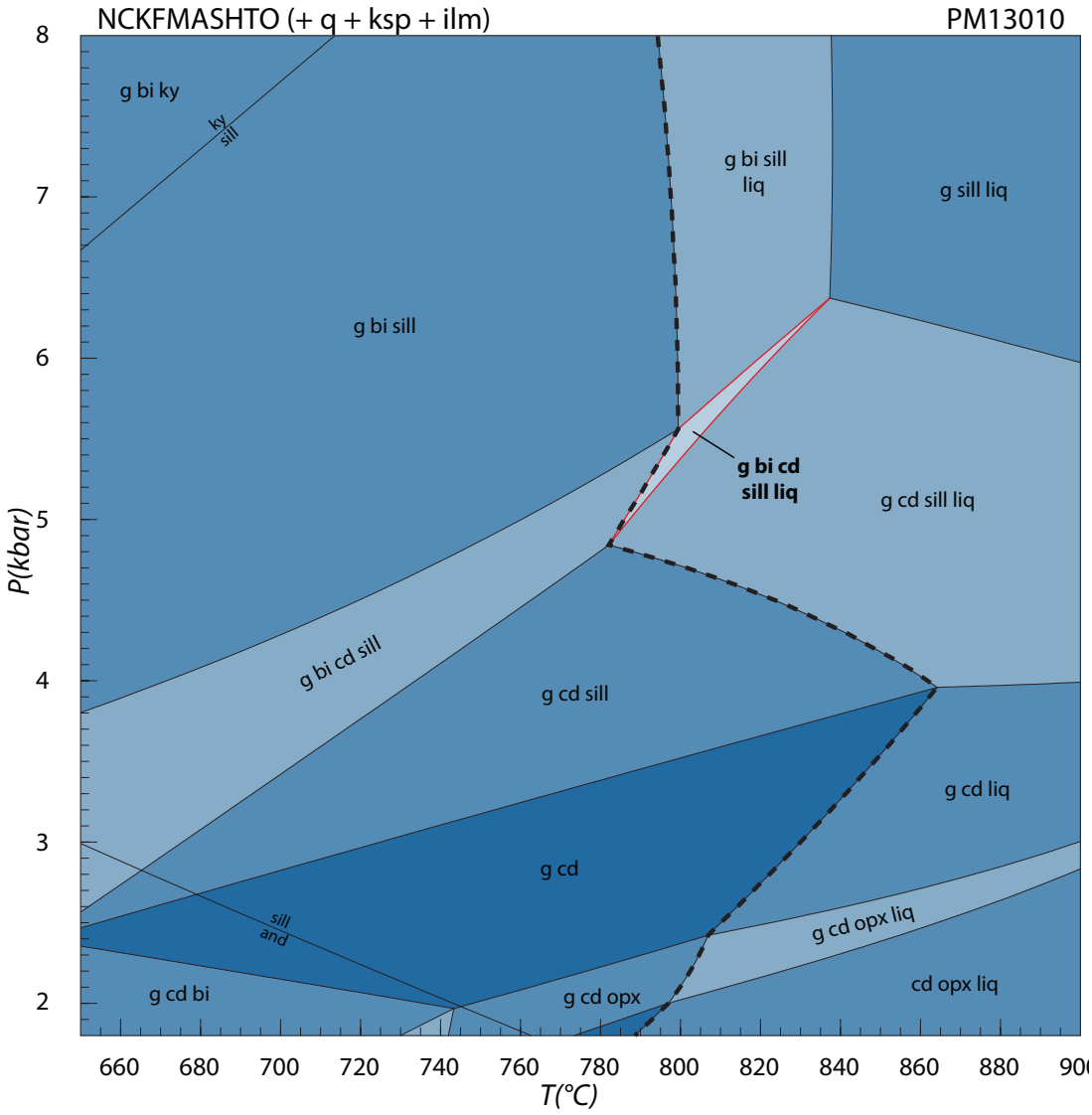

Figure 8.1: Pseudosection for hangingwall pelitic granulite sample PM13010. P-T stability field of the inferred equilibrium assemblage (g-bi-cd-sill-liq; plus phases in excess) is outlined in red. Mineral and phase abbreviations as in Chapter 5.

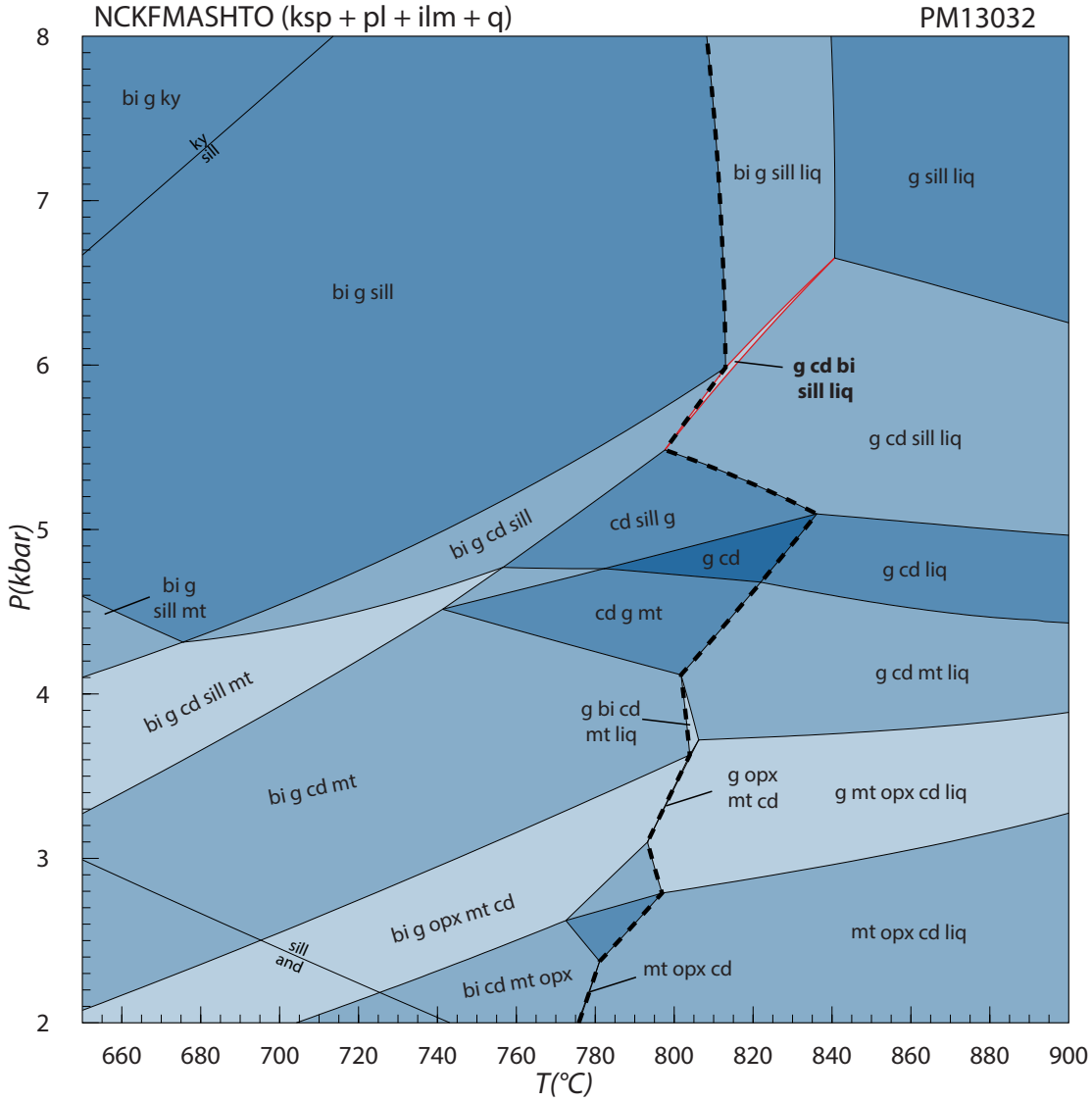

Figure 8.2: Pseudosection for hangingwall pelitic granulite sample PM13032. P-T stability field of the inferred equilibrium assemblage (g-bi-cd-sill-liq; plus phases in excess) is outlined in red. Mineral and phase abbreviations as in Chapter 5.

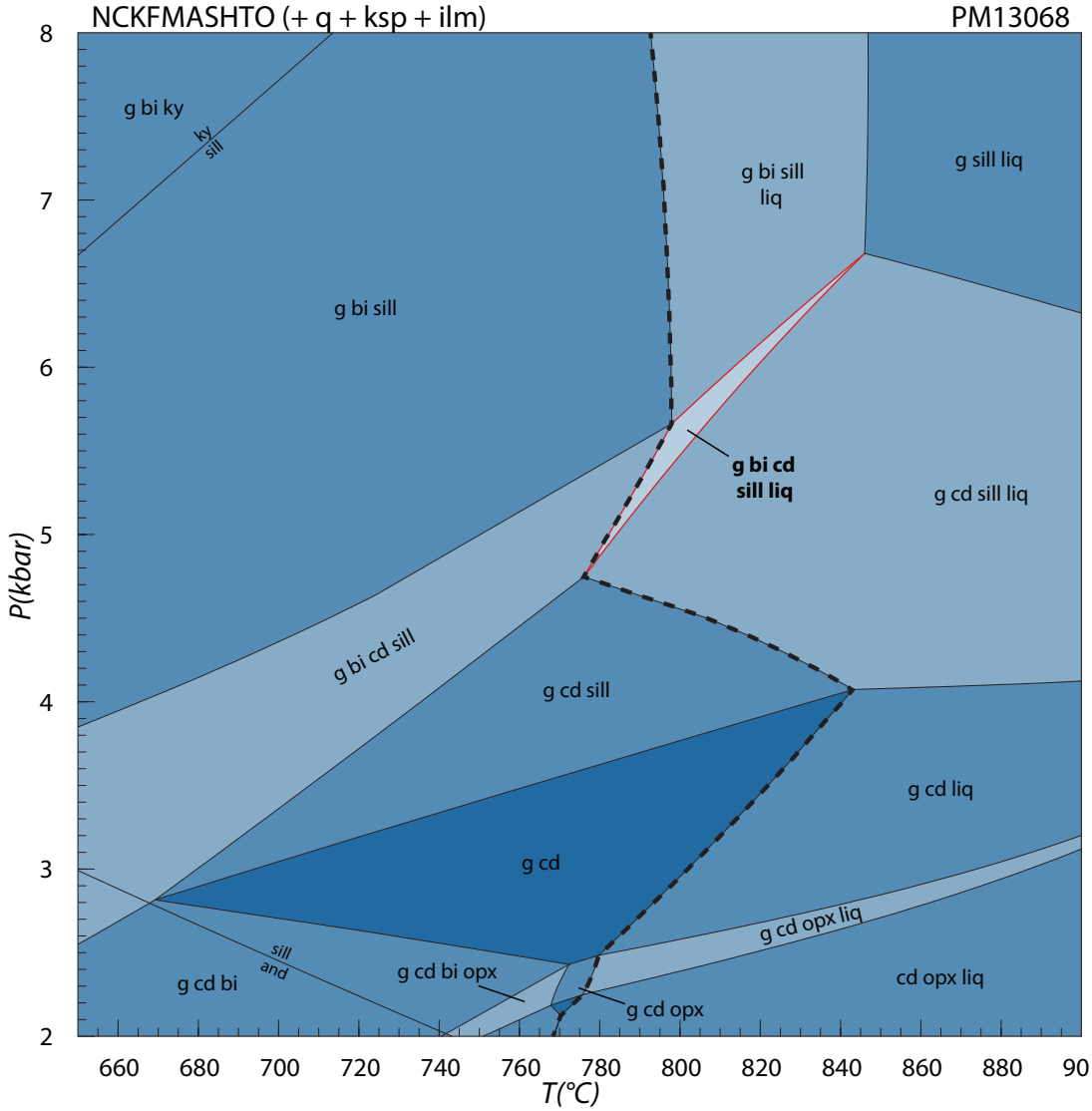

Figure 8.3: Pseudosection for hangingwall pelitic granulite sample PM13068. P-T stability field of the inferred equilibrium assemblage (g-bi-cd-sill-liq; plus phases in excess) is outlined in red. Mineral and phase abbreviations as in Chapter 5.

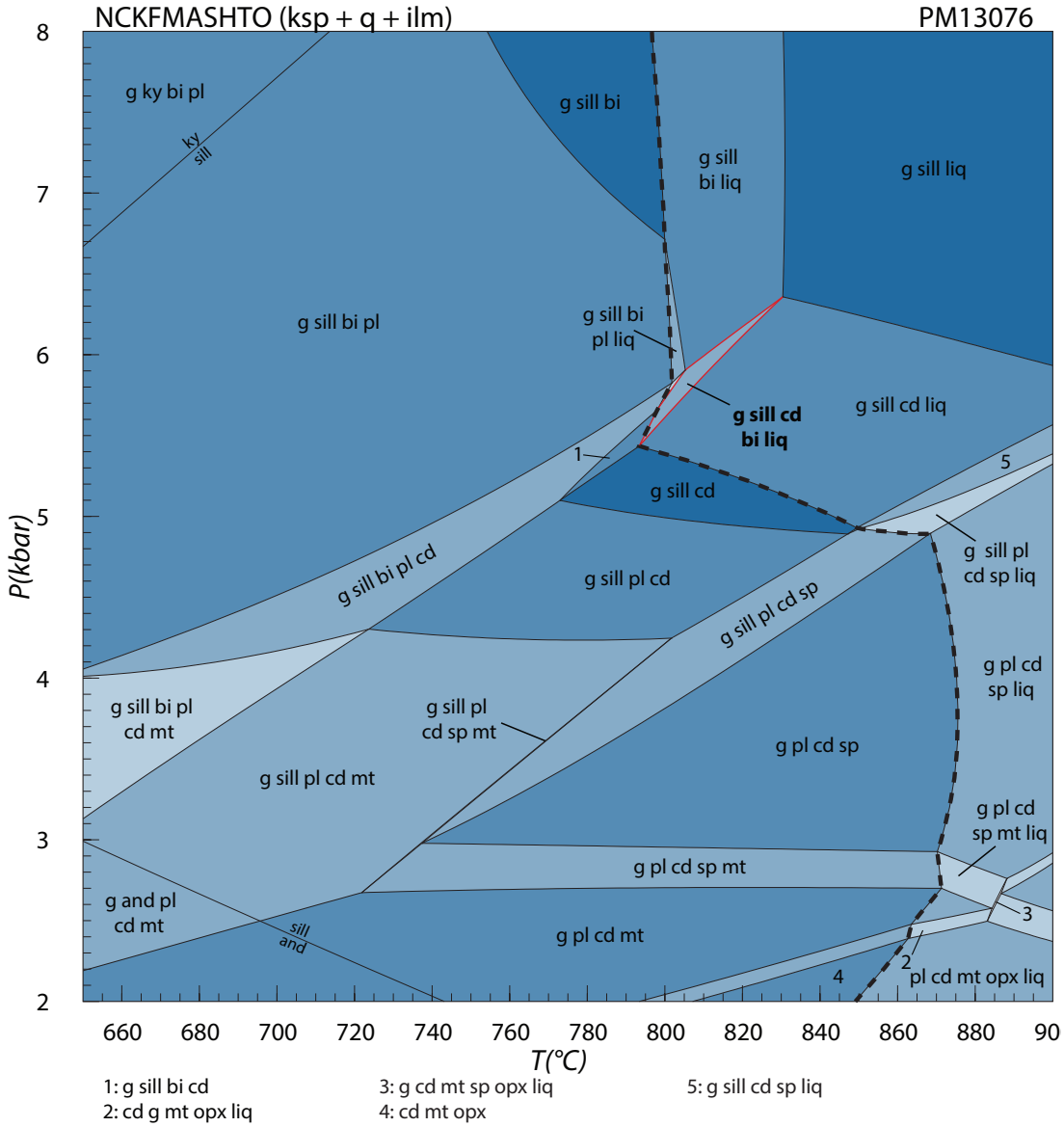

Figure 8.4: Pseudosection for hangingwall pelitic granulite sample PM13076. P-T stability field of the inferred equilibrium assemblage (g-bi-cd-sill-liq; plus phases in excess) is outlined in red. Mineral and phase abbreviations as in Chapter 5.

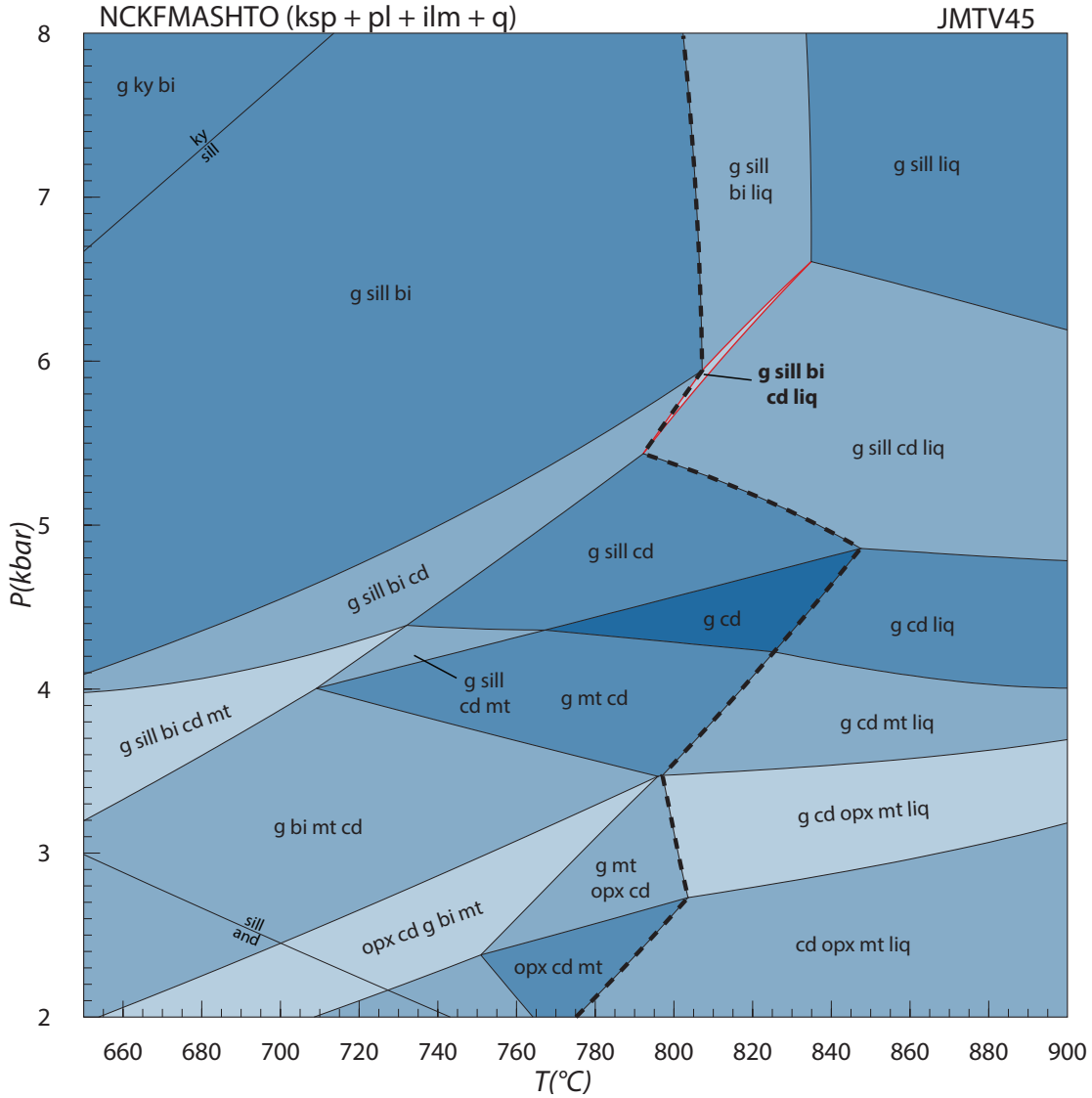

Figure 8.5: Pseudosection for hangingwall pelitic granulite sample JMTV45. P-T stability field of the inferred equilibrium assemblage (g-bi-cd-sill-liq; plus phases in excess) is outlined in red. Mineral and phase abbreviations as in Chapter 5.

8.4 Results: SZ Pelitic Granulites

Pseudosections for five sheared pelitic granulite samples (KK02, KK04, KK10, KK28 and KK29) from various locations within the LFRTZ were calculated and are presented in Figure 8.6 to 8.10.

These rocks were selected specifically to constrain the conditions of post-peak P-T shearing in the LFRTZ and were thus chosen based on the following criteria: i) the rocks were sampled from within the LFRTZ and exhibit a high temperature, solid-state ductile deformation fabric attributable to shearing in the LFRTZ; ii) the degree of strain experienced by the rocks is representative of deformation in the LFRTZ (i.e. strain shadows and competent phacoids were avoided) and; iii) the rocks exhibit no significant evidence of recent alteration.

On the basis of field evidence, petrography and major oxide chemistry, sheared pelitic granulites are postulated represent the sheared variants of the hangingwall pelitic granuliltes which have been texturally reworked; thus, like the hangingwall pelitic granulites, the solidi of these rocks is H_2O absent. The P-T distribution of phase assemblages in the sheared pelitic granulites is broadly similar to that of the hangingwall pelitic granulites. Morever, the solidi of sheared pelitic granulites, which range between 740°C and 815°C occur at similar temperatures to those of the hangingwall pelitic granulites.

For each of the sheared pelitic granulite pseudosections (except KK10), the P-T stability of the inferred equilibrium assemblage is bounded by the cordierite-out and sillimanite-out phase boundaries at high and low pressures respectively. However, for KK02 and KK28 – at low temperatures, the low pressure boundary of the equilibrium assemblage stability field is defined by both the sillimanite-out (low temperatures) and garnet-out (high temperatures) phase boundaries. In each of the pseudosections, the low temperature boundary of the inferred equilibrium phase field is partially bounded by the sillimanite-andalusite transition. In each case (except KK10) the equilibrium assemblage field is characterised by a relatively narrow pressure range and extends diagonally across a wide temperature range between ∼640°C (which is the low temperature limit of all pseudosections) and 790°C.

For KK10 the P-T stability of the inferred equilibrium assemblage spans a large pressure range from 2.4 kbar to the upper pressure limit of the pseudosection P-T window at 8 kbar. The low pressure extent of this phase field is bounded by the orthopyroxene-in (high temperatures) phase boundary and the sillimanite-andalusite transition (low temperatures), while the high temperature limits are defined by the solidus.

With exception of KK10, in order of increasing pressure, the solidi of each of the pseudsections are intersected by the: garnet, orthopyroxene, sillimanite, biotite and the cordierite phase boundaries. However, in the cases of KK02 and KK28, the orthopyroxene phase boundary does not intersect the solidus as it deflects to pressures below the range being considered as it approaches from up-temperature of the solidus. For KK02 the plagioclase phase bound-

ary occurs at marginally higher temperatures than the solidus for most of the pressure window being considered, but intersects it at ∼6.8 kbar. No plagioclase phase boundary occurs for the rest of the sheared pelitic granulite samples.

For KK10, the inferred equilibrium assemblage field covers a broad P-T range which is bounded by the solidus at high temperatures while the lower pressure extent is delineated by both the orthopyroxene-in phase boundary (high temperature) and the sillimanite-andalusite transition (low temperatures).

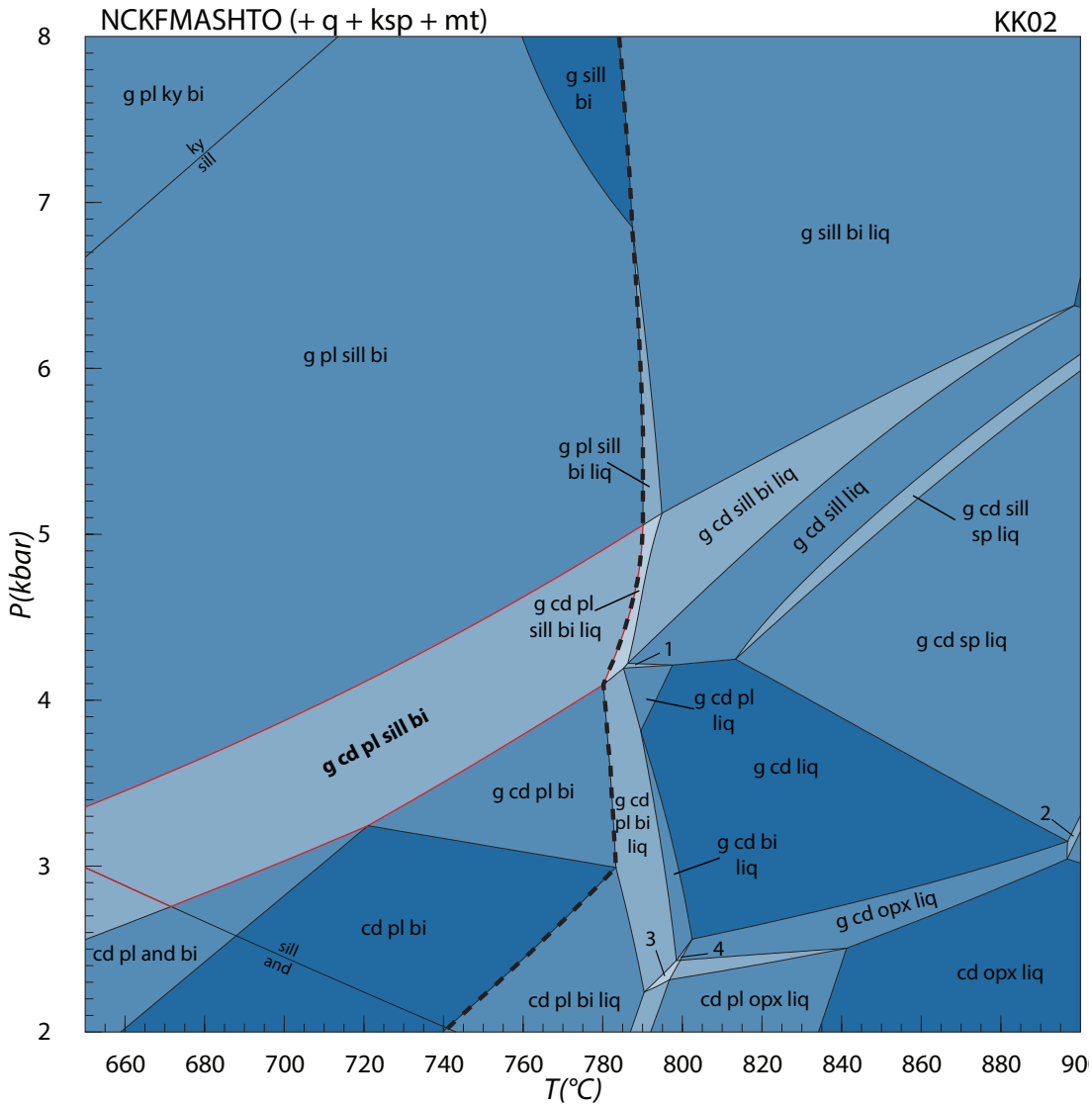

Figure 8.6: Pseudosection for sheared pelitic granulite sample KK02. P-T stability field of the inferred equilibrium assemblage (g-cd-pl-sill-bi; plus phases in excess) is outlined in red. Mineral and phase abbreviations as in Chapter 5.

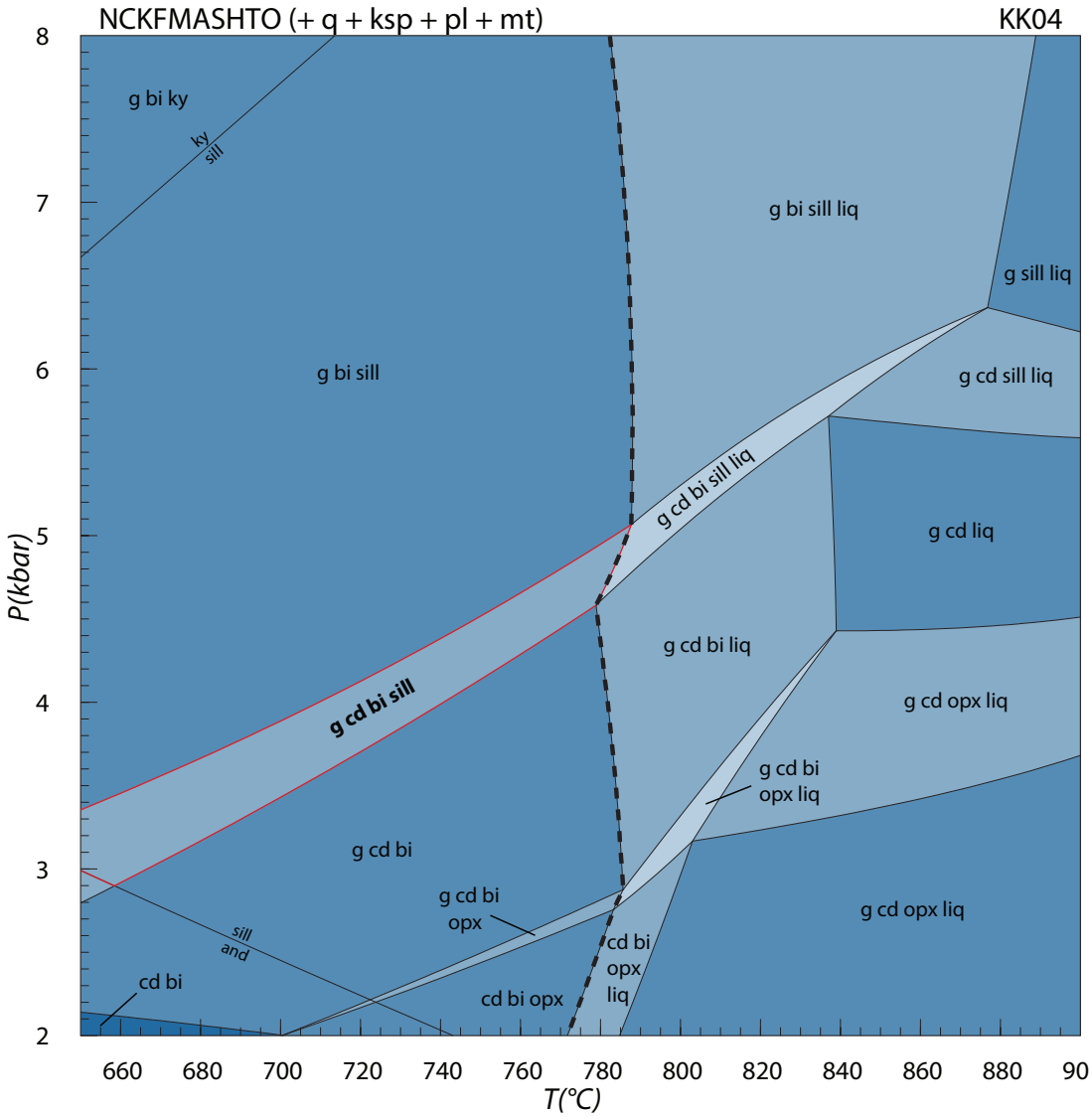

Figure 8.7: Pseudosection for sheared pelitic granulite sample KK04. P-T stability field of the inferred equilibrium assemblage (g-bi-cd-sill; plus phases in excess) is outlined in red. Mineral and phase abbreviations as in Chapter 5.

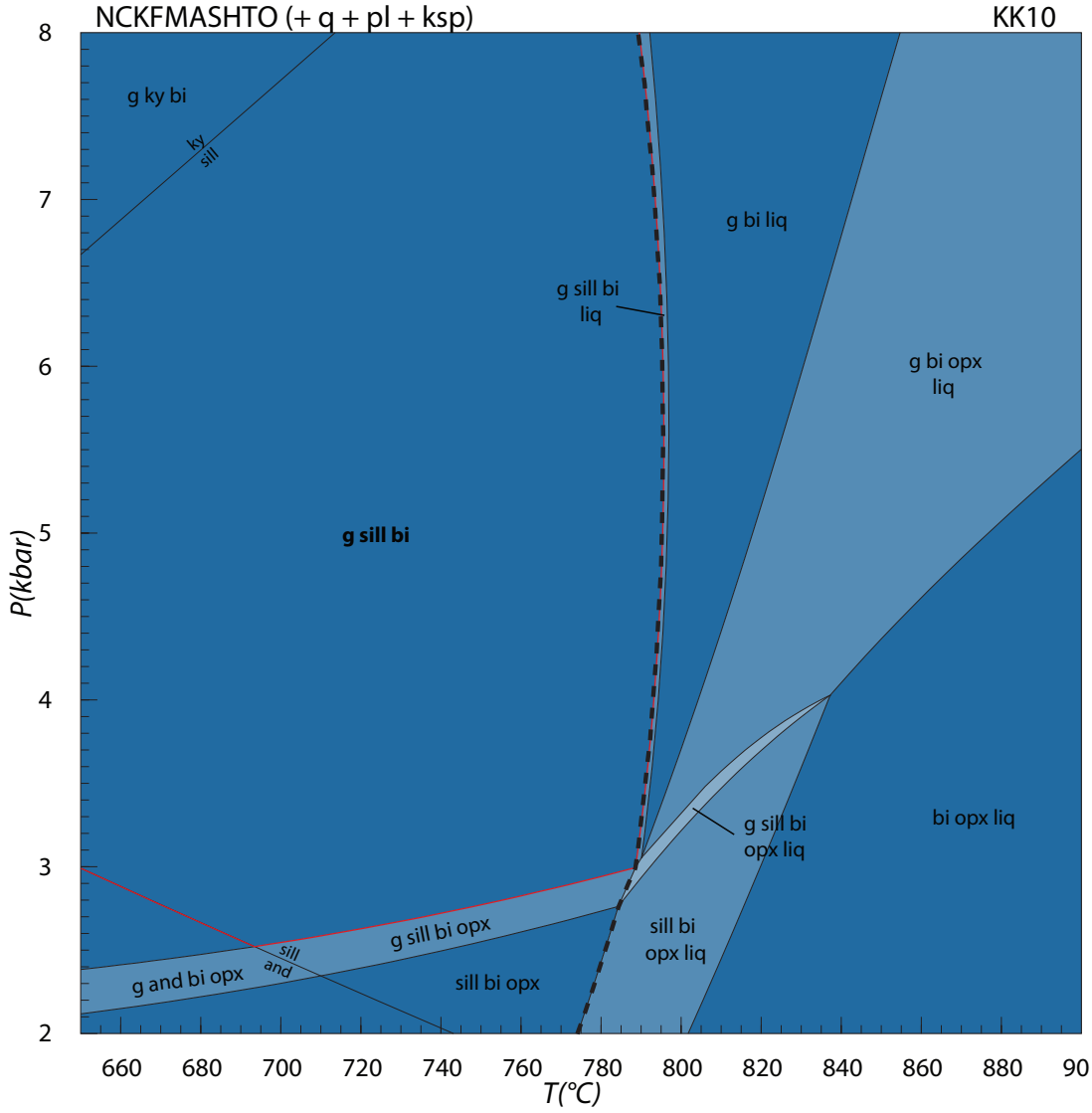

Figure 8.8: Pseudosection for sheared pelitic granulite sample KK10. P-T stability field of the inferred equilibrium assemblage (g-sill-bi; plus phases in excess) is outlined in red. Mineral and phase abbreviations as in Chapter 5.

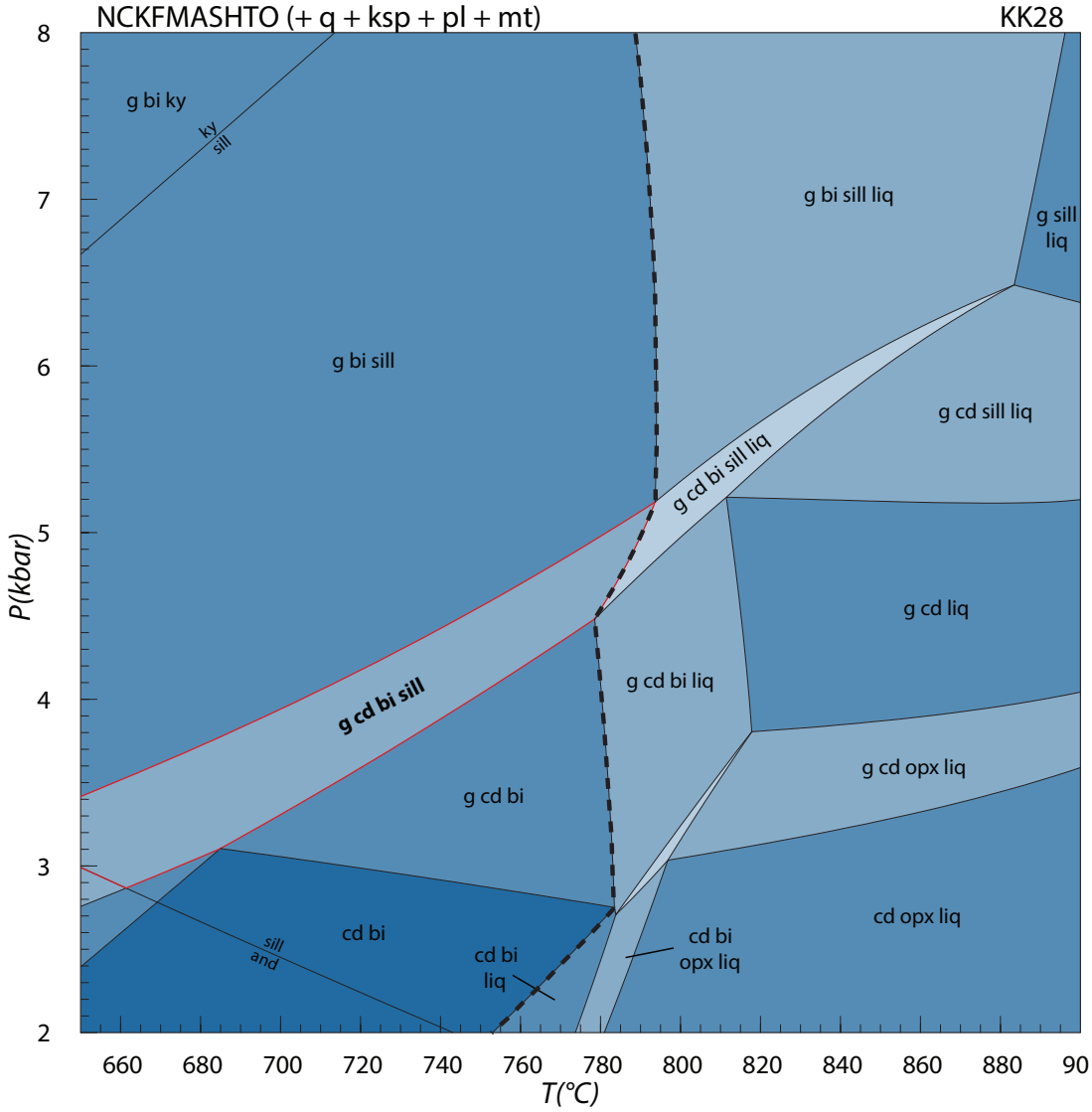

Figure 8.9: Pseudosection for sheared pelitic granulite sample KK28. P-T stability field of the inferred equilibrium assemblage (g-cd-bi-sill; plus phases in excess) is outlined in red. Mineral and phase abbreviations as in Chapter 5.

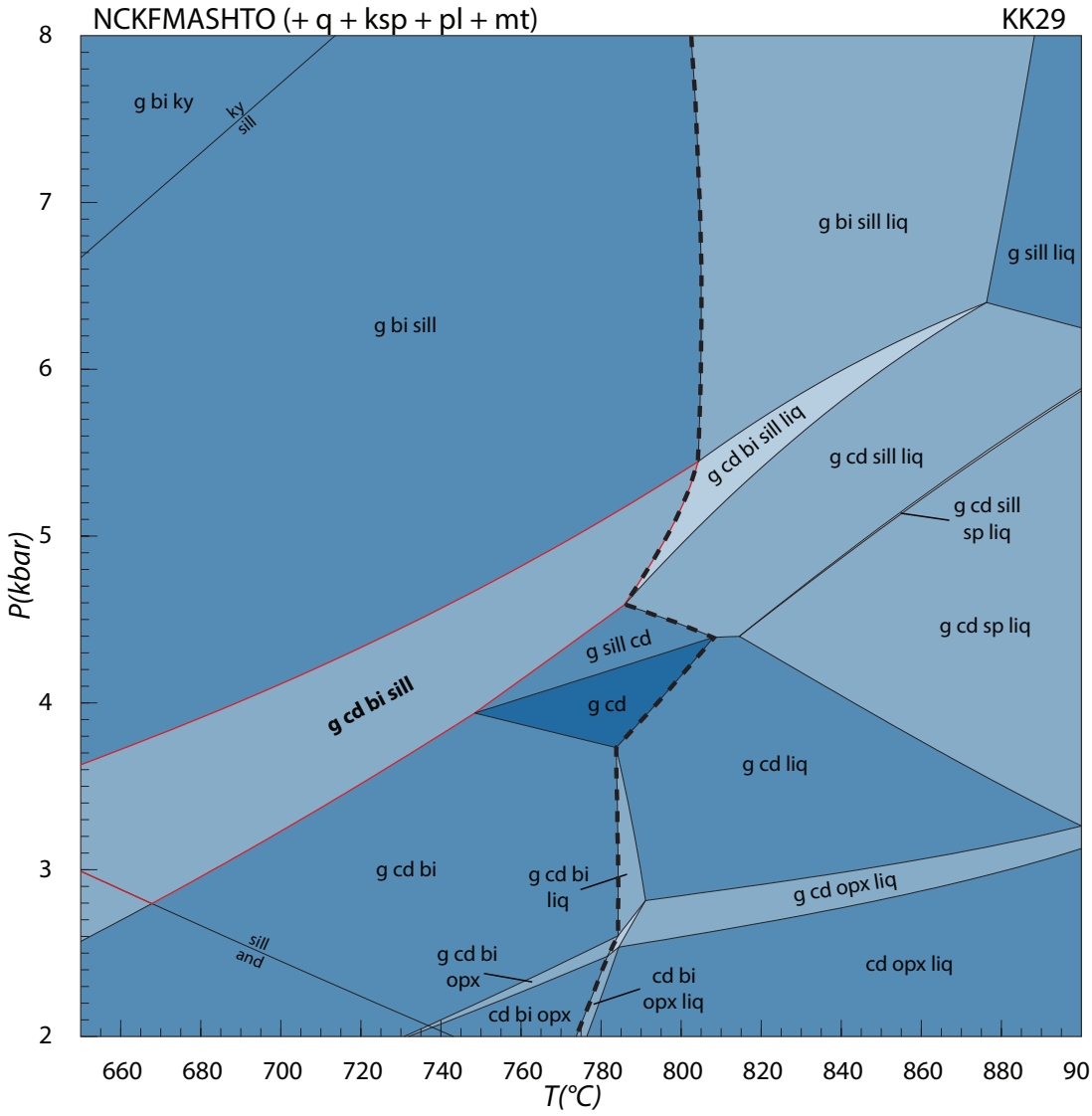

Figure 8.10: Pseudosection for sheared pelitic granulite sample KK29. P-T stability field of the inferred equilibrium assemblage (g-cd-bi-sill; plus phases in excess) is outlined in red. Mineral and phase abbreviations as in Chapter 5.

8.5 Results: Pella Amphibolites

Pseudosections for two Pella amphibolite samples (KK14 and KK19) which were sampled from the LFRTZ and the Footwall Pella respectively, were calculated and are presented in Figures 8.11 and 8.12.

Sample KK14 is interpreted to represent Pella Terrane rock that was incorporated into the LFRTZ during the latest stages of ductile shearing, during exhumation after there had been significant cooling of the hangingwall block. KK19 represents Footwall Pella material that was less extensively affected by LFRTZ deformation and was metamorphosed as a result of tectonic emplacement of the mid-crustal Grunau Terrane on top of the Pella Terrane. Consequently, these Pella amphibolite samples are likely to provide P-T constraints on late-stage shearing in the LFRTZ along with the depth and temperature at which final juxtaposition occurred. Thus, the Pella amphibolites were chosen to satisfy the following criteria: i) the rocks represent Pella Terrane material (in this case KK14 represents Pella Terrane material which was incorporated into the LFRTZ during late-stage shearing); ii) the rocks show no evidence of ever bearing melt; iii) the rocks are compositionally suitable for pseudosections calculation and have sufficient interesting textural features (i.e. amphibolites were sampled preferrentially over the vast granitoids of the Pella Terrane, which are not compositionally favourable for pseudosection calculation) and; iv) there is no significant evidence of recent alteration.

Pseudosections for KK14 and KK19 have very different topologies. In general, the pseudosection for KK19 is characterised by wider ranging variances and significantly larger number of smaller phase fields in comparison to KK14 – where the variances for KK19 range between 2 (lightest shades) and 7 (darkest shades), while those for KK14 occur between 4 (lightest shades) and 6 (darkest shades).

In the pseudosection for KK14, the phase field of the equilibrium assemblage (of hornblende, plagioclase and ilmenite; plus phases in excess) is four-sided with an irregular shape. The high pressure extent of this phase field is defined by both the sphene-in (at low temperatures) and the diopside-in (at high temperatures) phase boundaries, while the low pressure limit is defined by the cummingtonite-in (at low temperatures) and the orthopyroxene-in (at high temperatures) phase boundaries. This phase field covers a relatively broad range in pressures (∼2.0–5.6 kbar) and temperatures (∼500–770°C).

In the pseudosection for KK19, the phase field of the equilibrium assemblage (of hornblende, chlorite, quartz, rutile and plagioclase; plus phases in excess) is also four sided, occurring over a narrow temperature range (∼520–580°C) with a comparatively broad pressure range (∼2.2–5.2 Kbar). Cummingtonite-in and actinolite-in phase boundaries bound the equilibrium assemblage phase field at high and low temperatures respectively, while at high pressures – the albite-in and plagioclase-out (to a lesser extent) phase boundaries delineate

the boundary.

In order to allow for tighter constraints on the P-T conditions represented by the equlibrium assemblage (and associated mineral chemistry), compositional isopleths of anorthite in plagioclase (X_{An}) and A-site sodium in hornblende were calculated for the inferred equilibrium assemblage field of KK14. The X_{An} isopleths are characterised by a steep, positive dP/dT, with X_{An} values for isopleths within the equilibrium assemblage phase field occurring between 0.40 and 0.52. The isopleths for A-site Na in hornblende are characterised by a shallow, positive dP/dT, with values for isopleths ranging between 0.40 and 0.48 within the inferred equilibrium assemblage field.

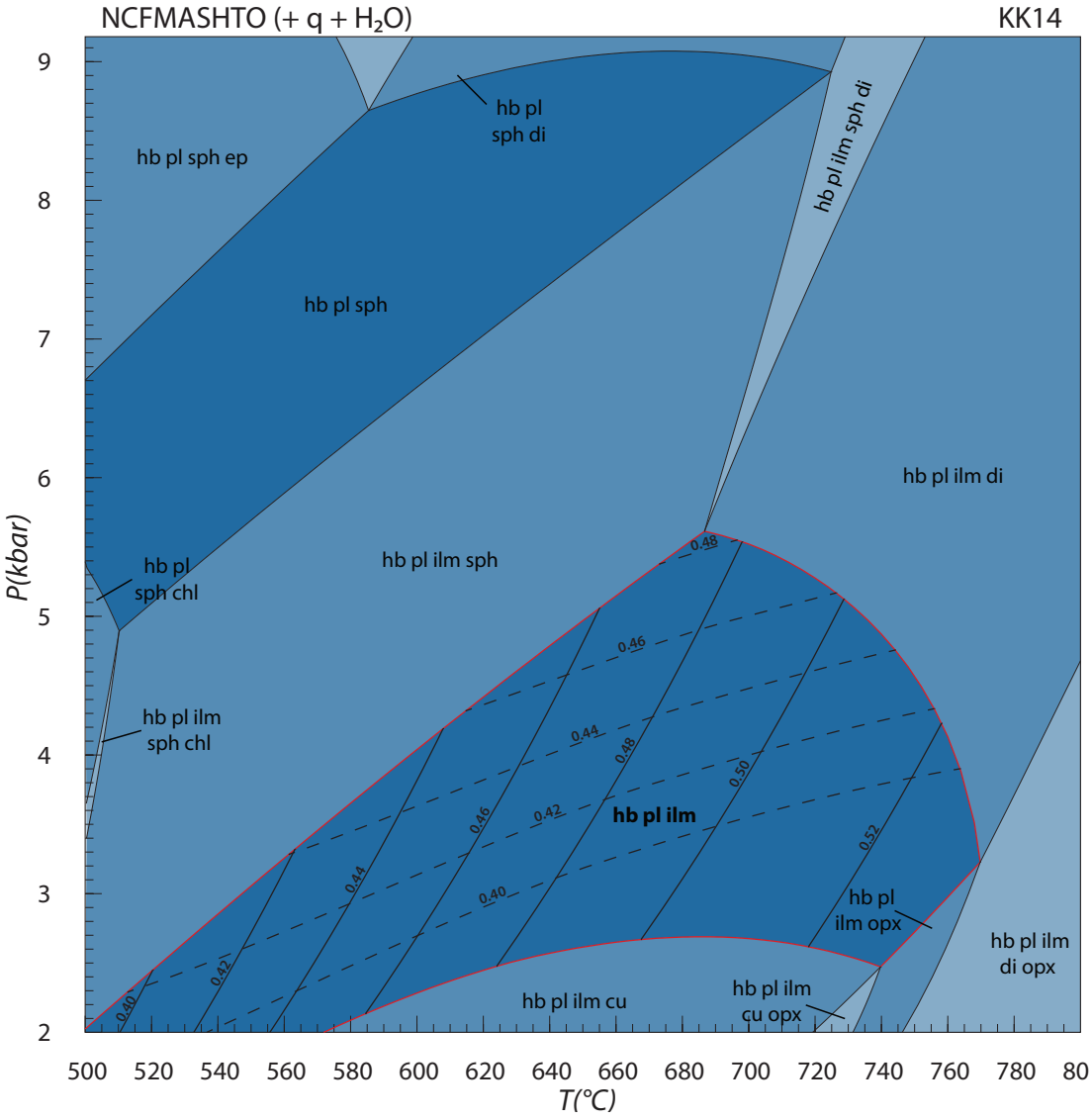

Figure 8.11: Pseudosection for Pella amphibolite sample KK14. P-T stability field of the inferred equilibrium assemblage (hb-pl-ilm; plus phases in excess) is outlined in red and has been contoured for anorthite content (measured at ~ 0.42) in plagioclase (solid lines) along with A-site sodium (measured at ~ 0.43) in hornblende (dotted lines). Mineral and phase abbreviations as in Chapter 5.

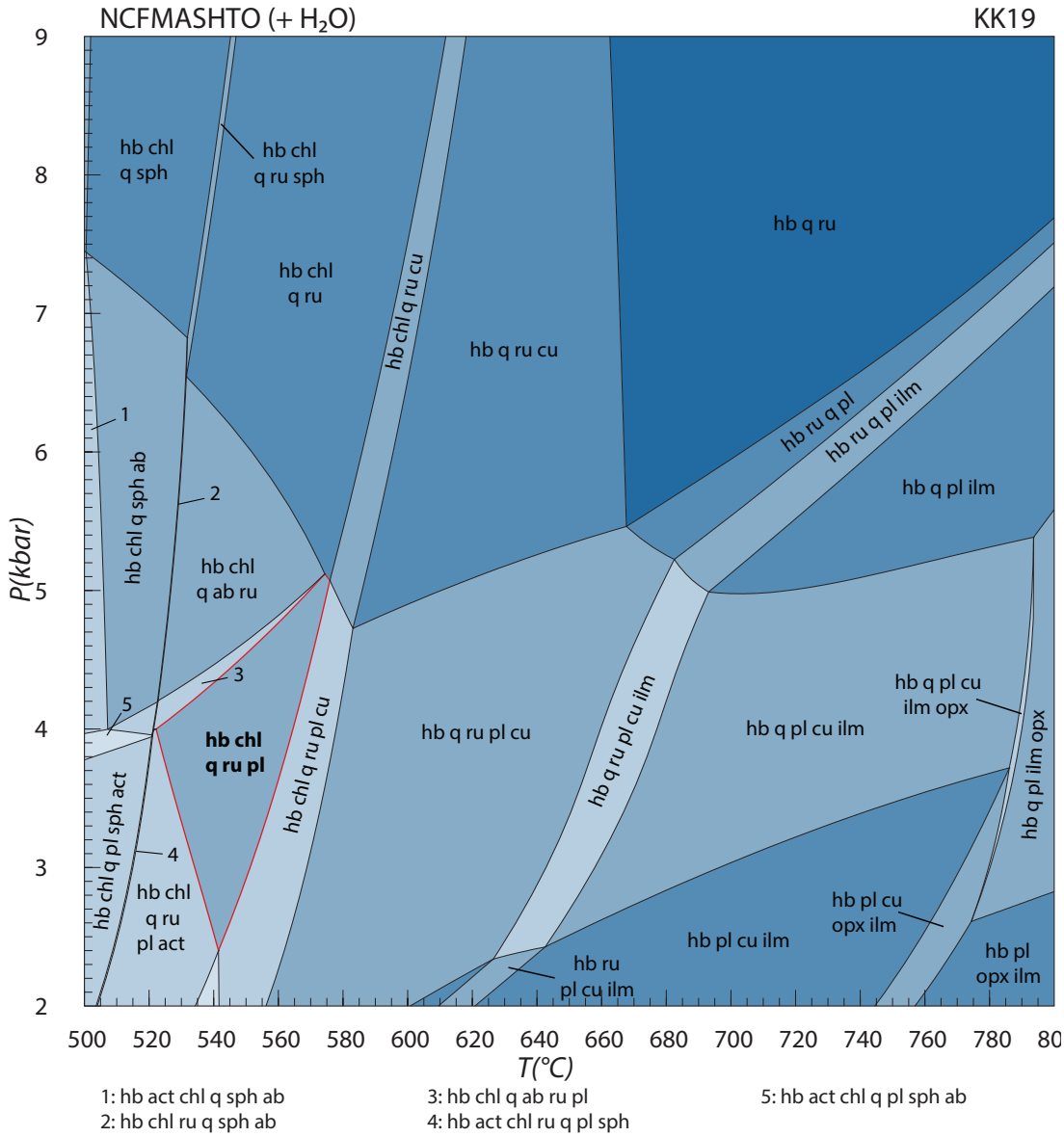

Figure 8.12: Pseudosection for Pella amphibolite sample KK19. P-T stability field of the inferred equilibrium assemblage (hb-ru-chl-q-pl; plus phases in excess) is outlined in red. Mineral and phase abbreviations as in Chapter 5.

Chapter 9

Monazite U-Pb dating

This chapter will present the methods and resuts of *in situ* U-Pb isotopic dating of monazite.

Seven samples (PM13007, PM13010, PM13032, PM13068, PM13084, PM13163 and PM13175) were selected for *in situ* U-Pb spot analysis of monazite grains using a laser ablation sector field inductively coupled mass spectrometer (LA-SF-ICP-MS). Of these – PM13007, PM13010, PM13032, PM13068 and PM13160 are all residual pelitic granulites which, with exception of PM13007, PM13160 and PM13175 were collected from the Kum Kum Klippe. Sample PM13007 was collected from the Keimasmund Complex, while PM13160 and PM13175 were both collected from the Sandfontein Klippe. Sample PM13084 is a mylonitised pelitic granulite from the Keimasmund Complex (all sample locations indicated on Figure 3.1).

Samples for LA-ICP-MS U-Pb analysis were prepared as polished thick sections (80 to 100 μm thick). Monazite grains analysed were located by petrographic microscope, followed by electron microprobe (EMP) analysis and back-scatter electron (BSE) imaging on an EMP housed at the University of Cape Town. All U-Pb isotopic analyses were carried out on *in situ* monazite grains.

9.1 Analytical Techniques

All U-Pb isotopic analyses for age determination were undertaken at the University of Stellenbosch Central Analytical Facility (CAF) using a Thermo Element II LA-SF-ICP-MS coupled to a Resonetics 193 nm Excimer laser with a tear-drop, low-volume ablation cell following the methods described by Gerdes & Zeh (2006) and Frei & Gerdes (2009). Isotope data were acquired with single spot analyses with a spot diameter of 9 μm and a crater depth of approximately 15–20 μm. The USGS 44069 monazite was used as the primary calibration material (Aleinikoff *et al.*, 2006); a detailed account of instrument settings is supplied in Appendix B.

Sample analyses were bracketed with analyses of the Thompson Mine monazite standard (1766 Ma; Couëslan *et al.*, 2013) and the Itambe monazite (c. 515 Ma Prabhakar, 2013) which

were both used as reference standard monazites in order to ensure accurate and precise data for a larger range of ages (Frei & Gerdes, 2009). The instrumental mass bias and ablation related fractionation of U and Pb isotopes were corrected using the results of bracketing standard analyses, by normalising against the reference standard monazites. Mass ^{202}Hg was measured to monitor the ^{204}Hg interference on ^{204}Pb (using a ^{202}Hg/^{204}Hg ratio of 4.36). Where necessary, common Pb corrections were carried out using the interference and background corrected ^{204}Pb signal in combination with the model Pb composition from Stacey & Kramers (1975).

U-Pb LA-ICP-MS ages of the standards obtained from this study (Appendix B) are in excellent agreement with the published ages of the standards (Couëslan *et al.*, 2013; Prabhakar, 2013). All errors on ratios and ages are reported at the 2σ confidence level. Detailed data processing and error propagation methods applied in this study are outlined in Gerdes & Zeh (2006) and Frei & Gerdes (2009). The calculation of concordia ages and plotting of concordia diagrams were performed using Isoplot/Ex 3.0 (Ludwig, 2003).

9.2 Results

A total of 86 U-Pb analyses were carried out on 56 monazite grains from the 7 samples. The number of U-Pb analyses per sample varies from 20 in sample PM13007 to 5 analyses in sample PM13032. Monazites grains analysed in each of the samples occur in the q-fsp-bi±cd±sill matrix, except in the case of PM13175 where monazite occurring as inclusions in garnet porphyroblasts was also analysed. The monazite grains analysed vary in size from approximately 25 to 130 μm and occur with various morphologies including rounded and subspherical, elongate and well-rounded to irregular grain shapes (Figure 9.2). A large proportion of the monazite analysed exhibits zoning in terms of BSE brightness, with a variety of patterns (Figure 9.2). For all analyses, the interiors of monazite grains were preferentially targeted and rims were avoided. All Concordant (98–102 % concordance) ^{206}Pb/^{238}U ages have been plotted on an age frequency distribution diagram (Figure 9.1); discordant analyses are excluded from the histogram since the the accuracy of ^{206}Pb/^{238}U ages is highly susceptible to Pb-loss (Schoene, 2014). ^{206}Pb/^{238}U ages are plotted in preference to ^{207}Pb/^{235}U and ^{207}Pb/^{206}Pb ages due to the generally higher level of precision in analytical results (Appendix B).

The ^{206}Pb/^{238}U ages obtained from concordant analyses in all samples occur over wide age range spanning between 985±28 Ma and 1886±51 Ma. There is a large hiatus separating Paleoproterozoic and Mesoproterozoic ^{206}Pb/^{238}U ages between 1262±37 Ma and 1821±49 Ma (Figure 9.1). Four main clusterings in the ^{206}Pb/^{238}U age data are distinguishable from the age frequency distribution histogram, these occur at 1886±51–1821±49 Ma, 1262±37–1184±33 Ma, 1091±30–1067±29 Ma and 1017±28–985±28 Ma (Figure 9.1). A summary of

U-Pb concordia age data for each sample is provided in Table 9.1 and all U-Pb isotopic data are presented in Appendix B. In the text below, all monazite grains analysed occur in the matrix unless otherwise stated. Each of these U-Pb age clusterings can be characterised as follows:

- The oldest clustering at 1886±51–1821±49 Ma is of relatively weak intesity and is defined by 10 U-Pb ages from PM13032 and PM13175;
- The second oldest clustering at 1262±37–1184±33 Ma is the most intense and is defined by 31 U-Pb ages from PM13010, PM13032, PM13064 and PM13084;
- The second youngest clustering at 1091±30–1067±29 Ma is of relatively high intesity and is defined by 20 U-Pb ages, all of which were analysed from PM13007 and;
- The youngest clustering at 1017±28–985±28 Ma is the smallest and least intense and is defined by 4 U-Pb ages from PM13160.

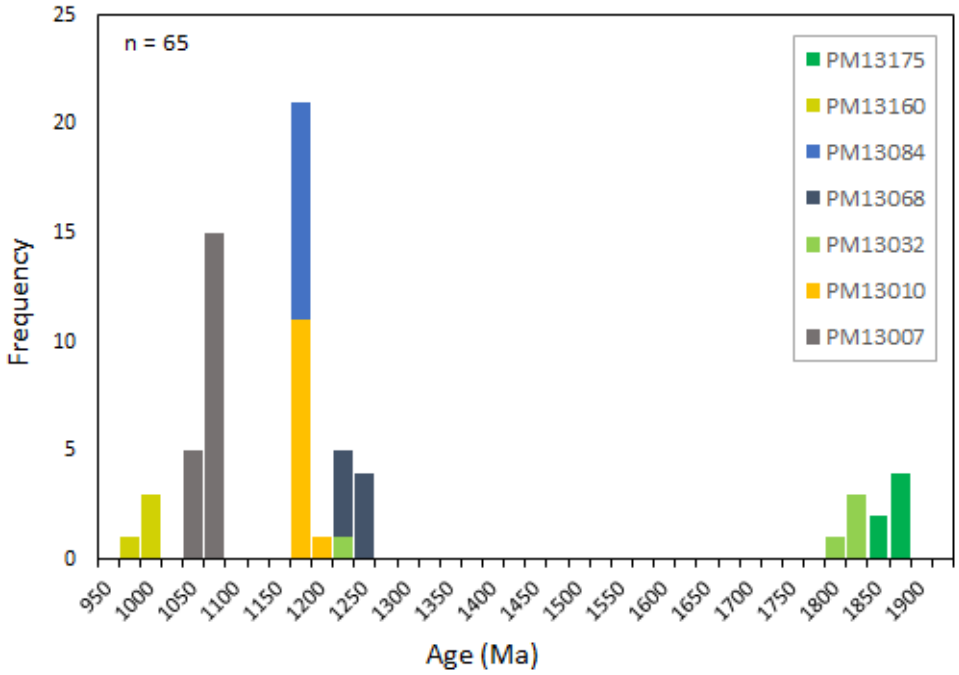

Figure 9.1: Frequency distribution histogram showing concordant $^{206}Pb/^{238}U$ ages from monazite U-Pb analyses in each of the samples. Based on 65 concordant analyses; bin range is 25 My.

Table 9.1: Summary of U-Pb concordia ages. [a]Mean square weighted deviation; [b]Probability of concordance.

			Concordia age or intercept (Ma)					
Sample	Calculation	No. of spots used	Upper	2σ	Lower	2σ	[a]MSWD	[b]Prob Conc.
Kum Kum Klippe								
PM13010	Concordia	9	1191	6	-	-	0.19	1
PM13010	Discordia	18	1191	9	-17	340	0.23	-
PM13032	Concordia	5	1829	10	-	-	0.22	0.98
PM13068	Concordia	8	1251	9	-	-	0.39	0.98
PM13068	Discordia	11	1256	17	334	450	0.25	-
Other Localities								
PM13007	Concordia	20	1082	4	-	-	0.29	1
PM13084	Concordia	10	1189	7	-	-	0.32	1
PM13163	Concordia	4	1013	10	-	-	0.13	0.99
PM13163	Discordia	9	1013	16	197	330	0.19	-
PM13175	Concordia	6	1880	9	-	-	0.31	0.98
PM13175	Discordia	13	1882	10	88	220	0.71	-

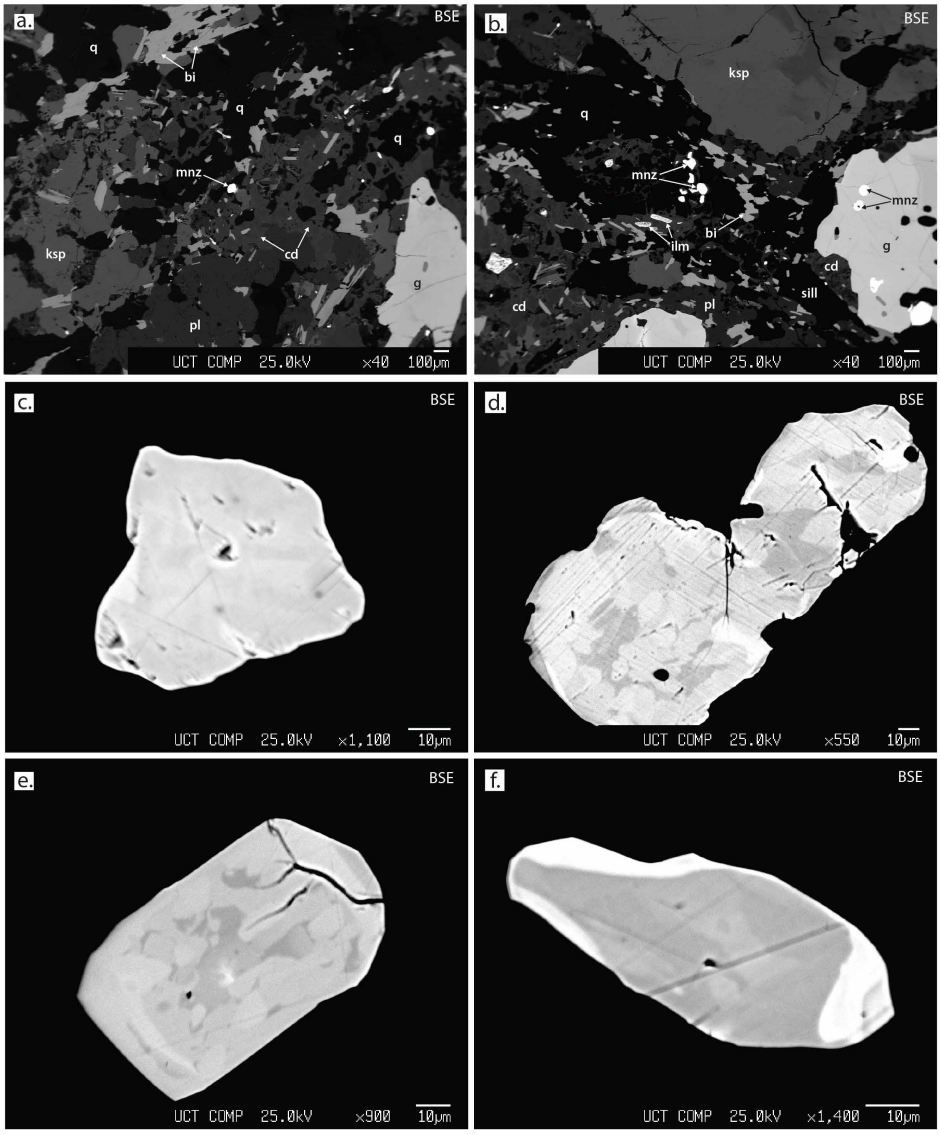

Figure 9.2: Representative back-scattered electron (BSE) images of textural setting (a, b) and physical characteristics (c, d, e, f) of monazite analysed; a) matrix monazite occurring in a qz-fsp-bi±cd±sill dominated matrix in metapelite sample PM13084; b) matrix and garnet-inclusion monazite in residual metapelite sample PM13175; c) relatively homogeneous monazite with irregular grain shape in PM13010; d) relatively large, elongate monazite exhibiting patchy zoning in PM13175; e) relatively large monazite exhibiting a rectangular shape and patchy zoning in PM13007; f) elongate monazite grain exhibiting distinct BSE-bright patches along the rim in PM13068.

9.2.1 Kum Kum Klippe

PM13010

Sample PM13010 is a (partially retrogressed) g-cd-sill-bi pelitic granulite. Monazite grains in this sample range in size from 30 to 70 μm. A total of 18 spots from 14 monazite grains were analysed, of which 9 yield concordant U-Pb ages which define a concordia age of 1191±6 Ma. The discordant analyses define a discordia with an upper interept concordia age of 1191±9 Ma (Figure 9.3 (a, b)).

PM13032

Sample PM13032 is a garnet-rich g-cd-sill-bi pelitic granulite. Monazite grains in this sample range in size between 40 and 80 μm in diameter. A total of 5 spots from three monazite grains were analysed for age calculation, and all yield concordant U-Pb ages which define a concordia age of 1829±10 Ma (Figure 9.3 (c)).

PM13068

Sample PM13068 is a relatively quartzofeldspathic g-cd-sill-bi pelitic granulite. Monazite grains analysed in this sample range in size between 50 and 100 μm in diameter. In total, 11 spots from 5 monazite grains were analysed of which 8 yield concordant U-Pb ages, defining a concordia age of 1251±9 Ma. The discordant analyses define a discordia with an upper intercept age of 1256±17 Ma (Figure 9.3 (d, e)).

9.2.2 Other localities

PM13007

Sample PM13007 is a garnet-rich g-cd-sill-bi pelitic granulite from the Keimasmund Complex. Monazite grains in this sample range in size from 40 to 120 μm in diameter. A total of 20 spots on 16 monazite grains were analysed for age calculation and all yield concordant U-Pb ages which define concordia age of 1082±4 Ma (Figure 9.4 (a)).

PM13084

Sample PM13084 is a gt-cd-sill-bi schist from the sheared basal sheet of the Keimasmund Complex. Monazite grains analysed in this sample include matrix monazite as well as a single monazite grain which occurs as an inclusion in garnet. The grain size of the monazite analysed ranges between 25 and 110 μm. In total, 10 spots from 5 monazite grains were analysed and all yield concordant U-Pb ages which define a concordia age of 1189±7 Ma (Figure 9.4 (b)).

PM13160

Sample PM13160 is a highly deformed residual pelitic graulite from the Sandfontein Klippe. Monazite grains analysed in this sample range in size from 40 to 120 μm in diameter. A total of 9 spots from the same number of monzite grains were analysed, 4 of these yield concordant U-Pb ages which define a concordia age of 1013±10 Ma. Discordant analyses define a discordia with an upper intercept age of 1013±16 Ma (Figure 9.4 (c, d)).

PM13175

Sample PM13175 is a g-cd-sill-bi pelitic granulite from the Sandfontein Klippe. Monazite grains in this sample range in size from 50 to 130 μm in diameter. In total, 13 spots from 9 monazite grains were analysed, 6 of these yield concordant U-Pb ages which define a concordia age of 1880±9 Ma. The discordant analyses define a discordia with an upper intercept age of 1882±10 Ma (Figure 9.4 (e, f)).

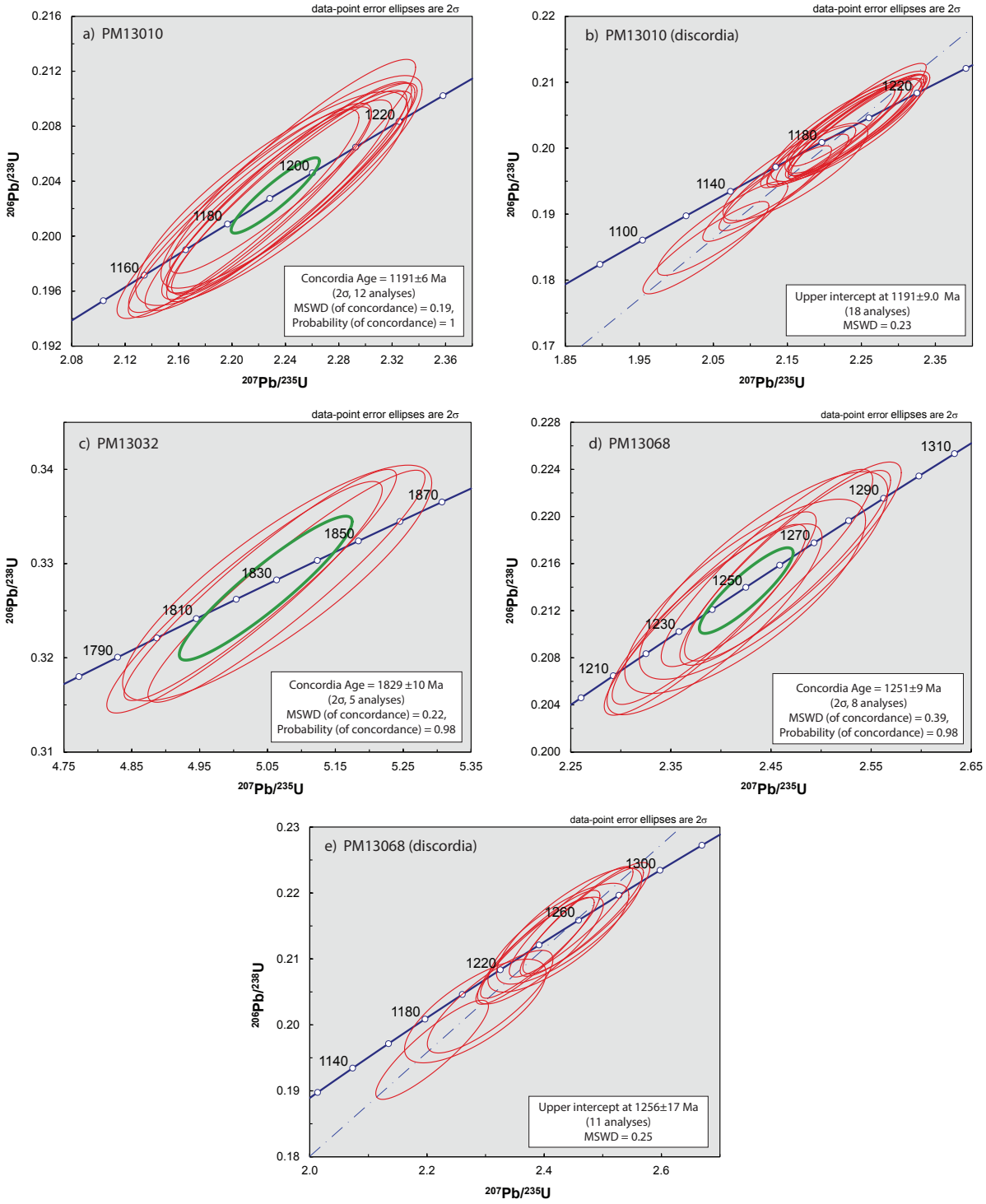

Figure 9.3: U-Pb concordia diagrams for pelitic granulites from the Kum Kum Klippe, with insets showing the corresponding age data. a) PM13010 – concordant analyses; b) PM13010 – discordia; c) PM13032; d) PM13068 – concordant analyses; e) PM13068 – discordia. Decay constant errors ignored for all diagrams; MSWD – Mean square weighted deviation.

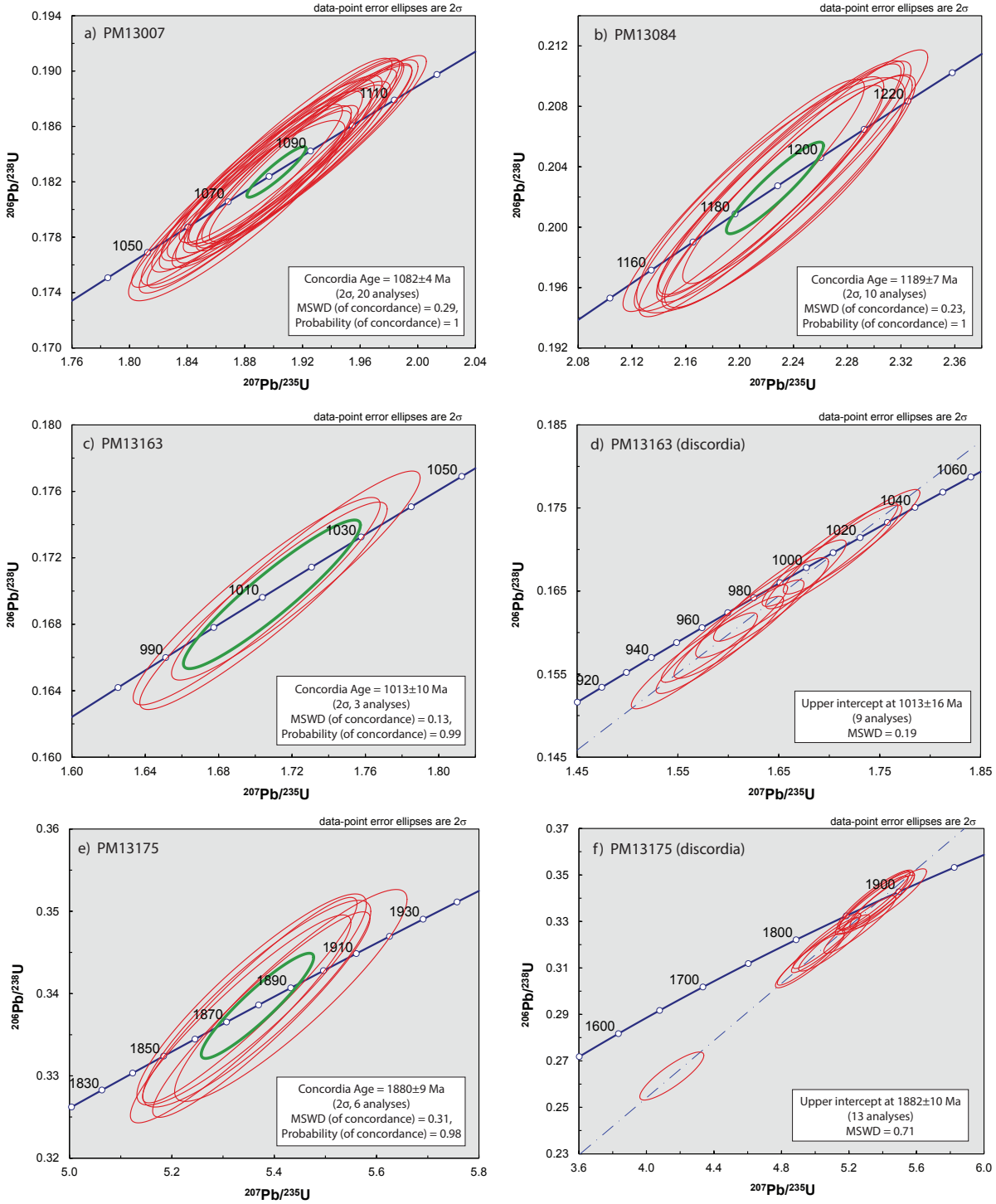

Figure 9.4: U-Pb concordia diagrams for pelitic granulites from the Keimasmund Complex and Sandfontein Klippe, with insets showing corresponding age data; a) PM13007; b) PM13084; c) PM13160 – concordant analyses; d) PM13163 – discordia; e) PM13175 – concordant analyses; f) PM13175 – discordant analyses. Decay constant errors ignored for all diagrams.

Chapter 10

Discussion

10.1 Interpretation of monazite U-Pb age data

As outlined in Section 9.2 there are four distinct clusterings in U-Pb ages (Figure 9.1) occurring at c. 1886–1821, 1262–1184, 1091–1067 and 1017–985 Ma, each of the clusterings are inferred to represent a distinct monazite population.

The Paleoproterozoic monazite age population at 1886–1821 Ma coincides well with the period of the Orange River Orogeny (ORO) at c. 1.7 to 2.0 Ga (Reid, 1979; Clifford *et al.*, 2004), this orogeny has been recognised as a major crust forming event (Clifford *et al.*, 2004). Thus it is viewed that these ages correspond to inherited monazites which grew as a result of ORO related tectonomagmatism, but were not destroyed by Namaquan tectonometamorphism. The occurrence of similar "Eburnian" ages has been well-documented elsewhere within the western NMC (Colliston & Schoch, 2006; Miller, 2008; Blignault *et al.*, 1983).

Although there are long periods where no monazite growth is recorded by the U-Pb ages within the range of the three youngest monazite age populations, the occurrence of these populations within a period which broadly overlaps with the Mesoproterozoic Namaqua Orogeny (c. 1.0–1.2 Ga; Thomas *et al.*, 1994) indicates that the events which triggered monazite growth are likely all related Namaqua Orogeny (NMO) tectonometamorphism. Thus, the three monazite populations at c. 1262–1184, 1091–1067 and 1017–985 Ma are referred to as Namaquan. Moreover, ages overlapping with the c. 1262–1184 and 1091–1067 Ma monazite populations are well-documented elsewhere in the western NMC (Diener *et al.*, 2013; Bial *et al.*, 2015a; Colliston *et al.*, 2015) and these ages are thus correlated to the Namaqua Orogeny *sensu stricto*.

As outlined in Chapter 9 the youngest monazite age population at c. 1017–985 Ma is defined by U-Pb ages exclusively from sample PM13160 which was sampled from the Sandfontein Klippe and is affected by a well-developed shear fabric. Macey *et al.* (2013) document the occurrence of pronounced reworking of the Sandfontein Klippe by late-Namaquan tran-

scurrent shearing (D_4) in the Pofadder Shear Zone (PSZ), dated at c. 1005–958 Ma by Lambert (2013). These ages overlap well with the youngest monazite population at c. 1017–985 Ma. This population is thus correlated to late-Namaquan (D_4) transcurrent shearing associated with shearing in the PSZ.

Due to the anatectic nature of the rocks, and the fact that monazites analysed occur almost exclusively in the matrix it is most likely that the c. 1262–1184 Ma and 1091–1067 Ma monazite populations grew in response to a tectonothermal event which resulted in partial melting and subsequent growth of monazite from the melt during cooling (e.g. Catlos *et al.*, 2002). Moreover, it is unlikely that any of the Namaquan monazite growth episodes are related to fluid infiltration as any post-peak, high temperature fluid involvement would have resulted in partial replacement of the peak metamorphic assemblage. This is not consistent with the observation that the pelitic granulites are generally constituted by a well-equilibrated assemblage which shows little evidence of retrogression (Chapter 5).

The Eburnian monazite population is defined exclusively by monazite U-Pb ages from samples PM13032 and PM13175. Since PM13032 and PM13175 were each collected from the Kum Kum and Sandfontein klippen respectively (which are geographically separated by >30 km), it is unlikely that the Eburnian ages are an isolated feature. However, while it appears that Eburnian ages may not be an isolated feature in the region of the study area, they are also not ubiquitous, this is exemplified by the occurrence of these ages in only 2 of the 7 samples where monazite U-Pb dating was undertaken. Conversely, the Namaquan U-Pb monazite ages are much more dominant and widespread in this portion of the Richetersveld–Gordonia Subprovince marginal zone as suggested by: a) the significantly higher proportion of Namaquan vs. Eburnian ages and; b) the occurrence of Namaquan ages in all but one of the samples (PM13175) collected from various locations along the marginal zone (Figure 3.1).

In general, the spread in U-Pb ages in Figure 9.1 correlates well with the concordia ages reported for each sample in Table 9.1. The general high level of concordancy in the analytical data suggests that the corcordia ages place reliable and robust constraints on the timing of the monazite growth events recorded by the monazite analyses in each sample. The occurrence of discordant analyses in PM13010, PM13068, PM13160 and PM13175 is interpreted to represent minor recent Pb loss, as suggested by the recent lower intercept ages (Table 9.1). The advantage of the concordia and discordia upper intercept ages is that they provide a higher level of precision, with the drawback that they do not easily allow for distinction of peaks in monazite growth or the identification of distinct monazite populations (which is in contrast to Figure 9.1).

In summary, the Namaquan ages at c. 1262–1184, 1091–1067 and 1017–985 Ma are correlated to distinct tectonometamorphic episodes within the broader Namaquan Orogeny

between c. 1262 and 985 Ma. The youngest of these at c. 1017–985 Ma is correlated to late-Namaquan transcurrent shearing (D_4) of the Sandfontein Klippe in the PSZ, while the populations at c. 1262–1184 and 1091–1067 Ma are ascribed to the Namaqua Orogeny *sensu stricto*. The Eburnian ages at c. 1885–1821 Ma are inferred to represent remnants of the Orange River Orogeny (ORO) – which on the basis of geochronological results appears to have been largely overprinted along the studied portion of marginal zone.

10.2 Constraints on the conditions and timing of peak metamorphism

Pelitic granulites of the Hangingwall Gordonia preserve a high grade metamorphic assemblage along with a high temperature regional deformation fabric and evidence of partial melting – this lithology is inferred to be representative of peak metamorphism (Chapter 5). Thus, the most likely peak metamorphic conditions are constrained by the area of best mutual overlap of the inferred (equilibrium) peak metamorphic fields for each of the hangingwall pelitic granulite pseudosections (Figure 10.1).

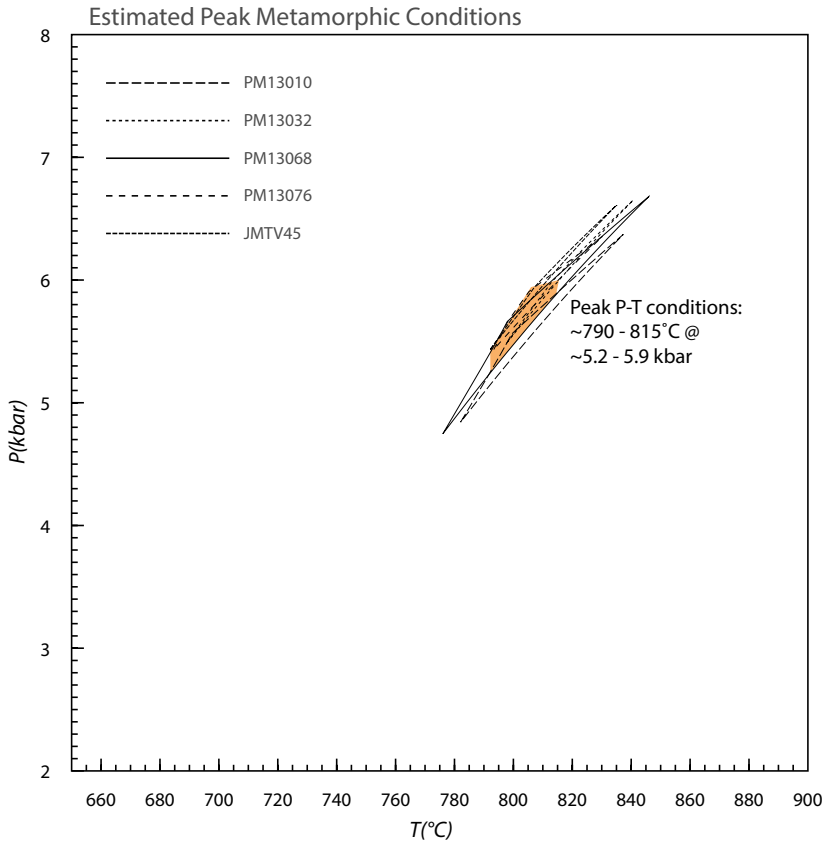

Figure 10.1: Estimated P-T range for peak metamorphic conditions, based on the overlap of inferred peak metamorphic fields for hangingwall pelitic granulite samples.

Although there is no single area of complete mutual overlap of inferred peak metamorphic fields (due largely to thier exceedingly narrow coverage in P-T space) all fields lie within a relatively small area in P-T space, providing tight constraints on the most likely peak P-T conditions to temperatures of 790–815°C and pressures of 5.2–5.9 kbar (Figure 10.1). These conditions correspond to a highly elevated apparent gethermal gradient of ∼41°C\km, which is significantly hotter than the stable continental geotherm (15–25°C\km). Assuming an average rock density of 2800 kg.m^{-3} the pressure constraints correspond to a depth of approximately 20 km.

These conditions are in good agreement with the observed evidence of partial melting, high temperature ductile deformations fabrics, lack of well-developed zoning in garnet and the residual nature of the rocks. Evidence of suprasolidus conditions is also provided by the occurrence of peritectic garnet which contains inclusions which are interpreted to represent the remnants of melt (Section 5.3). The fact that these textures are largely undisturbed in this lithology within the hangingwall, suggests that there was likely no significant post-peak temperature reworking of the peak assemblage due to subsequent deformation.

Considering that the Mesoproterozoic monazite populations at c. 1262–1184 Ma and 1091–1067 Ma have been shown to represent the timing of monazite crystallisation related to some suprasolidus event (Section 10.1) – it may be said with great certainty that at least two distinct and separate suprasolidus events were experienced within the period of the broader Namaqua Orogeny at the studied portion of the Richterveld-Gordonia Subprovince marginal zone – these are manifested as clusterings in monazite crystallisation ages. However, since the younger of the two suprasolidus monazite populations (at c. 1091–1067 Ma) is constituted by ages from only the Keimasmund Complex it follows that the suprasolidus event which resulted in the growth of this population did not result in remelting of pelitic granulites at what is now the Kum Kum Klippe. Had this been the case it would be expected that samples from the Kum Kum Klippe would yield some monazite ages falling within the c. 1091–1067 Ma age range – however, this is not observed.

If peak metamorphism at the Kum Kum Klippe is assumed to have occurred at c. 1262–1184 Ma, the effects of the inferred late thermal event at c. 1091–1067 Ma at the Kum Kum Klippe must have been experienced at lower grade (than the initial melting event), fluid absent conditions as well as in the absence of any significant shearing to prevent the development of any evidence of overprinting and/or reworking of hangingwall pelitic granulites of the Kum Kum Klippe.

This combined with the fact that all Mesoproterozoic ages derived from samples collected at the Kum Kum Klippe yield ages which fall within the c. 1262–1184 Ma monazite population indicates that this period provides the most likely constraints on the timing of peak metamorphism experienced at the Kum Kum Klippe.

10.3 Constraints on the conditions and timing of retrograde metamorphism and tectonic juxtaposition

The P-T conditions of retrograde metamorphism are represented by: a) the sheared pelitic granulites of the LFRTZ and; b) the amphibolites of the Footwall Pella domain. The sheared pelitic granulites of the LFRTZ were affected by the early stages of post-peak temperature shearing and the fabric developed in this lithology has been shown to be representative of shearing subsequent to peak P-T conditions (Section 5.3). The Footwall Pella amphibolites are relatively mildly affected by LFRTZ fabrics – the mineralogy and textures preserved in this lithology have been shown to be representative of the conditions of late stage shearing and tectonic juxtaposition of the Grunau Terrane against the Pella Terrane along the LFRTZ (Section 5.3).

The best estimates for the P-T conditions of early stage shearing are thus provided by overlapping the phase fields of the inferred equilibrium assemblages for each of the sheared pelitic granulite pseudosections (Figure 10.2). Similarly, the P-T estimates for the conditions of late stage shearing and tectonic juxtaposition of the Grunau Terrane against the Pella Terrane are provided by overlapping the phase fields of the inferred equilibrum assemblages for the Pella amphibolite pseudosections (Figure 10.3).

The P-T conditions for early stage retrograde shearing in the LFRTZ are constrained to temperatures of ∼640–785°C and pressures of 2.8–5.0 kbar. These conditions are consistent with the observed equilibrium assemblage and the nature of the ductile deformaton fabrics developed in this lithology. Moreover, this fabric truncates the peak P-T regional deformation fabric in the hangingwall pelitic granulites in places (Figure 3.8), indicating that the shearing occurred subsequent to peak P-T conditions.

Although the constrained P-T field extends to temperatures outside (to lower temperatures) of the window considered during pseudosection calculation – the field is truncated by the sillimanite-andalusite phase transition not far beyond the low temperature limit of the P-T window (Figure 10.2).

Inferred equilibrium assemblage fields for Pella amphibolites overlap over small a P-T area which places the conditions of late stage shearing and tectonic juxtaposition at ∼542 °C and ∼ 2.7 kbar. Calculated isopleths for X_{An} in plagioclase (measured at ∼0.42) and A-site sodium in hornblende (measured at ∼0.43) are in good agreement with the area of overlap and thus provide added confidence to these constraints. The P-T constraints of late stage shearing and juxtaposition correspond to mid-amphibolite facies conditions and are consistent with the observation that the Pella amphibolites show no evidence of anatexis. This suggests that the leucosome observed in the Pella Terrane was injected from an external source – this can be easily accounted for considering that the observed highyly elevated geothermal gradients

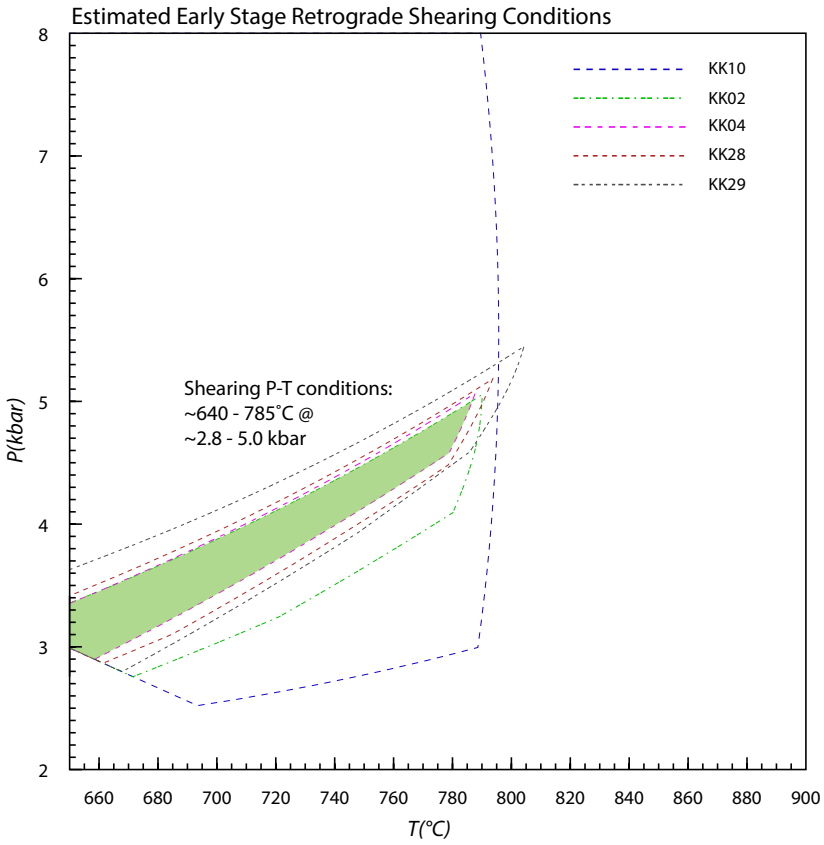

Figure 10.2: Estimated P-T conditions for early retrograde shearing, based on overlap of inferred equilibrium assemblage phase fields.

(Section 10.2) likely continued to produces melt in the middle crust at the time of shearing and the LFRTZ likely behaved as a conduit for the melt to be transported to shallower crustal levels (Brown & Solar, 1998).

Since none of the samples used for monazite U-Pb dating were sampled from within the LFRTZ, the timing of shearing in the LFRTZ can only be indirectly constrained by considering that a) suprasolidus (peak) P-T conditions in the Kum Kum Klippe have been placed at c. 1262–1184 Ma and; b) there is no evidence of any subsequent suprasolidus thermal event preserved in pelitic granulites of the Kum Kum Klippe. The implication of this is that shearing must have initiated after the c. 1262–1184 Ma period (i.e. at <1184 Ma) at subsolidus P-T conditions. Evidence of subsolidus shearing in the LFRTZ is indicated by the occurrence of mylonites (e.g. Figure 3.5) and the general lack of evidence of anatexis in sheared Pella amphibolites of the LFRTZ. This is consistent with the solid-state ductile deformation fabric preserved in sheared pelitic granulites as well as the mid-amphibolite facies peak conditions constrained for the Pella Terrane by the Pella amphibolites (Figure 10.3).

Similarly, there are no direct age constraints for the timing of tectonic juxtaposition. However, since juxtaposition of tectonic domains has been shown to have occurred at sub-

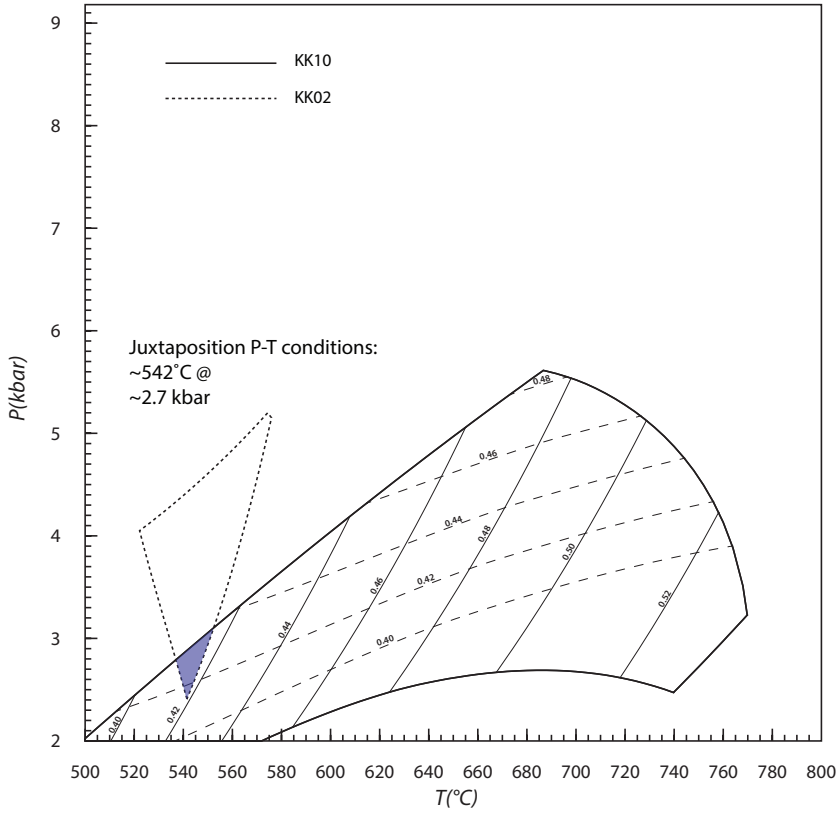

Figure 10.3: Estimated P-T conditions for late shearing and juxtaposition of the Grunau Terrane against the Pella Terrane along the LFRTZ.

solidus conditions, it is only possible to constrain the timing of this event to some period subsequent to the timing of (peak) suprasolidus conditions at c. <1184 Ma.

10.4 Constraints on the peak to retrograde P-T-t path

Using our constraints on the conditions and timing of peak and retrograde metamorphism, combined with key microtextural evidence – a peak to retrograde P-T-t path is constructed for the studied portion of the Richtersveld-Gordonia Subprovince marginal zone.

The peak assemblage stability fields for each of the pelitic granulite samples are bounded by the solidus to low temperatures and the biotite-out phase boundary to higher temperatures. Thus, preservation of the observed peak assemblage indicates that the solidus must have been crossed soon after cooling from peak conditions because further heating subsequent to the solidus being crossed would have resulted in the perservation of biotite absent assemblages (assuming post-peak hydrous retrogression was not an important process).

In both the hangingwall and sheared pelitic granulites, the widespread occurrence of peritectic garnet (g_1) being replaced by a cordierite corona (e.g. Figure 5.4), is consistent with

the initial segment of the retrograde P-T-t path, immediately following peak metamorphism being dominated by decompression. Similarly, the prominent occurrence of fabric defining sillimanite being rimmed by xenomorphic cordierite in some samples (e.g. Figure 5.2) is also consistent with an early stage of decompression immediately subsequent to the metamorphic peak. However, the presence of garnet in most sheared pelitic granulites samples, combined with the lack orthopyroxene all samples limits the extent to which post-peak decompression could have occurred to ∼3 kbar for peak metamorphic temperatures.

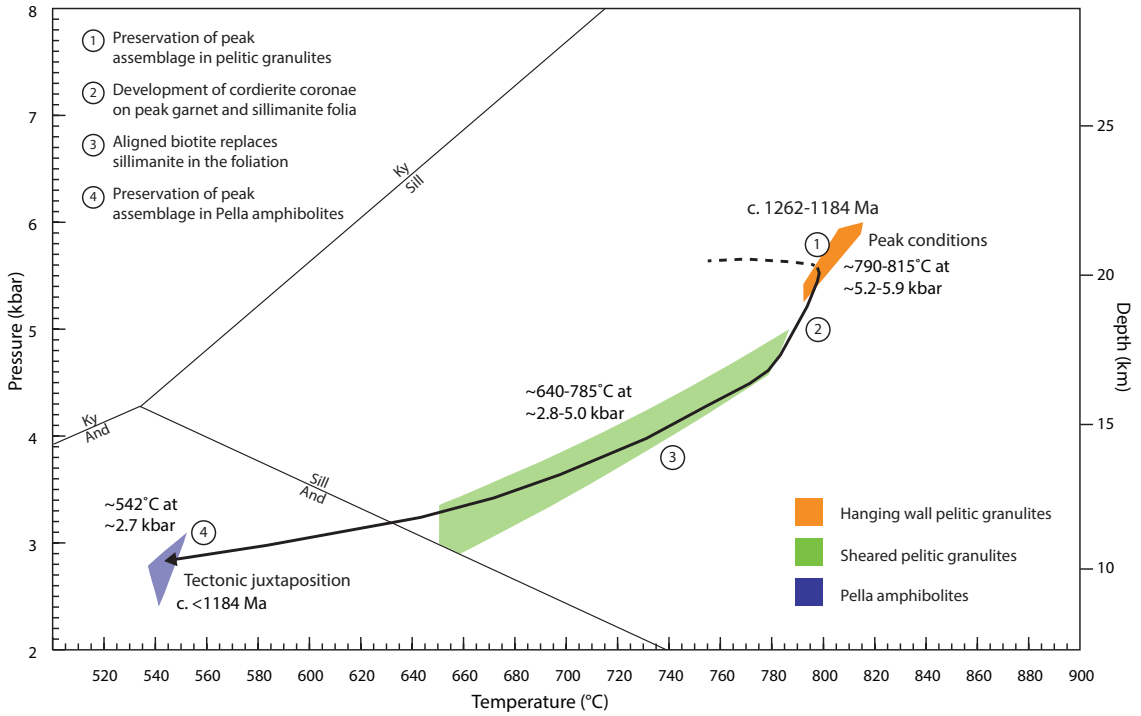

Figure 10.4: Inferred peak to retrograde P-T-t path for the Kum Kum Klippe. The P-T-t path documents the evolution of the Kum Kum Klippe from the thermal peak through to conditions of juxtaposition.

The resolved conditions of peak metamorphism, retrograde shearing and subsequent tectonic juxtaposition constrain a peak to retrograde P-T-t path characterised by a decrease in temperature (ΔT) of ∼265°C accompanied by a pressure decrease (ΔP) of ∼2.8 kbar (Figure 10.4). Assuming an average rock density of 2800 kg.m^{-3}, this corresponds to approximately 10 km of exhumation.

The occurrence of textures where aligned biotite mimetically overgrows fabric defining sillimanite in sheared pelitic granulites (Figure 5.3 (a, c)) is ascribed to post-peak P-T reworking of the fabric (Figure 10.4) and is consistent with a decrease in temperature during shearing (Brown, 2002, Section 5.3).

Textures of fibrolitic sillimanite beards rimming cordierite such as those observed in pelitic granulites of the current study (e.g. Figure 5.2 (b) and 5.4 (d)) have previously been correlated

to a cooling dominated retrograde segment (e.g. Boger & White, 2003; White *et al.*, 2004; Diener *et al.*, 2013, Section 5.3). Since the retrograde P-T trajectory implied by the shape of P-T field constrained for sheared pelitic granulites is characterised by both a decrease in pressure and temperature with a more dominant cooling component (Figure 10.4) – this becomes an attractive explanation to account for this texture. However, since this P-T field is both cordierite and sillimanite present, continuous evolution along this field to lower P-T conditions does not allow for the crossing of cordierite and sillimanite phase boundaries. Thus, to account for this texture in the framework of a cooling dominated retrograde segment it must be considered that cordierite and sillimanite modal isopleths were intersected at low angles along a cooling dominated path (with a small component of concurrent decompression) within a P-T field of their mutual stability. Such a scenario is consistent with fibrolitic sillimanite forming only thin films around cordierite (Figure 5.2 (b)), reflecting only a small change in equilibrium modal proportions of sillimanite and cordierite due to the low angle intersection of their isopleths along the retrograde P-T trajectory.

The occurrence of the fine grained, late textural variant of garnet (g_2) in some pelitic granulite samples (e.g. Figure 5.1 (a) and 5.2 (h)) may necessitate some transient increment of heating, possibly accompanied by a small increase in pressure at some point subsequent to peak metamorphism (e.g. Bial *et al.*, 2015a). It may be speculated that the heat required for this could have been provided by the thermal anomaly which resulted in melting at the nearby Keimasmund Complex at c. 1091–1067 Ma. This would imply that although the effects of the inferred localised thermal anomaly at the Keimasmund Complex did not result in remelting at the Kum Kum Klippe – the effects would have been sufficient enough to result in growth of a second generation of garnet. Should these assumptions be true, then the growth of g_2 can be placed at c. 1091–1067 Ma. Such transient heating (and possible pressure increase) would be superimposed on the overall cooling dominated retrograde P-T segment.

Shearing in the LFRTZ is assumed to have continued through the conditions of stability of the equibrium assemblage of sheared pelitic granulites until final juxtaposition at amphibolite facies conditions of ∼542°C and ∼2.7 kbar. The implication of this is that the sillimanite–andalusite phase transition must have been crossed at some point during shearing in the LFRTZ (Figure 10.4) and it thus would be expected that andalusite should have developed at the expense of sillimanite in sheared pelitic granulites. However, andalusite is not observed in any of the sheared pelitic granulite samples. This is not veiwed as a complication to the current peak to retrograde model, but is viewed rather as evidence that only the earliest stages of shearing were accomodated by pelitic granulites of the Kum Kum Klippe. Thus, in the latter stages of shearing at conditions leading up to tectonic juxtaposition – shearing is postulated to have been accomodated entirely within the Pella Terrane. This would have

precluded any low temperature textural reworking of sheared pelitic granulites which would have otherwise aided the replacement of sillimanite by andalusite to reflect the equilibrium assemblage at those conditions. Thus once shearing of the pelitic granulites had ceased at conditions up temperature of the sillimanite–andalusite transition, their assemblage was effectively frozen in – even though late stage shearing continued in Pella Terrane lithologies prior to final juxtaposition.

The partitioning of strain into the Pella Terrane subsequent to the earliest stages of shearing can be accounted for considering that at conditions leading up to the juxtaposition of tectonic domains, the pelitic granulites of the Grunau Terrane had already lost significant amounts of melt at peak conditions and would have thus been highly refractory and strong due to the loss of most of their intrinsically weak hydrous mineral content (i.e. biotite) during melting reactions. Moreover, although the Grunua Terrane was at higher temperature (and thus might be considered to have been weaker as dictated by power law rheology; Sibson, 1983), the abundant occurrence of injected leucosome (Chapter 5) in the Pella Terrane means that the strength of the Pella Terrane during late stage shearing would have been largely controlled by that of its weakest containing phase i.e. melt (Handy *et al.*, 2001). The association of shear bands with high leucosome content zones in the Footwall Pella domain, provides good evidence that the leucosome was present (as melt) at the time of shearing and likely promoted weakening. These factors would have contributed to the Pella lithologies being significantly weaker than the warmer, residual Grunau Terrane lithologies at the time subsequent to the earliest stages of shearing, this resulted in shear strain being localised into the Pella Terrane at this time.

In summary, the constrained peak to retrograde P-T-t path is characterised by a short segment of substantial decompression subsequent to peak metamorphic conditions at c. 1262–1184 Ma. This is followed by a period dominated by cooling with only a moderate component of decompression, which together with the early decompressive segment likely correspond to the period of retrograde shearing. Shearing along the cooling dominated segment led to final tectonic juxtaposition in the mid-amphibolite facies at c. <1184 Ma (Figure 10.4).

10.5 Summary of P-T-t path and comparison with previous works

The peak metamorphic P-T conditions resolved in this study are broadly similar to most of those previously deduced elsewhere in the western NMC (e.g. Waters, 1989; Raith & Harley, 1998; Robb *et al.*, 1999; Diener *et al.*, 2013). A notable exception is Bial *et al.* (2015a) where ultra-high temperature (UHT) conditions of 900°C at 5 kbar are constrained for the highest grade zone in their study area.

The P-T-t path resolved in this study involves substantial decompression immediately following peak conditions and to a lesser extent in the subsequent cooling dominated retrograde segment of the P-T path. Although this magnitude of exhumation (∼2.8 kbar) is unique in recent literature, Cornell *et al.* (1992) record substantial decompression (up to 5 kbar) in a characteristic, clockwise, collisional P-T loop at the Prieska region, along the eastern margin of the NMC near its boundary with the Kaapvaal Craton. In the South African extent of the Grunau Terrane, near the terrane bounding Onseepkans Thrust (i.e. the southeastern extent of the LFRTZ in South Africa), Bial *et al.* (2015a) invoke up to 1 kbar of near isothermal decompression in parts of their study area – although the P-T path they deduce for the highest grade areas is isobaric (Figure 1.4).

Importantly, with exception of Bial *et al.* (2015a), all P-T paths which invoke purely isobaric post-peak cooling correspond to areas towards the interior of the Bushmanland Terrane (Waters, 1989; Raith & Harley, 1998; Robb *et al.*, 1999; Diener, 2014) and Aus Terrane (Diener *et al.*, 2013), away from any major tectonic features which are capable of resulting in any significant uplift during compressional tectonics (e.g. major regional thrust or any structural ramp). Regional mapping by Blignault *et al.* (1983) along a north–south transect across the terranes of the western NMC reveals that the LFRTZ, in terms of thrust geometry, is constituted by a major ramp structure at the frontal zone of the Grunau Terrane, accompanied by an extensive 'flat' further north in the interior of the Grunau Terrane (Figure 1.3). Thus, it would be expected that during Namaquan shearing, horizonal motion along the basal surface of the LFRTZ would have resulted in appreciable uplift of the Grunau Terrane sheet along the ramp structure at the frontal zone, while the interior of the terrane would not have experienced any uplift. This model accounts for the apparent discrepency in the degree of exhumation inferred in this study compared to the widely accepted norm of post-peak isobaric cooling in the western NMC. Uplift along the LFRTZ ramp at the frontal zone of the Grunau Terrane immediately following peak Namaquan metamorphism is evidenced in the petrographic record by the occurrence of decompression textures of cordierite replacing garnet and sillimanite folia (e.g. Figure 5.2 and 5.4).

In the case of the Prieska region, the pronounced decompression modelled by Cornell *et al.* (1992) is consistent with the collisional model they adopt for that region where different tectonic processes (e.g. vertical extrusion) may well have been at play during Namaquan tectonogenesis due to the immediately adjacent Kaapvaal Craton.

In situ U-Pb analyses on monazite cores in this study yield three distinct Mesoproterozoic monazite age populations (at c. 1262–1184, 1091–1067, 1017–985 Ma) of which the oldest at c. 1262–1184 Ma is interpreted to represent the timing of peak metamorphism (Section 10.1). These constraints are in good agreement with dates obtained by earlier workers for parts of the Bushmanland Subprovince (Raith & Harley, 1998; Clifford *et al.*, 2004) and the

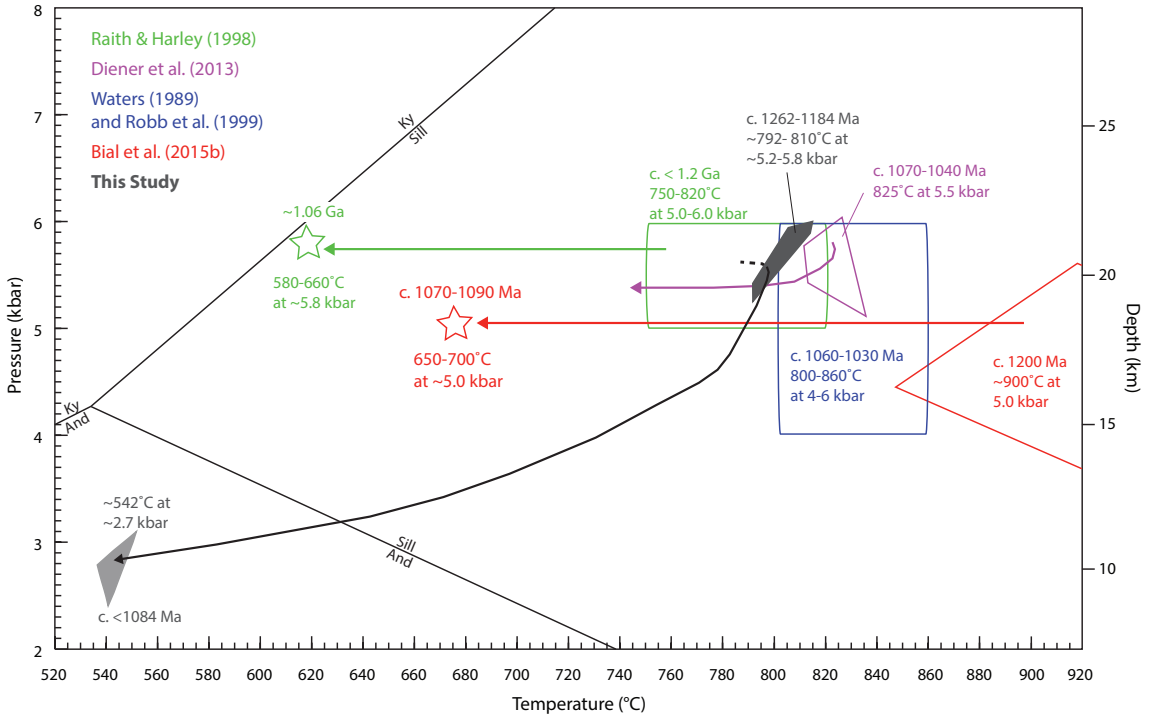

Figure 10.5: Metamorphic P-T conditions and retrograde P-T paths in the western NMC constrained by previous workers plotted with P-T conditions and retrograde P-T path constrained in the current study. Arrows indicate early retrograde trajectories deduced in the respective studies. The timing of P-T constraints are indicated as per the relevant studies.

Gruanau Terrane (Bial *et al.*, 2015a). These workers place the timing of peak metamorphism at c. <1.2 Ga (Raith & Harley, 1998), c. 1180–1200 Ma (Clifford *et al.*, 2004) and c. 1200 Ma (Bial *et al.*, 2015a). Nonetheless, peak metamorphism has been dated at younger ages in the Aus Terrane of Namibia (c. 1070-1040 Ma; Diener *et al.*, 2013) and the Okiep Copper District of the Bushmanland Subprovince (1060-1030 Ma; Waters, 1989; Robb *et al.*, 1999).

Taking into consideration the reported errors on U-Pb ages (Section 9.2), the constraints on the timing of peak metamorphism at the Kum Kum Klippe presented in this study show some overlap with the Okiepian (∼1190±30 Ma) tectonothermal event while the second youngest monazite population shows limited overlap with the Klondikean (∼1040±30 Ma) tectonothermal event. Thus it could be argued that an attractive interpretation would be to correlate these two populations to the Okiepian and Klondikean respectively – however, the relatively poor overlap renders a large portion of the ages constituting the c. 1262–1184 Ma population unaccounted for (by the Okiepian), while the majority of the c. 1091–1067 Ma population is also unaccounted for (by the Klondikean). Elsewhere in the Grunau Terrane, ∼80 km southeast of the current study area Bial *et al.* (2015a) record three major thermal events at ∼1299–1351, ∼1200 and ∼1100 Ma – which they attribute to Namaqua tectonogenesis. Bial *et al.* (2015a) suggest that the apparent capricous spread of Mesopro-

terozoic ages in the western NMC is not consistent with the presence of two discrete regional tectonothermal events, but is more compatible with a prolonged period of highly elevated crustal temperatures during Namaquan times, suitable of producing magmatic and metamorphic zircon. Thus, rather than forcefully correlating our monazite populations to the Okiepian and Klondikean under unconvincing circumstances and given the assortment of ages available in literature, it may be more appropriate to view the thermal history of the western NMC as episodic with heat flow being spatially heterogeneous as implied by Bial *et al.* (2015a). Such a scenario would not only account for the Namaquan ages presenetd in this study, but would also account for the assortment of Namaquan ages in the western NMC available in literature to date.

In summary, the P-T-t path presented in this study records the time intergrated retrograde P-T evolution of the Kum Kum Klippe from peak conditions through to the conditions of juxtaposition of the Grunau Terrane against the Pella Terrane in Mesoproterozoic times. The appreciable levels of decompression recorded in the current P-T-t path have not been observed elsewhere in the interior of the western NMC. Such decompression is consistent with a 'ramp-flat' geomtery of the LFRTZ (Blignault *et al.*, 1983), where the frontal zone would be subject to appreciable uplift during horizontal tectonics, while no uplift would be expected at the interior of terranes. As with Bial *et al.* (2015a), the timing of tectonothermal events recorded in this study cannot be convincingly reconciled with the Okiepian and Klondikean tectonothermal events. Thus, in agreement with Bial *et al.* (2015a) it is suggested that the timing of thermal events within the broader Namaqua Orogeny in the western NMC could be more episodic and less regular than suggested by Clifford *et al.* (2004) and Eglington (2006).

10.6 Implications for the geodynamic significance of the LFRTZ

The P-T-t path constrained in the current study reflects the thrusting of a hot crustal block (Hangingwall Gordonia) from depth, on to a shallower crustal entity (Footwall Pella) along the LFRTZ (Figure 10.4). If the collisional model invoked in the traditional literature were correct (Miller, 2012), the LFRTZ would represent a terrane boundary along which continental fragments have collided and would thus represent a suture zone (Dewey, 1977). By definition, suture zones are high strain fault zones that likely penetrate the lithosphere and should contain the remnants of oceanic crust and upper mantle (i.e. ophiolites) or blueschist melanges or other trench related deposits (Dewey, 1977). The P-T paths preserved by rocks exposed at suture zones should show retrograde P-T trajectories charaterised by rapid, near isothermal decompression (ITD), reflecting rapid exhumation largely driven by isostatic readjustment and post-orogenic collapse (Dewey *et al.*, 1993; Ernst, 1988). Furthermore, rocks affected by collisional orgenesis should preserve HP-LT metamorphic signatures reflecting the cold geotherms typically associated with subduction zones (Ernst, 1988; Brown, 2008; Ernst,

2010).

However, the studied portion of the Richtersveld-Gordonia Subprovince marginal zone shows none of these characteristics. Peak metamorphic conditions recorded by peltic granulites reflect highly elevated geothermal gradients (∼41°C/kbar) which cannot be easily reconciled with subduction to collision orogenesis. Moreover, the cooling dominated retrograde P-T trajectory (Figure 10.4) determined for the study site is not compatible with the rapid exhumation (often accompanied by heating) expected for subduction to collision orogenesis retrograde trajectories. Lastly, no HP-LT parageneses such as blueschists and eclogites have been noted in this, or any previous studies of the western NMC.

Consequently, the P-T evidence presented suggests that the LFRTZ is not a terrane bounadry that juxtasposes crustal entities which converged and collided as the result of Wilson cycle subduction to collision tectonics (i.e. a suture zone) as the traditional literature suggests (Miller, 2012; Becker *et al.*, 2006). By contrast, the scenrio proposed by Bial *et al.* (2015a, 2016) where the major regional thrusts in the western NMC are suggested to represent internal structures within coherent entities, formed in the contractional episode of a continental backarc setting is more consistent with the P-T path presented (Figure 10.4). Such a tectonic setting is also consistent with the highly elevated geothermal gradients and LP-HT peak metamorphic conditions determined (Section 10.2).

Thus, results presented in this study contradict the collisional model and terrane concept which has been advocated for the western NMC in the traditional literature.

Chapter 11

Conclusions

The current study comes to the following conclusions with respect to the tectonometamorphic evolution of the marginal zone between the Richterveld and Gordonia Subprovinces in the region of the Kum Kum Klippe:

1. Peak metamorphic conditions at the frontal zone of the Grunau Terrane are constrained at granulite facies conditions of 5.2–5.9 kbar and 790–815°C at 1262–1184 Ma

2. The P-T-t path deduced for the study area indicates that the Grunau Terrane experienced a decompression dominated retrograde segment immediately following peak metamorphism. This was followed by a cooling dominated segment with a relatively small component of concomitant decompression leading up to the P-T conditions of tectonic juxtaposition at mid-amphibolite facies conditions of ∼2.7 kbar and 542°C. The entire post-peak P-T-t path is correlated to retrograde shearing in the LFRTZ, which led to tectonic juxtaposition at <1184 Ma subsequent to suprasolidus conditions;

3. The extent of post-peak P-T decompression determined in the current study has not been reported elsewhere in the interior of the western NMC, with all previous authors implicating isobaric or near isobaric cooling in the early retrograde evolution (Waters, 1989; Raith & Harley, 1998; Diener *et al.*, 2013; Bial *et al.*, 2015a). The apparent discrepancy between the current study and P-T paths deduced by previous authors towards the interior of the Bushmanland and Aus Terranes reflects the 'ramp-flat' geometry of the LFRTZ (Blignault *et al.*, 1983) where the frontal zone of the Grunau Terrane represent a northeasterly dipping ramp while towards the interior of the Grunau Terrane, to the northeast, the LFRTZ represent an extensive subhorzontal 'flat' (Figure 1.3; Blignault *et al.*, 1983). Top-to-SW directed shearing along the basal plane of the LFRTZ resulted in appreciable uplift of the Grunau Terrane at frontal zone while the interior of the tectonic domain experienced no uplift since it overlies an extensive flat. Post-peak P-T decompression is reflected by the widespread development of cordierite

coronae around peritectic garnet porphyroblasts. The P-T-t path resolved in the current study thus reflects cooling which occurred concomitantly with uplift related to SW directed thrusting at the frontal zone of the Grunua Terrane which resulted in tectonic juxtaposition;

4. The P-T path determined for the studied portion of the Richtersveld-Gordonia Subprovince marginal zone is not consistent with a suture zone as would be expected with the collisional model that has been advocated for the western NMC in the traditional literature. Conversely, the P-T path is more compatible with thrusting during a contractional episode in a continetal backarc setting as suggested by Bial *et al.* (2015a, 2016).

The findings presented in this study provide new insight on the nature and timing of the tectonometamorphic events which led to the juxtaposition of the Richtersveld and Gordonia Subprovinces along the LFRTZ. Insight is also gained on the geodynamic significance of the LFRTZ.

11.1 Future work

The western NMC has continued to receive attention from metamorphic and structural geologists over the decades, however, there are still some key and fundamental points of disagreement regarding: i) the timing of specific tectonometamorphic events and; ii) the geodynamic setting that resulted in the current configuration of tectonic domains.

In addressing the first point it will be of primary importance to attain more comprehensive coverage of high quality (preferrably *in situ*) age constraints that directly constrain the date of metamorphism and tectonism. In doing so we will be able to establish whether the western NMC was indeed subject two discrete tectonothermal episodes (as early models suggest, e.g. Eglington, 2006) or whether the thermal history of the western NMC was more episodic (as new evidence seems to suggest, e.g. Bial *et al.*, 2015a).

Developing a coherent geodynamic model for the western NMC will be largely dependent on our understanding of the metamorphic signature and P-T-t path of the processes which led to the juxtaposition of tectonic domains. While the current study addresses this issue at a small portion of the Richtersveld-Gordonia Subprovince marginal zone – more work will be required to establish whether the findings presented in this study are regionally applicable.

Appendix A

Mineral Chemistry

Table A.1: Electron microprobe results for garnet.

	PM13010 gt1_int	PM13010 gt1_rim	PM13010 gt2_int	PM13010 gt2_rim	PM13010 gt3_int	PM13010 gt3_rim	PM13032 gt4_core	PM13032 gt4_rim	PM13032 gt5_core	PM13032 gt5_rim	PM13032 gt6_core	PM13032 gt6_rim	PM13032 gt7_core	PM13032 gt7_rim	PM13032 gt8_core	PM13032 gt8_rim	PM13032 gt9
SiO_2	37.53	37.47	37.41	37.31	37.01	37.50	37.95	36.99	37.28	37.34	37.45	36.81	38.05	37.78	37.74	37.56	37.89
TiO_2	0.04	0.03	0.00	0.00	0.00	0.00	0.00	0.00	0.02	0.00	0.00	0.05	0.01	0.02	0.02	0.00	0.00
Al_2O_3	22.22	22.53	22.00	22.20	22.14	22.43	22.72	22.71	22.93	22.58	22.39	22.29	22.43	22.03	22.15	22.47	22.27
Cr_2O_3	0.01	0.01	0.01	0.03	0.01	0.00	0.00	0.07	0.04	0.05	0.04	0.03	0.05	0.00	0.06	0.06	0.03
FeO	26.89	27.28	27.14	27.46	26.60	26.43	30.36	32.63	30.78	31.40	32.44	33.69	31.56	33.21	31.61	32.09	30.25
MnO	8.18	8.32	8.12	8.31	8.94	8.54	0.92	0.95	0.92	1.03	1.06	1.12	0.95	0.89	1.00	1.01	0.93
MgO	4.57	4.42	4.44	4.25	4.51	4.52	7.05	5.55	6.72	6.09	5.40	4.39	6.03	5.05	6.09	5.59	7.03
CaO	1.17	1.11	1.22	1.07	0.95	1.15	1.28	1.44	1.26	1.36	1.30	1.35	1.37	1.37	1.27	1.40	1.30
Na_2O	0.03	0.00	0.02	0.04	0.03	0.03	0.01	0.04	0.04	0.03	0.02	0.10	0.13	0.03	0.04	0.10	0.04
K_2O	0.00	0.00	0.00	0.00	0.00	0.00	0.00	0.00	0.00	0.00	0.00	0.00	0.00	0.00	0.00	0.00	0.00
Total	100.64	101.17	100.37	100.67	100.19	100.61	100.30	100.37	99.99	99.89	100.10	99.83	100.58	100.39	99.98	100.28	99.74
Oxygens	12	12	12	12	12	12	12	12	12	12	12	12	12	12	12	12	12
Si	2.96	2.95	2.97	2.96	2.95	2.96	2.95	2.92	2.92	2.94	2.96	2.94	2.97	2.98	2.97	2.95	2.97
Ti	0.00	0.00	0.00	0.00	0.00	0.00	0.00	0.00	0.00	0.00	0.00	0.00	0.00	0.00	0.00	0.00	0.00
Al	2.07	2.09	2.06	2.07	2.08	2.09	2.09	2.11	2.12	2.10	2.08	2.10	2.07	2.05	2.05	2.08	2.06
Cr	0.00	0.00	0.00	0.00	0.00	0.00	0.00	0.00	0.00	0.00	0.00	0.00	0.00	0.00	0.00	0.00	0.00
Fe	1.78	1.80	1.80	1.82	1.77	1.74	1.98	2.15	2.02	2.07	2.14	2.25	2.06	2.19	2.08	2.11	1.98
Mn	0.55	0.55	0.55	0.56	0.60	0.57	0.06	0.06	0.06	0.07	0.07	0.08	0.06	0.06	0.07	0.07	0.06
Mg	0.54	0.52	0.52	0.50	0.53	0.53	0.82	0.65	0.78	0.71	0.64	0.52	0.70	0.59	0.71	0.66	0.82
Ca	0.10	0.09	0.10	0.09	0.08	0.10	0.11	0.12	0.11	0.11	0.11	0.12	0.11	0.12	0.11	0.12	0.11
Na	0.00	0.00	0.00	0.01	0.00	0.01	0.00	0.01	0.01	0.00	0.00	0.02	0.02	0.01	0.01	0.02	0.01
K	0.00	0.00	0.00	0.00	0.00	0.00	0.00	0.00	0.00	0.00	0.00	0.00	0.00	0.00	0.00	0.00	0.00
Total	8.00	8.00	8.00	8.01	8.02	8.00	8.00	8.03	8.02	8.01	8.00	8.02	8.00	8.00	8.00	8.01	8.01

Table A.2: Electron microprobe results for garnet – continued.

	PM13032 gt10_int	PM13032 gt11_rim	PM13068 gt11_int	PM13068 gt12_rim	PM13068 gt12_int	PM13068 gt12_rim	PM13068 gt13_int	PM13068 gt13_rim	JMTV45 gt16_int	JMTV45 gt16_rim	JMTV45 gt17_int	JMTV45 gt17_rim	JMTV45 gt20_int	JMTV45 gt20_rim	JMTV45 gt21(b)_int	JMTV45 gt21(b)_rim	JMTV45 gt23(b)_int
SiO_2	37.91	37.69	37.54	37.55	38.11	37.99	37.70	37.99	37.33	37.65	37.44	37.53	37.77	37.75	37.97	37.11	37.45
TiO_2	0.03	0.02	0.06	0.12	0.01	0.00	0.06	0.06	0.00	0.03	0.04	0.01	0.00	0.04	0.05	0.02	0.03
Al_2O_3	22.53	22.09	21.95	21.40	21.90	21.86	21.87	21.92	21.75	21.72	21.64	21.88	21.89	21.88	21.83	21.83	21.57
Cr_2O_3	0.00	0.00	0.00	0.01	0.00	0.02	0.01	0.02	0.08	0.03	0.07	0.00	0.07	0.02	0.00	0.01	0.00
FeO	31.29	30.91	30.91	30.22	30.19	30.33	30.82	29.83	33.11	32.85	32.92	33.31	32.54	32.81	33.79	35.22	34.38
MnO	0.96	0.96	3.52	3.35	2.91	3.00	3.14	2.96	0.74	0.62	0.69	0.71	0.85	0.78	0.63	0.68	0.56
MgO	6.40	6.36	5.80	5.68	7.03	6.62	6.71	6.34	6.17	6.31	5.96	6.26	6.26	6.23	5.69	4.89	5.79
CaO	1.43	1.41	1.00	1.22	0.66	0.73	0.66	1.07	1.06	1.00	1.04	1.03	1.01	1.06	0.93	0.94	0.98
Na_2O	0.01	0.00	0.06	0.04	0.00	0.01	0.04	0.00	0.00	0.00	0.02	0.01	0.03	0.03	0.02	0.00	0.00
K_2O	0.00	0.00	0.00	0.00	0.00	0.00	0.00	0.00	0.00	0.00	0.00	0.00	0.00	0.00	0.00	0.00	0.00
Total	100.56	99.45	100.84	99.60	100.81	100.56	101.02	100.18	100.24	100.22	99.81	100.74	100.41	100.60	100.91	100.69	100.75
Oxygens	12	12	12	12	12	12	12	12	12	12	12	12	12	12	12	12	12
Si	2.96	2.97	2.95	2.98	2.97	2.98	2.95	2.98	2.95	2.97	2.97	2.95	2.97	2.96	2.98	2.95	2.96
Ti	0.00	0.00	0.00	0.01	0.00	0.00	0.00	0.00	0.00	0.00	0.00	0.00	0.00	0.00	0.00	0.00	0.00
Al	2.07	2.05	2.04	2.00	2.01	2.02	2.02	2.03	2.03	2.02	2.02	2.03	2.03	2.03	2.02	2.04	2.01
Cr	0.00	0.00	0.00	0.00	0.00	0.00	0.00	0.00	0.00	0.00	0.00	0.00	0.00	0.00	0.00	0.00	0.00
Fe	2.04	2.04	2.03	2.01	1.97	1.99	2.02	1.96	2.19	2.17	2.18	2.19	2.14	2.15	2.22	2.34	2.27
Mn	0.06	0.06	0.23	0.23	0.19	0.20	0.21	0.20	0.05	0.04	0.05	0.05	0.06	0.05	0.04	0.05	0.04
Mg	0.74	0.75	0.68	0.67	0.82	0.77	0.78	0.74	0.73	0.74	0.70	0.73	0.73	0.73	0.67	0.58	0.68
Ca	0.12	0.12	0.08	0.10	0.06	0.06	0.06	0.09	0.09	0.08	0.09	0.09	0.08	0.09	0.08	0.08	0.08
Na	0.00	0.00	0.01	0.01	0.00	0.00	0.01	0.00	0.00	0.00	0.00	0.00	0.00	0.00	0.00	0.00	0.00
K	0.00	0.00	0.00	0.00	0.00	0.00	0.00	0.00	0.00	0.00	0.00	0.00	0.00	0.00	0.00	0.00	0.00
Total	8.00	8.00	8.03	8.01	8.02	8.02	8.04	8.00	8.03	8.02	8.02	8.04	8.02	8.02	8.01	8.03	8.04

Table A.3: Electron microprobe results for garnet – continued.

	JMTV45 gt23(b)_rim	JMTV45 gt24(b)_int	JMTV45 gt24(b)_rim	JMTV45 gt25_int	JMTV45 gt25_rim	JMTV45 gt18(b)_int	JMTV45 gt19(b)_int	JMTV45 gt22(b)_int	JMTV45 gt14_int	JMTV45 gt15_rim	PM13076 gt26(b)_int	PM13076 gt26(b)_rim	PM13076 gt34(int)	PM13076 gt34(rim)	PM13076 gt27_core	PM13076 gt27(2)	PM13076 gt27(3)
SiO_2	37.38	37.57	37.63	37.38	37.21	37.07	37.68	37.67	37.51	37.20	38.08	37.48	37.69	37.77	37.76	37.85	37.97
TiO_2	0.00	0.00	0.01	0.00	0.00	0.02	0.01	0.08	0.00	0.00	0.00	0.00	0.03	0.02	0.00	0.02	0.00
Al_2O_3	21.80	21.74	22.03	21.50	21.77	21.77	21.92	21.90	21.51	21.62	21.72	22.02	21.79	21.76	22.01	22.11	22.13
Cr_2O_3	0.00	0.05	0.01	0.01	0.02	0.01	0.02	0.00	0.08	0.09	0.04	0.03	0.03	0.04	0.04	0.08	0.06
FeO	34.68	34.69	35.10	32.46	32.88	34.02	34.41	35.01	33.60	33.45	34.54	34.82	32.50	33.43	32.68	32.73	32.44
MnO	0.66	0.56	0.60	0.54	0.52	0.54	0.53	0.57	0.71	0.81	0.42	0.59	0.53	0.51	0.56	0.49	0.51
MgO	5.19	5.37	5.12	6.67	6.48	5.53	5.55	5.31	6.00	6.16	4.77	4.49	5.33	5.36	5.84	5.68	5.88
CaO	0.99	0.97	0.97	0.98	1.03	1.00	0.97	0.96	1.07	0.97	0.89	0.88	1.27	0.90	1.20	1.20	1.17
Na_2O	0.03	0.00	0.02	0.06	0.01	0.05	0.02	0.02	0.06	0.01	0.06	0.07	0.03	0.03	0.03	0.02	0.00
K_2O	0.00	0.00	0.00	0.00	0.00	0.00	0.00	0.00	0.00	0.00	0.00	0.00	0.00	0.00	0.00	0.00	0.00
Total	100.73	100.94	101.48	99.60	99.93	100.01	101.12	101.52	100.55	100.31	100.53	100.37	99.19	99.83	100.11	100.18	100.15
Oxygens	12	12	12	12	12	12	12	12	12	12	12	12	12	12	12	12	12
Si	2.96	2.96	2.96	2.96	2.94	2.95	2.96	2.96	2.96	2.94	3.01	2.97	3.00	2.99	2.98	2.98	2.98
Ti	0.00	0.00	0.00	0.00	0.00	0.00	0.00	0.00	0.00	0.00	0.00	0.00	0.00	0.00	0.00	0.00	0.00
Al	2.03	2.02	2.04	2.01	2.03	2.04	2.03	2.03	2.00	2.02	2.02	2.06	2.04	2.03	2.04	2.05	2.05
Cr	0.00	0.00	0.00	0.00	0.00	0.00	0.00	0.00	0.01	0.01	0.00	0.00	0.00	0.00	0.00	0.00	0.00
Fe	2.29	2.29	2.31	2.15	2.18	2.26	2.26	2.30	2.22	2.21	2.28	2.31	2.16	2.21	2.15	2.15	2.13
Mn	0.04	0.04	0.04	0.04	0.03	0.04	0.04	0.04	0.05	0.05	0.03	0.04	0.04	0.03	0.04	0.03	0.03
Mg	0.61	0.63	0.60	0.79	0.76	0.66	0.65	0.62	0.71	0.73	0.56	0.53	0.63	0.63	0.69	0.67	0.69
Ca	0.08	0.08	0.08	0.08	0.09	0.08	0.08	0.08	0.09	0.08	0.08	0.07	0.11	0.08	0.10	0.10	0.10
Na	0.00	0.00	0.00	0.01	0.00	0.01	0.00	0.00	0.01	0.00	0.01	0.01	0.00	0.01	0.00	0.00	0.00
K	0.00	0.00	0.00	0.00	0.00	0.00	0.00	0.00	0.00	0.00	0.00	0.00	0.00	0.00	0.00	0.00	0.00
Total	8.03	8.02	8.03	8.04	8.04	8.04	8.02	8.03	8.04	8.05	7.99	8.00	7.98	7.99	8.00	7.99	7.99

Table A.4: Electron microprobe results for garnet – continued.

	PM13076 gt27(4)	PM13076 gt27(5)	PM13076 gt27(6)	PM13076 gt27(7)	PM13076 gt27(8)	PM13076 gt27(9)	PM13076 gt29(b)_rim	PM13076 gt32(b)_rim	PM13076 gt31(b)_int	PM13076 gt28(b)	PM13076 gt29(b)	PM13076 gt30(b)	PM13076 gt33(a)	KK16 gt38	KK16 gt38_int	KK16 gt38_rim	KK16 gt39_int
SiO_2	37.83	38.09	38.19	37.99	37.86	37.79	37.83	37.92	37.91	37.41	37.70	37.66	37.97	37.88	36.98	36.77	37.79
TiO_2	0.00	0.00	0.08	0.00	0.01	0.04	0.03	0.00	0.00	0.02	0.04	0.00	0.03	0.01	0.00	0.00	0.00
Al_2O_3	21.78	22.08	21.95	22.05	21.96	21.93	21.71	21.75	21.80	21.96	21.78	21.75	21.86	22.17	21.90	21.88	22.19
Cr_2O_3	0.07	0.03	0.00	0.05	0.03	0.05	0.02	0.02	0.00	0.04	0.05	0.00	0.11	0.03	0.01	0.00	0.03
FeO	32.88	33.28	32.67	32.53	32.84	33.88	35.70	35.21	34.88	34.95	34.78	35.63	33.75	31.70	31.65	31.57	30.18
MnO	0.50	0.57	0.52	0.50	0.55	0.53	0.57	0.55	0.54	0.64	0.53	0.60	0.53	2.59	2.60	2.68	2.53
MgO	5.76	5.67	6.10	5.97	5.65	5.11	4.14	4.23	4.74	4.68	4.60	4.62	5.00	5.77	5.45	5.29	6.94
CaO	1.13	0.85	1.20	1.15	1.14	0.84	0.80	0.90	0.98	0.83	0.86	0.85	0.97	0.63	0.67	0.78	0.65
Na_2O	0.04	0.03	0.01	0.03	0.05	0.03	0.01	0.03	0.02	0.01	0.01	0.10	0.03	0.03	0.02	0.03	0.00
K_2O	0.00	0.00	0.00	0.00	0.00	0.00	0.00	0.00	0.00	0.00	0.00	0.00	0.00	0.01	0.00	0.00	0.01
Total	99.99	100.60	100.72	100.27	100.08	100.20	100.82	100.61	100.87	100.53	100.35	101.22	100.24	100.81	99.28	99.00	100.33
Oxygens	12	12	12	12	12	12	12	12	12	12	12	12	12	12	12	12	12
Si	2.99	2.99	2.99	2.98	2.98	2.99	3.00	3.00	2.99	2.97	2.99	2.97	3.00	2.97	2.95	2.95	2.96
Ti	0.00	0.00	0.00	0.00	0.00	0.00	0.00	0.00	0.00	0.00	0.00	0.00	0.00	0.00	0.00	0.00	0.00
Al	2.03	2.04	2.02	2.04	2.04	2.04	2.03	2.03	2.03	2.05	2.04	2.02	2.04	2.05	2.06	2.07	2.05
Cr	0.00	0.00	0.00	0.00	0.00	0.00	0.00	0.00	0.00	0.00	0.00	0.00	0.01	0.00	0.00	0.00	0.00
Fe	2.17	2.18	2.14	2.14	2.17	2.24	2.36	2.33	2.30	2.32	2.31	2.35	2.23	2.08	2.11	2.12	1.98
Mn	0.03	0.04	0.03	0.03	0.04	0.04	0.04	0.04	0.04	0.04	0.04	0.04	0.04	0.17	0.18	0.18	0.17
Mg	0.68	0.66	0.71	0.70	0.66	0.60	0.49	0.50	0.56	0.55	0.54	0.54	0.59	0.67	0.65	0.63	0.81
Ca	0.10	0.07	0.10	0.10	0.10	0.07	0.07	0.08	0.08	0.07	0.07	0.07	0.08	0.05	0.06	0.07	0.05
Na	0.01	0.00	0.00	0.00	0.01	0.01	0.00	0.00	0.00	0.00	0.00	0.02	0.00	0.00	0.00	0.00	0.00
K	0.00	0.00	0.00	0.00	0.00	0.00	0.00	0.00	0.00	0.00	0.00	0.00	0.00	0.00	0.00	0.00	0.00
Total	8.00	7.99	8.00	8.00	8.00	7.99	7.99	7.98	8.00	8.01	7.99	8.02	7.98	8.01	8.02	8.02	8.02

Table A.5: Electron microprobe results for garnet – continued.

	KK16 gt40_int	KK16 gt40_rim	KK16 gt41_int	KK16 gt41_rim	KK16 gt42_int	KK16 gt43_int	KK16 gt43_rim	KK16 gt44_int	KK16 gt45_int	KK16 gt45_rim	KK27 gt46_int	KK27 gt46_rim	KK27 gt47_int	KK27 gt47_rim	KK27 gt48_int	KK27 gt48_rim	KK27 gt49
SiO_2	37.22	37.86	37.15	37.11	37.15	37.59	37.79	38.05	37.73	37.64	36.28	37.10	36.96	36.92	37.02	36.84	37.31
TiO_2	0.01	0.00	0.01	0.02	0.06	0.01	0.02	0.00	0.02	0.03	0.01	0.00	0.00	0.00	0.00	0.00	0.00
Al_2O_3	22.02	21.93	22.03	22.06	21.95	22.32	22.29	22.11	22.14	22.01	22.14	21.82	22.08	22.00	22.02	22.00	22.04
Cr_2O_3	0.00	0.03	0.00	0.02	0.00	0.02	0.02	0.00	0.00	0.00	0.05	0.04	0.01	0.04	0.00	0.00	0.00
FeO	30.96	31.71	31.34	31.83	31.35	30.71	31.11	30.14	31.22	31.36	34.06	33.94	33.24	34.28	32.90	33.58	34.20
MnO	2.55	2.67	2.67	2.74	2.72	2.50	2.48	2.43	2.55	2.65	1.86	1.91	1.78	1.91	1.81	2.01	1.94
MgO	5.95	5.24	5.64	4.71	5.55	6.03	5.88	6.45	5.94	5.54	4.58	4.27	4.83	4.05	4.88	4.29	4.25
CaO	0.63	0.72	0.79	0.94	0.92	0.74	0.70	0.75	0.86	0.84	0.99	0.98	1.03	1.01	1.07	1.00	0.99
Na_2O	0.00	0.02	0.02	0.00	0.00	0.00	0.00	0.01	0.01	0.03	0.03	0.00	0.04	0.03	0.02	0.01	0.00
K_2O	0.00	0.00	0.01	0.03	0.02	0.01	0.01	0.00	0.00	0.01	0.00	0.01	0.01	0.01	0.01	0.03	0.00
Total	99.34	100.19	99.66	99.45	99.72	99.92	100.30	99.94	100.47	100.10	100.00	100.07	99.98	100.24	99.73	99.76	100.73
Oxygens	12	12	12	12	12	12	12	12	12	12	12	12	12	12	12	12	12
Si	2.96	2.99	2.95	2.96	2.95	2.96	2.97	2.99	2.97	2.97	2.91	2.96	2.94	2.95	2.95	2.95	2.96
Ti	0.00	0.00	0.00	0.00	0.00	0.00	0.00	0.00	0.00	0.00	0.00	0.00	0.00	0.00	0.00	0.00	0.00
Al	2.06	2.04	2.06	2.08	2.06	2.07	2.07	2.05	2.05	2.05	2.09	2.05	2.07	2.07	2.07	2.08	2.06
Cr	0.00	0.00	0.00	0.00	0.00	0.00	0.00	0.00	0.00	0.00	0.00	0.00	0.00	0.00	0.00	0.00	0.00
Fe	2.06	2.09	2.08	2.13	2.08	2.02	2.04	1.98	2.05	2.07	2.28	2.27	2.21	2.29	2.19	2.25	2.27
Mn	0.17	0.18	0.18	0.19	0.18	0.17	0.17	0.16	0.17	0.18	0.13	0.13	0.12	0.13	0.12	0.14	0.13
Mg	0.70	0.62	0.67	0.56	0.66	0.71	0.69	0.75	0.70	0.65	0.55	0.51	0.57	0.48	0.58	0.51	0.50
Ca	0.05	0.06	0.07	0.08	0.08	0.06	0.06	0.06	0.07	0.07	0.08	0.08	0.09	0.09	0.09	0.09	0.08
Na	0.00	0.00	0.00	0.00	0.00	0.00	0.00	0.00	0.00	0.00	0.01	0.00	0.01	0.01	0.00	0.00	0.00
K	0.00	0.00	0.00	0.00	0.00	0.00	0.00	0.00	0.00	0.00	0.00	0.00	0.00	0.00	0.00	0.00	0.00
Total	8.01	7.99	8.02	8.00	8.02	8.00	8.00	7.99	8.01	8.00	8.05	8.01	8.02	8.02	8.01	8.01	8.01

Table A.6: Electron microprobe results for garnet – continued.

	KK27 gt50_int	KK27 gt50_rim	KK27 gt51_int	KK27 gt51_rim	KK27 gt52_int	KK27 gt52_rim	KK28 gt53_int	KK28 gt53_rim	KK28 gt54_int	KK28 gt54_rim	KK28 gt55_int	KK28 gt56_int	KK28 gt56_rim	KK29 gt57_int	KK29 gt57_rim	KK29 gt58_int	KK29 gt58_rim
SiO_2	37.36	37.34	37.16	37.15	37.84	37.47	37.77	37.43	37.68	37.42	37.75	37.76	37.50	38.50	38.02	38.21	37.52
TiO_2	0.01	0.00	0.05	0.00	0.03	0.00	0.00	0.00	0.00	0.00	0.00	0.00	0.02	0.01	0.01	0.00	0.00
Al_2O_3	21.90	21.79	21.77	21.97	22.06	21.94	22.08	21.78	22.07	22.02	21.99	21.84	21.96	22.02	22.09	22.00	22.11
Cr_2O_3	0.00	0.00	0.00	0.01	0.00	0.04	0.01	0.01	0.03	0.00	0.00	0.03	0.01	0.01	0.01	0.00	0.00
FeO	33.56	32.99	33.18	33.43	31.95	33.26	32.73	33.45	32.97	32.77	32.75	32.52	33.00	31.04	31.94	31.37	30.42
MnO	1.80	1.82	1.80	1.90	1.49	1.56	1.37	1.44	1.36	1.29	1.32	1.54	1.54	2.32	3.08	3.23	3.27
MgO	5.13	4.89	4.81	4.43	5.95	5.24	5.63	4.95	5.18	5.41	5.48	5.48	4.91	5.94	4.74	4.60	4.43
CaO	0.99	1.02	0.98	1.02	0.81	0.89	0.99	0.92	1.08	1.06	1.07	1.13	1.04	0.99	1.00	1.27	1.07
Na_2O	0.03	0.03	0.05	0.00	0.03	0.01	0.00	0.04	0.00	0.01	0.04	0.00	0.00	0.08	0.04	0.05	0.14
K_2O	0.00	0.00	0.00	0.00	0.01	0.00	0.01	0.01	0.01	0.00	0.00	0.00	0.01	0.00	0.00	0.00	0.05
Total	100.78	99.88	99.80	99.91	100.17	100.41	100.59	100.04	100.38	99.98	100.40	100.30	99.98	100.92	100.93	100.73	99.01
Oxygens	12	12	12	12	12	12	12	12	12	12	12	12	12	12	12	12	12
Si	2.95	2.97	2.96	2.96	2.98	2.96	2.97	2.97	2.97	2.96	2.98	2.98	2.98	3.00	2.99	3.01	3.00
Ti	0.00	0.00	0.00	0.00	0.00	0.00	0.00	0.00	0.00	0.00	0.00	0.00	0.00	0.00	0.00	0.00	0.00
Al	2.04	2.04	2.05	2.07	2.05	2.05	2.05	2.04	2.05	2.06	2.04	2.03	2.05	2.02	2.05	2.04	2.08
Cr	0.00	0.00	0.00	0.00	0.00	0.00	0.00	0.00	0.00	0.00	0.00	0.00	0.00	0.00	0.00	0.00	0.00
Fe	2.22	2.20	2.21	2.23	2.10	2.20	2.15	2.22	2.18	2.17	2.16	2.15	2.19	2.02	2.10	2.06	2.03
Mn	0.12	0.12	0.12	0.13	0.10	0.10	0.09	0.10	0.09	0.09	0.09	0.10	0.10	0.15	0.21	0.22	0.22
Mg	0.60	0.58	0.57	0.53	0.70	0.62	0.66	0.59	0.61	0.64	0.64	0.64	0.58	0.69	0.56	0.54	0.53
Ca	0.08	0.09	0.08	0.09	0.07	0.08	0.08	0.08	0.09	0.09	0.09	0.10	0.09	0.08	0.08	0.11	0.09
Na	0.00	0.00	0.01	0.00	0.00	0.00	0.00	0.01	0.00	0.00	0.01	0.00	0.00	0.01	0.01	0.01	0.02
K	0.00	0.00	0.00	0.00	0.00	0.00	0.00	0.00	0.00	0.00	0.00	0.00	0.00	0.00	0.00	0.00	0.00
Total	8.03	8.01	8.01	8.00	8.00	8.01	8.01	8.01	8.00	8.01	8.01	8.00	8.00	7.99	7.99	7.98	7.98

Table A.7: Electron microprobe results for garnet – continued.

	KK29 gt59_int	KK29 gt59_rim	KK29 gt60_int	KK29 gt60_rim	KK29 gt61	KK29 gt62_int	KK29 gt62_rim	KK29 gt63_int	KK29 gt63_rim	KK29 gt64_int	KK29 gt64_rim	KK29 gt1(core)	KK29 gt1(a)	KK29 gt1(b)	KK29 gt1(c)	KK29 gt1(d)	KK29 gt1(e)	KK29 gt1(f)	KK29 gt1(g)	KK29 gt1(h)
SiO_2	38.26	38.24	38.16	38.30	38.06	38.19	38.18	38.01	38.07	38.23	37.84	36.66	36.76	36.33	36.11	36.10	36.33	36.60	36.47	36.77
TiO_2	0.00	0.02	0.00	0.00	0.00	0.00	0.00	0.00	0.02	0.00	0.05	0.00	0.05	0.04	0.00	0.02	0.00	0.02	0.03	0.01
Al_2O_3	22.24	22.05	21.95	21.99	22.09	22.11	22.18	22.03	22.28	22.30	22.11	22.28	22.28	22.48	22.16	22.26	22.25	22.40	22.28	22.38
Cr_2O_3	0.01	0.00	0.03	0.02	0.00	0.07	0.00	0.00	0.04	0.02	0.00	0.00	0.01	0.00	0.03	0.00	0.00	0.04	0.00	0.02
FeO	31.43	32.12	31.91	32.09	31.92	31.58	32.08	31.79	31.09	31.66	32.18	30.99	30.75	30.93	30.96	31.40	30.92	30.99	30.60	31.28
MnO	3.18	3.25	2.80	3.19	3.27	2.28	3.29	2.78	2.93	2.96	3.50	2.62	2.65	2.78	2.93	3.14	2.48	2.58	2.76	3.22
MgO	5.01	4.42	5.02	4.25	4.37	5.65	4.22	5.02	4.72	4.73	3.87	6.25	5.82	5.80	5.75	5.21	6.11	6.11	5.85	5.16
CaO	0.96	0.91	0.90	0.96	1.03	0.96	1.06	1.10	1.02	1.06	1.04	1.10	1.12	1.14	1.08	1.09	1.06	1.00	1.02	1.05
Na_2O	0.07	0.09	0.01	0.01	0.01	0.02	0.00	0.03	0.01	0.01	0.01	0.01	0.03	0.03	0.03	0.00	0.00	0.03	0.01	0.04
K_2O	0.01	0.00	0.00	0.01	0.00	0.01	0.00	0.00	0.02	0.00	0.01	0.00	0.00	0.00	0.00	0.00	0.00	0.00	0.00	0.00
Total	101.18	101.10	100.78	100.82	100.75	100.87	101.01	100.76	100.20	100.97	100.61	99.91	99.47	99.54	99.05	99.22	99.16	99.78	99.03	99.92
Oxygens	12	12	12	12	12	12	12	12	12	12	12	12	12	12	12	12	12	12	12	12
Si	2.99	3.00	3.00	3.02	3.00	2.99	3.00	2.99	3.00	3.00	2.99	2.91	2.92	2.89	2.90	2.90	2.90	2.90	2.91	2.92
Ti	0.00	0.00	0.00	0.00	0.00	0.00	0.00	0.00	0.00	0.00	0.00	0.00	0.00	0.00	0.00	0.00	0.00	0.00	0.00	0.00
Al	2.05	2.04	2.03	2.04	2.05	2.04	2.06	2.04	2.07	2.06	2.06	2.08	2.09	2.11	2.10	2.11	2.10	2.10	2.10	2.10
Cr	0.00	0.00	0.00	0.00	0.00	0.00	0.00	0.00	0.00	0.00	0.00	0.00	0.00	0.00	0.00	0.00	0.00	0.00	0.00	0.00
Fe	2.06	2.11	2.10	2.11	2.10	2.07	2.11	2.09	2.05	2.08	2.13	2.05	2.05	2.06	2.08	2.11	2.07	2.06	2.05	2.08
Mn	0.21	0.22	0.19	0.21	0.22	0.15	0.22	0.19	0.20	0.20	0.23	0.18	0.18	0.19	0.20	0.21	0.17	0.17	0.19	0.22
Mg	0.58	0.52	0.59	0.50	0.51	0.66	0.49	0.59	0.55	0.55	0.46	0.74	0.69	0.69	0.69	0.62	0.73	0.72	0.70	0.61
Ca	0.08	0.08	0.08	0.08	0.09	0.08	0.09	0.09	0.09	0.09	0.09	0.09	0.10	0.10	0.09	0.09	0.09	0.09	0.09	0.09
Na	0.01	0.01	0.00	0.00	0.00	0.00	0.00	0.00	0.00	0.00	0.00	0.00	0.00	0.00	0.00	0.00	0.00	0.00	0.00	0.01
K	0.00	0.00	0.00	0.00	0.00	0.00	0.00	0.00	0.00	0.00	0.00	0.00	0.00	0.00	0.00	0.00	0.00	0.00	0.00	0.00
Total	7.99	7.98	7.98	7.97	7.98	7.99	7.97	7.99	7.96	7.97	7.97	8.05	8.03	8.05	8.06	8.05	8.05	8.05	8.03	8.03

Table A.8: Electron microprobe results for cordierite.

	PM13010 cd2	PM13010 cd2b_int	PM13010 cd2_rim	PM13010 cd3_int	PM13010 cd3b_int	PM13010 cd3b_rim	PM13010 cd4_rim	PM13010 cd5_int	PM13010 cd5_rim	PM13010 cd6_int	PM13010 cd6_rim	PM13010 cd1	PM13010 cd1b	PM13010 cd_corona1c	PM13010 cd_corona1e_pm13010	PM13010 cd_corona1f	PM13032 cd7_rim	PM13032 cd13_int
SiO_2	48.89	49.00	48.95	49.14	49.79	48.91	48.84	47.99	48.65	49.24	49.13	48.24	47.52	47.13	48.98	48.86	49.78	47.79
TiO_2	0.00	0.00	0.00	0.02	0.00	0.02	0.00	0.00	0.02	0.03	0.01	0.01	0.00	0.00	0.03	0.02	0.03	0.00
Al_2O_3	34.38	34.23	34.41	34.80	35.00	34.45	34.59	34.31	34.56	34.75	34.35	35.20	34.84	33.91	34.07	34.28	34.06	33.65
Cr_2O_3	0.00	0.00	0.00	0.00	0.00	0.00	0.02	0.07	0.00	0.01	0.02	0.01	0.00	0.00	0.01	0.00	0.00	0.02
FeO	5.90	5.79	5.60	5.70	5.88	5.80	5.79	5.97	5.79	5.77	5.85	5.87	5.92	5.82	5.78	5.66	6.73	6.89
MnO	0.54	0.62	0.65	0.55	0.54	0.53	0.55	0.53	0.54	0.52	0.58	0.54	0.47	0.50	0.50	0.51	0.07	0.10
MgO	9.71	9.68	9.59	9.60	9.46	8.94	9.60	9.52	9.55	9.52	9.73	10.01	9.80	9.51	9.73	9.79	9.38	9.17
CaO	0.06	0.08	0.06	0.05	0.00	0.15	0.02	0.06	0.03	0.00	0.06	0.01	0.04	0.02	0.03	0.03	0.03	0.06
Na_2O	0.09	0.12	0.13	0.14	0.12	0.29	0.14	0.34	0.12	0.15	0.17	0.12	0.14	0.11	0.09	0.07	0.13	0.11
K_2O	0.03	0.01	0.01	0.01	0.01	0.74	0.02	0.22	0.08	0.03	0.02	0.03	0.02	0.01	0.01	0.01	0.04	0.02
Total	99.60	99.53	99.40	100.01	100.80	99.83	99.57	99.00	99.34	100.01	99.91	100.04	98.75	97.02	99.23	99.23	100.24	97.81
Oxygens	18	18	18	18	18	18	18	18	18	18	18	18	18	18	18	18	18	18
Si	4.93	4.94	4.94	4.93	4.95	4.94	4.92	4.88	4.91	4.94	4.94	4.85	4.84	4.88	4.95	4.93	4.99	4.92
Ti	0.00	0.00	0.00	0.00	0.00	0.00	0.00	0.00	0.00	0.00	0.00	0.00	0.00	0.00	0.00	0.00	0.00	0.00
Al	4.08	4.07	4.09	4.11	4.10	4.10	4.11	4.12	4.12	4.11	4.07	4.17	4.18	4.14	4.06	4.08	4.02	4.08
Cr	0.00	0.00	0.00	0.00	0.00	0.00	0.00	0.01	0.00	0.00	0.00	0.00	0.00	0.00	0.00	0.00	0.00	0.00
Fe	0.50	0.49	0.47	0.48	0.49	0.49	0.49	0.51	0.49	0.48	0.49	0.49	0.50	0.50	0.49	0.48	0.56	0.59
Mn	0.05	0.05	0.06	0.05	0.05	0.05	0.05	0.05	0.05	0.04	0.05	0.05	0.04	0.04	0.04	0.04	0.01	0.01
Mg	1.46	1.45	1.44	1.43	1.40	1.34	1.44	1.44	1.44	1.42	1.46	1.50	1.49	1.47	1.47	1.47	1.40	1.41
Ca	0.01	0.01	0.01	0.01	0.00	0.02	0.00	0.01	0.00	0.00	0.01	0.00	0.00	0.00	0.00	0.00	0.00	0.01
Na	0.02	0.02	0.03	0.03	0.02	0.06	0.03	0.07	0.02	0.03	0.03	0.02	0.03	0.02	0.02	0.01	0.03	0.02
K	0.00	0.00	0.00	0.00	0.00	0.10	0.00	0.03	0.01	0.00	0.00	0.00	0.00	0.00	0.00	0.00	0.00	0.00
Total	11.04	11.04	11.03	11.03	11.01	11.09	11.04	11.10	11.04	11.03	11.05	11.08	11.09	11.06	11.03	11.03	11.01	11.05

Table A.9: Electron microprobe results for cordierite – continued.

	PM13032 cd13_rim	PM13032 cd14_int	PM13032 cd14_rim	PM13032 cd15_int	PM13032 cd15_rim	PM13032 cd7(gt4_rim)	PM13032 cd7b(gt4_rim)	PM13032 cd8	PM13032 cd9(gt_rim)	PM13032 cd10(gt_rim)	PM13032 cd11(gt_rim)	PM13032 cd12(gt_rim)	PM13032 cd16	PM13068 cd17_int	PM13068 cd17_rim	PM13068 cd18_int	PM13068 cd18_rim	PM13068 cd19_int
SiO_2	47.43	47.82	47.62	47.72	47.29	47.98	48.27	48.11	47.81	47.99	47.87	47.43	47.72	48.34	48.49	48.41	48.40	48.69
TiO_2	0.02	0.00	0.00	0.00	0.02	0.00	0.00	0.01	0.00	0.00	0.01	0.03	0.00	0.00	0.00	0.00	0.00	0.01
Al_2O_3	33.47	33.72	33.72	33.76	33.56	34.04	34.10	34.00	33.88	33.61	33.83	33.39	33.85	34.19	34.11	34.05	34.42	34.21
Cr_2O_3	0.00	0.00	0.00	0.01	0.00	0.00	0.02	0.00	0.02	0.00	0.02	0.02	0.02	0.01	0.00	0.00	0.01	0.00
FeO	6.91	6.95	6.80	7.15	6.94	6.87	7.13	6.80	6.96	6.33	6.89	6.49	7.14	5.85	5.94	6.20	6.23	6.15
MnO	0.06	0.03	0.11	0.13	0.07	0.12	0.08	0.12	0.02	0.06	0.13	0.04	0.06	0.27	0.18	0.18	0.19	0.24
MgO	9.35	9.43	9.38	9.10	8.95	9.29	9.16	9.47	9.40	9.61	9.37	9.35	9.13	9.90	9.85	9.56	9.67	9.68
CaO	0.07	0.04	0.06	0.04	0.11	0.08	0.02	0.05	0.08	0.08	0.05	0.08	0.04	0.03	0.01	0.00	0.00	0.02
Na_2O	0.13	0.12	0.16	0.10	0.20	0.15	0.12	0.10	0.11	0.12	0.10	0.07	0.12	0.08	0.12	0.07	0.07	0.07
K_2O	0.02	0.02	0.18	0.01	0.05	0.04	0.01	0.02	0.03	0.09	0.00	0.02	0.01	0.02	0.03	0.02	0.01	0.01
Total	97.45	98.14	98.03	98.03	97.18	98.57	98.91	98.69	98.32	97.89	98.26	96.92	98.08	98.69	98.72	98.49	99.00	99.08
Oxygens	18	18	18	18	18	18	18	18	18	18	18	18	18	18	18	18	18	18
Si	4.91	4.91	4.90	4.91	4.91	4.90	4.92	4.91	4.90	4.93	4.91	4.92	4.91	4.91	4.92	4.93	4.91	4.93
Ti	0.00	0.00	0.00	0.00	0.00	0.00	0.00	0.00	0.00	0.00	0.00	0.00	0.00	0.00	0.00	0.00	0.00	0.00
Al	4.08	4.08	4.09	4.09	4.10	4.10	4.10	4.09	4.09	4.07	4.09	4.08	4.10	4.10	4.08	4.09	4.11	4.08
Cr	0.00	0.00	0.00	0.00	0.00	0.00	0.00	0.00	0.00	0.00	0.00	0.00	0.00	0.00	0.00	0.00	0.00	0.00
Fe	0.60	0.60	0.59	0.62	0.60	0.59	0.61	0.58	0.60	0.54	0.59	0.56	0.61	0.50	0.50	0.53	0.53	0.52
Mn	0.00	0.00	0.01	0.01	0.01	0.01	0.01	0.01	0.00	0.01	0.01	0.00	0.00	0.02	0.02	0.02	0.02	0.02
Mg	1.44	1.44	1.44	1.40	1.38	1.42	1.39	1.44	1.44	1.47	1.43	1.45	1.40	1.50	1.49	1.45	1.46	1.46
Ca	0.01	0.00	0.01	0.00	0.01	0.01	0.00	0.01	0.01	0.01	0.01	0.01	0.00	0.00	0.00	0.00	0.00	0.00
Na	0.03	0.02	0.03	0.02	0.04	0.03	0.02	0.02	0.02	0.02	0.02	0.01	0.02	0.02	0.02	0.01	0.01	0.01
K	0.00	0.00	0.02	0.00	0.01	0.00	0.00	0.00	0.00	0.01	0.00	0.00	0.00	0.00	0.00	0.00	0.00	0.00
Total	11.07	11.06	11.08	11.05	11.06	11.06	11.05	11.06	11.07	11.06	11.06	11.04	11.06	11.05	11.05	11.03	11.04	11.03

Table A.10: Electron microprobe results for cordierite – continued.

	PM13068 cd19_rim	PM13068 cd20(gt11_corona)	PM13068 cd21(gt11_corona)	JMTV45 cd22_int	JMTV45 cd22_rim	JMTV45 cd23_core	JMTV45 cd23_rim	PM13076 cd26_int	PM13076 cd26_rim	PM13076 cd28_int	PM13076 cd28_rim	PM13076 cd24	PM13076 cd25	PM13076 cd27	PM13076 cd29(gt_rim)	PM13076 cd30(gt_rim)	PM13076 cd31	PM13076 cd32(gt_rim)
SiO_2	48.99	48.75	48.95	48.13	48.11	48.21	47.83	46.97	47.29	47.55	47.55	47.18	47.24	46.97	47.71	47.82	47.69	47.44
TiO_2	0.02	0.03	0.01	0.01	0.05	0.00	0.00	0.03	0.00	0.02	0.02	0.00	0.01	0.00	0.03	0.00	0.00	0.00
Al_2O_3	34.47	34.70	34.49	34.01	34.33	33.70	33.75	33.68	33.72	33.53	33.89	33.53	33.81	33.84	33.95	34.00	33.71	33.79
Cr_2O_3	0.01	0.05	0.00	0.00	0.03	0.00	0.02	0.00	0.00	0.00	0.02	0.01	0.00	0.01	0.00	0.00	0.00	0.02
FeO	6.15	5.13	4.97	7.30	7.05	7.27	7.05	8.00	8.06	8.00	7.97	7.84	8.66	8.11	8.14	7.28	8.38	8.61
MnO	0.25	0.17	0.17	0.01	0.08	0.06	0.07	0.01	0.06	0.06	0.03	0.04	0.10	0.10	0.02	0.03	0.06	0.09
MgO	9.58	10.42	10.56	8.96	8.87	9.21	9.07	8.38	8.36	8.65	8.60	8.54	8.28	8.44	8.68	8.77	8.28	8.30
CaO	0.02	0.00	0.02	0.02	0.03	0.01	0.00	0.03	0.00	0.01	0.03	0.06	0.02	0.03	0.02	0.02	0.01	0.02
Na_2O	0.08	0.09	0.08	0.09	0.13	0.11	0.10	0.24	0.21	0.21	0.21	0.23	0.24	0.16	0.16	0.15	0.21	0.16
K_2O	0.01	0.02	0.01	0.01	0.11	0.02	0.02	0.04	0.02	0.04	0.02	0.04	0.02	0.03	0.02	0.38	0.03	0.02
Total	99.59	99.36	99.27	98.54	98.78	98.60	97.90	97.37	97.72	98.06	98.33	97.47	98.38	97.70	98.73	98.45	98.37	98.45
Oxygens	18	18	18	18	18	18	18	18	18	18	18	18	18	18	18	18	18	18
Si	4.93	4.90	4.92	4.92	4.91	4.93	4.92	4.89	4.90	4.91	4.90	4.90	4.88	4.87	4.89	4.91	4.92	4.89
Ti	0.00	0.00	0.00	0.00	0.00	0.00	0.00	0.00	0.00	0.00	0.00	0.00	0.00	0.00	0.00	0.00	0.00	0.00
Al	4.09	4.11	4.09	4.10	4.13	4.06	4.09	4.13	4.12	4.08	4.11	4.11	4.12	4.14	4.11	4.11	4.10	4.11
Cr	0.00	0.00	0.00	0.00	0.00	0.00	0.00	0.00	0.00	0.00	0.00	0.00	0.00	0.00	0.00	0.00	0.00	0.00
Fe	0.52	0.43	0.42	0.62	0.60	0.62	0.61	0.70	0.70	0.69	0.69	0.68	0.75	0.70	0.70	0.62	0.72	0.74
Mn	0.02	0.01	0.01	0.00	0.01	0.01	0.01	0.00	0.01	0.00	0.00	0.00	0.01	0.01	0.00	0.00	0.01	0.01
Mg	1.44	1.56	1.58	1.37	1.35	1.40	1.39	1.30	1.29	1.33	1.32	1.32	1.27	1.31	1.33	1.34	1.27	1.28
Ca	0.00	0.00	0.00	0.00	0.00	0.00	0.00	0.00	0.00	0.00	0.00	0.01	0.00	0.00	0.00	0.00	0.00	0.00
Na	0.02	0.02	0.02	0.02	0.03	0.02	0.02	0.05	0.04	0.04	0.04	0.05	0.05	0.03	0.03	0.03	0.04	0.03
K	0.00	0.00	0.00	0.00	0.01	0.00	0.00	0.00	0.00	0.00	0.00	0.01	0.00	0.00	0.00	0.05	0.00	0.00
Total	11.03	11.05	11.04	11.04	11.04	11.05	11.04	11.07	11.06	11.07	11.07	11.07	11.08	11.07	11.07	11.07	11.06	11.07

Table A.11: Electron microprobe results for cordierite – continued.

	PM13076	PM13076	KK16	KK16	KK16	KK16	KK16	KK16	KK16	KK16	KK16	KK16	KK16	KK16	KK16	KK16	KK16	KK16
	cd33(gt(b)_rim)	cd34(gt(b)rim)	cd45_int	cd45_rim	cd46_int	cd46_rim	cd47_int	cd47_rim	cd48_rim	cd49_int	cd49_rim	cd1(b)	cd2(b)	cd3(b)	cd4(b)	cd5(b)	cd6(b)	cd7(a)
SiO_2	47.93	47.72	49.63	49.55	49.47	49.74	49.51	49.70	49.75	49.21	49.36	50.12	49.89	49.88	49.36	49.49	49.90	49.89
TiO_2	0.00	0.01	0.00	0.00	0.01	0.00	0.00	0.02	0.00	0.01	0.00	0.00	0.00	0.01	0.01	0.04	0.00	0.00
Al_2O_3	33.69	33.84	33.90	33.70	33.72	33.89	33.55	33.74	34.05	33.38	33.41	33.67	33.60	33.61	33.35	33.19	33.85	33.55
Cr_2O_3	0.00	0.02	0.04	0.03	0.04	0.00	0.00	0.02	0.00	0.01	0.01	0.00	0.03	0.00	0.01	0.00	0.00	0.01
FeO	8.49	8.70	6.15	6.20	6.29	6.08	6.56	6.14	6.01	6.17	6.29	5.51	6.02	5.85	5.71	5.48	5.66	6.61
MnO	0.08	0.01	0.19	0.14	0.19	0.12	0.23	0.16	0.15	0.13	0.18	0.14	0.16	0.06	0.17	0.10	0.16	0.22
MgO	8.31	8.29	10.03	10.18	10.12	10.36	10.08	10.33	10.06	9.97	10.01	11.30	10.91	11.26	10.96	10.93	11.23	10.40
CaO	0.00	0.00	0.01	0.00	0.01	0.00	0.01	0.00	0.00	0.00	0.00	0.01	0.02	0.01	0.00	0.03	0.00	0.01
Na_2O	0.19	0.20	0.10	0.12	0.09	0.09	0.12	0.13	0.13	0.10	0.10	0.09	0.12	0.07	0.11	0.12	0.09	0.10
K_2O	0.01	0.03	0.01	0.01	0.01	0.02	0.00	0.00	0.01	0.01	0.00	0.01	0.01	0.02	0.01	0.17	0.02	0.02
Total	98.69	98.81	100.05	99.93	99.96	100.30	100.06	100.23	100.15	98.98	99.36	100.85	100.76	100.77	99.70	99.55	100.91	100.80
Oxygens	18	18	18	18	18	18	18	18	18	18	18	18	18	18	18	18	18	18
Si	4.93	4.90	4.97	4.97	4.97	4.97	4.97	4.97	4.98	4.98	4.98	4.97	4.97	4.96	4.96	4.98	4.95	4.98
Ti	0.00	0.00	0.00	0.00	0.00	0.00	0.00	0.00	0.00	0.00	0.00	0.00	0.00	0.00	0.00	0.00	0.00	0.00
Al	4.08	4.10	4.01	3.99	3.99	3.99	3.97	3.98	4.01	3.99	3.98	3.94	3.94	3.94	3.95	3.94	3.96	3.95
Cr	0.00	0.00	0.00	0.00	0.00	0.00	0.00	0.00	0.00	0.00	0.00	0.00	0.00	0.00	0.00	0.00	0.00	0.00
Fe	0.73	0.75	0.52	0.52	0.53	0.51	0.55	0.51	0.50	0.52	0.53	0.46	0.50	0.49	0.48	0.46	0.47	0.55
Mn	0.01	0.00	0.02	0.01	0.02	0.01	0.02	0.01	0.01	0.01	0.02	0.01	0.01	0.01	0.01	0.01	0.01	0.02
Mg	1.27	1.27	1.50	1.52	1.51	1.54	1.51	1.54	1.50	1.51	1.51	1.67	1.62	1.67	1.64	1.64	1.66	1.55
Ca	0.00	0.00	0.00	0.00	0.00	0.00	0.00	0.00	0.00	0.00	0.00	0.00	0.00	0.00	0.00	0.00	0.00	0.00
Na	0.04	0.04	0.02	0.02	0.02	0.02	0.02	0.03	0.02	0.02	0.02	0.02	0.02	0.01	0.02	0.02	0.02	0.02
K	0.00	0.00	0.00	0.00	0.00	0.00	0.00	0.00	0.00	0.00	0.00	0.00	0.00	0.00	0.00	0.02	0.00	0.00
Total	11.05	11.07	11.03	11.04	11.04	11.04	11.05	11.05	11.03	11.03	11.04	11.07	11.07	11.08	11.07	11.07	11.08	11.06

Table A.12: Electron microprobe results for cordierite – continued.

	KK16 cd8(a)	KK16 cd9(a)	KK29 cd50_int	KK29 cd50_rim	KK29 cd51_int	KK29 cd51_rim	KK29 cd52_int	KK29 cd52_rim	KK29 cd53	KK29 cd11(b)	KK29 cd12(b)	KK29 cd13(b)	KK29 cd14(a)	KK29 cd15(a)	KK29 cd16(a)	KK29 cd17(a)	KK29 cd18(a)
SiO_2	49.54	49.65	48.51	48.61	48.44	48.50	48.58	48.81	48.15	48.92	49.15	49.11	48.76	48.76	49.17	48.78	49.08
TiO_2	0.00	0.00	0.00	0.00	0.00	0.00	0.01	0.03	0.04	0.00	0.00	0.00	0.00	0.00	0.01	0.02	0.01
Al_2O_3	33.25	33.22	34.68	34.69	34.37	34.48	34.71	34.59	34.65	32.81	33.03	32.57	33.10	32.66	33.32	32.81	32.69
Cr_2O_3	0.00	0.03	0.00	0.00	0.00	0.01	0.00	0.00	0.03	0.01	0.00	0.00	0.02	0.00	0.04	0.00	0.00
FeO	6.43	6.28	7.33	7.04	7.43	7.16	7.51	7.33	7.43	7.82	7.48	7.46	7.60	7.64	7.58	7.61	7.92
MnO	0.14	0.18	0.25	0.26	0.28	0.23	0.21	0.23	0.24	0.21	0.17	0.24	0.25	0.25	0.29	0.28	0.26
MgO	10.49	10.23	8.75	8.80	8.88	8.71	8.41	8.32	8.52	9.44	9.63	9.76	9.74	9.58	9.37	9.37	9.13
CaO	0.00	0.00	0.02	0.00	0.01	0.01	0.00	0.04	0.01	0.02	0.01	0.03	0.00	0.01	0.02	0.02	0.02
Na_2O	0.07	0.07	0.12	0.11	0.12	0.11	0.15	0.10	0.09	0.09	0.14	0.13	0.15	0.03	0.10	0.13	0.15
K_2O	0.01	0.02	0.01	0.01	0.01	0.02	0.00	0.01	0.00	0.01	0.01	0.03	0.00	0.00	0.01	0.01	0.03
Total	99.94	99.68	99.67	99.53	99.55	99.23	99.59	99.46	99.16	99.33	99.62	99.33	99.62	98.92	99.91	99.02	99.29
Oxygens	18	18	18	18	18	18	18	18	18	18	18	18	18	18	18	18	18
Si	4.98	5.00	4.91	4.92	4.91	4.92	4.92	4.94	4.90	4.98	4.98	4.99	4.95	4.98	4.97	4.98	5.00
Ti	0.00	0.00	0.00	0.00	0.00	0.00	0.00	0.00	0.00	0.00	0.00	0.00	0.00	0.00	0.00	0.00	0.00
Al	3.94	3.94	4.14	4.14	4.11	4.13	4.15	4.13	4.16	3.94	3.95	3.91	3.96	3.93	3.97	3.95	3.93
Cr	0.00	0.00	0.00	0.00	0.00	0.00	0.00	0.00	0.00	0.00	0.00	0.00	0.00	0.00	0.00	0.00	0.00
Fe	0.54	0.53	0.62	0.60	0.63	0.61	0.64	0.62	0.63	0.67	0.63	0.63	0.65	0.65	0.64	0.65	0.68
Mn	0.01	0.02	0.02	0.02	0.02	0.02	0.02	0.02	0.02	0.02	0.01	0.02	0.02	0.02	0.02	0.02	0.02
Mg	1.57	1.53	1.32	1.33	1.34	1.32	1.27	1.26	1.29	1.43	1.45	1.48	1.47	1.46	1.41	1.43	1.39
Ca	0.00	0.00	0.00	0.00	0.00	0.00	0.00	0.00	0.00	0.00	0.00	0.00	0.00	0.00	0.00	0.00	0.00
Na	0.01	0.01	0.02	0.02	0.02	0.02	0.03	0.02	0.02	0.02	0.03	0.03	0.03	0.01	0.02	0.03	0.03
K	0.00	0.00	0.00	0.00	0.00	0.00	0.00	0.00	0.00	0.00	0.00	0.00	0.00	0.00	0.00	0.00	0.00
Total	11.06	11.04	11.03	11.02	11.05	11.02	11.02	11.00	11.03	11.06	11.06	11.07	11.08	11.05	11.05	11.06	11.05

Table A.13: Electron microprobe results for biotite.

	PM13010 bi3(b)_int	PM13010 bi3(b)_rim	PM13010 bi6(b)_int	PM13010 bi7(b)_int	PM13010 bi7(b)_rim	PM13010 bi8(b)_int	PM13010 bi8(b)_rim	PM13010 bi4(b)_int	PM13010 bi5(b)_int	PM13010 bi1(b)	PM13010 bi2(b)	PM13032 bi12(c)_int	PM13032 bi12(c)_rim	PM13032 bi13(c)_int	PM13032 bi13(c)_rim	PM13032 bi14(c)_int
SiO_2	34.18	34.73	36.08	36.46	40.34	37.19	37.69	34.57	34.77	35.05	35.41	34.42	34.47	34.80	34.85	34.75
TiO_2	3.69	4.18	4.04	3.93	3.60	4.18	4.35	4.17	3.76	3.87	4.06	5.07	5.14	4.70	4.79	5.24
Al_2O_3	19.27	18.64	18.88	18.53	18.23	19.19	19.06	18.54	18.97	18.97	18.88	17.35	17.09	17.87	17.57	17.24
Cr_2O_3	0.00	0.00	0.06	0.09	0.08	0.02	0.03	0.03	0.05	0.00	0.05	0.08	0.10	0.09	0.08	0.11
FeO	16.64	17.50	17.97	17.24	16.60	17.48	17.51	17.38	16.72	17.47	17.08	19.95	19.27	19.31	19.14	19.77
MnO	0.33	0.36	0.34	0.33	0.30	0.33	0.30	0.37	0.31	0.28	0.30	0.11	0.05	0.07	0.00	0.05
MgO	10.92	10.80	11.24	11.08	10.70	10.46	10.37	10.77	11.02	10.81	11.01	9.58	9.74	9.98	10.08	9.60
CaO	0.08	0.01	0.06	0.00	0.00	0.00	0.00	0.00	0.02	0.04	0.05	0.01	0.00	0.00	0.00	0.00
Na_2O	0.18	0.16	0.06	0.13	0.15	0.17	0.11	0.16	0.16	0.15	0.14	0.06	0.09	0.10	0.07	0.09
K_2O	9.63	9.67	7.98	9.15	8.89	8.95	9.81	9.77	9.26	9.73	9.80	9.69	9.51	9.86	9.88	9.90
Total	94.92	96.05	96.71	96.95	98.89	97.98	99.23	95.76	95.04	96.38	96.78	96.33	95.46	96.78	96.46	96.76
Oxygens	11	11	11	11	11	11	11	11	11	11	11	11	11	11	11	11
Si	2.60	2.62	2.66	2.69	2.88	2.71	2.72	2.61	2.63	2.63	2.64	2.62	2.64	2.62	2.64	2.63
Ti	0.21	0.24	0.22	0.22	0.19	0.23	0.24	0.24	0.21	0.22	0.23	0.29	0.30	0.27	0.27	0.30
Al	1.73	1.65	1.64	1.61	1.53	1.65	1.62	1.65	1.69	1.68	1.66	1.56	1.54	1.59	1.57	1.54
Cr	0.00	0.00	0.00	0.01	0.00	0.00	0.00	0.00	0.00	0.00	0.00	0.01	0.01	0.01	0.00	0.01
Fe	1.06	1.10	1.11	1.07	0.99	1.07	1.06	1.10	1.06	1.09	1.06	1.27	1.23	1.22	1.21	1.25
Mn	0.02	0.02	0.02	0.02	0.02	0.02	0.02	0.02	0.02	0.02	0.02	0.01	0.00	0.00	0.00	0.00
Mg	1.24	1.21	1.24	1.22	1.14	1.14	1.12	1.21	1.24	1.21	1.22	1.09	1.11	1.12	1.14	1.08
Ca	0.01	0.00	0.00	0.00	0.00	0.00	0.00	0.00	0.00	0.00	0.00	0.00	0.00	0.00	0.00	0.00
Na	0.03	0.02	0.01	0.02	0.02	0.02	0.02	0.02	0.02	0.02	0.02	0.01	0.01	0.01	0.01	0.01
K	0.93	0.93	0.75	0.86	0.81	0.83	0.90	0.94	0.89	0.93	0.93	0.94	0.93	0.95	0.95	0.96
Total	7.81	7.80	7.67	7.72	7.58	7.67	7.69	7.81	7.77	7.79	7.78	7.78	7.77	7.79	7.79	7.78

Table A.14: Electron microprobe results for biotite – continued.

	PM13032 bi14(c)_rim	PM13032 bi15(c)_int	PM13032 bi15(c)_rim	PM13032 bi16(c)_int	PM13032 bi16(c)_rim	PM13032 bi17(gt10_incl)	PM13032 bi18(incl)	PM13032 bi(gt4_incl)	PM13032 bi2(gt4_incl)	PM13032 bi1(gt5_incl)	PM13032 bi2(gt5_incl)	PM13068 bi20(b)_int	PM13068 bi21(b)_int	PM13068 bi22(b)_int	PM13068 bi25(b)_rim	PM13068 bi19(b)_rim
SiO_2	34.42	35.09	35.01	34.23	34.67	34.83	35.08	35.51	35.30	34.73	35.03	35.55	34.14	34.17	35.27	35.57
TiO_2	5.10	4.90	4.78	4.83	4.64	3.97	4.77	4.17	5.19	4.38	4.74	3.47	4.27	3.55	4.40	3.61
Al_2O_3	17.39	17.53	17.54	17.36	17.39	17.91	17.80	18.14	17.82	17.85	17.92	18.50	17.87	17.79	18.52	18.36
Cr_2O_3	0.11	0.14	0.10	0.16	0.09	0.12	0.18	0.11	0.16	0.14	0.07	0.06	0.02	0.07	0.01	0.07
FeO	19.78	19.08	19.04	18.68	18.62	15.89	14.07	13.26	13.89	15.97	15.29	16.81	18.39	17.69	17.85	17.39
MnO	0.02	0.04	0.01	0.06	0.02	0.08	0.08	0.07	0.06	0.00	0.07	0.10	0.08	0.11	0.14	0.10
MgO	9.54	10.15	10.11	10.29	10.54	12.22	12.75	14.19	13.14	12.46	12.65	11.52	11.53	10.83	11.06	11.25
CaO	0.02	0.00	0.00	0.13	0.02	0.05	0.00	0.04	0.00	0.01	0.04	0.00	0.01	0.11	0.02	0.07
Na_2O	0.10	0.07	0.04	0.26	0.17	0.20	0.23	0.51	0.27	0.17	0.33	0.15	0.15	0.23	0.15	0.19
K_2O	9.82	9.84	9.78	9.64	9.71	8.92	9.55	9.66	9.54	9.81	9.17	9.41	8.13	8.67	9.63	9.23
Total	96.30	96.84	96.41	95.65	95.87	94.18	94.50	95.66	95.37	95.51	95.31	95.57	94.59	93.21	97.05	95.85
Oxygens	11	11	11	11	11	11	11	11	11	11	11	11	11	11	11	11
Si	2.62	2.64	2.64	2.61	2.63	2.64	2.64	2.63	2.63	2.61	2.62	2.67	2.60	2.64	2.63	2.67
Ti	0.29	0.28	0.27	0.28	0.26	0.23	0.27	0.23	0.29	0.25	0.27	0.20	0.24	0.21	0.25	0.20
Al	1.56	1.56	1.56	1.56	1.56	1.60	1.58	1.58	1.56	1.58	1.58	1.64	1.61	1.62	1.63	1.62
Cr	0.01	0.01	0.01	0.01	0.01	0.01	0.01	0.01	0.01	0.01	0.00	0.00	0.00	0.00	0.00	0.00
Fe	1.26	1.20	1.20	1.19	1.18	1.01	0.89	0.82	0.87	1.01	0.96	1.06	1.17	1.15	1.11	1.09
Mn	0.00	0.00	0.00	0.00	0.00	0.00	0.00	0.00	0.00	0.00	0.00	0.01	0.01	0.01	0.01	0.01
Mg	1.08	1.14	1.14	1.17	1.19	1.38	1.43	1.57	1.46	1.40	1.41	1.29	1.31	1.25	1.23	1.26
Ca	0.00	0.00	0.00	0.01	0.00	0.00	0.00	0.00	0.00	0.00	0.00	0.00	0.00	0.01	0.00	0.01
Na	0.02	0.01	0.01	0.04	0.02	0.03	0.03	0.07	0.04	0.02	0.05	0.02	0.02	0.03	0.02	0.03
K	0.95	0.94	0.94	0.94	0.94	0.86	0.92	0.91	0.91	0.94	0.88	0.90	0.79	0.86	0.91	0.88
Total	7.79	7.78	7.77	7.81	7.80	7.77	7.77	7.84	7.77	7.82	7.78	7.78	7.76	7.78	7.78	7.77

Table A.15: Electron microprobe results for biotite – continued.

	PM13068 bi23(c)	PM13068 bi24(c)	PM13068 bi25(b)	PM13068 bi26(b)	PM13068 bi26(b)	JMTV45 bi28(c)_int	JMTV45 bi28(c)_rim	JMTV45 bi29(c)_int	JMTV45 bi29(c)_rim	JMTV45 bi31(c)_int	JMTV45 bi31(c)_rim	JMTV45 bi34(b)_int	JMTV45 bi34(b)_rim	JMTV45 bi36(b)_int	JMTV45 bi36(b)_rim	JMTV45 bi27(c)
SiO_2	34.51	34.35	35.29	34.96	34.69	34.70	34.71	34.63	34.24	34.25	34.10	34.05	34.84	35.32	34.13	34.83
TiO_2	4.57	4.40	3.98	4.54	4.49	4.41	4.36	4.97	4.79	5.00	5.04	4.12	4.19	4.61	4.13	4.47
Al_2O_3	17.91	17.95	18.18	18.31	18.03	18.48	18.48	17.51	17.90	18.03	17.83	18.00	17.84	18.03	18.11	18.42
Cr_2O_3	0.04	0.02	0.06	0.02	0.00	0.18	0.22	0.37	0.27	0.09	0.09	0.14	0.14	0.05	0.06	0.22
FeO	18.31	17.82	18.03	17.69	17.29	18.90	18.97	18.89	18.46	19.20	20.06	18.52	17.93	16.59	16.92	19.80
MnO	0.07	0.05	0.15	0.19	0.11	0.10	0.04	0.08	0.06	0.06	0.08	0.01	0.00	0.10	0.05	0.07
MgO	10.72	10.33	11.01	11.12	11.39	9.52	9.39	9.18	9.50	9.38	8.93	10.98	10.61	11.28	11.40	9.44
CaO	0.00	0.04	0.04	0.02	0.00	0.03	0.00	0.00	0.06	0.00	0.00	0.06	0.04	0.03	0.14	0.00
Na_2O	0.12	0.16	0.20	0.14	0.08	0.12	0.13	0.09	0.23	0.11	0.17	0.12	0.20	0.11	0.14	0.10
K_2O	8.68	9.55	9.48	9.66	9.59	9.14	9.46	9.65	9.30	9.00	9.22	8.42	9.07	9.71	8.64	8.09
Total	94.92	94.67	96.42	96.65	95.67	95.58	95.77	95.37	94.80	95.12	95.52	94.42	94.86	95.83	93.73	95.44
Oxygens	11	11	11	11	11	11	11	11	11	11	11	11	11	11	11	11
Si	2.63	2.63	2.65	2.62	2.62	2.63	2.63	2.65	2.62	2.62	2.61	2.61	2.65	2.65	2.62	2.64
Ti	0.26	0.25	0.22	0.26	0.25	0.25	0.25	0.29	0.28	0.29	0.29	0.24	0.24	0.26	0.24	0.25
Al	1.61	1.62	1.61	1.62	1.60	1.65	1.65	1.58	1.62	1.62	1.61	1.62	1.60	1.59	1.64	1.65
Cr	0.00	0.00	0.00	0.00	0.00	0.01	0.01	0.02	0.02	0.01	0.01	0.01	0.01	0.00	0.00	0.01
Fe	1.16	1.14	1.13	1.11	1.09	1.20	1.20	1.21	1.18	1.23	1.28	1.19	1.14	1.04	1.08	1.25
Mn	0.00	0.00	0.01	0.01	0.01	0.01	0.00	0.01	0.00	0.00	0.01	0.00	0.00	0.01	0.00	0.00
Mg	1.22	1.18	1.23	1.24	1.28	1.08	1.06	1.05	1.09	1.07	1.02	1.25	1.20	1.26	1.30	1.07
Ca	0.00	0.00	0.00	0.00	0.00	0.00	0.00	0.00	0.01	0.00	0.00	0.00	0.00	0.00	0.01	0.00
Na	0.02	0.02	0.03	0.02	0.01	0.02	0.02	0.01	0.03	0.02	0.02	0.02	0.03	0.02	0.02	0.01
K	0.84	0.93	0.91	0.92	0.92	0.88	0.92	0.94	0.91	0.88	0.90	0.82	0.88	0.93	0.84	0.78
Total	7.74	7.79	7.79	7.79	7.79	7.73	7.75	7.74	7.75	7.73	7.75	7.76	7.76	7.76	7.76	7.67

Table A.16: Electron microprobe results for biotite – continued.

	JMTV45 bi32(c)	JMTV45 bi33(c)	JMTV45 bi35(b)	PM13076 bi37(c)	PM13076 bi38(c)	PM13076 bi39(c)	PM13076 bi40(c)	PM13076 bi41(c)	PM13076 bi42(c)	PM13076 bi43(b)	KK02 bi44(b)	KK02 bi45(b)	KK02 bi46(b)	KK02 bi47(b)_int	KK02 bi47(b)_rim	KK02 bi48(b)_int
SiO_2	34.32	34.50	35.11	34.79	34.54	34.61	34.50	34.68	34.75	34.78	35.10	34.99	34.84	34.91	35.60	35.58
TiO_2	4.71	4.30	3.73	3.55	3.98	4.21	3.00	4.56	3.95	3.94	3.00	2.98	2.89	2.93	2.95	2.93
Al_2O_3	18.10	18.14	18.29	19.17	19.30	18.41	19.43	18.54	18.67	18.66	19.16	19.05	19.15	18.97	19.24	19.25
Cr_2O_3	0.20	0.17	0.10	0.27	0.14	0.15	0.20	0.14	0.20	0.23	0.03	0.04	0.03	0.04	0.00	0.02
FeO	19.19	18.30	17.06	18.40	20.34	18.89	19.00	21.27	20.53	19.68	18.34	18.62	18.88	18.53	18.67	17.90
MnO	0.06	0.08	0.04	0.03	0.07	0.05	0.01	0.04	0.04	0.02	0.35	0.34	0.31	0.43	0.39	0.49
MgO	9.55	9.85	11.07	9.66	8.15	9.29	9.79	8.14	8.93	9.23	10.17	10.17	10.11	10.31	10.27	9.58
CaO	0.00	0.00	0.00	0.00	0.02	0.02	0.03	0.03	0.01	0.00	0.00	0.00	0.00	0.01	0.01	0.00
Na_2O	0.10	0.16	0.22	0.26	0.17	0.21	0.17	0.11	0.22	0.22	0.16	0.17	0.20	0.19	0.18	0.18
K_2O	9.66	9.48	9.74	9.62	9.61	9.68	9.63	9.74	9.61	9.73	9.60	9.77	9.68	9.52	9.57	9.69
Total	95.88	94.98	95.36	95.75	96.32	95.52	95.76	97.26	96.91	96.49	95.91	96.13	96.09	95.83	96.88	95.62
Oxygens	11	11	11	11	11	11	11	11	11	11	11	11	11	11	11	11
Si	2.61	2.64	2.65	2.63	2.62	2.64	2.62	2.62	2.63	2.63	2.65	2.64	2.64	2.64	2.66	2.69
Ti	0.27	0.25	0.21	0.20	0.23	0.24	0.17	0.26	0.22	0.22	0.17	0.17	0.16	0.17	0.17	0.17
Al	1.62	1.63	1.63	1.71	1.73	1.65	1.74	1.65	1.66	1.66	1.71	1.70	1.71	1.69	1.69	1.71
Cr	0.01	0.01	0.01	0.02	0.01	0.01	0.01	0.01	0.01	0.01	0.00	0.00	0.00	0.00	0.00	0.00
Fe	1.22	1.17	1.08	1.16	1.29	1.20	1.21	1.34	1.30	1.25	1.16	1.18	1.19	1.17	1.17	1.13
Mn	0.00	0.01	0.00	0.00	0.00	0.00	0.00	0.00	0.00	0.00	0.02	0.02	0.02	0.03	0.02	0.03
Mg	1.08	1.12	1.25	1.09	0.92	1.05	1.11	0.92	1.01	1.04	1.14	1.15	1.14	1.16	1.14	1.08
Ca	0.00	0.00	0.00	0.00	0.00	0.00	0.00	0.00	0.00	0.00	0.00	0.00	0.00	0.00	0.00	0.00
Na	0.01	0.02	0.03	0.04	0.03	0.03	0.02	0.02	0.03	0.03	0.02	0.02	0.03	0.03	0.03	0.03
K	0.94	0.92	0.94	0.93	0.93	0.94	0.93	0.94	0.93	0.94	0.92	0.94	0.93	0.92	0.91	0.93
Total	7.78	7.77	7.80	7.78	7.76	7.78	7.81	7.77	7.79	7.79	7.80	7.82	7.83	7.82	7.80	7.77

Table A.17: Electron microprobe results for biotite – continued.

	KK02 bi48(b)_rim	KK02 bi49(b)_int	KK02 bi49(b)_rim	KK02 bi50(b)_int	KK02 bi51(b)_int	KK02 bi51(b)_rim	KK02 bi52_int	KK02 bi52	KK02 bi53_int	KK02 bi53_rim	KK04 bi54_int	KK04 bi54_rim	KK04 bi55_int	KK04 bi55(a)_rim	KK04 bi57(a)	KK04 bi58(a)_rim
SiO_2	35.32	34.99	35.56	35.03	35.01	35.18	35.51	35.50	35.80	35.55	35.77	35.82	37.95	35.69	27.16	37.64
TiO_2	2.84	2.97	2.80	2.89	2.78	2.90	3.06	2.91	2.98	2.95	2.68	2.57	2.62	2.66	5.98	2.47
Al_2O_3	19.23	19.05	19.74	19.34	19.36	19.00	19.28	19.55	19.23	19.32	19.47	19.12	20.56	19.36	22.74	20.90
Cr_2O_3	0.00	0.03	0.04	0.01	0.06	0.04	0.02	0.06	0.02	0.03	0.06	0.03	0.07	0.03	0.03	0.06
FeO	18.15	18.31	17.93	17.23	17.52	17.35	17.17	17.88	17.49	17.49	17.84	18.18	16.06	18.06	25.22	17.15
MnO	0.43	0.39	0.40	0.52	0.49	0.45	0.47	0.43	0.42	0.51	0.44	0.40	0.38	0.45	0.48	0.35
MgO	10.26	10.19	9.93	10.45	10.07	10.08	10.16	10.64	10.51	10.24	10.24	10.44	9.01	10.14	10.28	8.49
CaO	0.01	0.00	0.00	0.00	0.00	0.00	0.00	0.01	0.00	0.00	0.00	0.00	0.03	0.00	0.09	0.00
Na_2O	0.23	0.17	0.29	0.19	0.17	0.15	0.22	0.17	0.18	0.11	0.15	0.15	0.20	0.16	0.08	0.13
K_2O	9.68	9.72	9.31	9.64	9.38	9.58	9.63	9.56	9.57	9.45	9.57	9.62	8.22	9.66	0.78	9.26
Total	96.15	95.82	96.00	95.29	94.83	94.72	95.53	96.71	96.20	95.66	96.22	96.33	95.09	96.21	92.86	96.45
Oxygens	11	11	11	11	11	11	11	11	11	11	11	11	11	11	11	11
Si	2.66	2.65	2.67	2.65	2.66	2.68	2.68	2.65	2.68	2.67	2.68	2.69	2.80	2.68	2.12	2.77
Ti	0.16	0.17	0.16	0.16	0.16	0.17	0.17	0.16	0.17	0.17	0.15	0.14	0.15	0.15	0.35	0.14
Al	1.71	1.70	1.75	1.73	1.73	1.70	1.71	1.72	1.70	1.71	1.72	1.69	1.79	1.71	2.09	1.81
Cr	0.00	0.00	0.00	0.00	0.00	0.00	0.00	0.00	0.00	0.00	0.00	0.00	0.00	0.00	0.00	0.00
Fe	1.14	1.16	1.12	1.09	1.11	1.10	1.08	1.12	1.09	1.10	1.12	1.14	0.99	1.13	1.64	1.06
Mn	0.03	0.03	0.03	0.03	0.03	0.03	0.03	0.03	0.03	0.03	0.03	0.03	0.02	0.03	0.03	0.02
Mg	1.15	1.15	1.11	1.18	1.14	1.14	1.14	1.18	1.17	1.15	1.14	1.17	0.99	1.13	1.19	0.93
Ca	0.00	0.00	0.00	0.00	0.00	0.00	0.00	0.00	0.00	0.00	0.00	0.00	0.00	0.00	0.01	0.00
Na	0.03	0.03	0.04	0.03	0.03	0.02	0.03	0.02	0.03	0.02	0.02	0.02	0.03	0.02	0.01	0.02
K	0.93	0.94	0.89	0.93	0.91	0.93	0.93	0.91	0.91	0.91	0.91	0.92	0.77	0.92	0.08	0.87
Total	7.81	7.81	7.77	7.80	7.78	7.78	7.77	7.79	7.78	7.76	7.78	7.80	7.56	7.79	7.53	7.63

Table A.18: Electron microprobe results for biotite – continued.

	KK04 bi58(a)_int	KK04 bi59(a)_int	KK04 bi59(a)_rim	KK04 bi60(a)_int	KK04 bi60(a)_rim	KK10 bi62(a)	KK10 bi63(a)_int	KK10 bi64(a)	KK10 bi65(a)_int	KK10 bi65(a)_rim	KK10 bi66(a)_int	KK10 bi66(a)_rim	KK10 bi67_int	KK10 bi67_rim	KK16 bi68(b)	KK16 bi69(b)
SiO_2	35.63	35.87	35.82	35.54	35.92	36.03	35.26	36.15	35.35	35.99	36.27	36.08	36.49	35.96	38.77	36.37
TiO_2	2.47	2.91	2.66	2.75	2.64	1.77	1.66	2.10	1.75	1.94	1.68	1.75	1.82	1.79	3.17	3.41
Al_2O_3	19.36	19.40	19.34	19.59	19.71	18.26	17.96	18.01	18.01	17.91	18.11	17.88	18.03	17.90	18.10	18.25
Cr_2O_3	0.04	0.05	0.03	0.04	0.06	0.00	0.05	0.03	0.02	0.00	0.02	0.00	0.02	0.00	0.01	0.05
FeO	18.12	18.23	17.63	17.45	17.74	16.86	17.57	17.59	17.12	17.22	17.17	16.93	17.03	16.88	17.40	16.95
MnO	0.38	0.46	0.50	0.49	0.52	0.36	0.47	0.39	0.44	0.39	0.46	0.48	0.41	0.41	0.10	0.05
MgO	10.02	9.96	9.87	10.53	10.45	12.66	13.43	12.37	13.36	12.55	13.04	12.75	12.67	12.87	10.82	11.20
CaO	0.00	0.00	0.00	0.01	0.00	0.00	0.00	0.00	0.02	0.00	0.01	0.01	0.00	0.00	0.01	0.07
Na_2O	0.18	0.17	0.17	0.20	0.17	0.04	0.11	0.05	0.12	0.16	0.17	0.16	0.07	0.06	0.08	0.14
K_2O	9.64	9.85	9.62	9.71	9.46	9.53	8.71	9.80	8.75	9.47	9.43	9.45	9.62	9.69	8.01	9.55
Total	95.85	96.91	95.64	96.31	96.67	95.51	95.22	96.49	94.93	95.63	96.36	95.48	96.16	95.56	96.47	96.05
Oxygens	11	11	11	11	11	11	11	11	11	11	11	11	11	11	11	11
Si	2.68	2.68	2.70	2.66	2.67	2.71	2.66	2.70	2.67	2.71	2.71	2.72	2.72	2.71	2.84	2.71
Ti	0.14	0.16	0.15	0.15	0.15	0.10	0.09	0.12	0.10	0.11	0.09	0.10	0.10	0.10	0.17	0.19
Al	1.72	1.71	1.72	1.73	1.73	1.62	1.60	1.59	1.60	1.59	1.59	1.59	1.59	1.59	1.56	1.61
Cr	0.00	0.00	0.00	0.00	0.00	0.00	0.00	0.00	0.00	0.00	0.00	0.00	0.00	0.00	0.00	0.00
Fe	1.14	1.14	1.11	1.09	1.10	1.06	1.11	1.10	1.08	1.08	1.07	1.07	1.06	1.06	1.07	1.06
Mn	0.02	0.03	0.03	0.03	0.03	0.02	0.03	0.02	0.03	0.02	0.03	0.03	0.03	0.03	0.01	0.00
Mg	1.13	1.11	1.11	1.17	1.16	1.42	1.51	1.38	1.51	1.41	1.45	1.43	1.41	1.44	1.18	1.25
Ca	0.00	0.00	0.00	0.00	0.00	0.00	0.00	0.00	0.00	0.00	0.00	0.00	0.00	0.00	0.00	0.01
Na	0.03	0.02	0.02	0.03	0.02	0.01	0.02	0.01	0.02	0.02	0.02	0.02	0.01	0.01	0.01	0.02
K	0.93	0.94	0.92	0.93	0.90	0.91	0.84	0.93	0.84	0.91	0.90	0.91	0.92	0.93	0.75	0.91
Total	7.79	7.79	7.77	7.80	7.77	7.84	7.87	7.86	7.86	7.85	7.86	7.86	7.84	7.87	7.59	7.76

Table A.19: Electron microprobe results for biotite – continued

	KK16 bi70(b)	KK16 bi71(b)	KK16 bi72(b)	KK27 bi73	KK27 bi74_int	KK27 bi74_rim	KK27 bi75_int	KK28 bi76_int	KK28 bi76_rim	KK28 bi77_int	KK28 bi77_rim	KK28 bi78(b)_int	KK28 bi78(b)_rim	KK28 bi79(b)_int	KK29 bi80(a)_int	KK29 bi80(a)_rim
SiO_2	35.91	36.00	35.05	35.94	35.37	35.48	35.56	40.14	34.97	35.58	35.64	35.87	35.65	34.89	35.54	35.87
TiO_2	3.29	3.69	2.70	3.18	3.24	3.37	3.02	1.49	2.94	2.81	2.82	2.79	2.77	2.71	3.07	2.76
Al_2O_3	18.44	18.47	18.83	18.09	18.05	18.40	18.25	23.46	17.89	18.12	18.67	18.53	18.51	18.71	19.49	19.87
Cr_2O_3	0.06	0.01	0.03	0.05	0.04	0.01	0.00	0.06	0.01	0.02	0.03	0.05	0.08	0.06	0.03	0.06
FeO	17.50	17.35	18.50	21.18	21.27	21.57	20.38	18.81	20.20	19.86	19.18	19.46	19.11	20.84	18.82	18.31
MnO	0.09	0.06	0.04	0.10	0.06	0.12	0.10	0.02	0.06	0.04	0.06	0.09	0.08	0.09	0.12	0.10
MgO	10.58	10.14	11.18	9.60	9.37	9.87	9.85	8.45	9.73	10.51	10.08	9.93	10.16	10.50	10.12	9.70
CaO	0.00	0.00	0.00	0.00	0.00	0.00	0.00	0.00	0.00	0.00	0.00	0.00	0.02	0.00	0.00	0.01
Na_2O	0.11	0.08	0.06	0.14	0.16	0.10	0.08	0.08	0.10	0.14	0.11	0.18	0.16	0.11	0.16	0.20
K_2O	9.58	9.64	8.51	9.71	9.68	9.65	9.58	5.43	8.91	9.71	9.60	9.50	9.44	8.66	9.08	9.17
Total	95.56	95.44	94.90	97.99	97.25	98.56	96.82	97.94	94.82	96.79	96.19	96.40	95.98	96.57	96.43	96.06
Oxygens	11	11	11	11	11	11	11	11	11	11	11	11	11	11	11	11
Si	2.70	2.71	2.66	2.69	2.67	2.64	2.68	2.83	2.69	2.68	2.69	2.70	2.69	2.63	2.66	2.68
Ti	0.19	0.21	0.15	0.18	0.18	0.19	0.17	0.08	0.17	0.16	0.16	0.16	0.16	0.15	0.17	0.16
Al	1.64	1.64	1.68	1.59	1.61	1.62	1.62	1.95	1.62	1.61	1.66	1.64	1.65	1.66	1.72	1.75
Cr	0.00	0.00	0.00	0.00	0.00	0.00	0.00	0.00	0.00	0.00	0.00	0.00	0.00	0.00	0.00	0.00
Fe	1.10	1.09	1.17	1.32	1.34	1.34	1.28	1.11	1.30	1.25	1.21	1.22	1.21	1.31	1.18	1.15
Mn	0.01	0.00	0.00	0.01	0.00	0.01	0.01	0.00	0.00	0.00	0.00	0.01	0.01	0.01	0.01	0.01
Mg	1.19	1.14	1.26	1.07	1.05	1.10	1.11	0.89	1.11	1.18	1.13	1.11	1.14	1.18	1.13	1.08
Ca	0.00	0.00	0.00	0.00	0.00	0.00	0.00	0.00	0.00	0.00	0.00	0.00	0.00	0.00	0.00	0.00
Na	0.02	0.01	0.01	0.02	0.02	0.01	0.01	0.01	0.01	0.02	0.02	0.03	0.02	0.02	0.02	0.03
K	0.92	0.93	0.82	0.93	0.93	0.92	0.92	0.49	0.87	0.93	0.92	0.91	0.91	0.83	0.87	0.88
Total	7.76	7.73	7.76	7.81	7.82	7.83	7.80	7.36	7.78	7.83	7.79	7.79	7.79	7.80	7.75	7.73

Table A.20: Electron microprobe results for biotite – continued.

	KK29 bi81(a)_int	KK29 bi81(a)_rim	KK29 bi82(a)_int	KK29 bi82(a)_rim	KK29 bi83(a)_int	KK29 bi83(a)_rim	KK29 bi84(a)_int	KK29 bi84(a)_rim	KK29 bi85(b)_int	KK29 bi86(b)	KK29 bi87(b)	KK29 bi88(b)
SiO_2	35.48	35.49	35.54	35.48	35.49	35.59	35.39	35.47	41.43	35.31	35.22	35.12
TiO_2	3.06	2.95	3.02	2.98	3.42	3.11	3.16	3.13	2.62	3.18	3.12	3.45
Al_2O_3	19.19	19.69	19.64	19.56	18.79	18.91	18.86	18.71	18.68	19.21	18.64	19.01
Cr_2O_3	0.05	0.03	0.07	0.08	0.01	0.02	0.08	0.08	0.02	0.03	0.05	0.06
FeO	18.86	19.03	18.83	19.24	19.27	19.58	18.93	18.55	18.67	19.07	18.84	18.76
MnO	0.11	0.17	0.11	0.11	0.19	0.12	0.09	0.15	0.10	0.14	0.14	0.12
MgO	9.90	10.10	10.23	10.17	10.18	10.14	10.44	10.60	10.44	10.60	10.45	10.35
CaO	0.01	0.00	0.00	0.00	0.00	0.00	0.00	0.00	0.00	0.00	0.00	0.00
Na_2O	0.17	0.10	0.08	0.18	0.18	0.16	0.16	0.15	0.26	0.22	0.02	0.13
K_2O	9.48	9.54	9.33	9.42	9.40	9.60	9.38	9.37	8.73	9.59	9.53	9.45
Total	96.31	97.11	96.85	97.21	96.93	97.23	96.49	96.21	100.95	97.35	96.02	96.45
Oxygens	11	11	11	11	11	11	11	11	11	11	11	11
Si	2.67	2.65	2.65	2.64	2.66	2.66	2.66	2.67	2.90	2.63	2.66	2.64
Ti	0.17	0.17	0.17	0.17	0.19	0.17	0.18	0.18	0.14	0.18	0.18	0.19
Al	1.70	1.73	1.73	1.72	1.66	1.67	1.67	1.66	1.54	1.69	1.66	1.68
Cr	0.00	0.00	0.00	0.00	0.00	0.00	0.00	0.00	0.00	0.00	0.00	0.00
Fe	1.19	1.19	1.17	1.20	1.21	1.22	1.19	1.17	1.09	1.19	1.19	1.18
Mn	0.01	0.01	0.01	0.01	0.01	0.01	0.01	0.01	0.01	0.01	0.01	0.01
Mg	1.11	1.12	1.14	1.13	1.14	1.13	1.17	1.19	1.09	1.18	1.18	1.16
Ca	0.00	0.00	0.00	0.00	0.00	0.00	0.00	0.00	0.00	0.00	0.00	0.00
Na	0.03	0.01	0.01	0.03	0.03	0.02	0.02	0.02	0.04	0.03	0.00	0.02
K	0.91	0.91	0.89	0.90	0.90	0.92	0.90	0.90	0.78	0.91	0.92	0.91
Total	7.78	7.78	7.77	7.79	7.78	7.80	7.79	7.79	7.59	7.82	7.79	7.79

Table A.21: Electron microprobe results for sillimanite.

	PM13010 sill2(b)	PM13010 sill3(b)	PM13010 sill4(b)	PM13010 sill5(b)	PM13010 sill6(b)	PM13010 sill7(b)	PM13010 sill8(a)	PM13010 sill8b(a)	PM13010 sill9(c)	PM13010 sill10(c)	PM13010 sill12(a)	PM13010 sill13(a)	PM13032 sill15	PM13032 sill16(c)	PM13068 sill20(a)	PM13068 sill20(a)	PM13068 sill21(a)	PM13068 sill22(a)
SiO_2	35.41	34.68	34.86	34.88	33.98	34.90	36.06	40.20	36.04	36.09	46.36	35.86	35.91	35.90	36.04	36.33	36.24	40.02
TiO_2	0.00	0.04	0.00	0.00	0.00	0.00	0.00	0.02	0.00	0.00	0.00	0.01	0.02	0.03	0.00	0.00	0.00	0.00
Al_2O_3	64.33	64.21	64.32	64.29	62.41	64.79	62.70	57.88	63.19	62.82	53.76	63.83	62.45	62.18	63.20	62.86	63.16	59.33
Cr_2O_3	0.06	0.05	0.02	0.05	0.00	0.00	0.00	0.03	0.00	0.00	0.02	0.00	0.07	0.11	0.05	0.01	0.00	0.04
FeO	0.71	0.96	0.80	0.62	1.53	0.67	0.68	0.68	1.14	0.91	0.56	1.05	0.95	0.89	0.93	1.05	0.95	0.84
MnO	0.01	0.08	0.02	0.00	0.04	0.04	0.03	0.04	0.03	0.03	0.00	0.04	0.02	0.04	0.00	0.04	0.07	0.04
MgO	0.00	0.00	0.00	0.00	0.31	0.00	0.02	0.00	0.02	0.02	0.00	0.00	0.00	0.01	0.02	0.02	0.02	0.15
CaO	0.00	0.02	0.01	0.02	0.15	0.00	0.07	0.02	0.05	0.07	0.02	0.00	0.05	0.01	0.03	0.04	0.05	0.05
Na_2O	0.02	0.00	0.02	0.03	0.00	0.01	0.01	0.01	0.00	0.00	0.01	0.01	0.02	0.02	0.02	0.00	0.00	0.08
K_2O	0.00	0.01	0.01	0.00	0.05	0.02	0.00	0.01	0.02	0.00	0.02	0.01	0.03	0.02	0.01	0.01	0.02	0.03
Total	100.54	100.06	100.05	99.89	98.48	100.44	99.57	98.89	100.50	99.94	100.74	100.82	99.51	99.23	100.30	100.36	100.52	100.59
Oxygens	5	5	5	5	5	5	5	5	5	5	5	5	5	5	5	5	5	5
Si	0.96	0.94	0.95	0.95	0.94	0.94	0.98	1.10	0.97	0.98	1.23	0.97	0.98	0.98	0.98	0.98	0.98	1.08
Ti	0.00	0.00	0.00	0.00	0.00	0.00	0.00	0.00	0.00	0.00	0.00	0.00	0.00	0.00	0.00	0.00	0.00	0.00
Al	2.05	2.06	2.06	2.06	2.04	2.06	2.01	1.86	2.01	2.01	1.68	2.03	2.01	2.01	2.02	2.00	2.01	1.88
Cr	0.00	0.00	0.00	0.00	0.00	0.00	0.00	0.00	0.00	0.00	0.00	0.00	0.00	0.00	0.00	0.00	0.00	0.00
Fe	0.02	0.02	0.02	0.01	0.04	0.02	0.02	0.02	0.03	0.02	0.01	0.02	0.02	0.02	0.02	0.02	0.02	0.02
Mn	0.00	0.00	0.00	0.00	0.00	0.00	0.00	0.00	0.00	0.00	0.00	0.00	0.00	0.00	0.00	0.00	0.00	0.00
Mg	0.00	0.00	0.00	0.00	0.01	0.00	0.00	0.00	0.00	0.00	0.00	0.00	0.00	0.00	0.00	0.00	0.00	0.01
Ca	0.00	0.00	0.00	0.00	0.00	0.00	0.00	0.00	0.00	0.00	0.00	0.00	0.00	0.00	0.00	0.00	0.00	0.00
Na	0.00	0.00	0.00	0.00	0.00	0.00	0.00	0.00	0.00	0.00	0.00	0.00	0.00	0.00	0.00	0.00	0.00	0.00
K	0.00	0.00	0.00	0.00	0.00	0.00	0.00	0.00	0.00	0.00	0.00	0.00	0.00	0.00	0.00	0.00	0.00	0.00
Total	3.02	3.03	3.03	3.02	3.04	3.03	3.01	2.97	3.02	3.01	2.93	3.02	3.02	3.01	3.02	3.01	3.02	2.99

Table A.22: Electron microprobe results for sillimanite – continued.

	PM13068 sill23(a)	PM13068 sill24(a)	PM13068 sill25(a)	PM13068 sill26(a)	PM13068 sill28(a)	PM13068 sill29(a)	PM13068 sill30(a)	PM13068 sill31(a)	PM13068 sill32(a)	PM13076 sill33(a)	PM13076 sill33(c)	PM13076 sill36(c)	PM13076 sill37(c)	PM13076 sill38(c)	KK02 sill43	KK02 sill44	KK02 sill45	KK02 sill46
SiO_2	36.53	36.50	36.22	36.57	36.21	36.00	36.16	36.08	35.96	36.04	35.95	40.15	36.47	36.20	35.88	35.84	36.27	36.25
TiO_2	0.02	0.00	0.00	0.00	0.04	0.00	0.00	0.00	0.00	0.00	0.00	0.00	0.00	0.01	0.02	0.00	0.02	0.01
Al_2O_3	63.07	63.31	63.25	62.81	62.81	62.92	63.21	62.85	63.33	63.09	63.90	60.05	63.70	63.81	63.18	63.35	62.65	63.55
Cr_2O_3	0.00	0.01	0.04	0.01	0.08	0.01	0.06	0.05	0.06	0.02	0.09	0.01	0.02	0.06	0.03	0.02	0.00	0.01
FeO	0.78	0.85	0.97	0.99	1.18	1.35	1.49	1.30	1.16	1.21	0.75	0.48	0.56	0.60	1.32	0.96	0.94	1.02
MnO	0.00	0.05	0.08	0.04	0.06	0.01	0.02	0.03	0.04	0.01	0.05	0.05	0.03	0.04	0.05	0.03	0.00	0.03
MgO	0.01	0.01	0.00	0.00	0.01	0.00	0.00	0.01	0.06	0.03	0.00	0.03	0.00	0.00	0.01	0.00	0.03	0.00
CaO	0.04	0.04	0.00	0.02	0.01	0.02	0.00	0.02	0.05	0.00	0.03	0.01	0.00	0.01	0.02	0.00	0.02	0.00
Na_2O	0.02	0.01	0.09	0.06	0.02	0.03	0.02	0.03	0.01	0.03	0.01	0.02	0.00	0.02	0.00	0.01	0.01	0.00
K_2O	0.01	0.01	0.04	0.00	0.01	0.01	0.00	0.00	0.01	0.00	0.00	0.02	0.01	0.03	0.00	0.00	0.00	0.00
Total	100.48	100.77	100.69	100.49	100.44	100.34	100.96	100.37	100.68	100.43	100.80	100.81	100.79	100.79	100.50	100.22	99.93	100.87
Oxygens	5	5	5	5	5	5	5	5	5	5	5	5	5	5	5	5	5	5
Si	0.99	0.98	0.98	0.99	0.98	0.98	0.97	0.98	0.97	0.98	0.97	1.07	0.98	0.97	0.97	0.97	0.98	0.98
Ti	0.00	0.00	0.00	0.00	0.00	0.00	0.00	0.00	0.00	0.00	0.00	0.00	0.00	0.00	0.00	0.00	0.00	0.00
Al	2.01	2.01	2.01	2.00	2.00	2.01	2.01	2.01	2.02	2.01	2.03	1.89	2.02	2.02	2.02	2.02	2.00	2.02
Cr	0.00	0.00	0.00	0.00	0.00	0.00	0.00	0.00	0.00	0.00	0.00	0.00	0.00	0.00	0.00	0.00	0.00	0.00
Fe	0.02	0.02	0.02	0.02	0.03	0.03	0.03	0.03	0.03	0.03	0.02	0.01	0.01	0.01	0.03	0.02	0.02	0.02
Mn	0.00	0.00	0.00	0.00	0.00	0.00	0.00	0.00	0.00	0.00	0.00	0.00	0.00	0.00	0.00	0.00	0.00	0.00
Mg	0.00	0.00	0.00	0.00	0.00	0.00	0.00	0.00	0.00	0.00	0.00	0.00	0.00	0.00	0.00	0.00	0.00	0.00
Ca	0.00	0.00	0.00	0.00	0.00	0.00	0.00	0.00	0.00	0.00	0.00	0.00	0.00	0.00	0.00	0.00	0.00	0.00
Na	0.00	0.00	0.00	0.00	0.00	0.00	0.00	0.00	0.00	0.00	0.00	0.00	0.00	0.00	0.00	0.00	0.00	0.00
K	0.00	0.00	0.00	0.00	0.00	0.00	0.00	0.00	0.00	0.00	0.00	0.00	0.00	0.00	0.00	0.00	0.00	0.00
Total	3.01	3.01	3.02	3.01	3.02	3.02	3.02	3.02	3.02	3.02	3.02	2.98	3.01	3.02	3.02	3.02	3.01	3.02

Table A.23: Electron microprobe results for sillimanite – continued.

	KK02 sill47	KK02 sill48	KK02 sill49	KK02 sill41	KK02 sill42	KK16 sill55	KK16 sill56	KK16 sill57	KK16 sill58	KK29 sill60	KK29 sill61	KK29 sill62	KK29 sill63	KK29 sill64	KK29 sill65
SiO_2	36.15	36.07	36.27	36.22	36.68	36.81	36.82	36.22	36.24	36.44	36.89	37.22	36.59	36.67	36.82
TiO_2	0.00	0.00	0.00	0.01	0.00	0.00	0.00	0.01	0.01	0.01	0.00	0.34	0.00	0.03	0.02
Al_2O_3	63.29	63.53	63.83	62.24	63.83	63.18	64.01	63.45	63.32	63.65	63.44	62.35	63.63	63.61	63.50
Cr_2O_3	0.05	0.04	0.08	0.04	0.03	0.04	0.04	0.01	0.01	0.02	0.08	0.02	0.02	0.01	0.00
FeO	1.29	1.22	0.64	1.25	1.09	0.79	0.63	1.02	0.61	0.79	0.89	1.22	0.90	1.12	0.81
MnO	0.00	0.05	0.04	0.05	0.02	0.07	0.04	0.03	0.02	0.03	0.03	0.00	0.03	0.00	0.03
MgO	0.01	0.00	0.00	0.03	0.00	0.02	0.00	0.03	0.02	0.00	0.02	0.94	0.04	0.03	0.00
CaO	0.01	0.00	0.00	0.06	0.01	0.01	0.00	0.01	0.01	0.00	0.00	0.01	0.00	0.00	0.00
Na_2O	0.01	0.00	0.04	0.02	0.01	0.01	0.02	0.00	0.00	0.02	0.04	0.04	0.01	0.02	0.00
K_2O	0.00	0.00	0.00	0.02	0.03	0.01	0.00	0.01	0.00	0.00	0.01	0.05	0.01	0.03	0.01
Total	100.80	100.91	100.90	99.94	101.69	100.94	101.56	100.79	100.23	100.97	101.40	102.19	101.24	101.51	101.19
Oxygens	5	5	5	5	5	5	5	5	5	5	5	5	5	5	5
Si	0.97	0.97	0.97	0.99	0.98	0.99	0.98	0.98	0.98	0.98	0.99	0.99	0.98	0.98	0.99
Ti	0.00	0.00	0.00	0.00	0.00	0.00	0.00	0.00	0.00	0.00	0.00	0.01	0.00	0.00	0.00
Al	2.01	2.02	2.02	2.00	2.01	2.00	2.01	2.02	2.02	2.02	2.00	1.96	2.01	2.01	2.01
Cr	0.00	0.00	0.00	0.00	0.00	0.00	0.00	0.00	0.00	0.00	0.00	0.00	0.00	0.00	0.00
Fe	0.03	0.03	0.01	0.03	0.02	0.02	0.01	0.02	0.01	0.02	0.02	0.03	0.02	0.02	0.02
Mn	0.00	0.00	0.00	0.00	0.00	0.00	0.00	0.00	0.00	0.00	0.00	0.00	0.00	0.00	0.00
Mg	0.00	0.00	0.00	0.00	0.00	0.00	0.00	0.00	0.00	0.00	0.00	0.04	0.00	0.00	0.00
Ca	0.00	0.00	0.00	0.00	0.00	0.00	0.00	0.00	0.00	0.00	0.00	0.00	0.00	0.00	0.00
Na	0.00	0.00	0.00	0.00	0.00	0.00	0.00	0.00	0.00	0.00	0.00	0.00	0.00	0.00	0.00
K	0.00	0.00	0.00	0.00	0.00	0.00	0.00	0.00	0.00	0.00	0.00	0.00	0.00	0.00	0.00
Total	3.02	3.02	3.01	3.02	3.02	3.01	3.01	3.02	3.01	3.01	3.01	3.02	3.01	3.02	3.01

Table A.24: Electron microprobe results for feldspars.

	PM13010 fsp3_int	PM13010 fsp3_rim	PM13010 fsp4_int	PM13010 fsp4_rim	PM13010 fsp5_int	PM13010 fsp5_rim	PM13010 fsp6_int	PM13010 fsp6_rim	PM13010 fsp2	PM13010 fsp2b	PM13010 fsp_corona1	PM13010 fsp_corona1b	PM13010 fsp_corona1d	PM13010 fsp_corona1g	PM13032 fsp8_int	PM13032 fsp8_rim	PM13032 fsp9_int	PM13032 fsp9_rim
SiO_2	64.80	64.44	64.64	64.49	64.18	64.63	65.04	64.56	65.53	58.97	57.72	57.53	58.20	60.05	64.46	64.84	57.27	58.77
TiO_2	0.00	0.02	0.04	0.00	0.02	0.03	0.00	0.05	0.03	0.00	0.00	0.00	0.00	0.01	0.04	0.04	0.00	0.00
Al_2O_3	20.06	19.20	19.16	19.03	19.09	18.91	19.11	19.16	19.35	26.75	26.52	26.41	26.87	26.49	19.14	18.97	27.99	27.26
Cr_2O_3	0.00	0.00	0.00	0.00	0.00	0.03	0.03	0.00	0.00	0.00	0.00	0.00	0.02	0.00	0.00	0.04	0.02	0.04
FeO	0.06	0.07	0.04	0.17	0.01	0.06	0.05	0.07	0.20	0.10	0.08	0.08	0.05	0.06	0.03	0.00	0.09	0.05
MnO	0.02	0.03	0.01	0.04	0.05	0.00	0.03	0.05	0.00	0.00	0.05	0.01	0.07	0.03	0.03	0.00	0.00	0.05
MgO	0.00	0.00	0.02	0.00	0.00	0.00	0.00	0.00	0.00	0.00	0.00	0.01	0.03	0.01	0.02	0.00	0.02	0.00
CaO	0.05	0.03	0.02	0.00	0.01	0.00	0.00	0.01	0.04	7.09	7.09	7.07	7.37	6.70	0.06	0.04	8.81	7.88
Na_2O	2.21	1.80	2.57	1.18	1.12	1.60	1.14	1.42	2.77	6.97	7.00	7.11	6.77	7.12	1.18	1.21	5.97	6.47
K_2O	12.02	13.99	12.86	14.57	14.96	13.92	15.07	14.44	12.49	0.07	0.09	0.09	0.08	0.09	14.68	14.57	0.17	0.12
Total	99.22	99.58	99.37	99.48	99.46	99.18	100.47	99.76	100.40	99.96	98.56	98.30	99.46	100.56	99.64	99.72	100.34	100.64
Oxygens	8	8	8	8	8	8	8	8	8	8	8	8	8	8	8	8	8	8
Si	2.96	2.97	2.97	2.98	2.97	2.98	2.98	2.97	2.98	2.62	2.61	2.61	2.61	2.65	2.97	2.98	2.55	2.60
Ti	0.00	0.00	0.00	0.00	0.00	0.00	0.00	0.00	0.00	0.00	0.00	0.00	0.00	0.00	0.00	0.00	0.00	0.00
Al	1.08	1.04	1.04	1.04	1.04	1.03	1.03	1.04	1.04	1.40	1.41	1.41	1.42	1.38	1.04	1.03	1.47	1.42
Cr	0.00	0.00	0.00	0.00	0.00	0.00	0.00	0.00	0.00	0.00	0.00	0.00	0.00	0.00	0.00	0.00	0.00	0.00
Fe	0.00	0.00	0.00	0.01	0.00	0.00	0.00	0.00	0.01	0.00	0.00	0.00	0.00	0.00	0.00	0.00	0.00	0.00
Mn	0.00	0.00	0.00	0.00	0.00	0.00	0.00	0.00	0.00	0.00	0.00	0.00	0.00	0.00	0.00	0.00	0.00	0.00
Mg	0.00	0.00	0.00	0.00	0.00	0.00	0.00	0.00	0.00	0.00	0.00	0.00	0.00	0.00	0.00	0.00	0.00	0.00
Ca	0.00	0.00	0.00	0.00	0.00	0.00	0.00	0.00	0.00	0.34	0.34	0.34	0.35	0.32	0.00	0.00	0.42	0.37
Na	0.20	0.16	0.23	0.11	0.10	0.14	0.10	0.13	0.24	0.60	0.61	0.63	0.59	0.61	0.11	0.11	0.52	0.56
K	0.70	0.82	0.75	0.86	0.88	0.82	0.88	0.85	0.72	0.00	0.01	0.01	0.00	0.00	0.86	0.86	0.01	0.01
Total	4.95	5.00	5.00	4.99	5.00	4.98	5.00	4.99	4.99	4.98	4.99	5.00	4.98	4.97	4.99	4.98	4.97	4.97

Table A.25: Electron microprobe results for feldspars – continued.

	PM13032 fsp10_int	PM13032 fsp10_rim	PM13032 fsp11_int	PM13032 fsp11_rim	PM13032 fsp12_int	PM13032 fsp13_rim	PM13032 fsp14_int	PM13032 fsp14_rim	PM13032 fsp15_int	PM13032 fsp15_rim	PM13032 fsp16_int	PM13032 fsp16_rim	PM13032 fsp17_core	PM13032 fsp17_rim	PM13032 fsp18_int	PM13032 fsp18_rim	PM13032 fsp19_int	PM13032 fsp7_int
SiO_2	58.09	58.33	59.02	58.42	58.53	58.46	58.52	59.19	64.85	65.00	65.52	65.21	64.57	64.37	64.56	64.16	65.40	64.28
TiO_2	0.01	0.04	0.00	0.00	0.04	0.00	0.00	0.00	0.02	0.05	0.06	0.02	0.04	0.06	0.09	0.05	0.02	0.00
Al_2O_3	27.38	27.12	26.89	27.36	26.99	26.50	26.60	26.85	18.90	18.93	19.24	19.14	19.18	19.03	19.01	18.93	18.90	26.73
Cr_2O_3	0.02	0.00	0.02	0.01	0.00	0.00	0.00	0.01	0.00	0.00	0.01	0.00	0.00	0.03	0.00	0.00	0.02	0.00
FeO	0.07	0.05	0.06	0.05	0.06	0.05	0.05	0.08	0.01	0.09	0.06	0.03	0.00	0.05	0.04	0.05	0.03	0.06
MnO	0.04	0.00	0.09	0.03	0.00	0.00	0.04	0.01	0.00	0.05	0.04	0.08	0.01	0.02	0.03	0.01	0.00	0.04
MgO	0.00	0.01	0.00	0.00	0.00	0.01	0.01	0.01	0.03	0.01	0.01	0.01	0.00	0.01	0.01	0.01	0.02	0.00
CaO	8.17	8.11	7.80	8.04	7.72	7.66	7.74	7.71	0.05	0.02	0.04	0.04	0.03	0.03	0.05	0.02	0.03	7.38
Na_2O	6.48	6.37	6.60	6.52	6.57	6.62	6.54	6.61	1.30	1.19	1.41	1.25	1.30	1.22	1.21	1.12	1.50	6.57
K_2O	0.17	0.14	0.19	0.17	0.17	0.16	0.12	0.16	14.51	14.67	14.24	14.83	14.62	14.72	14.65	15.03	14.23	0.12
Total	100.42	100.17	100.67	100.61	100.08	99.45	99.62	100.64	99.67	100.01	100.62	100.61	99.76	99.54	99.66	99.38	100.15	105.18
Oxygens	8	8	8	8	8	8	8	8	8	8	8	8	8	8	8	8	8	8
Si	2.58	2.60	2.61	2.59	2.61	2.62	2.62	2.62	2.99	2.98	2.98	2.98	2.97	2.97	2.98	2.97	2.99	2.70
Ti	0.00	0.00	0.00	0.00	0.00	0.00	0.00	0.00	0.00	0.00	0.00	0.00	0.00	0.00	0.00	0.00	0.00	0.00
Al	1.44	1.42	1.40	1.43	1.42	1.40	1.40	1.40	1.03	1.02	1.03	1.03	1.04	1.04	1.03	1.03	1.02	1.32
Cr	0.00	0.00	0.00	0.00	0.00	0.00	0.00	0.00	0.00	0.00	0.00	0.00	0.00	0.00	0.00	0.00	0.00	0.00
Fe	0.00	0.00	0.00	0.00	0.00	0.00	0.00	0.00	0.00	0.00	0.00	0.00	0.00	0.00	0.00	0.00	0.00	0.00
Mn	0.00	0.00	0.00	0.00	0.00	0.00	0.00	0.00	0.00	0.00	0.00	0.00	0.00	0.00	0.00	0.00	0.00	0.00
Mg	0.00	0.00	0.00	0.00	0.00	0.00	0.00	0.00	0.00	0.00	0.00	0.00	0.00	0.00	0.00	0.00	0.00	0.00
Ca	0.39	0.39	0.37	0.38	0.37	0.37	0.37	0.37	0.00	0.00	0.00	0.00	0.00	0.00	0.00	0.00	0.00	0.33
Na	0.56	0.55	0.57	0.56	0.57	0.58	0.57	0.57	0.12	0.11	0.12	0.11	0.12	0.11	0.11	0.10	0.13	0.54
K	0.01	0.01	0.01	0.01	0.01	0.01	0.01	0.01	0.85	0.86	0.83	0.86	0.86	0.87	0.86	0.89	0.83	0.01
Total	4.98	4.97	4.97	4.98	4.97	4.97	4.97	4.97	4.98	4.98	4.97	4.99	4.99	4.99	4.99	5.00	4.98	4.91

Table A.26: Electron microprobe results for feldspars – continued.

	PM13068 fsp19_int	PM13068 fsp19_rim	PM13068 fsp20_int	PM13068 fsp20_rim	PM13068 fsp21_core	PM13068 fsp21_rim	PM13068 fsp22_int	PM13068 fsp22_rim	PM13068 fsp24_rim	PM13068 fsp23_int	JMTV45 fsp26	JMTV45 fsp27	JMTV45 fsp28	JMTV45 fsp30	JMTV45 fsp31	JMTV45 fsp32	JMTV45 fsp33	JMTV45 fsp34
SiO_2	65.40	65.12	65.21	66.04	65.81	66.04	65.33	62.78	65.11	65.35	64.80	61.57	61.94	61.71	62.24	67.02	65.57	60.25
TiO_2	0.02	0.01	0.04	0.00	0.05	0.02	0.01	0.01	0.13	0.06	0.05	0.03	0.00	0.02	0.01	0.05	0.04	0.01
Al_2O_3	18.90	18.59	19.12	18.94	19.13	19.08	18.78	20.26	18.68	18.99	18.96	24.72	24.85	25.12	24.98	19.33	19.18	24.10
Cr_2O_3	0.02	0.01	0.00	0.00	0.00	0.04	0.00	0.00	0.00	0.00	0.00	0.00	0.01	0.00	0.03	0.01	0.00	0.02
FeO	0.03	0.06	0.03	0.05	0.02	0.01	0.01	0.65	0.06	0.04	0.05	0.05	0.05	0.08	0.04	0.16	0.02	0.07
MnO	0.00	0.03	0.00	0.06	0.12	0.02	0.06	0.07	0.10	0.00	0.01	0.06	0.03	0.03	0.02	0.03	0.00	0.00
MgO	0.02	0.01	0.02	0.02	0.00	0.01	0.00	0.50	0.00	0.00	0.00	0.00	0.02	0.00	0.03	0.00	0.00	0.00
CaO	0.03	0.00	0.08	0.04	0.09	0.11	0.02	0.03	0.00	0.03	0.05	5.32	5.34	5.63	5.34	0.07	0.02	5.26
Na_2O	1.50	1.17	2.65	2.93	2.27	3.08	2.07	1.09	1.07	1.80	1.61	7.99	7.87	8.02	8.01	3.86	1.67	7.31
K_2O	14.23	14.78	12.71	11.65	13.11	12.37	13.08	13.43	15.00	13.54	14.41	0.14	0.12	0.07	0.12	10.38	14.46	0.09
Total	100.15	99.78	99.86	99.74	100.60	100.79	99.37	98.81	100.14	99.81	99.94	99.87	100.22	100.68	100.82	100.91	100.97	97.10
Oxygens	8	8	8	8	8	8	8	8	8	8	8	8	8	8	8	8	8	8
Si	2.99	3.00	2.98	3.00	2.99	2.99	3.00	2.91	2.99	2.99	2.98	2.73	2.73	2.72	2.73	3.00	2.98	2.74
Ti	0.00	0.00	0.00	0.00	0.00	0.00	0.00	0.00	0.00	0.00	0.00	0.00	0.00	0.00	0.00	0.00	0.00	0.00
Al	1.02	1.01	1.03	1.01	1.02	1.02	1.02	1.11	1.01	1.02	1.03	1.29	1.29	1.30	1.29	1.02	1.03	1.29
Cr	0.00	0.00	0.00	0.00	0.00	0.00	0.00	0.00	0.00	0.00	0.00	0.00	0.00	0.00	0.00	0.00	0.00	0.00
Fe	0.00	0.00	0.00	0.00	0.00	0.00	0.00	0.03	0.00	0.00	0.00	0.00	0.00	0.00	0.00	0.01	0.00	0.00
Mn	0.00	0.00	0.00	0.00	0.00	0.00	0.00	0.00	0.00	0.00	0.00	0.00	0.00	0.00	0.00	0.00	0.00	0.00
Mg	0.00	0.00	0.00	0.00	0.00	0.00	0.00	0.03	0.00	0.00	0.00	0.00	0.00	0.00	0.00	0.00	0.00	0.00
Ca	0.00	0.00	0.00	0.00	0.00	0.01	0.00	0.00	0.00	0.00	0.00	0.25	0.25	0.27	0.25	0.00	0.00	0.26
Na	0.13	0.10	0.23	0.26	0.20	0.27	0.18	0.10	0.10	0.16	0.14	0.69	0.67	0.68	0.68	0.33	0.15	0.64
K	0.83	0.87	0.74	0.68	0.76	0.71	0.77	0.80	0.88	0.79	0.84	0.01	0.01	0.00	0.01	0.59	0.84	0.01
Total	4.98	4.98	4.99	4.96	4.98	5.00	4.97	4.98	4.99	4.97	5.00	4.97	4.96	4.98	4.97	4.96	5.00	4.94

Table A.27: Electron microprobe results for feldspars – continued.

	JMTV45	JMTV45	JMTV45	JMTV45	PM13076	PM13076	PM13076	PM13076	PM13076	PM13076	PM13076	PM13076	PM13076	PM13076	PM13076	KK02	KK02	KK02
	fsp35	fsp37	fsp38	fsp39	fsp41_int	fsp41_rim	fsp42_int	fsp42_rim	fsp43_rim	fsp44_int	fsp44_rim	fsp45_int	fsp45_rim	fsp40	fsp46	fsp47	fsp48	fsp49
SiO_2	62.40	65.73	65.38	65.24	64.80	64.21	64.90	64.91	64.86	64.87	65.67	65.15	65.16	64.87	64.65	65.27	63.85	64.77
TiO_2	0.00	0.04	0.00	0.01	0.03	0.02	0.02	0.00	0.00	0.01	0.03	0.01	0.02	0.02	0.00	0.01	0.02	0.07
Al_2O_3	24.80	19.27	19.16	19.14	19.10	19.14	19.17	19.18	19.28	19.08	19.38	19.20	19.29	19.05	19.09	19.82	19.60	19.73
Cr_2O_3	0.00	0.00	0.00	0.01	0.00	0.03	0.00	0.00	0.00	0.00	0.00	0.00	0.00	0.00	0.01	0.01	0.00	0.00
FeO	0.02	0.10	0.06	0.09	0.04	0.08	0.00	0.01	0.12	0.13	0.11	0.08	0.08	0.05	0.00	0.04	0.13	0.05
MnO	0.03	0.00	0.02	0.06	0.09	0.00	0.04	0.00	0.04	0.03	0.04	0.05	0.03	0.06	0.00	0.05	0.00	0.00
MgO	0.00	0.00	0.02	0.00	0.02	0.02	0.02	0.03	0.00	0.01	0.01	0.02	0.00	0.00	0.00	0.03	0.01	0.00
CaO	5.30	0.02	0.03	0.04	0.02	0.00	0.02	0.00	0.00	0.01	0.00	0.00	0.01	0.00	0.01	0.01	0.00	0.00
Na_2O	8.07	0.96	0.95	0.99	0.88	0.89	1.45	1.71	1.05	1.66	2.01	1.62	1.77	0.95	0.92	3.12	1.29	1.80
K_2O	0.15	15.39	15.28	15.21	15.79	15.51	14.80	12.91	15.31	14.08	13.04	15.14	14.14	15.27	15.35	11.50	14.23	13.25
Total	100.77	101.51	100.91	100.80	100.76	99.90	100.42	98.77	100.66	99.88	100.29	101.25	100.51	100.27	100.03	99.85	99.13	99.67
Oxygens	8	8	8	8	8	8	8	8	8	8	8	8	8	8	8	8	8	8
Si	2.74	2.98	2.98	2.98	2.97	2.97	2.97	2.99	2.97	2.98	2.98	2.97	2.97	2.98	2.98	2.97	2.96	2.96
Ti	0.00	0.00	0.00	0.00	0.00	0.00	0.00	0.00	0.00	0.00	0.00	0.00	0.00	0.00	0.00	0.00	0.00	0.00
Al	1.28	1.03	1.03	1.03	1.03	1.04	1.04	1.04	1.04	1.03	1.04	1.03	1.04	1.03	1.04	1.06	1.07	1.06
Cr	0.00	0.00	0.00	0.00	0.00	0.00	0.00	0.00	0.00	0.00	0.00	0.00	0.00	0.00	0.00	0.00	0.00	0.00
Fe	0.00	0.00	0.00	0.00	0.00	0.00	0.00	0.00	0.00	0.00	0.00	0.00	0.00	0.00	0.00	0.00	0.00	0.00
Mn	0.00	0.00	0.00	0.00	0.00	0.00	0.00	0.00	0.00	0.00	0.00	0.00	0.00	0.00	0.00	0.00	0.00	0.00
Mg	0.00	0.00	0.00	0.00	0.00	0.00	0.00	0.00	0.00	0.00	0.00	0.00	0.00	0.00	0.00	0.00	0.00	0.00
Ca	0.25	0.00	0.00	0.00	0.00	0.00	0.00	0.00	0.00	0.00	0.00	0.00	0.00	0.00	0.00	0.00	0.00	0.00
Na	0.69	0.08	0.08	0.09	0.08	0.08	0.13	0.15	0.09	0.15	0.18	0.14	0.16	0.08	0.08	0.27	0.12	0.16
K	0.01	0.89	0.89	0.89	0.92	0.91	0.86	0.76	0.89	0.82	0.76	0.88	0.82	0.89	0.90	0.67	0.84	0.77
Total	4.97	4.99	4.99	4.99	5.01	5.01	5.01	4.95	5.00	4.99	4.96	5.03	5.00	4.99	5.00	4.97	4.99	4.97

Table A.28: Electron microprobe results for feldspars – continued.

	KK02 fsp50	KK02 fsp51	KK02 fsp52	KK02 fsp53	KK02 fsp54	KK02 fsp55	KK02 fsp56	KK02 fsp57	KK04 fsp58_int	KK04 fsp59_int	KK04 fsp59_rim	KK04 fsp60_int	KK04 fsp60_rim	KK04 fsp61_int	KK04 fsp61_rim	KK04 fsp62_int	KK04 fsp62_rim	KK04 fsp63_int
SiO_2	64.46	61.89	39.29	64.31	62.00	65.80	62.09	64.22	63.50	63.54	63.30	63.36	63.22	63.61	63.37	63.76	62.69	63.32
TiO_2	0.04	0.00	0.00	0.02	0.00	0.00	0.00	0.02	0.00	0.00	0.00	0.03	0.01	0.01	0.03	0.03	0.02	0.02
Al_2O_3	19.61	25.08	56.86	19.65	25.18	19.82	25.45	19.26	24.37	23.49	23.82	23.83	23.79	23.90	23.81	23.77	24.00	23.64
Cr_2O_3	0.00	0.00	0.01	0.01	0.01	0.00	0.00	0.00	0.01	0.00	0.01	0.00	0.00	0.00	0.04	0.01	0.00	0.00
FeO	0.03	0.08	0.67	0.00	0.00	0.04	0.08	0.03	0.11	0.07	0.13	0.05	0.06	0.04	0.01	0.04	0.00	0.05
MnO	0.01	0.05	0.04	0.02	0.03	0.06	0.02	0.00	0.00	0.00	0.00	0.06	0.02	0.00	0.04	0.04	0.07	0.00
MgO	0.00	0.00	0.02	0.00	0.01	0.02	0.00	0.00	0.04	0.01	0.00	0.02	0.00	0.01	0.01	0.02	0.01	0.02
CaO	0.00	5.39	0.00	0.00	5.34	0.03	5.35	0.00	4.40	4.27	4.36	4.36	4.33	4.33	4.28	4.20	4.47	4.23
Na_2O	1.43	8.06	0.08	1.66	7.76	3.95	7.97	1.69	8.04	8.36	8.35	8.54	8.36	8.42	8.19	8.43	8.44	8.49
K_2O	13.94	0.13	2.52	13.84	0.12	11.00	0.14	13.64	0.21	0.24	0.16	0.21	0.16	0.22	0.16	0.27	0.22	0.24
Total	99.53	100.68	99.48	99.52	100.46	100.73	101.10	98.86	100.67	99.98	100.14	100.45	99.95	100.54	99.93	100.57	99.91	100.00
Oxygens	8	8	8	8	8	8	8	8	8	8	8	8	8	8	8	8	8	8
Si	2.96	2.72	1.73	2.96	2.73	2.96	2.72	2.97	2.78	2.80	2.79	2.78	2.79	2.79	2.79	2.79	2.77	2.79
Ti	0.00	0.00	0.00	0.00	0.00	0.00	0.00	0.00	0.00	0.00	0.00	0.00	0.00	0.00	0.00	0.00	0.00	0.00
Al	1.06	1.30	2.96	1.07	1.31	1.05	1.31	1.05	1.26	1.22	1.24	1.23	1.24	1.24	1.24	1.23	1.25	1.23
Cr	0.00	0.00	0.00	0.00	0.00	0.00	0.00	0.00	0.00	0.00	0.00	0.00	0.00	0.00	0.00	0.00	0.00	0.00
Fe	0.00	0.00	0.02	0.00	0.00	0.00	0.00	0.00	0.00	0.00	0.00	0.00	0.00	0.00	0.00	0.00	0.00	0.00
Mn	0.00	0.00	0.00	0.00	0.00	0.00	0.00	0.00	0.00	0.00	0.00	0.00	0.00	0.00	0.00	0.00	0.00	0.00
Mg	0.00	0.00	0.00	0.00	0.00	0.00	0.00	0.00	0.00	0.00	0.00	0.00	0.00	0.00	0.00	0.00	0.00	0.00
Ca	0.00	0.25	0.00	0.00	0.25	0.00	0.25	0.00	0.21	0.20	0.21	0.21	0.20	0.20	0.20	0.20	0.21	0.20
Na	0.13	0.69	0.01	0.15	0.66	0.34	0.68	0.15	0.68	0.71	0.71	0.73	0.71	0.72	0.70	0.72	0.72	0.73
K	0.82	0.01	0.14	0.81	0.01	0.63	0.01	0.81	0.01	0.01	0.01	0.01	0.01	0.01	0.01	0.02	0.01	0.01
Total	4.98	4.98	4.86	4.99	4.95	5.00	4.97	4.98	4.94	4.95	4.96	4.97	4.96	4.96	4.94	4.96	4.97	4.96

Table A.29: Electron microprobe results for feldspars – continued.

	KK04	KK04	KK10	KK10	KK10	KK10	KK10	KK10	KK10	KK10	KK10	KK10	KK10	KK27	KK27	KK27	KK27	KK27
	fsp63_rim	fsp64	fsp65_int	fsp66_int	fsp66_rim	fsp67_int	fsp67_rim	fsp68_int	fsp68_rim	fsp69_int	fsp69_rim	fsp70_int	fsp70_rim	fsp72_int	fsp72_rim	fsp73_int	fsp73_rim	fsp74_int
SiO_2	63.58	64.43	64.34	64.60	64.22	61.47	61.31	61.39	61.54	60.74	60.98	63.92	64.26	64.28	64.60	64.41	64.43	61.71
TiO_2	0.03	0.02	0.04	0.02	0.07	0.01	0.01	0.00	0.00	0.01	0.00	0.04	0.02	0.02	0.03	0.04	0.02	0.01
Al_2O_3	23.69	18.98	18.91	19.08	19.00	24.79	24.93	24.61	24.55	24.98	24.89	18.96	19.25	18.83	19.01	18.93	18.89	24.55
Cr_2O_3	0.01	0.00	0.00	0.00	0.00	0.02	0.00	0.00	0.00	0.00	0.00	0.02	0.01	0.02	0.00	0.00	0.04	0.00
FeO	0.05	0.01	0.00	0.02	0.03	0.07	0.10	0.05	0.46	0.05	0.09	0.03	0.12	0.03	0.01	0.05	0.03	0.00
MnO	0.04	0.06	0.05	0.02	0.02	0.04	0.02	0.09	0.11	0.02	0.04	0.00	0.04	0.03	0.06	0.00	0.00	0.02
MgO	0.01	0.00	0.00	0.00	0.00	0.00	0.00	0.01	0.37	0.00	0.02	0.00	0.00	0.00	0.00	0.02	0.00	0.01
CaO	4.26	0.01	0.00	0.00	0.00	5.68	5.66	5.60	1.72	5.66	5.64	0.00	0.00	0.02	0.04	0.03	0.03	5.27
Na_2O	8.58	1.24	1.17	1.08	1.09	7.77	7.79	7.51	6.34	7.66	7.40	1.15	1.09	1.43	1.46	1.39	1.40	7.78
K_2O	0.19	14.65	14.75	14.87	14.83	0.18	0.21	0.22	2.13	0.24	0.25	14.58	14.72	14.41	14.48	14.58	14.53	0.23
Total	100.44	99.40	99.26	99.70	99.25	100.03	100.03	99.47	97.22	99.36	99.31	98.70	99.51	99.07	99.68	99.44	99.36	99.58
Oxygens	8	8	8	8	8	8	8	8	8	8	8	8	8	8	8	8	8	8
Si	2.79	2.98	2.98	2.98	2.97	2.72	2.72	2.73	2.78	2.71	2.72	2.97	2.97	2.98	2.98	2.98	2.98	2.74
Ti	0.00	0.00	0.00	0.00	0.00	0.00	0.00	0.00	0.00	0.00	0.00	0.00	0.00	0.00	0.00	0.00	0.00	0.00
Al	1.23	1.03	1.03	1.04	1.04	1.29	1.30	1.29	1.31	1.31	1.31	1.04	1.05	1.03	1.03	1.03	1.03	1.28
Cr	0.00	0.00	0.00	0.00	0.00	0.00	0.00	0.00	0.00	0.00	0.00	0.00	0.00	0.00	0.00	0.00	0.00	0.00
Fe	0.00	0.00	0.00	0.00	0.00	0.00	0.00	0.00	0.02	0.00	0.00	0.00	0.00	0.00	0.00	0.00	0.00	0.00
Mn	0.00	0.00	0.00	0.00	0.00	0.00	0.00	0.00	0.00	0.00	0.00	0.00	0.00	0.00	0.00	0.00	0.00	0.00
Mg	0.00	0.00	0.00	0.00	0.00	0.00	0.00	0.00	0.03	0.00	0.00	0.00	0.00	0.00	0.00	0.00	0.00	0.00
Ca	0.20	0.00	0.00	0.00	0.00	0.27	0.27	0.27	0.08	0.27	0.27	0.00	0.00	0.00	0.00	0.00	0.00	0.25
Na	0.73	0.11	0.10	0.10	0.10	0.67	0.67	0.65	0.56	0.66	0.64	0.10	0.10	0.13	0.13	0.12	0.13	0.67
K	0.01	0.86	0.87	0.87	0.88	0.01	0.01	0.01	0.12	0.01	0.01	0.87	0.87	0.85	0.85	0.86	0.86	0.01
Total	4.96	4.99	4.99	4.99	4.99	4.97	4.97	4.95	4.90	4.97	4.96	4.99	4.99	4.99	5.00	5.00	5.00	4.96

Table A.30: Electron microprobe results for feldspars – continued.

	KK27 fsp74_rim	KK27 fsp75_int	KK27 fsp75_rim	KK27 fsp76_int	KK27 fsp76_rim	KK27 fsp77_int	KK27 fsp77_rim	KK27 fsp78_int	KK27 fsp79_int	KK28 fsp80_int	KK28 fsp80_rim	KK28 fsp81_int	KK28 fsp81_rim	KK28 fsp82_int	KK28 fsp82_rim	KK28 fsp83_int	KK28 fsp83_rim	KK28 fsp84_int
SiO_2	60.87	61.47	61.60	61.25	62.04	61.34	61.00	64.06	61.41	60.73	60.81	61.38	61.12	65.36	65.28	65.70	64.99	65.05
TiO_2	0.00	0.00	0.03	0.00	0.00	0.01	0.00	0.01	0.02	0.01	0.00	0.03	0.00	0.05	0.03	0.02	0.02	0.04
Al_2O_3	24.84	24.50	24.71	24.77	24.55	24.64	25.04	19.32	24.75	25.65	25.64	25.44	25.41	19.09	19.34	19.29	19.25	19.40
Cr_2O_3	0.00	0.00	0.00	0.00	0.03	0.00	0.00	0.00	0.04	0.00	0.00	0.00	0.00	0.00	0.02	0.01	0.00	0.02
FeO	0.00	0.00	0.03	0.05	0.06	0.01	0.04	0.02	0.05	0.10	0.04	0.04	0.00	0.01	0.02	0.02	0.06	0.03
MnO	0.06	0.04	0.05	0.02	0.04	0.04	0.05	0.05	0.04	0.03	0.04	0.02	0.01	0.03	0.03	0.04	0.00	0.00
MgO	0.03	0.01	0.00	0.02	0.01	0.00	0.01	0.00	0.02	0.00	0.00	0.00	0.00	0.03	0.01	0.00	0.00	0.00
CaO	5.55	5.39	5.33	5.40	5.23	5.50	6.14	0.03	5.62	6.08	6.13	5.72	6.02	0.02	0.05	0.04	0.01	0.02
Na_2O	7.87	7.79	7.81	7.84	7.90	8.17	7.41	1.26	7.74	7.47	7.32	7.53	7.19	1.30	1.34	1.96	1.10	1.29
K_2O	0.16	0.24	0.13	0.25	0.20	0.28	0.20	14.57	0.25	0.16	0.16	0.21	0.17	14.71	14.41	13.64	14.89	14.22
Total	99.38	99.44	99.68	99.60	100.06	99.99	99.89	99.31	99.95	100.22	100.14	100.36	99.92	100.60	100.53	100.71	100.32	100.07
Oxygens	8	8	8	8	8	8	8	8	8	8	8	8	8	8	8	8	8	8
Si	2.71	2.74	2.73	2.72	2.74	2.72	2.71	2.96	2.72	2.69	2.69	2.71	2.71	2.98	2.98	2.98	2.98	2.98
Ti	0.00	0.00	0.00	0.00	0.00	0.00	0.00	0.00	0.00	0.00	0.00	0.00	0.00	0.00	0.00	0.00	0.00	0.00
Al	1.31	1.29	1.29	1.30	1.28	1.29	1.31	1.05	1.29	1.34	1.34	1.32	1.33	1.03	1.04	1.03	1.04	1.05
Cr	0.00	0.00	0.00	0.00	0.00	0.00	0.00	0.00	0.00	0.00	0.00	0.00	0.00	0.00	0.00	0.00	0.00	0.00
Fe	0.00	0.00	0.00	0.00	0.00	0.00	0.00	0.00	0.00	0.00	0.00	0.00	0.00	0.00	0.00	0.00	0.00	0.00
Mn	0.00	0.00	0.00	0.00	0.00	0.00	0.00	0.00	0.00	0.00	0.00	0.00	0.00	0.00	0.00	0.00	0.00	0.00
Mg	0.00	0.00	0.00	0.00	0.00	0.00	0.00	0.00	0.00	0.00	0.00	0.00	0.00	0.00	0.00	0.00	0.00	0.00
Ca	0.27	0.26	0.25	0.26	0.25	0.26	0.29	0.00	0.27	0.29	0.29	0.27	0.29	0.00	0.00	0.00	0.00	0.00
Na	0.68	0.67	0.67	0.68	0.68	0.70	0.64	0.11	0.67	0.64	0.63	0.64	0.62	0.12	0.12	0.17	0.10	0.11
K	0.01	0.01	0.01	0.01	0.01	0.02	0.01	0.86	0.01	0.01	0.01	0.01	0.01	0.86	0.84	0.79	0.87	0.83
Total	4.98	4.97	4.96	4.97	4.96	4.99	4.96	5.00	4.97	4.97	4.96	4.96	4.94	4.99	4.98	4.98	4.99	4.97

Table A.31: Electron microprobe results for feldspars – continued.

	KK28	KK28	KK28	KK29	KK29	KK29	KK29	KK29	KK29	KK29	KK29	KK12	KK12	KK12	KK12	KK12	KK12	KK12
	fsp84_rim	fsp85_int	fsp85_rim	fsp86	fsp87	fsp88	fsp89	fsp89_rim	fsp90	fsp91	fsp92	fsp93_int	fsp93_rim	fsp94_int	fsp94_rim	fsp95_int	fsp95_rim	fsp96_int
SiO_2	65.10	61.87	61.94	61.27	61.52	61.85	60.50	61.94	61.46	61.24	60.88	44.22	44.16	43.73	44.13	44.24	44.01	44.34
TiO_2	0.02	0.01	0.01	0.01	0.00	0.00	0.00	0.00	0.01	0.00	0.00	0.00	0.00	0.00	0.00	0.04	0.00	0.02
Al_2O_3	19.12	25.09	25.03	25.39	25.74	25.63	26.04	25.82	25.16	25.57	25.84	37.59	37.75	37.30	37.36	37.54	37.72	37.75
Cr_2O_3	0.00	0.00	0.00	0.02	0.00	0.02	0.00	0.00	0.00	0.00	0.01	0.02	0.04	0.01	0.00	0.00	0.01	0.01
FeO	0.03	0.03	0.05	0.00	0.11	0.00	0.00	0.03	0.08	0.10	0.04	0.07	0.11	0.25	0.20	0.10	0.09	0.20
MnO	0.03	0.03	0.00	0.03	0.00	0.00	0.02	0.06	0.00	0.02	0.02	0.03	0.01	0.01	0.01	0.04	0.01	0.00
MgO	0.01	0.03	0.00	0.00	0.00	0.00	0.03	0.01	0.02	0.00	0.01	0.00	0.00	0.00	0.00	0.01	0.00	0.02
CaO	0.00	5.42	5.48	5.39	5.41	5.46	5.99	5.56	5.44	5.37	5.56	18.02	18.06	17.78	18.14	18.19	18.08	18.19
Na_2O	1.22	7.82	7.64	7.90	7.98	8.04	7.71	7.47	7.79	7.79	7.66	0.48	0.43	0.47	0.31	0.39	0.39	0.34
K_2O	14.71	0.17	0.14	0.18	0.15	0.18	0.22	0.20	0.14	0.14	0.14	0.01	0.01	0.00	0.02	0.01	0.01	0.01
Total	100.24	100.48	100.29	100.20	100.91	101.18	100.52	101.09	100.11	100.24	100.17	100.45	100.56	99.54	100.18	100.56	100.31	100.87
Oxygens	8	8	8	8	8	8	8	8	8	8	8	8	8	8	8	8	8	8
Si	2.98	2.72	2.73	2.71	2.70	2.71	2.67	2.71	2.72	2.70	2.69	2.02	2.02	2.02	2.03	2.02	2.02	2.02
Ti	0.00	0.00	0.00	0.00	0.00	0.00	0.00	0.00	0.00	0.00	0.00	0.00	0.00	0.00	0.00	0.00	0.00	0.00
Al	1.03	1.30	1.30	1.32	1.33	1.32	1.36	1.33	1.31	1.33	1.35	2.03	2.03	2.03	2.02	2.02	2.04	2.03
Cr	0.00	0.00	0.00	0.00	0.00	0.00	0.00	0.00	0.00	0.00	0.00	0.00	0.00	0.00	0.00	0.00	0.00	0.00
Fe	0.00	0.00	0.00	0.00	0.00	0.00	0.00	0.00	0.00	0.00	0.00	0.00	0.00	0.01	0.01	0.00	0.00	0.01
Mn	0.00	0.00	0.00	0.00	0.00	0.00	0.00	0.00	0.00	0.00	0.00	0.00	0.00	0.00	0.00	0.00	0.00	0.00
Mg	0.00	0.00	0.00	0.00	0.00	0.00	0.00	0.00	0.00	0.00	0.00	0.00	0.00	0.00	0.00	0.00	0.00	0.00
Ca	0.00	0.26	0.26	0.26	0.25	0.26	0.28	0.26	0.26	0.25	0.26	0.88	0.88	0.88	0.89	0.89	0.89	0.89
Na	0.11	0.67	0.65	0.68	0.68	0.68	0.66	0.63	0.67	0.67	0.66	0.04	0.04	0.04	0.03	0.03	0.03	0.03
K	0.86	0.01	0.01	0.01	0.01	0.01	0.01	0.01	0.01	0.01	0.01	0.00	0.00	0.00	0.00	0.00	0.00	0.00
Total	4.99	4.96	4.95	4.97	4.98	4.98	4.99	4.95	4.97	4.97	4.97	4.98	4.98	4.98	4.98	4.98	4.98	4.98

Table A.32: Electron microprobe results for feldspars – continued.

	KK12	KK12	KK14	KK14	KK14	KK14	KK14	KK14	KK14	KK14	KK19	KK19	KK19	KK19	KK19	KK19	KK19	KK19	KK19	KK19	KK19
	fsp97	fsp98	fsp101	fsp102	fsp103_int	fsp103_rim	fsp104_int	fsp104_rim	fsp105_int	fsp105_rim	fsp106_int	fsp106_rim	fsp107_int	fsp107_rim	fsp108_int	fsp108_rim	fsp109	fsp110_int	fsp110_rim	fsp111	fsp112_int	fsp112_rim
SiO_2	45.93	43.94	57.57	58.43	59.46	57.72	57.76	58.14	58.02	57.83	55.59	55.97	56.26	54.89	56.18	55.09	56.02	56.46	55.59	54.93	55.72	56.31
TiO_2	0.01	0.00	0.00	0.03	0.00	0.00	0.00	0.00	0.00	0.01	0.00	0.00	0.00	0.01	0.00	0.00	0.05	0.00	0.00	0.00	0.00	0.01
Al_2O_3	35.83	37.58	28.36	27.78	25.84	27.96	28.04	28.05	27.59	28.04	28.73	28.98	28.95	29.47	28.70	29.31	28.95	28.41	28.71	29.59	29.50	29.30
Cr_2O_3	0.03	0.01	0.05	0.00	0.00	0.00	0.00	0.02	0.02	0.00	0.00	0.00	0.00	0.00	0.01	0.00	0.01	0.00	0.03	0.01	0.00	0.00
FeO	0.08	0.08	0.14	0.11	0.10	0.13	0.08	0.13	0.12	0.18	0.01	0.07	0.10	0.08	0.02	0.04	0.02	0.04	0.09	0.04	0.04	0.06
MnO	0.01	0.02	0.07	0.03	0.02	0.05	0.06	0.05	0.05	0.06	0.01	0.00	0.00	0.01	0.04	0.01	0.01	0.06	0.02	0.00	0.03	0.03
MgO	0.01	0.00	0.00	0.01	0.00	0.00	0.01	0.00	0.01	0.00	0.02	0.02	0.00	0.01	0.00	0.00	0.00	0.02	0.01	0.00	0.00	0.01
CaO	15.87	18.23	8.47	7.81	6.07	8.01	7.77	7.99	7.72	8.15	9.54	9.33	9.27	10.05	9.21	9.87	9.32	9.00	9.49	10.07	9.39	9.60
Na_2O	1.64	0.35	5.73	6.25	4.38	6.05	6.43	6.02	6.41	6.06	5.36	5.40	5.72	5.10	5.82	5.47	5.62	5.91	5.67	5.07	5.42	5.39
K_2O	0.02	0.00	0.27	0.27	4.31	0.21	0.33	0.27	0.30	0.25	0.04	0.04	0.05	0.06	0.04	0.05	0.05	0.06	0.06	0.05	0.04	0.05
Total	99.43	100.21	100.65	100.72	100.18	100.12	100.48	100.66	100.24	100.59	99.30	99.82	100.35	99.67	100.02	99.84	100.06	99.96	99.66	99.76	100.15	100.76
Oxygens	8	8	8	8	8	8	8	8	8	8	8	8	8	8	8	8	8	8	8	8	8	8
Si	2.11	2.02	2.55	2.59	2.67	2.57	2.57	2.58	2.58	2.57	2.51	2.51	2.51	2.47	2.51	2.48	2.51	2.53	2.50	2.47	2.49	2.50
Ti	0.00	0.00	0.00	0.00	0.00	0.00	0.00	0.00	0.00	0.00	0.00	0.00	0.00	0.00	0.00	0.00	0.00	0.00	0.00	0.00	0.00	0.00
Al	1.94	2.03	1.48	1.45	1.37	1.47	1.47	1.46	1.45	1.47	1.53	1.53	1.52	1.56	1.51	1.55	1.53	1.50	1.52	1.57	1.55	1.53
Cr	0.00	0.00	0.00	0.00	0.00	0.00	0.00	0.00	0.00	0.00	0.00	0.00	0.00	0.00	0.00	0.00	0.00	0.00	0.00	0.00	0.00	0.00
Fe	0.00	0.00	0.01	0.00	0.00	0.00	0.00	0.00	0.00	0.01	0.00	0.00	0.00	0.00	0.00	0.00	0.00	0.00	0.00	0.00	0.00	0.00
Mn	0.00	0.00	0.00	0.00	0.00	0.00	0.00	0.00	0.00	0.00	0.00	0.00	0.00	0.00	0.00	0.00	0.00	0.00	0.00	0.00	0.00	0.00
Mg	0.00	0.00	0.00	0.00	0.00	0.00	0.00	0.00	0.00	0.00	0.00	0.00	0.00	0.00	0.00	0.00	0.00	0.00	0.00	0.00	0.00	0.00
Ca	0.78	0.90	0.40	0.37	0.29	0.38	0.37	0.38	0.37	0.39	0.46	0.45	0.44	0.48	0.44	0.48	0.45	0.43	0.46	0.49	0.45	0.46
Na	0.15	0.03	0.49	0.54	0.38	0.52	0.55	0.52	0.55	0.52	0.47	0.47	0.49	0.45	0.51	0.48	0.49	0.51	0.49	0.44	0.47	0.46
K	0.00	0.00	0.02	0.02	0.25	0.01	0.02	0.02	0.02	0.01	0.00	0.00	0.00	0.00	0.00	0.00	0.00	0.00	0.00	0.00	0.00	0.00
Total	4.99	4.98	4.96	4.96	4.96	4.96	4.98	4.96	4.98	4.97	4.97	4.96	4.98	4.97	4.98	4.99	4.97	4.98	4.99	4.97	4.97	4.96

Table A.33: Electron microprobe results for ilmenite and rutile.

	PM13010	JMTV45	JMTV45	JMTV45	JMTV45	JMTV45	JMTV45	JMTV45	PM13076	PM13076	PM13076	PM13076	PM13076	PM13076	PM13076	PM13076	KK14	KK14	KK14	KK14	KK19	KK19
	ilm6	ilm15	ilm16	ilm17	ilm20	ilm22(gt_incl)	ilm23(gt_incl)	ilm26	ilm28	ilm29	ilm32(a)	ilm33(b)	ilm34(b)	ilm36(b)	ilm37(b)	ilm30(gt_incl)	ilm40	ilm43	ilm44	ru45	ru47	ru49
SiO_2	0.00	0.00	0.00	0.00	0.00	0.00	0.00	0.00	0.00	0.00	0.00	0.00	0.00	0.00	0.00	0.00	0.00	0.00	0.00	0.00	0.00	0.00
TiO_2	49.45	48.04	47.49	47.47	48.80	49.09	49.09	49.17	48.72	49.41	49.16	48.15	47.72	47.81	48.62	48.71	38.50	41.31	38.54	82.80	83.57	83.55
Al_2O_3	0.00	0.00	0.00	0.00	0.00	0.00	0.00	0.00	0.00	0.00	0.00	0.00	0.00	0.02	0.00	0.01	0.01	0.03	0.04	0.01	0.02	0.02
Cr_2O_3	0.06	0.07	0.06	0.07	0.07	0.03	0.00	0.09	0.03	0.04	0.08	0.19	0.21	0.13	0.11	0.17	0.01	0.02	0.00	0.07	0.13	0.01
FeO	43.38	47.11	48.37	46.90	45.15	43.93	43.98	44.02	48.51	47.05	46.79	46.49	46.35	45.31	45.05	47.08	38.91	36.76	38.92	0.64	0.55	0.37
MnO	0.95	1.48	0.49	0.23	0.52	0.48	0.46	0.46	0.15	0.21	0.18	0.19	0.26	0.12	0.13	0.25	6.40	6.76	6.29	0.01	0.05	0.01
MgO	0.03	0.01	0.02	0.05	0.03	0.00	0.05	0.08	0.03	0.01	0.04	0.04	0.05	0.02	0.01	0.03	0.05	0.02	0.01	0.02	0.02	0.00
CaO	0.00	0.00	0.00	0.00	0.00	0.00	0.00	0.00	0.00	0.00	0.00	0.00	0.00	0.00	0.00	0.00	0.00	0.00	0.00	0.00	0.00	0.00
Na_2O	0.00	0.00	0.00	0.00	0.00	0.00	0.00	0.00	0.00	0.00	0.00	0.00	0.00	0.00	0.00	0.00	0.00	0.00	0.00	0.00	0.00	0.00
K_2O	0.00	0.00	0.00	0.00	0.00	0.00	0.00	0.00	0.00	0.00	0.00	0.00	0.00	0.00	0.00	0.00	0.00	0.00	0.00	0.00	0.00	0.00
Total	93.87	96.71	96.43	94.72	94.56	93.55	93.61	93.83	97.46	96.73	96.26	95.09	94.58	93.44	93.93	96.32	83.88	84.90	83.80	83.55	84.35	84.01
Oxygens	3	3	3	3	3	3	3	3	3	3	3	3	3	3	3	3	3	3	3	2	2	2
Si	0.00	0.00	0.00	0.00	0.00	0.00	0.00	0.00	0.00	0.00	0.00	0.00	0.00	0.00	0.00	0.00	0.00	0.00	0.00	0.00	0.00	0.00
Ti	1.00	0.96	0.95	0.97	0.99	1.00	1.00	1.00	0.96	0.98	0.98	0.97	0.97	0.98	0.99	0.97	0.90	0.94	0.91	0.99	0.99	1.00
Al	0.00	0.00	0.00	0.00	0.00	0.00	0.00	0.00	0.00	0.00	0.00	0.00	0.00	0.00	0.00	0.00	0.00	0.00	0.00	0.00	0.00	0.00
Cr	0.00	0.00	0.00	0.00	0.00	0.00	0.00	0.00	0.00	0.00	0.00	0.00	0.00	0.00	0.00	0.00	0.00	0.00	0.00	0.00	0.00	0.00
Fe	0.98	1.05	1.08	1.06	1.01	0.99	0.99	0.99	1.07	1.04	1.04	1.04	1.05	1.03	1.02	1.04	1.02	0.93	1.02	0.01	0.01	0.00
Mn	0.02	0.03	0.01	0.01	0.01	0.01	0.01	0.01	0.00	0.00	0.00	0.00	0.01	0.00	0.00	0.01	0.17	0.17	0.17	0.00	0.00	0.00
Mg	0.00	0.00	0.00	0.00	0.00	0.00	0.00	0.00	0.00	0.00	0.00	0.00	0.00	0.00	0.00	0.00	0.00	0.00	0.00	0.00	0.00	0.00
Ca	0.00	0.00	0.00	0.00	0.00	0.00	0.00	0.00	0.00	0.00	0.00	0.00	0.00	0.00	0.00	0.00	0.00	0.00	0.00	0.00	0.00	0.00
Na	0.00	0.00	0.00	0.00	0.00	0.00	0.00	0.00	0.00	0.00	0.00	0.00	0.00	0.00	0.00	0.00	0.00	0.00	0.00	0.00	0.00	0.00
K	0.00	0.00	0.00	0.00	0.00	0.00	0.00	0.00	0.00	0.00	0.00	0.00	0.00	0.00	0.00	0.00	0.00	0.00	0.00	0.00	0.00	0.00
Total	2.00	2.04	2.05	2.03	2.01	2.00	2.00	2.00	2.04	2.02	2.02	2.03	2.03	2.02	2.01	2.03	2.09	2.06	2.09	1.00	1.00	1.00

Table A.34: Electron microprobe results for magnetite.

	PM13010 mt3_core	PM13010 mt3_rim	PM13010 mt4_core	PM13010 mt4_rim	PM13010 mt5_core	PM13010 mt5_rim	PM13010 mt6_core	PM13010 mt6_rim	PM13010 mt7_core	PM13010 mt7_rim	PM13010 mt8_core	PM13010 mt8_rim	PM13010 mt9_core	PM13010 mt9_rim	PM13010 mt18(gt_incl)	PM13010 mt10	PM13010 mt11	PM13010 mt12
SiO_2	0.00	0.00	0.00	0.00	0.00	0.00	0.00	0.00	0.00	0.00	0.00	0.00	0.00	0.00	0.00	0.00	0.00	0.00
TiO_2	0.00	0.11	0.02	0.08	0.04	0.05	0.00	0.00	0.00	0.01	0.06	0.04	0.04	0.00	0.16	0.03	0.01	0.00
Al_2O_3	0.11	0.12	0.14	0.16	0.31	0.23	0.43	0.70	0.17	0.14	0.43	0.20	0.14	0.24	0.78	0.14	0.61	0.13
Cr_2O_3	0.21	0.20	0.19	0.19	0.19	0.22	0.27	0.23	0.12	0.11	0.19	0.16	0.28	0.30	0.40	0.25	0.28	0.19
FeO	86.74	84.49	84.28	82.64	82.55	81.47	81.32	81.20	81.97	81.37	81.29	81.62	81.43	80.96	85.58	81.03	89.68	90.08
MnO	0.11	0.07	0.13	0.07	0.10	0.08	0.07	0.09	0.06	0.07	0.07	0.10	0.14	0.12	0.17	0.14	0.09	0.13
MgO	0.05	0.01	0.01	0.02	0.03	0.00	0.04	0.00	0.02	0.00	0.00	0.00	0.03	0.02	0.04	0.03	0.01	0.00
CaO	0.00	0.00	0.00	0.00	0.00	0.00	0.00	0.00	0.00	0.00	0.00	0.00	0.00	0.00	0.00	0.00	0.00	0.00
Na_2O	0.00	0.00	0.00	0.00	0.00	0.00	0.00	0.00	0.00	0.00	0.00	0.00	0.00	0.00	0.00	0.00	0.00	0.00
K_2O	0.00	0.00	0.00	0.00	0.00	0.00	0.00	0.00	0.00	0.00	0.00	0.00	0.00	0.00	0.00	0.00	0.00	0.00
Total	87.21	85.02	84.81	83.20	83.27	82.05	82.15	82.21	82.37	81.73	82.05	82.12	82.07	81.63	87.14	81.66	90.72	90.54
Oxygens	4	4	4	4	4	4	4	4	4	4	4	4	4	4	4	4	4	4
Si	0.00	0.00	0.00	0.00	0.00	0.00	0.00	0.00	0.00	0.00	0.00	0.00	0.00	0.00	0.00	0.00	0.00	0.00
Ti	0.00	0.00	0.00	0.00	0.00	0.00	0.00	0.00	0.00	0.00	0.00	0.00	0.00	0.00	0.00	0.00	0.00	0.00
Al	0.00	0.00	0.00	0.00	0.01	0.00	0.01	0.01	0.00	0.00	0.01	0.00	0.00	0.00	0.01	0.00	0.01	0.00
Cr	0.00	0.00	0.00	0.00	0.00	0.00	0.00	0.00	0.00	0.00	0.00	0.00	0.00	0.00	0.00	0.00	0.00	0.00
Fe	2.99	2.99	2.99	2.99	2.99	2.99	2.99	2.98	2.99	3.00	2.99	2.99	2.99	2.99	2.98	2.99	2.98	2.99
Mn	0.00	0.00	0.00	0.00	0.00	0.00	0.00	0.00	0.00	0.00	0.00	0.00	0.00	0.00	0.00	0.00	0.00	0.00
Mg	0.00	0.00	0.00	0.00	0.00	0.00	0.00	0.00	0.00	0.00	0.00	0.00	0.00	0.00	0.00	0.00	0.00	0.00
Ca	0.00	0.00	0.00	0.00	0.00	0.00	0.00	0.00	0.00	0.00	0.00	0.00	0.00	0.00	0.00	0.00	0.00	0.00
Na	0.00	0.00	0.00	0.00	0.00	0.00	0.00	0.00	0.00	0.00	0.00	0.00	0.00	0.00	0.00	0.00	0.00	0.00
K	0.00	0.00	0.00	0.00	0.00	0.00	0.00	0.00	0.00	0.00	0.00	0.00	0.00	0.00	0.00	0.00	0.00	0.00
Total	3.00	3.00	3.00	3.00	3.00	3.00	3.00	3.00	3.00	3.00	3.00	3.00	3.00	3.00	3.00	3.00	3.00	3.00

Table A.35: Electron microprobe results for magnetite – continued.

	PM13010 mt13	PM13010 mt14	PM13010 mt15	PM13010 mt17	PM13010 mt19	PM13010 mt20	PM13010 mt1_core	PM13010 mt2_core	PM13068 mt21	PM13068 mt22	PM13068 mt23	PM13068 mt24	KK02 mt38	KK02 mt26	KK02 mt27	KK02 mt29	KK02 mt31	KK02 mt32
SiO_2	0.00	0.00	0.00	0.00	0.00	0.00	0.00	0.00	0.00	0.00	0.00	0.00	0.00	0.00	0.00	0.00	0.00	0.00
TiO_2	0.14	0.04	0.05	0.03	0.05	0.03	0.01	0.06	0.00	0.00	0.02	0.01	0.00	0.04	0.02	0.02	0.24	0.03
Al_2O_3	0.31	0.23	0.21	0.33	0.07	0.11	0.38	0.12	0.13	0.18	0.15	0.15	0.06	0.05	0.09	0.09	0.09	0.03
Cr_2O_3	0.29	0.25	0.28	0.19	0.21	0.28	0.34	0.30	0.34	0.29	0.27	0.26	0.26	0.25	0.27	0.23	0.37	0.22
FeO	88.07	85.69	88.84	86.97	89.27	89.62	89.82	86.88	92.31	89.98	88.64	85.69	87.53	83.51	82.60	83.73	82.77	81.40
MnO	0.09	0.13	0.11	0.09	0.06	0.09	0.13	0.15	0.03	0.05	0.04	0.10	0.11	0.10	0.05	0.08	0.09	0.08
MgO	0.05	0.01	0.00	0.00	0.00	0.00	0.00	0.00	0.00	0.03	0.00	0.00	0.00	0.00	0.00	0.04	0.02	0.00
CaO	0.00	0.00	0.00	0.00	0.00	0.00	0.00	0.00	0.00	0.00	0.00	0.00	0.00	0.00	0.00	0.00	0.00	0.00
Na_2O	0.00	0.00	0.00	0.00	0.00	0.00	0.00	0.00	0.00	0.00	0.00	0.00	0.00	0.00	0.00	0.00	0.00	0.00
K_2O	0.00	0.00	0.00	0.00	0.00	0.00	0.00	0.00	0.00	0.00	0.00	0.00	0.00	0.00	0.00	0.00	0.00	0.00
Total	88.95	86.38	89.53	87.66	89.67	90.17	90.68	87.51	92.83	90.56	89.18	86.27	88.00	83.95	83.07	84.20	83.58	81.77
Oxygens	4	4	4	4	4	4	4	4	4	4	4	4	4	4	4	4	4	4
Si	0.00	0.00	0.00	0.00	0.00	0.00	0.00	0.00	0.00	0.00	0.00	0.00	0.00	0.00	0.00	0.00	0.00	0.00
Ti	0.00	0.00	0.00	0.00	0.00	0.00	0.00	0.00	0.00	0.00	0.00	0.00	0.00	0.00	0.00	0.00	0.00	0.00
Al	0.01	0.00	0.00	0.00	0.00	0.00	0.01	0.00	0.00	0.00	0.00	0.00	0.00	0.00	0.00	0.00	0.00	0.00
Cr	0.00	0.00	0.00	0.00	0.00	0.00	0.00	0.00	0.00	0.00	0.00	0.00	0.00	0.00	0.00	0.00	0.00	0.00
Fe	2.99	2.99	2.99	2.99	3.00	3.00	2.99	2.99	2.99	2.99	2.99	2.99	2.99	2.99	2.99	2.99	2.99	3.00
Mn	0.00	0.00	0.00	0.00	0.00	0.00	0.00	0.00	0.00	0.00	0.00	0.00	0.00	0.00	0.00	0.00	0.00	0.00
Mg	0.00	0.00	0.00	0.00	0.00	0.00	0.00	0.00	0.00	0.00	0.00	0.00	0.00	0.00	0.00	0.00	0.00	0.00
Ca	0.00	0.00	0.00	0.00	0.00	0.00	0.00	0.00	0.00	0.00	0.00	0.00	0.00	0.00	0.00	0.00	0.00	0.00
Na	0.00	0.00	0.00	0.00	0.00	0.00	0.00	0.00	0.00	0.00	0.00	0.00	0.00	0.00	0.00	0.00	0.00	0.00
K	0.00	0.00	0.00	0.00	0.00	0.00	0.00	0.00	0.00	0.00	0.00	0.00	0.00	0.00	0.00	0.00	0.00	0.00
Total	3.00	3.00	3.00	3.00	3.00	3.00	3.00	3.00	3.00	3.00	3.00	3.00	3.00	3.00	3.00	3.00	3.00	3.00

Table A.36: Electron microprobe results for magnetite – continued.

	KK04 mt33	KK04 mt34	KK04 mt35	KK04 mt36	KK04 mt37	KK04 mt38	KK04 mt39	KK16 mt40	KK16 mt41	KK16 mt42	KK16 mt43	KK16 mt44	KK16 mt45	KK16 mt46	KK29 mt47	KK29 mt48	KK29 mt49	KK29 mt50
SiO_2	0.00	0.00	0.00	0.00	0.00	0.00	0.00	0.00	0.00	0.00	0.00	0.00	0.00	0.00	0.00	0.00	0.00	0.00
TiO_2	0.04	0.07	0.00	0.00	0.02	0.00	0.00	0.00	0.00	0.20	0.14	0.11	0.05	0.00	0.01	0.00	0.08	0.02
Al_2O_3	0.01	0.08	0.16	0.02	0.08	0.11	0.13	0.08	0.06	1.48	0.08	0.06	0.12	0.04	0.11	0.09	0.53	0.13
Cr_2O_3	0.34	0.35	0.41	0.31	0.40	0.36	0.32	0.46	0.36	0.26	0.26	0.33	0.29	0.26	0.40	0.29	0.24	0.35
FeO	85.18	80.98	82.87	78.66	76.49	81.67	80.77	86.94	86.04	84.25	84.90	84.10	84.12	82.99	88.00	87.56	85.51	85.12
MnO	0.05	0.06	0.07	0.08	0.09	0.02	0.05	0.14	0.07	0.10	0.04	0.06	0.04	0.00	0.07	0.08	0.10	0.02
MgO	0.01	0.00	0.00	0.00	0.04	0.00	0.03	0.01	0.03	0.21	0.03	0.00	0.01	0.01	0.00	0.01	0.00	0.06
CaO	0.00	0.00	0.00	0.00	0.00	0.00	0.00	0.00	0.00	0.00	0.00	0.00	0.00	0.00	0.00	0.00	0.00	0.00
Na_2O	0.00	0.00	0.00	0.00	0.00	0.00	0.00	0.00	0.00	0.00	0.00	0.00	0.00	0.00	0.00	0.00	0.00	0.00
K_2O	0.00	0.00	0.00	0.00	0.00	0.00	0.00	0.00	0.00	0.00	0.00	0.00	0.00	0.00	0.00	0.00	0.00	0.00
Total	85.64	81.55	83.50	79.10	77.11	82.17	81.29	87.68	86.59	86.55	85.51	84.72	84.67	83.34	88.67	88.04	86.45	85.70
Oxygens	4	4	4	4	4	4	4	4	4	4	4	4	4	4	4	4	4	4
Si	0.00	0.00	0.00	0.00	0.00	0.00	0.00	0.00	0.00	0.00	0.00	0.00	0.00	0.00	0.00	0.00	0.00	0.00
Ti	0.00	0.00	0.00	0.00	0.00	0.00	0.00	0.00	0.00	0.00	0.00	0.00	0.00	0.00	0.00	0.00	0.00	0.00
Al	0.00	0.00	0.00	0.00	0.00	0.00	0.00	0.00	0.00	0.02	0.00	0.00	0.00	0.00	0.00	0.00	0.01	0.00
Cr	0.00	0.00	0.00	0.00	0.00	0.00	0.00	0.01	0.00	0.00	0.00	0.00	0.00	0.00	0.00	0.00	0.00	0.00
Fe	2.99	2.99	2.99	2.99	2.99	2.99	2.99	2.99	2.99	2.96	2.99	2.99	2.99	3.00	2.99	2.99	2.99	2.99
Mn	0.00	0.00	0.00	0.00	0.00	0.00	0.00	0.00	0.00	0.00	0.00	0.00	0.00	0.00	0.00	0.00	0.00	0.00
Mg	0.00	0.00	0.00	0.00	0.00	0.00	0.00	0.00	0.00	0.00	0.00	0.00	0.00	0.00	0.00	0.00	0.00	0.00
Ca	0.00	0.00	0.00	0.00	0.00	0.00	0.00	0.00	0.00	0.00	0.00	0.00	0.00	0.00	0.00	0.00	0.00	0.00
Na	0.00	0.00	0.00	0.00	0.00	0.00	0.00	0.00	0.00	0.00	0.00	0.00	0.00	0.00	0.00	0.00	0.00	0.00
K	0.00	0.00	0.00	0.00	0.00	0.00	0.00	0.00	0.00	0.00	0.00	0.00	0.00	0.00	0.00	0.00	0.00	0.00
Total	3.00	3.00	3.00	3.00	3.00	3.00	3.00	3.00	3.00	3.00	3.00	3.00	3.00	3.00	3.00	3.00	3.00	3.00

Table A.37: Electron microprobe results for magnetite – continued.

	KK29 mt51	KK29 mt52	KK29 mt53	KK29 mt54	KK28 mt55	KK28 mt56	KK28 mt57	KK28 mt58	KK28 mt59	KK27 mt60	KK27 mt61	KK27 mt62	KK12 mt63	KK12 mt64	KK12 mt65	KK12 mt66	KK12 mt67	KK12 mt68
SiO_2	0.00	0.00	0.00	0.00	0.00	0.00	0.00	0.00	0.00	0.00	0.00	0.00	0.00	0.00	0.00	0.00	0.00	0.00
TiO_2	0.00	0.03	0.02	0.00	0.03	0.01	0.00	0.00	0.06	0.01	0.07	0.03	0.02	0.04	0.00	0.00	0.02	0.17
Al_2O_3	0.04	0.06	0.07	0.07	0.03	0.01	0.05	0.05	0.02	0.34	0.14	0.16	0.06	0.04	0.01	0.06	0.04	0.22
Cr_2O_3	0.47	0.40	0.31	0.35	0.54	0.43	0.57	0.53	0.34	0.42	0.26	0.11	0.07	0.05	0.13	0.09	0.08	0.05
FeO	83.59	83.41	83.14	83.32	83.91	83.03	83.23	83.54	81.15	79.84	83.39	81.82	87.83	87.21	85.56	84.67	83.69	83.19
MnO	0.11	0.07	0.05	0.02	0.06	0.02	0.08	0.07	0.04	0.05	0.00	0.05	0.06	0.07	0.10	0.06	0.12	0.05
MgO	0.00	0.00	0.02	0.00	0.01	0.00	0.00	0.00	0.00	0.09	0.00	0.04	0.00	0.04	0.00	0.02	0.00	0.05
CaO	0.00	0.00	0.00	0.00	0.00	0.00	0.00	0.00	0.00	0.00	0.00	0.00	0.00	0.00	0.00	0.00	0.00	0.00
Na_2O	0.00	0.00	0.00	0.00	0.00	0.00	0.00	0.00	0.00	0.00	0.00	0.00	0.00	0.00	0.00	0.00	0.00	0.00
K_2O	0.00	0.00	0.00	0.00	0.00	0.00	0.00	0.00	0.00	0.00	0.00	0.00	0.00	0.00	0.00	0.00	0.00	0.00
Total	84.25	84.01	83.62	83.77	84.59	83.51	83.98	84.19	81.64	80.83	83.87	82.22	88.13	87.45	85.84	84.91	83.93	83.80
Oxygens	4	4	4	4	4	4	4	4	4	4	4	4	4	4	4	4	4	4
Si	0.00	0.00	0.00	0.00	0.00	0.00	0.00	0.00	0.00	0.00	0.00	0.00	0.00	0.00	0.00	0.00	0.00	0.00
Ti	0.00	0.00	0.00	0.00	0.00	0.00	0.00	0.00	0.00	0.00	0.00	0.00	0.00	0.00	0.00	0.00	0.00	0.00
Al	0.00	0.00	0.00	0.00	0.00	0.00	0.00	0.00	0.00	0.01	0.00	0.00	0.00	0.00	0.00	0.00	0.00	0.00
Cr	0.01	0.00	0.00	0.00	0.01	0.00	0.01	0.01	0.00	0.00	0.00	0.00	0.00	0.00	0.00	0.00	0.00	0.00
Fe	2.99	2.99	2.99	2.99	2.99	2.99	2.99	2.99	2.99	2.99	2.99	2.99	3.00	3.00	3.00	3.00	3.00	2.99
Mn	0.00	0.00	0.00	0.00	0.00	0.00	0.00	0.00	0.00	0.00	0.00	0.00	0.00	0.00	0.00	0.00	0.00	0.00
Mg	0.00	0.00	0.00	0.00	0.00	0.00	0.00	0.00	0.00	0.00	0.00	0.00	0.00	0.00	0.00	0.00	0.00	0.00
Ca	0.00	0.00	0.00	0.00	0.00	0.00	0.00	0.00	0.00	0.00	0.00	0.00	0.00	0.00	0.00	0.00	0.00	0.00
Na	0.00	0.00	0.00	0.00	0.00	0.00	0.00	0.00	0.00	0.00	0.00	0.00	0.00	0.00	0.00	0.00	0.00	0.00
K	0.00	0.00	0.00	0.00	0.00	0.00	0.00	0.00	0.00	0.00	0.00	0.00	0.00	0.00	0.00	0.00	0.00	0.00
Total	3.00	3.00	3.00	3.00	3.00	3.00	3.00	3.00	3.00	3.00	3.00	3.00	3.00	3.00	3.00	3.00	3.00	3.00

Table A.38: Electron microprobe results for amphibole.

	KK12 amp1_int	KK12 amp2	KK12 amp3_int	KK12 amp3_rim	KK12 amp4_int	KK12 amp4_rim	KK12 amp5_int	KK12 amp5_rim	KK12 amp6_int	KK12 amp6_rim	KK12 amp7_int	KK12 amp7_rim	KK12 amp8_int	KK12 amp8_rim	KK12 amp9_mt_incl	KK12 amp11_mt_rim	KK14 amp12	KK14 amp13_int
SiO_2	41.66	41.41	42.45	41.75	42.07	42.75	42.31	41.64	41.53	41.56	41.72	42.49	41.87	41.41	41.44	50.45	41.87	42.03
TiO_2	1.15	1.28	1.14	1.21	0.99	1.00	0.98	1.15	1.13	1.18	1.18	1.16	1.00	1.14	1.05	0.41	1.88	1.77
Al_2O_3	13.58	13.92	13.30	14.02	13.63	13.00	13.13	13.51	13.71	13.50	13.74	13.46	13.05	13.71	13.70	3.08	11.62	11.49
Cr_2O_3	0.02	0.03	0.06	0.03	0.01	0.01	0.06	0.04	0.00	0.03	0.01	0.01	0.00	0.01	0.00	0.00	0.04	0.07
FeO	14.66	14.73	14.10	14.42	14.41	13.30	14.42	14.83	14.60	14.46	14.53	13.27	14.87	14.24	13.51	7.70	18.38	18.05
MnO	0.23	0.25	0.22	0.22	0.22	0.26	0.23	0.25	0.19	0.29	0.22	0.24	0.29	0.20	0.20	0.29	0.50	0.48
MgO	12.71	12.94	13.01	12.63	12.71	13.57	13.01	12.23	12.60	12.70	12.86	13.17	12.90	12.71	13.25	14.02	10.41	10.53
CaO	11.03	11.53	11.57	11.72	11.69	11.68	11.36	11.69	11.62	11.59	11.74	11.71	11.57	11.58	11.16	22.95	10.92	10.90
Na_2O	1.70	1.75	1.59	1.87	1.70	1.55	1.60	1.76	1.81	1.72	1.83	1.64	1.67	1.74	1.77	0.33	1.39	1.37
K_2O	0.74	0.87	0.82	0.89	0.84	0.82	0.77	0.90	0.90	0.87	0.89	0.85	0.85	0.91	0.78	0.01	1.43	1.39
Total	97.49	98.71	98.27	98.76	98.26	97.94	97.87	97.99	98.10	97.91	98.72	97.99	98.06	97.65	96.86	99.24	98.44	98.09
Oxygens	23	23	23	23	23	23	23	23	23	23	23	23	23	23	23	23	23	23
Si	6.20	6.11	6.26	6.15	6.22	6.30	6.27	6.20	6.16	6.18	6.15	6.26	6.22	6.17	6.19	7.28	6.32	6.35
Ti	0.13	0.14	0.13	0.13	0.11	0.11	0.11	0.13	0.13	0.13	0.13	0.13	0.11	0.13	0.12	0.04	0.21	0.20
Al	2.38	2.42	2.31	2.43	2.37	2.26	2.29	2.37	2.40	2.37	2.39	2.34	2.29	2.41	2.41	0.52	2.07	2.05
Cr	0.00	0.00	0.01	0.00	0.00	0.00	0.01	0.00	0.00	0.00	0.00	0.00	0.00	0.00	0.00	0.00	0.00	0.01
Fe	1.83	1.82	1.74	1.78	1.78	1.64	1.79	1.85	1.81	1.80	1.79	1.63	1.85	1.77	1.69	0.93	2.32	2.28
Mn	0.03	0.03	0.03	0.03	0.03	0.03	0.03	0.03	0.02	0.04	0.03	0.03	0.04	0.03	0.03	0.04	0.06	0.06
Mg	2.82	2.85	2.86	2.77	2.80	2.98	2.87	2.71	2.79	2.81	2.83	2.89	2.86	2.82	2.95	3.01	2.34	2.37
Ca	1.76	1.82	1.83	1.85	1.85	1.84	1.80	1.86	1.85	1.85	1.86	1.85	1.84	1.85	1.79	3.55	1.77	1.76
Na	0.49	0.50	0.45	0.53	0.49	0.44	0.46	0.51	0.52	0.50	0.52	0.47	0.48	0.50	0.51	0.09	0.41	0.40
K	0.14	0.16	0.15	0.17	0.16	0.15	0.15	0.17	0.17	0.17	0.17	0.16	0.16	0.17	0.15	0.00	0.28	0.27
Total	15.79	15.87	15.76	15.85	15.81	15.76	15.77	15.83	15.86	15.84	15.87	15.76	15.84	15.84	15.82	15.46	15.77	15.76

Table A.39: Electron microprobe results for amphibole – continued.

	KK14 amp13_rim	KK14 amp14_int	KK14 amp15	KK14 amp16_int	KK14 amp16_rim	KK14 amp17_int	KK14 amp17_rim	KK19 amp18_int	KK19 amp18_rim	KK19 amp19_int	KK19 amp19_rim	KK19 amp20_int	KK19 amp20_rim	KK19 amp21_int	KK19 amp21_rim	KK19 amp22_int	KK19 amp22_rim	KK19 amp23_int	KK19 amp23_rim	KK19 amp_alt	KK19 amp24_int
SiO_2	42.14	42.18	42.35	41.98	41.91	42.13	42.47	48.35	46.88	48.64	46.93	47.85	47.72	47.44	46.64	47.92	46.77	47.79	47.26	54.68	48.96
TiO_2	1.86	1.82	1.63	1.89	1.94	1.85	1.87	0.55	0.54	0.59	0.64	0.63	0.61	0.57	0.55	0.68	0.67	0.64	0.67	0.08	0.43
Al_2O_3	11.71	11.75	11.49	11.95	11.94	11.82	11.29	8.15	9.96	7.80	9.96	8.69	9.50	8.97	9.71	8.35	9.71	8.28	9.39	1.68	7.67
Cr_2O_3	0.09	0.13	0.05	0.00	0.04	0.03	0.02	0.25	0.30	0.45	0.16	0.14	0.20	0.24	0.17	0.33	0.31	0.15	0.24	0.02	0.32
FeO	17.97	17.95	18.17	18.62	18.75	18.42	18.65	11.47	11.91	11.86	11.87	11.90	11.65	12.20	11.65	11.61	11.87	11.12	11.68	8.62	10.92
MnO	0.50	0.54	0.53	0.47	0.52	0.50	0.52	0.18	0.25	0.23	0.19	0.24	0.23	0.24	0.20	0.24	0.18	0.20	0.20	0.32	0.27
MgO	10.47	10.39	10.29	10.04	9.85	10.15	10.08	17.06	15.30	17.44	15.41	16.38	16.05	16.27	15.23	16.65	15.78	17.00	15.77	20.27	17.24
CaO	10.98	10.85	10.85	10.90	10.86	10.84	10.74	10.10	10.93	10.32	11.03	10.58	11.00	10.50	10.79	10.55	10.94	10.86	10.79	11.79	10.80
Na_2O	1.36	1.35	1.30	1.46	1.32	1.37	1.35	0.90	1.15	0.75	1.18	0.89	1.09	0.99	1.13	0.93	1.07	0.94	1.02	0.22	0.92
K_2O	1.39	1.39	1.35	1.43	1.42	1.40	1.40	0.37	0.37	0.42	0.49	0.50	0.50	0.48	0.47	0.41	0.53	0.46	0.55	0.02	0.36
Total	98.47	98.35	98.01	98.74	98.55	98.51	98.39	97.38	97.58	98.50	97.88	97.81	98.54	97.90	96.54	97.69	97.83	97.44	97.58	97.70	97.89
Oxygens	23	23	23	23	23	23	23	23	23	23	23	23	23	23	23	23	23	23	23	23	23
Si	6.34	6.35	6.40	6.32	6.32	6.34	6.40	6.98	6.80	6.96	6.79	6.91	6.84	6.86	6.83	6.92	6.77	6.91	6.85	7.71	7.03
Ti	0.21	0.21	0.18	0.21	0.22	0.21	0.21	0.06	0.06	0.06	0.07	0.07	0.07	0.06	0.06	0.07	0.07	0.07	0.07	0.01	0.05
Al	2.08	2.09	2.05	2.12	2.12	2.10	2.01	1.39	1.70	1.32	1.70	1.48	1.61	1.53	1.68	1.42	1.66	1.41	1.60	0.28	1.30
Cr	0.01	0.02	0.01	0.00	0.01	0.00	0.00	0.03	0.03	0.05	0.02	0.02	0.02	0.03	0.02	0.04	0.04	0.02	0.03	0.00	0.04
Fe	2.26	2.26	2.30	2.34	2.36	2.32	2.35	1.38	1.44	1.42	1.44	1.44	1.40	1.48	1.43	1.40	1.44	1.35	1.42	1.02	1.31
Mn	0.06	0.07	0.07	0.06	0.07	0.06	0.07	0.02	0.03	0.03	0.02	0.03	0.03	0.03	0.02	0.03	0.02	0.02	0.03	0.04	0.03
Mg	2.35	2.33	2.32	2.25	2.21	2.28	2.27	3.67	3.31	3.72	3.32	3.53	3.43	3.51	3.32	3.58	3.41	3.66	3.40	4.26	3.69
Ca	1.77	1.75	1.76	1.76	1.75	1.75	1.74	1.56	1.70	1.58	1.71	1.64	1.69	1.63	1.69	1.63	1.70	1.68	1.67	1.78	1.66
Na	0.40	0.39	0.38	0.43	0.39	0.40	0.39	0.25	0.32	0.21	0.33	0.25	0.30	0.28	0.32	0.26	0.30	0.26	0.29	0.06	0.26
K	0.27	0.27	0.26	0.27	0.27	0.27	0.27	0.07	0.07	0.08	0.09	0.09	0.09	0.09	0.09	0.08	0.10	0.09	0.10	0.00	0.07
Total	15.74	15.73	15.71	15.76	15.73	15.73	15.71	15.41	15.47	15.43	15.49	15.45	15.48	15.48	15.46	15.44	15.50	15.48	15.46	15.17	15.42

Appendix B

U-Pb monazite dating

Table B.1: Operating conditions and instrument settings used for U-Pb LA-ICP-MS analyses.

Laboratory & Sample Preparation	
Laboratory name	Central Analytical Facility, Stellenbosch University
Sample type / mineral	Thin section / Monazite
Sample preparation	Conventional thin section preparation
Imaging	JEOL Superprobe JXA-8100 Electron Probe Microanalyzer (BSE imaging)
Laser Ablation System	
Make, Model & type	Resonetics Resolution S155, ArF Excimer Coherent CompexPro 110
Ablation cell & volume	Laurin Technology S155 double Helix large volume cell
Laser wavelength	193 nm
Pulse width	20 ns
Fluence	2.8 J/cm^{-2} (measured with external energy meter above sample funnel)
Repetition rate	5.5 Hz
Spot size	9 m
Sampling mode / pattern	20 m single spot analyses
Cell carrier gas	100% He, Ar and N_2 make-up gases combined using injectors into double Helix sampling funnel
Pre-ablation laser warm-up (background collection)	3 cleaning shots followed by 20 seconds background collection
Ablation duration	20 seconds
Wash-out delay	15 seconds
Cell carrier gas flows	330 ml/min He
ICP-MS Instrument	
Make, Model & type	Thermo Finnigan Element2 single collector HR-SF-ICP-MS
Sample introduction	Via Nylon 10 tubing
RF power	1350 W
Make-up gas flow	910 ml/min Ar & 0.03 ml/min N_2
Detection system	Single collector secondary electron multiplier
Masses measured	202, 204, 206, 207, 208, 232, 233, 235, 238
Integration time per peak	4 ms
Total integration time per reading	1 sec (Represents the time resolution of the data)
Sensitvity	30000 cps/ppm Pb
Dead time	6 ns

Table B.2: Monazite U-Pb isotopic data for samples PM13010.

						Ratio							Ages (Ma)						Conc.
Sample	Analysis	U [ppm]	Pb [ppm]	Th [ppm]	Th/U meas.	$^{207}Pb/^{235}U$	2σ	$^{206}Pb/^{238}U$	2σ	rho	$^{207}Pb/^{206}Pb$	2σ	$^{207}Pb/^{235}U$	2σ	$^{206}Pb/^{238}U$	2σ	$^{207}Pb/^{206}Pb$	2σ	%
PM013010	A67	424	87	32944	77.65	2.245	0.075	0.2051	0.0064	0.93	0.0794	0.0020	1195	40	1203	34	1182	50	102
PM013010	A68	473	95	15000	31.72	2.213	0.074	0.2018	0.0063	0.92	0.0796	0.0021	1185	40	1185	34	1186	51	100
PM013010	A69	464	94	24650	53.18	2.247	0.075	0.2034	0.0063	0.93	0.0801	0.0020	1196	40	1194	34	1199	49	100
PM013010	A70	565	115	19660	34.82	2.245	0.080	0.2040	0.0063	0.87	0.0798	0.0028	1195	43	1197	34	1193	68	100
PM013010	A71	536	109	35658	66.57	2.243	0.075	0.2029	0.0063	0.92	0.0802	0.0021	1195	40	1191	34	1202	51	99
PM013010	A73	481	97	29232	60.72	2.227	0.075	0.2023	0.0063	0.91	0.0799	0.0022	1190	40	1187	34	1194	54	99
PM013010	A74	149	30	19479	131.01	2.230	0.083	0.2027	0.0064	0.84	0.0798	0.0032	1190	44	1190	34	1191	79	100
PM013010	A75	497	101	43271	87.01	2.243	0.075	0.2036	0.0063	0.92	0.0799	0.0021	1195	40	1194	34	1195	51	100
PM013010	A80	522	98	25999	49.79	2.062	0.072	0.1879	0.0058	0.89	0.0796	0.0026	1136	40	1110	32	1188	63	93
PM013010	A81	513	95	16823	32.81	2.040	0.069	0.1849	0.0057	0.91	0.0800	0.0023	1129	38	1094	31	1197	56	91
PM013010	A82	555	108	17132	30.84	2.145	0.072	0.1948	0.0060	0.92	0.0799	0.0021	1164	39	1147	32	1194	51	96
PM013010	A83	689	133	27015	39.24	2.123	0.071	0.1931	0.0059	0.92	0.0797	0.0021	1156	39	1138	32	1190	52	96
PM013010	A84	563	114	18652	33.10	2.204	0.074	0.2016	0.0062	0.92	0.0793	0.0021	1182	40	1184	33	1180	52	100
PM013010	A85	472	93	20258	42.92	2.153	0.073	0.1960	0.0060	0.91	0.0797	0.0023	1166	40	1154	32	1189	56	97
PM013010	A86	592	120	20177	34.10	2.213	0.074	0.2021	0.0062	0.92	0.0795	0.0021	1185	40	1186	33	1183	52	100
PM013010	A87	271	53	25302	93.35	2.161	0.080	0.1964	0.0060	0.83	0.0798	0.0033	1169	43	1156	33	1192	80	97
PM013010	A88	603	123	21531	35.69	2.244	0.076	0.2035	0.0063	0.91	0.0800	0.0022	1195	40	1194	34	1197	55	100
PM013010	A89	737	150	9994	13.56	2.239	0.075	0.2030	0.0062	0.92	0.0800	0.0022	1193	40	1191	33	1197	53	100
LA-ICP-MS data for primary and secondary standards																			
Itamb	IT90	1609	133	67235	41.79	0.656	0.022	0.0828	0.0025	0.91	0.0575	0.0016	512	17	513	15	510	60	101
Itamb	IT91	1529	128	63463	41.52	0.662	0.022	0.0836	0.0026	0.91	0.0574	0.0016	516	17	518	15	508	61	102
Tom. Mine	TOM76	1606	505	101422	63.15	4.66	0.15	0.315	0.010	0.93	0.1074	0.0027	1760	58	1763	47	1755	45	100
Tom. Mine	TOM77	1509	478	59850	39.67	4.72	0.16	0.317	0.010	0.92	0.1081	0.0028	1771	59	1775	48	1767	46	100
Tom. Mine	TOM92	1365	433	57043	41.78	4.72	0.16	0.317	0.010	0.91	0.1080	0.0030	1770	59	1774	47	1766	51	100
Tom. Mine	TOM93	3540	1117	159619	45.09	4.69	0.16	0.315	0.010	0.91	0.1078	0.0030	1765	59	1768	47	1763	50	100

Table B.3: Monazite U-Pb isotopic data for samples PM13032 and PM13068.

						Ratios							Ages (Ma)						Conc.
Sample	Analysis	U [ppm]	Pb [ppm]	Th [ppm]	Th/U meas.	$^{207}Pb/^{235}U$	2σ	$^{206}Pb/^{238}U$	2σ	rho	$^{207}Pb/^{206}Pb$	2σ	$^{207}Pb/^{235}U$	2σ	$^{206}Pb/^{238}U$	2σ	$^{207}Pb/^{206}Pb$	2σ	%
PM13032	A096	135	29	28988	215.0	2.41	0.08	0.213	0.007	0.90	0.0821	0.0025	1246	43	1246	35	1248	58	100
PM13032	A097	192	63	49	0.26	5.06	0.19	0.328	0.010	0.85	0.1120	0.0044	1830	67	1828	50	1832	70	100
PM13032	A098	331	108	99	0.30	5.02	0.17	0.326	0.010	0.93	0.1115	0.0027	1822	60	1821	49	1823	44	100
PM13032	A099	1730	567	35952	20.8	5.04	0.16	0.328	0.010	0.94	0.1115	0.0025	1826	59	1827	49	1824	40	100
PM13032	A100	794	260	36066	45.4	5.08	0.17	0.328	0.010	0.93	0.1124	0.0026	1832	60	1827	49	1839	42	99
LA-ICP-MS data for primary and secondary standards																			
Tom. Mine	TOM101	1790	566	75734	42.3	4.71	0.16	0.316	0.010	0.91	0.1082	0.0030	1769	60	1770	48	1768	50	100
Tom. Mine	TOM102	1779	560	93936	52.8	4.67	0.16	0.315	0.010	0.93	0.1076	0.0027	1762	59	1764	48	1759	45	100
PM13068	A52	166	36	48475	291.41	2.46	0.09	0.216	0.007	0.90	0.0829	0.0025	1262	44	1259	36	1266	59	99
PM13068	A53	347	68	56443	162.44	2.21	0.08	0.196	0.006	0.88	0.0816	0.0028	1184	42	1155	33	1237	65	93
PM13068	A54	197	42	30404	154.03	2.38	0.08	0.211	0.007	0.91	0.0819	0.0024	1238	43	1235	35	1242	57	99
PM13068	A55	126	27	38258	302.80	2.42	0.10	0.213	0.007	0.78	0.0825	0.0042	1250	51	1246	36	1256	97	99
PM13068	A56	194	42	63776	328.22	2.44	0.10	0.215	0.007	0.81	0.0824	0.0040	1255	52	1255	38	1255	94	100
PM13068	A57	221	47	25988	117.44	2.39	0.08	0.212	0.007	0.91	0.0818	0.0024	1241	43	1241	36	1241	57	100
PM13068	A58	835	176	45857	54.95	2.39	0.09	0.211	0.007	0.86	0.0822	0.0031	1241	45	1236	35	1250	73	99
PM13068	A59	179	39	42220	236.12	2.45	0.09	0.216	0.007	0.90	0.0823	0.0025	1256	44	1259	36	1252	60	101
PM13068	A60	385	78	19785	51.37	2.31	0.09	0.204	0.006	0.82	0.0822	0.0035	1215	46	1194	34	1251	83	95
PM13068	A61	157	34	49320	313.72	2.47	0.09	0.216	0.007	0.89	0.0829	0.0027	1264	45	1262	37	1268	62	100
PM13068	A62	108	22	11425	105.67	2.28	0.10	0.202	0.006	0.74	0.0819	0.0048	1207	52	1187	34	1243	113	95
LA-ICP-MS data for primary and secondary standards																			
Tom. Mine	Tom63	1469	466	90833	61.82	4.68	0.16	0.317	0.010	0.90	0.1071	0.0033	1764	62	1775	49	1750	55	101
Tom. Mine	Tom64	1641	518	92659	56.47	4.66	0.17	0.316	0.010	0.87	0.1071	0.0038	1761	64	1770	49	1750	64	101

Table B.4: Monazite U-Pb isotopic data for sample PM13007.

						Ratios							Ages (Ma)						Conc.
Sample	Analysis	U [ppm]	Pb [ppm]	Th [ppm]	Th/U meas.	$^{207}Pb/^{235}U$	2σ	$^{206}Pb/^{238}U$	2σ	rho	$^{207}Pb/^{206}Pb$	2σ	$^{207}Pb/^{235}U$	2σ	$^{206}Pb/^{238}U$	2σ	$^{207}Pb/^{206}Pb$	2σ	%
PM13007	A10	2509	461	44816	17.86	1.921	0.061	0.1837	0.0055	0.94	0.0758	0.0017	1088	35	1087	30	1091	44	100
PM13007	A11	2433	449	43996	18.08	1.931	0.062	0.1844	0.0055	0.94	0.0759	0.0017	1092	35	1091	30	1094	44	100
PM13007	A12	2134	393	41483	19.44	1.913	0.061	0.1842	0.0055	0.94	0.0753	0.0017	1086	35	1090	30	1077	45	101
PM13007	A13	4067	736	42655	10.49	1.875	0.060	0.1810	0.0054	0.94	0.0751	0.0017	1072	34	1072	29	1072	45	100
PM13007	A14	3534	638	49059	13.88	1.880	0.060	0.1806	0.0054	0.93	0.0755	0.0017	1074	34	1070	29	1083	46	99
PM13007	A15	1368	252	39875	29.14	1.915	0.061	0.1840	0.0055	0.93	0.0755	0.0018	1086	35	1089	30	1081	46	101
PM13007	A16	3842	695	35956	9.36	1.885	0.060	0.1809	0.0054	0.94	0.0756	0.0017	1076	34	1072	29	1084	44	99
PM13007	A23	2339	430	40251	17.21	1.921	0.061	0.1839	0.0054	0.93	0.0758	0.0017	1089	35	1088	30	1089	46	100
PM13007	A24	3160	582	39600	12.53	1.908	0.060	0.1843	0.0054	0.93	0.0751	0.0017	1084	34	1090	30	1071	45	102
PM13007	A25	3072	564	39634	12.90	1.911	0.061	0.1835	0.0054	0.93	0.0755	0.0017	1085	34	1086	30	1083	45	100
PM13007	A26	2483	453	41847	16.85	1.903	0.060	0.1824	0.0054	0.93	0.0757	0.0017	1082	34	1080	29	1087	46	99
PM13007	A27	1227	221	22228	18.11	1.874	0.061	0.1799	0.0053	0.90	0.0756	0.0021	1072	35	1067	29	1084	56	98
PM13007	A28	3476	640	41194	11.9	1.915	0.060	0.1842	0.0054	0.93	0.0754	0.0017	1086	34	1090	30	1079	46	101
PM13007	A29	3005	553	23938	8.0	1.925	0.061	0.1842	0.0054	0.92	0.0758	0.0018	1090	35	1090	30	1090	48	100
PM13007	A36	1963	359	49467	25.2	1.901	0.061	0.1831	0.0054	0.92	0.0753	0.0019	1081	35	1084	29	1077	50	101
PM13007	A37	3088	562	41085	13.3	1.889	0.060	0.1820	0.0053	0.93	0.0753	0.0018	1077	34	1078	29	1075	47	100
PM13007	A38	1102	201	50139	45.5	1.906	0.061	0.1827	0.0054	0.92	0.0757	0.0019	1083	35	1082	29	1087	50	100
PM13007	A39	2598	470	44196	17.0	1.881	0.060	0.1810	0.0053	0.92	0.0754	0.0018	1074	34	1073	29	1078	48	99
PM13007	A40	2391	436	28579	12.0	1.894	0.060	0.1822	0.0053	0.92	0.0754	0.0019	1079	34	1079	29	1079	50	100
PM13007	A42	2491	456	38069	15.3	1.896	0.060	0.1828	0.0053	0.92	0.0752	0.0019	1080	34	1082	29	1074	50	101
LA-ICP-MS data for primary and secondary standards																			
Itamb	IT07	2574	215	102851	40.0	0.668	0.022	0.0834	0.0025	0.93	0.0581	0.0014	519	17	516	15	533	54	97
Itamb	IT08	2386	200	94517	39.6	0.667	0.022	0.0838	0.0025	0.93	0.0577	0.0014	519	17	519	15	519	53	100
Itamb	IT09	2173	183	85509	39.4	0.669	0.022	0.0840	0.0025	0.92	0.0577	0.0014	520	17	520	15	520	55	100
Itamb	IT21	2398	198	94319	39.3	0.657	0.021	0.0826	0.0025	0.92	0.0577	0.0014	513	17	512	15	519	54	98
Itamb	IT22	2261	189	89963	39.8	0.659	0.021	0.0836	0.0025	0.92	0.0572	0.0014	514	17	518	15	498	55	104
Itamb	IT34	2304	191	90990	39.5	0.656	0.021	0.0829	0.0024	0.92	0.0574	0.0015	512	16	513	15	506	55	101
Itamb	IT35	2209	185	86811	39.3	0.669	0.022	0.0838	0.0025	0.91	0.0579	0.0015	520	17	519	15	526	57	99
Itamb	IT43	2268	189	89066	39.3	0.660	0.021	0.0832	0.0024	0.91	0.0575	0.0015	515	17	515	15	512	57	101
Itamb	IT44	2399	195	91946	38.3	0.647	0.021	0.0814	0.0024	0.91	0.0577	0.0015	507	16	505	14	516	58	98
Tom. Mine	TOM04	2753	859	71838	26.1	4.64	0.15	0.3121	0.0093	0.94	0.1078	0.0024	1757	56	1751	46	1763	41	99
Tom. Mine	TOM05	5483	1730	84516	15.4	4.68	0.15	0.3155	0.0094	0.94	0.1075	0.0023	1763	56	1768	46	1757	39	101
Tom. Mine	TOM06	7442	2355	135545	18.2	4.72	0.15	0.3164	0.0095	0.94	0.1082	0.0024	1771	57	1772	46	1769	40	100
Tom. Mine	TOM19	2993	946	80426	26.9	4.66	0.15	0.3162	0.0094	0.94	0.1069	0.0024	1760	56	1771	46	1747	41	101
Tom. Mine	TOM20	4109	1301	73949	18.0	4.72	0.15	0.3167	0.0094	0.93	0.1081	0.0025	1771	56	1774	46	1767	42	100
Tom. Mine	TOM32	2850	890	64078	22.5	4.67	0.15	0.3122	0.0092	0.93	0.1085	0.0026	1762	56	1751	45	1775	43	99
Tom. Mine	TOM33	3536	1117	61141	17.3	4.62	0.15	0.3159	0.0093	0.93	0.1062	0.0025	1754	56	1770	45	1735	44	102
Tom. Mine	TOM45	3610	1143	56288	15.6	4.65	0.15	0.3165	0.0092	0.92	0.1065	0.0027	1758	56	1773	45	1741	46	102
Tom. Mine	TOM46	3161	993	71548	22.6	4.71	0.15	0.3142	0.0093	0.92	0.1088	0.0027	1769	57	1761	46	1778	45	99

Table B.5: Monazite U-Pb isotopic data for samples PM13084 and PM13163.

						Ratios							Ages (Ma)						Conc.
Sample	Analysis	U [ppm]	Pb [ppm]	Th [ppm]	Th/U meas.	$^{207}Pb/^{235}U$	2σ	$^{206}Pb/^{238}U$	2σ	rho	$^{207}Pb/^{206}Pb$	2σ	$^{207}Pb/^{235}U$	2σ	$^{206}Pb/^{238}U$	2σ	$^{207}Pb/^{206}Pb$	2σ	%
PM13084	A105	676	137	46471	68.79	2.23	0.07	0.203	0.006	0.93	0.0796	0.0019	1190	40	1192	34	1187	47	100
PM13084	A106	1007	205	42717	42.41	2.25	0.07	0.204	0.006	0.94	0.0800	0.0019	1196	40	1197	34	1196	46	100
PM13084	A107	1002	202	54751	54.64	2.22	0.07	0.202	0.006	0.93	0.0797	0.0020	1186	40	1185	34	1189	49	100
PM13084	A108	896	181	48481	54.11	2.20	0.07	0.202	0.006	0.93	0.0791	0.0019	1182	39	1187	34	1174	47	101
PM13084	A109	822	167	116681	141.93	2.23	0.07	0.203	0.006	0.93	0.0796	0.0020	1191	40	1193	34	1187	48	100
PM13084	A110	414	84	54950	132.79	2.23	0.08	0.203	0.007	0.93	0.0798	0.0021	1191	41	1192	35	1191	50	100
PM13084	A111	296	60	46715	157.91	2.21	0.08	0.202	0.006	0.92	0.0794	0.0022	1186	41	1187	34	1183	54	100
PM13084	A112	149	30	35411	237.12	2.22	0.08	0.202	0.006	0.86	0.0798	0.0030	1188	44	1187	34	1192	73	100
PM13084	A113	670	136	54018	80.68	2.24	0.08	0.202	0.006	0.92	0.0802	0.0022	1193	41	1188	34	1202	53	99
PM13084	A114	480	97	50047	104.28	2.24	0.08	0.202	0.006	0.92	0.0801	0.0022	1192	41	1188	34	1200	53	99
LA-ICP-MS data for primary and secondary standards																			
Itamb	IT115	1761	145	78470	44.55	0.66	0.02	0.083	0.003	0.92	0.0577	0.0015	513	17	511	15	519	57	99
Itamb	IT116	1756	146	78062	44.45	0.66	0.02	0.083	0.003	0.92	0.0577	0.0015	516	17	516	15	517	58	100
Tho. Mine	TOM117	1110	350	73746	66.41	4.68	0.16	0.315	0.010	0.92	0.1076	0.0028	1764	59	1768	48	1760	46	100
Tho. Mine	TOM118	1617	512	115434	71.38	4.73	0.16	0.317	0.010	0.92	0.1083	0.0029	1773	60	1775	48	1771	48	100
PM13163	A09	2762	472	54833	19.85	1.72	0.06	0.171	0.005	0.94	0.0731	0.0017	1017	33	1017	28	1016	45	100
PM13163	A11	4176	668	65615	15.71	1.60	0.05	0.160	0.005	0.94	0.0724	0.0016	969	31	956	27	997	46	96
PM13163	A12	3703	594	83842	22.64	1.61	0.05	0.160	0.005	0.92	0.0728	0.0018	974	32	959	27	1009	50	95
PM13163	A13	2917	475	63974	21.93	1.63	0.05	0.163	0.005	0.92	0.0727	0.0019	983	32	973	27	1005	53	97
PM13163	A14	2669	451	56580	21.20	1.70	0.06	0.169	0.005	0.93	0.0731	0.0017	1010	33	1007	28	1017	47	99
PM13163	A15	3331	564	61823	18.56	1.70	0.06	0.169	0.005	0.93	0.0728	0.0017	1009	33	1009	28	1009	47	100
PM13163	A16	3693	585	44927	12.17	1.59	0.05	0.159	0.005	0.93	0.0728	0.0017	967	31	949	27	1009	48	94
PM13163	A20	4271	705	59074	13.83	1.65	0.05	0.165	0.005	0.93	0.0726	0.0018	990	32	985	28	1002	49	98
PM13163	A21	2361	370	22910	9.70	1.57	0.05	0.157	0.005	0.92	0.0725	0.0018	957	31	938	26	1001	50	94
LA-ICP-MS data for primary and secondary standards																			
Itamb	IT07	1945	162	98403	50.60	0.66	0.02	0.083	0.003	0.93	0.0573	0.0014	514	17	516	15	504	54	102
Itamb	IT08	1889	158	96044	50.83	0.67	0.02	0.084	0.003	0.93	0.0576	0.0014	518	17	519	15	515	53	101
Tho. Min	TOM04	1563	491	127685	81.68	4.66	0.15	0.314	0.009	0.94	0.1076	0.0024	1760	56	1761	46	1759	40	100
Tho. Min	TOM05	1536	479	127036	82.73	4.65	0.15	0.312	0.009	0.94	0.1080	0.0024	1758	56	1752	46	1767	40	99
Tho. Min	TOM06	1435	455	120403	83.90	4.72	0.15	0.317	0.010	0.94	0.1079	0.0024	1770	57	1775	47	1765	40	101
Tho. Min	TOM22	1203	376	121474	100.95	4.67	0.15	0.312	0.009	0.93	0.1083	0.0027	1761	58	1752	46	1771	45	99
Tho. Min	TOM23	1506	479	130781	86.83	4.73	0.16	0.318	0.010	0.92	0.1080	0.0027	1773	58	1779	47	1766	46	101

Table B.6: Monazite U-Pb isotopic data for samples PM13175.

						Ratio							Ages (Ma)						Conc.
Sample	Analysis	U [ppm]	Pb [ppm]	Th [ppm]	Th/U meas.	$^{207}Pb/^{235}U$	2σ	$^{206}Pb/^{238}U$	2σ	rho	$^{207}Pb/^{206}Pb$	2σ	$^{207}Pb/^{235}U$	2σ	$^{206}Pb/^{238}U$	2σ	$^{207}Pb/^{206}Pb$	2σ	%
PM13175	A26	2510	851	47755	19.03	5.35	0.17	0.339	0.010	0.94	0.1144	0.0025	1877	60	1883	49	1871	39	101
PM13175	A27	577	152	50918	88.17	4.15	0.15	0.263	0.008	0.86	0.1143	0.0044	1664	62	1508	43	1868	68	81
PM13175	A28	707	227	68144	96.35	5.07	0.16	0.322	0.010	0.94	0.1143	0.0026	1831	59	1798	47	1869	41	96
PM13175	A29	715	229	58209	81.46	5.06	0.16	0.320	0.010	0.94	0.1147	0.0026	1829	59	1789	47	1876	41	95
PM13175	A30	3802	1283	72186	18.99	5.37	0.17	0.337	0.010	0.94	0.1155	0.0026	1881	61	1874	49	1888	41	99
PM13175	A31	521	177	16254	31.19	5.37	0.18	0.339	0.010	0.89	0.1149	0.0035	1879	64	1881	49	1878	54	100
PM13175	A38	670	211	96467	143.96	4.98	0.16	0.314	0.010	0.93	0.1148	0.0027	1815	60	1762	47	1876	42	94
PM13175	A39	3359	1132	39732	11.83	5.33	0.18	0.337	0.010	0.93	0.1148	0.0028	1874	62	1872	50	1877	44	100
PM13175	A40	2312	724	56217	24.32	4.97	0.17	0.313	0.010	0.92	0.1150	0.0031	1814	61	1756	47	1880	47	93
PM13175	A41	3224	1060	48334	14.99	5.26	0.17	0.329	0.010	0.93	0.1162	0.0028	1863	62	1832	49	1898	44	97
PM13175	A43	721	231	23515	32.61	5.11	0.17	0.321	0.010	0.92	0.1156	0.0031	1838	62	1793	48	1890	48	95
PM13175	A44	1495	507	28610	19.14	5.36	0.18	0.339	0.010	0.90	0.1145	0.0034	1878	64	1883	50	1872	52	101
PM13175	A45	1757	597	28294	16.11	5.43	0.19	0.340	0.011	0.91	0.1160	0.0033	1890	65	1886	51	1895	51	100
LA-ICP-MS data for primary and secondary standards																			
Itamb	IT46	2023	168	101211	50.03	0.66	0.02	0.083	0.003	0.92	0.0579	0.0016	517	17	515	15	527	59	98
Itamb	IT47	1276	107	60757	47.62	0.67	0.02	0.084	0.003	0.85	0.0576	0.0022	519	19	520	16	513	84	101
Tho. Mine	TOM34	1382	436	114899	83.13	4.68	0.15	0.316	0.010	0.94	0.1077	0.0024	1764	57	1768	47	1760	41	100
Tho. Mine	TOM35	1113	351	136657	122.74	4.73	0.15	0.315	0.010	0.93	0.1088	0.0025	1773	58	1767	47	1779	43	99
Tho. Mine	TOM48	1283	407	115091	89.71	4.70	0.16	0.317	0.010	0.93	0.1073	0.0027	1766	59	1777	48	1754	45	101
Tho. Mine	TOM49	1471	465	118793	80.77	4.66	0.16	0.316	0.010	0.93	0.1069	0.0027	1760	59	1770	48	1747	46	101

References

Aleinikoff, J. N., Schenck, W. S., Plank, M. O., Srogi, L., Fanning, C. M., Kamo, S. L. & Bosbyshell, H., 2006. Deciphering igneous and metamorphic events in high-grade rocks of the Wilmington Complex, Delaware: Morphology, cathodoluminescence and backscattered electron zoning, and SHRIMP U-Pb geochronology of zircon and monazite. *Geological Society of America Bulletin*, **118**(1-2), 39–64.

Barton, E. & Burger, A., 1983. Reconnaissance isotopic investigations in the Namaqua Mobile Belt and implications for Proterozoic crustal evolution-Upington geotraverse, *Namaqualand metamorphic complex*.

Bateman, H., 1910. The solution of a system of differential equations occurring in the theory of radioactive transformations, *Proc. Cambridge Philos. Soc*, Vol. 15, pp. 423–427.

Becker, T., Schreiber, U., Kampunzu, A. & Armstrong, R., 2006. Mesoproterozoic rocks of Namibia and their plate tectonic setting. *Journal of African Earth Sciences*, **46**(1), 112–140.

Behrmann, J. & Mainprice, D., 1987. Deformation mechanisms in a high-temperature quartz-feldspar mylonite: evidence for superplastic flow in the lower continental crust. *Tectonophysics*, **140**(2), 297–305.

Bial, J., Büttner, S. & Appel, P., 2016. Timing and conditions of regional metamorphism and crustal shearing in the granulite facies basement of south Namibia: Implications for the crustal evolution of the Namaqualand metamorphic basement in the Mesoproterozoic. *Journal of African Earth Sciences*, **123**, 145–176.

Bial, J., Büttner, S. H. & Frei, D., 2015b. Formation and emplacement of two contrasting late-Mesoproterozoic magma types in the central Namaqua Metamorphic Complex (South Africa, Namibia): Evidence from geochemistry and geochronology. *Lithos*, **224**, 272–294.

Bial, J., Büttner, S. H., Schenk, V. & Appel, P., 2015a. The long-term high-temperature history of the central Namaqua Metamorphic Complex: Evidence for a Mesoproterozoic continental back-arc in southern Africa. *Precambrian Research*, **268**, 243–278.

Blignault, H., 1977. *Structural-metamorphic imprint on part of the Namaqua mobile belt in South West Africa*, Precambrian Research Unit, University of Cape Town.

Blignault, H., Jackson, M., Beukes, G. & Toogood, D., 1974. The Namaqua tectonic province in south west Africa. *Bulletin of the Precambrian Research Unit, University of Cape Town, South Africa*, **15**, 29–47.

Blignault, H., Van Aswegen, G., Van der Merwe, S. & Colliston, W., 1983. The Namaqualand geotraverse and environs: part of the Proterozoic Namaqua Mobile Belt. *Geological Society of South Africa, Special Publication*, **10**, 1–29.

Boger, S. & White, R., 2003. The metamorphic evolution of metapelitic granulites from Radok Lake, northern Prince Charles Mountains, east Antarctica; evidence for an anticlockwise P–T path. *Journal of Metamorphic Geology*, **21**(3), 285–298.

Brown, M., 2002. Retrograde processes in migmatites and granulites revisited. *Journal of Metamorphic Geology*, **20**(1), 25–40.

Brown, M., 2008. Characteristic thermal regimes of plate tectonics and their metamorphic imprint throughout Earth history: when did Earth first adopt a plate tectonics mode of behavior. *Geological Society of America Special Papers*, **440**, 97–128.

Brown, M., 2010. Melting of the continental crust during orogenesis: the thermal, rheological, and compositional consequences of melt transport from lower to upper continental crust. *Canadian Journal of Earth Sciences*, **47**(5), 655–694.

Brown, M. & Solar, G. S., 1998. Shear-zone systems and melts: feedback relations and self-organization in orogenic belts. *Journal of Structural Geology*, **20**(2-3), 211–227.

Catlos, E., Gilley, L. & Harrison, T. M., 2002. Interpretation of monazite ages obtained via in situ analysis. *Chemical Geology*, **188**(3), 193–215.

Cesare, B., Ferrero, S., Salvioli-Mariani, E., Pedron, D. & Cavallo, A., 2009. Nanogranite and glassy inclusions: The anatectic melt in migmatites and granulites. *Geology*, **37**(7), 627–630.

Cherniak, D., Watson, E. B., Grove, M. & Harrison, T. M., 2004. Pb diffusion in monazite: a combined RBS/SIMS study. *Geochimica et Cosmochimica Acta*, **68**(4), 829–840.

Clark, C., Kirkland, C. L., Spaggiari, C. V., Oorschot, C., Wingate, M. T. & Taylor, R. J., 2014. Proterozoic granulite formation driven by mafic magmatism: An example from the Fraser Range Metamorphics, Western Australia. *Precambrian Research*, **240**, 1–21.

Clifford, T. N., Barton, E., Stern, R. A. & Duchesne, J., 2004. U–Pb zircon calendar for Namaquan (Grenville) crustal events in the granulite-facies terrane of the O'okiep Copper District of South Africa. *Journal of Petrology*, **45**(4), 669–691.

Collins, W., 2002. Hot orogens, tectonic switching, and creation of continental crust. *Geology*, **30**(6), 535–538.

Colliston, W. & Schoch, A., 1998. Tectonostratigraphic features along the Orange River in the western part of the Mesoproterozoic Namaqua mobile belt. *South African Journal of Geology*, **101**(2), 91–100.

Colliston, W. & Schoch, A., 2000. Mid-Proterozoic tectonic evolution along the Orange River on the border between South Africa and Namibia. *Communications of the Geological Survey of Namibia*, **12**, 53–62.

Colliston, W. & Schoch, A., 2006. The distribition and diagnostic features of deformed plutonic rocks in two terranes of the Namaque mobile belt along the Orange (Gariep) River, South Africa. *South African Journal of Geology*, **109**(3), 369–392.

Colliston, W. & Schoch, A., 2013. Wrench-shearing during the Namaqua Orogenesis-Mesoproterozoic late stage deformation effects during Rodinia assembly. *Precambrian Research*, **233**, 44–58.

Colliston, W., Cornell, D., Schoch, A. & Praekelt, H., 2015. Geochronological constraints on the Hartbees River Thrust and Augrabies Nappe: new insights into the assembly of the Mesoproterozoic Namaqua-Natal Province of southern Africa. *Precambrian Research*, **265**, 150–165.

Cornell, D., Humphreys, H., Theart, H. & Scheepers, D., 1992. A collision-related pressure-temperature-time path for Prieska Copper Mine, Namaqua-Natal tectonic Province, South Africa. *Precambrian research*, **59**(1), 43–71.

Couëslan, C. G., Pattison, D. R. & Dufrane, S. A., 2013. Paleoproterozoic metamorphic and deformation history of the Thompson Nickel Belt, Superior Boundary Zone, Canada, from in situ U–Pb analysis of monazite. *Precambrian Research*, **237**, 13–35.

Dewey, J. F., 1977. Suture zone complexities: a review. *Tectonophysics*, **40**(1-2), 53–67.

Dewey, J., Ryan, P. & Andersen, T., 1993. Orogenic uplift and collapse, crustal thickness, fabrics and metamorphic phase changes: the role of eclogites. *Geological Society, London, Special Publications*, **76**(1), 325–343.

Diener, J., 2014. Low-P-high-T metamorphism of the Aggeneys Terrane, Namaqua Metamorphic Complex, South Africa. *South African Journal of Geology*, **117**(1), 31–44.

Diener, J. & Powell, R., 2010. Influence of ferric iron on the stability of mineral assemblages. *Journal of Metamorphic Geology*, **28**(6), 599–613.

Diener, J. F., White, R. W., Link, K., Dreyer, T. S. & Moodley, A., 2013. Clockwise, low-P metamorphism of the Aus granulite terrain, southern Namibia, during the Mesoproterozoic Namaqua Orogeny. *Precambrian Research*, **224**, 629–652.

Diener, J., White, R. & Powell, R., 2008. Granulite facies metamorphism and subsolidus fluid-absent reworking, Strangways Range, Arunta Block, central Australia. *Journal of Metamorphic Geology*, **26**(6), 603–622.

Eglington, B., 2006. Evolution of the Namaqua-Natal Belt, southern Africa – A geochronological and isotope geochemical review. *Journal of African Earth Sciences*, **46**(1), 93–111.

Ernst, W., 1988. Tectonic history of subduction zones inferred from retrograde blueschist PT paths. *Geology*, **16**(12), 1081–1084.

Ernst, W., 2010. Subduction zone metamorphism–pioneering contributions from the Alps. *International Geology Review*, **52**(10-12), 1021–1039.

Fitzsimons, I. & Harley, S., 1994. The influence of retrograde cation exchange on granulite P-T estimates and a convergence technique for the recovery of peak metamorphic conditions. *Journal of Petrology*, **35**(2), 543–576.

Foster, G., Gibson, H., Parrish, R., Horstwood, M., Fraser, J. & Tindle, A., 2002. Textural, chemical and isotopic insights into the nature and behaviour of metamorphic monazite. *Chemical Geology*, **191**(1), 183–207.

Frei, D. & Gerdes, A., 2009. Precise and accurate in situ U–Pb dating of zircon with high sample throughput by automated LA-SF-ICP-MS. *Chemical Geology*, **261**(3), 261–270.

Gerdes, A. & Zeh, A., 2006. Combined U–Pb and Hf isotope LA-(MC-) ICP-MS analyses of detrital zircons: comparison with SHRIMP and new constraints for the provenance and age of an Armorican metasediment in Central Germany. *Earth and Planetary Science Letters*, **249**(1), 47–61.

Green, E., White, R., Diener, J., Powell, R., Holland, T. & Palin, R., 2016. Activity–composition relations for the calculation of partial melting equilibria in metabasic rocks. *Journal of Metamorphic Geology*, **34**(9), 845–869.

Hand, M., Dirks, P., Powell, R. & Buick, I., 1992. How well established is isobaric cooling in Proterozoic orogenic belts? An example from the Arunta inlier, central Australia. *Geology*, **20**(7), 649–652.

Handy, M., Mulch, A., Rosenau, M. & Rosenberg, C., 2001. The role of fault zones and melts as agents of weakening, hardening and differentiation of the continental crust: a synthesis. *Geological Society, London, Special Publications*, **186**(1), 305–332.

Hartnady, C., Joubert, P. & Stowe, C., 1985. Proterozoic crustal evolution in southwestern Africa. *Episodes*, **8**(4), 236–244.

Hirth, G. & Tullis, J., 1992. Dislocation creep regimes in quartz aggregates. *Journal of Structural Geology*, **14**(2), 145–159.

Holland, T. & Powell, R., 2003. Activity–composition relations for phases in petrological calculations: an asymmetric multicomponent formulation. *Contributions to Mineralogy and Petrology*, **145**(4), 492–501.

Holland, T. & Powell, R., 2011. An improved and extended internally consistent thermodynamic dataset for phases of petrological interest, involving a new equation of state for solids. *Journal of Metamorphic Geology*, **29**(3), 333–383.

Iizuka, T., McCulloch, M. T., Komiya, T., Shibuya, T., Ohta, K., Ozawa, H., Sugimura, E. & Collerson, K. D., 2010. Monazite geochronology and geochemistry of meta-sediments in the Narryer Gneiss Complex, Western Australia: constraints on the tectonothermal history and provenance. *Contributions to Mineralogy and Petrology*, **160**(6), 803–823.

Imber, J., Holdsworth, R., Butler, C. & Lloyd, G., 1997. Fault-zone weakening processes along the reactivated Outer Hebrides Fault Zone, Scotland. *Journal of the Geological Society*, **154**(1), 105–109.

Jackson, M., 1976. *High-grade metamorphism and migmatization of the Namaqua Metamorphic Complex around Aus in the southern Namib Desert, south west Africa*, University of Cape Town, Department of Geology.

Jacobs, J., Thomas, R. & Weber, K., 1993. Accretion and indentation tectonics at the southern edge of the Kaapvaal craton during the Kibaran (Grenville) orogeny. *Geology*, **21**(3), 203–206.

Jessell, M., 1987. Grain-boundary migration microstructures in a naturally deformed quartzite. *Journal of Structural Geology*, **9**(8), 1007–1014.

Kröner, A., Barton, E., Burger, A., Allsopp, H. & Bertrand, J., 1983. The ages of the Goodhouse granite and grey gneisses from the marginal zone of the Richtersveld Province and their bearing on the timing of tectonic events in the Namaqua Mobile Belt, *Namaqualand Metamorphic Complex*.

Lambert, C. W., 2013. *Granitic melt transport and emplacement along transcurrent shear zones: case study of the Pofadder Shear Zone in South Africa and Namibia.* PhD thesis, Stellenbosch: Stellenbosch University.

Lasalle, S., Dunning, G. & Indares, A., 2014. In situ LA–ICP–MS dating of monazite from aluminous gneisses: insights on the tectono-metamorphic history of a granulite-facies domain in the central Grenville Province. *Canadian Journal of Earth Sciences*, **51**(6), 558–572.

Ludwig, K., 2003. Isoplot/EX, version 3, A geo-chronological toolkit for Microsoft Excel. *Berkeley Geochronology Center*, **4**, na.

Macey, P., Minaar, H., Miller, J. & Lambert, C., 2013. *The Precambrian geology of the region south of Warmbad from Haib to Velloorsdrif, Southern Namibia*, Council for Geoscience.

Miller, R., 2008. Namaqua Metamorphic Complex, *The Geology of Namibia: Archaean to Mesoproterozoic.*

Miller, R. M., 2012. Review of Mesoproterozoic magmatism, sedimentation and terrane amalgamation in southwestern Africa. *South African Journal of Geology*, **115**(4), 417–448.

Montési, L. G., 2013. Fabric development as the key for forming ductile shear zones and enabling plate tectonics. *Journal of Structural Geology*, **50**, 254–266.

Overstreet, W. C., (1967). The geologic occurrence of monazite, *Technical report*, US Geological Survey.

Paquette, J. L. & Tiepolo, M., 2007. High resolution (5 μm) U–Th–Pb isotope dating of monazite with excimer laser ablation (ELA)-ICPMS. *Chemical Geology*, **240**(3), 222–237.

Parrish, R. R., 1990. U-Pb dating of monazite and its application to geological problems. *Canadian Journal of Earth Sciences*, **27**(11), 1431–1450.

Pattison, D. R., Chacko, T., Farquhar, J. & McFarlane, C. R., 2003. Temperatures of granulite-facies metamorphism: constraints from experimental phase equilibria and thermobarometry corrected for retrograde exchange. *Journal of Petrology*, **44**(5), 867–900.

Pettersson, Å., Cornell, D. H., Yuhara, M. & Hirahara, Y., 2009. Sm-Nd data for granitoids across the Namaqua sector of the Namaqua-Natal Province, South Africa. *Geological Society, London, Special Publications*, **323**(1), 219–230.

Powell, R., 1983. Processes in granulite-facies metamorphism. *Migmatites, melting and metamorphism*, pp. 127–139.

Powell, R. & Holland, T., 1988. An internally consistent dataset with uncertainties and correlations: Applications to geobarometry, worked examples and a computer program. *Journal of Metamorphic Geology*, **6**(2), 173–204.

Powell, R. & Holland, T., 2008. On thermobarometry. *Journal of Metamorphic Geology*, **26**(2), 155–179.

Powell, R., Guiraud, M. & White, R. W., 2005. Truth and beauty in metamorphic phase-equilibria: conjugate variables and phase diagrams. *The Canadian Mineralogist*, **43**(1), 21–33.

Prabhakar, N., 2013. Resolving poly-metamorphic Paleoarchean ages by chemical dating of monazites using multi-spectrometer U, Th and Pb analyses and sub-counting methodology. *Chemical Geology*, **347**, 255–270.

Raith, J. & Harley, S., 1998. Low-P/high-T metamorphism in the Okiep Copper District, western Namaqualand, South Africa. *Journal of Metamorphic Geology*, **16**(2), 281–305.

Ramsay, J., 1980. Shear zone geometry: a review. *Journal of structural geology*, **2**(1), 83–99.

Reid, D., 1979. Age relationships within the mid-Proterozoic Vioolsdrif batholith, lower Orange River region. *Transactions of the Geological Society of South Africa*, **82**, 305–311.

Robb, L., Armstrong, R. & Waters, D., 1999. The history of granulite-facies metamorphism and crustal growth from single zircon U–Pb geochronology: Namaqualand, South Africa. *Journal of Petrology*, **40**(12), 1747–1770.

Sawyer, E. W. & Brown, M., 2008. *Working with migmatites*, Vol. 38, Mineralogical Assn of Canada.

Schaltegger, U., Fanning, C., Günther, D., Maurin, J., Schulmann, K. & Gebauer, D., 1999. Growth, annealing and recrystallization of zircon and preservation of monazite in high-grade metamorphism: conventional and in situ U-Pb isotope, cathodoluminescence and microchemical evidence. *Contributions to Mineralogy and Petrology*, **134**(2-3), 186–201.

Schoene, B., 2014. U–Th–Pb Geochronology. *Treatise on Geochemistry, Second Editionth edn. Elsevier, Oxford*, pp. 341–378.

Sibson, R. H., 1983. Continental fault structure and the shallow earthquake source. *Journal of the Geological Society*, **140**(5), 741–767.

Smith, H. A. & Giletti, B. J., 1997. Lead diffusion in monazite. *Geochimica et Cosmochimica Acta*, **61**(5), 1047–1055.

Stacey, J. & Kramers, J., 1975. Approximation of terrestrial lead isotope evolution by a two-stage model. *Earth and Planetary Science Letters*, **26**(2), 207–221.

Stipp, M., StuÈnitz, H., Heilbronner, R. & Schmid, S. M., 2002. The eastern Tonale fault zone: a natural laboratory for crystal plastic deformation of quartz over a temperature range from 250 to 700°C. *Journal of Structural Geology*, **24**(12), 1861–1884.

Tack, L., Liégeois, J. P., Deblond, A. & Duchesne, J. C., 1994. Kibaran A-type granitoids and mafic rocks generated by two mantle sources in a late orogenic setting (Burundi). *Precambrian Research*, **68**(3), 323–356.

Tam, P. Y., Zhao, G., Sun, M., Li, S., Iizuka, Y., Ma, G. S. K., Yin, C., He, Y. & Wu, M., 2012. Metamorphic P–T path and tectonic implications of medium-pressure pelitic granulites from the Jiaobei massif in the Jiao-Liao-Ji Belt, North China Craton. *Precambrian Research*, **220**, 177–191.

Thomas, R., Agenbacht, A., Cornell, D. & Moore, J., 1994. The Kibaran of southern Africa: tectonic evolution and metallogeny. *Ore Geology Reviews*, **9**(2), 131–160.

Toogood, D. J., 1976. *Structural and metamorphic evolution of a gneiss terrain in the Namaqua Belt near Onseepkans, South West Africa.* PhD thesis, University of Cape Town.

Tuccillo, M., Essene, E. & Van Der Pluijm, B., 1990. Growth and retrograde zoning in garnets from high-grade, metapelites: Implications for pressure-temperature paths. *Geology*, **18**(9), 839–842.

Tucker, N. M., Hand, M., Kelsey, D. E. & Dutch, R. A., 2015. A duality of timescales: Short-lived ultra-high temperature metamorphism preserving a long-lived monazite growth history in the Grenvillian Musgrave–Albany–Fraser Orogen. *Precambrian Research*, **264**, 204–234.

Ulmius, J., Andersson, J. & Möller, C., 2015. Hallandian 1.45 Ga high-temperature metamorphism in Baltica: P–T evolution and SIMS U–Pb zircon ages of aluminous gneisses, SW Sweden. *Precambrian Research*, **265**, 10–39.

Van Aswegen, G., Strydom, D., Colliston, W., Praekelt, H., Schoch, A., Blignault, H., Botha, B. & Van der Merwe, S., 1987. The structural-stratigraphic development of part of the Namaqua Metamorphic Complex, South Africa–an example of Proterozoic major thrust tectonics. *Proterozic Lithospheric Evolution*, pp. 207–216.

Van der Merwe, S. & Botha, B., 1989. The Groothoek thrust belt in western Namaqualand; an example of a mid-crustal structure. *South African journal of geology*, **92**(2), 155–166.

Vance, D., Müller, W. & Villa, I. M., 2003. Geochronology: linking the isotopic record with petrology and textures – an introduction. *Geological Society, London, Special Publications*, **220**(1), 1–24.

Vernon, R., 1974. Controls of mylonitic compositional layering during non-cataclastic ductile deformation. *Geological Magazine*, **111**(02), 121–123.

Vernon, R., 1996. Problems with inferring P–T–t paths in low-P granulite facies rocks. *Journal of Metamorphic Geology*, **14**(2), 143–153.

Vernon, R., White, R. & Clarke, G., 2008. False metamorphic events inferred from misinterpretation of microstructural evidence and P–T data. *Journal of Metamorphic Geology*, **26**(4), 437–449.

Villa, I. M., 1998. Isotopic closure. *Terra Nova-Oxford*, **10**(1), 42–47.

Wasserburg, G., 1963. Diffusion processes in lead-uranium systems. *Journal of Geophysical Research*, **68**(16), 4823–4846.

Waters, D., 1986. Metamorphic zonation and thermal history of pelitic gneisses from western Namaqualand, South Africa. *South African Journal of Geology*, **89**(2), 97–102.

Waters, D., 1988. Partial melting and the formation of granulite facies assemblages in Namaqualand, South Africa. *Journal of Metamorphic Geology*, **6**(4), 387–404.

Waters, D., 1989. Metamorphic evidence for the heating and cooling path of Namaqualand granulites. *Geological Society, London, Special Publications*, **43**(1), 357–363.

Wetherill, G. W., 1956. Discordant uranium-lead ages, I. *EOS, Transactions American Geophysical Union*, **37**(3), 320–326.

White, R. & Powell, R., 2010. Retrograde melt–residue interaction and the formation of near-anhydrous leucosomes in migmatites. *Journal of Metamorphic Geology*, **28**(6), 579–597.

White, R. & Powell, R., 2011. On the interpretation of retrograde reaction textures in granulite facies rocks. *Journal of Metamorphic Geology*, **29**(1), 131–149.

White, R., Powell, R. & Clarke, G., 2002. The interpretation of reaction textures in Fe-rich metapelitic granulites of the Musgrave Block, central Australia: constraints from mineral equilibria calculations in the system K_2O–FeO–MgO–Al_2O_3–SiO_2–H_2O–TiO_2–Fe_2O_3. *Journal of metamorphic Geology*, **20**(1), 41–55.

White, R., Powell, R. & Halpin, J., 2004. Spatially-focussed melt formation in aluminous metapelites from Broken Hill, Australia. *Journal of Metamorphic Geology*, **22**(9), 825–845.

White, R., Powell, R. & Holland, T., 2001. Calculation of partial melting equilibria in the system Na_2O–CaO–K_2O–FeO–MgO–Al_2O_3–SiO_2–H_2O (NCKFMASH). *Journal of Metamorphic Geology*, **19**(2), 139–153.

White, R., Powell, R. & Holland, T., 2007. Progress relating to calculation of partial melting equilibria for metapelites. *Journal of Metamorphic Geology*, **25**(5), 511–527.

White, R., Powell, R. & Johnson, T., 2014a. The effect of Mn on mineral stability in metapelites revisited: New a–x relations for manganese-bearing minerals. *Journal of Metamorphic Geology*, **32**(8), 809–828.

White, R., Powell, R., Holland, T., Johnson, T. & Green, E., 2014b. New mineral activity–composition relations for thermodynamic calculations in metapelitic systems. *Journal of Metamorphic Geology*, **32**(3), 261–286.

White, R. W., Powell, R. & Clarke, G. L., 2003. Prograde metamorphic assemblage evolution during partial melting of metasedimentary rocks at low pressures: migmatites from Mt Stafford, Central Australia. *Journal of Petrology*, **44**(11), 1937–1960.

Williams, M. L. & Jercinovic, M. J., 2002. Microprobe monazite geochronology: putting absolute time into microstructural analysis. *Journal of Structural Geology*, **24**(6), 1013–1028.

Williams, M. L., Jercinovic, M. J. & Hetherington, C. J., 2007. Microprobe monazite geochronology: understanding geologic processes by integrating composition and chronology. *Annual Review of Earth and Planetary Sciences*, **35**(1), 137.

Willis, J., 1999. Instrumental parameters and data quality for routine major and trace element determinations by WDXRFS. *Cape Town: Department of Geological Sciences Information Circular University of Cape Town*, **na**.

Zhu, X. & O'Nions, R., 1999a. Monazite chemical composition: some implications for monazite geochronology. *Contributions to Mineralogy and Petrology*, **137**(4), 351–363.

Zhu, X. & O'Nions, R., 1999b. Zonation of monazite in metamorphic rocks and its implications for high temperature thermochronology: a case study from the Lewisian terrain. *Earth and Planetary Science Letters*, **171**(2), 209–220.